

Copyright
by
Songcheng Li
2008

**The Dissertation Committee for Songcheng Li certifies that this is the approved
version of the following dissertation:**

**Deep Downhole Testing: Procedures and Analysis for
High-Resolution Vertical Seismic Profiling**

Committee:

Kenneth H. Stokoe II, Supervisor

Clark R. Wilson

Ellen M. Rathje

Fulvio Tonon

Loukas F. Kallivokas

**Deep Downhole Testing: Procedures and Analysis for
High-Resolution Vertical Seismic Profiling**

by

Songcheng Li, B.S.; M.S.

Dissertation

Presented to the Faculty of the Graduate School of

The University of Texas at Austin

in Partial Fulfillment

of the Requirements

for the Degree of

Doctor of Philosophy

The University of Texas at Austin

May 2008

Dedicated to My Body and Soul

Acknowledgements

This study is a result of a research effort that comprised the common effort of professors, professionals, and friends. As supervising professor and team leader, Dr. Kenneth H. Stokoe II played an irreplaceable role during the entire process of this research from the field test to the data processing stage. I would like to thank him for his insights into data analysis as well as his assistance on my field trips for data acquisition. His devotion to his chosen profession has inspired me to explore new frontiers of geotechnical engineering and geophysics. I also benefited from working for him as a Graduate Research Assistant.

I would like to thank Dr. Clark R. Wilson for his advice concerning the field signal quality and his ideas regarding data acquisition. He taught me virtually all the advanced data processing skills that expanded my knowledge of geophysics.

I appreciate Dr. Ellen M. Rathje for her extensive knowledge of geotechnical earthquake engineering that aided me in understanding the seismic site response and purpose of the current data analysis.

Special thanks also to Dr. Fulvio Tonon for discussions of differential equations and verification of some of my derivations. He also reminded me of the importance of anisotropy when considering travel time analysis.

Dr. Loukas F. Kallivokas imparted to me knowledge of wave propagation. I would like to thank him not only for giving me a better understanding in wave propagation, but also for assisting me with solving complex equations.

Dr. Farn-yuh Menq furthered my understanding of the process of field data acquisition, the functions of the field equipment, and related devices. I also thank him for directing me to outstanding references in the literature. In addition, I appreciate his support during my research involving data transfer, data analysis and other aspects.

Mr. Thomas M. Brouns, Dr. Alan C. Rohay, and their colleagues at the Pacific Northwest National Laboratory provided and edited helpful background knowledge of the project at Hanford, WA. They also helped me with revising the geological stratigraphy of the site and offered related references. I would also like to thank Dr. Alan C. Rohay for the inspiring discussions in signal processing.

I appreciate my friend Tianchun Zhou for our discussions regarding equations and solutions, which inspired some of my ideas in simplification of the derivations.

Without the support of my friend Laurel Meng Lelan Miller, the composition of the dissertation in such a short time would not have been possible. She performed significant editing work related to the dissertation. I am grateful for her hard work and her professional talent in languages.

I also benefited from help offered by my friend Minjae Jung, who provided many conveniences and assistance in my daily life that facilitated the progress of my research.

Crucial financial support for my study came from my brother Baiwan Li and his wife Huali Cao. I am grateful to their extensive care and love. I am also grateful to my friends and relatives, especially Bin Ma, Jiancheng Li, Yunquan Yang, Huojian Chen, Caifeng Liao, Zhijian Xiong and Haifeng Zhu, who also offered financial assistance.

I would like to thank Teresa Tice-Boggs, Chris Trevino, Norma Gonzales, Alicia Zapata and Kathleen Rose for their administrative support that advanced the progress of the research.

Deep Downhole Testing: Procedures and Analysis for High-Resolution Vertical Seismic Profiling

Publication No. _____

Songcheng Li, PhD

The University of Texas at Austin, 2008

Supervisor: Kenneth H. Stokoe, II

A study was undertaken to improve the signal quality and the resolution of the velocity profile for deep downhole seismic testing. Deep downhole testing is defined in this research as measurements below 225 m (750 ft). The study demonstrated that current testing procedures can be improved to result in higher signal quality by customizing the excitation frequency of the vibrator to local site conditions of the vibrator-earth system. The earth condition beneath the base plate can be an important factor in the signal quality subject to variations with time when tests are repetitive. This work proposes a convenient method to measure the site localized natural frequency and damping ratio, and recommends using different excitation frequencies for P- and S-wave generation. Properly increasing the excitation duration of the source signal also contributes to the quality of the receiver signal.

The source signature of sinusoidal vibratory source is identified. Conventional travel time analysis using vibratory source generally focuses on chirp sweeps. After

testing with impulsive sources and chirp sweeps and comparing the results with the durational sinusoidal source, the sinusoidal source was then chosen. This work develops an approach to identifying the source signature of the sinusoidal source and concludes that the normalized source signature is relevant only to four parameters: the fixed-sine excitation frequency, the duration of excitation, the damping ratio of the vibrator-earth system, and the damped natural frequency of the vibrator-earth system. Two of the parameters are designated input to the vibrator and the other two parameters are measured in the field test using the proposed method in this work.

A new wavelet-response technique based on deconvolution and consideration of velocity dispersion is explored in travel-time analyses. The wavelet-response technique is also used for development of a new approach to correcting disorientation of receiver tool. The improved downhole procedures and analyses are then used in the analysis of deep downhole test data obtained at Hanford, WA. Downhole testing was performed to a depth of about 420 m (1400 ft) at Hanford site. Improvements in resolving the wave velocity profiles to depths below 300 m (1000) ft are clearly shown.

Table of Contents

List of Tables	xiii
List of Figures.....	xiv
Chapter 1 Introduction.....	1
1.1 Background.....	1
1.2 Objectives of research.....	5
1.3 Organization of dissertation.....	6
Chapter 2 Wave Propagation in Anisotropic Layered Media.....	8
2.1 Introduction.....	8
2.2 Effect of anisotropy and heterogeneity.....	8
2.3 Effect of Nonlinearity.....	15
2.4 Transversely isotropic medium and Mode conversion.....	17
2.5 S-wave birefringence and S-wave splitting.....	20
2.6 Relationship of engineering constants and vertical velocities.....	21
2.7 Wave velocities in anisotropic media.....	25
2.8 Wave propagation in a homogeneous medium.....	31
2.9 Velocity dispersion.....	34
2.10 Phase velocity surface and group velocity surface.....	41
2.11 Summary.....	43
Chapter 3 Deep Downhole Testing.....	45
3.1 Introduction.....	45
3.2 Vibroseis Source.....	49
3.3 Nonlinear distortion in the vibroseis source.....	51
3.4 Field test configuration and test procedures.....	54
3.5 Travel times of multi-component signal.....	57
3.6 S-wave orientation and composition.....	63
3.7 Summary.....	66

Chapter 4	Simplified Analysis of Downhole Measurements.....	68
4.1	Introduction.....	68
4.2	Brief background of conventional analyses.....	69
4.3	Explanation of terminology used in DeepSeis 2.1.....	74
4.3.1	Record or signal.....	74
4.3.2	Input signal or drive signal.....	74
4.3.3	Reaction mass acceleration in vertical shaking.....	75
4.3.4	In-line and cross-line (x-line).....	76
4.3.5	Forward signal and reverse signal.....	77
4.3.6	Reaction mass acceleration in horizontal shaking.....	77
4.3.7	Weighted-sum force signal.....	78
4.3.8	Unfiltered signals.....	79
4.3.9	Filters and filtered signals.....	80
4.3.10	Pass band and low pass filter.....	82
4.3.11	Time shift.....	84
4.3.12	Relative travel times.....	86
4.3.13	Long lever arm and short lever arm.....	87
4.3.14	Reference receiver.....	87
4.3.15	Lower receiver.....	87
4.4	Waterfall plots of unfiltered and filtered P-wave records.....	88
4.5	Relative P-wave travel times and interpreted Vp profile.....	97
4.6	Unfiltered S-wave forward in-line records.....	104
4.7	Filtered and rotated S-wave in-line signals.....	114
4.8	Relative S-wave travel times and interpreted Vs profile.....	125
4.9	Summary.....	132
Chapter 5	Characteristics of Vibratory Source.....	134
5.1	Introduction.....	134
5.2	Source signature model.....	136
5.3	Damped forced vibration.....	141
5.2.1	Solution of steady-state vibration.....	142
5.2.2	Solution of transient vibration.....	145

5.2.3 Solution of damped forced vibration	148
5.4 Damped free vibration	148
5.5 Source signature.....	150
5.6 Fourier transform of source signature.....	157
5.6.1 Basic equations for Fourier transform	157
5.6.2 Fourier transform of sinusoidal wavelet	158
5.6.3 Fourier transform of transient wavelet.....	161
5.6.4 Fourier transform of trailing wavelet.....	163
5.6.5 Spectrum of the source signature.....	164
5.7 Summary	165
Chapter 6 Identification of Source Signature.....	168
6.1 Introduction.....	168
6.1.1 Impulsive source wavelet.....	168
6.1.2 Scalable source wavelet.....	169
6.1.3 Mixed-delay source wavelet	169
6.1.4 Source wavelet array.....	170
6.1.5 Source wavelet in this work.....	170
6.2 Logarithmic decrement method for damping ratio	171
6.3 Spectral analysis method for damping ratio.....	172
6.3.1 Measurement of damping ratio using displacement signal.....	176
6.3.2 Measurement of damping ratio using velocity signal	180
6.3.3 Measurement of damping ratio using acceleration signal.....	186
6.4 Identification of the source signature.....	186
6.4.1 Calculation of the normalized source signature.....	187
6.4.2 Calculation of the source signature.....	192
6.4.3 Calculation of the normalized velocity signature	195
6.4.4 Calculation of the normalized acceleration signature	197
6.5 Spectrum of the normalized source signature.....	199
6.6 Spectrum of the normalized velocity signature	204
6.7 Spectrum of the normalized acceleration signature	208
6.8 Summary	211

Chapter 7	Analysis of Wavelet Response	212
7.1	Introduction	212
7.2	Wavelet response for U-wavelet	214
7.3	Wavelet response for dual wavelets	220
7.4	Wavelet response for S-wave with negligible anisotropy	226
7.5	Wavelet response for S-wave with anisotropy	233
7.6	Numerical deconvolution and wavelet response	241
7.6.1	Zeros of source signature	241
7.6.2	Deconvolution of synthetic signal	242
7.6.3	Deconvolution of trace data	253
7.7	P-wave wavelet response in Borehole C4993	257
7.8	S-wave wavelet response in Borehole C4993	265
7.9	Summary	269
Chapter 8	Summary, Conclusions and Recommendations	271
8.1	Summary	271
8.2	Conclusions	274
8.3	Recommendations	275
References	276
Vita	288

List of Tables

Table 3.1	T-Rex features.....	47
-----------	---------------------	----

List of Figures

Figure 1.1	Geological stratigraphy of Borehole C4993 at Hanford WTP site	2
Figure 2.1	Wave propagation in an isotropic medium	10
Figure 2.2	Wave propagation in anisotropic medium	10
Figure 2.3	Illustration of pure and quasi polarizations.....	12
Figure 2.4	Scattering of P-wave particle motion.....	14
Figure 2.5	Transversely isotropic medium with a vertical symmetry axis	18
Figure 2.6	Slowness surface for an incident P-wave in isotropic medium	19
Figure 2.7	Slowness surface for an incident P-wave in anisotropic medium.....	19
Figure 2.8	Multiple wave reflections and refractions in TIV media	20
Figure 2.9	Illustration of velocity anisotropy.....	27
Figure 2.10	Comparison of phase velocity and group velocity.....	29
Figure 2.11	Deviation of the polarization and group direction from the phase direction	29
Figure 2.12	Experimentally observed velocities versus volume fraction of steel.....	36
Figure 2.13	(a) Experimental velocity versus the ratio λ /d and (b) numerical simulation velocity versus the ratio λ /d	38
Figure 2.14	Ray tracing based on Snell’s law through: (a) two layered media and (b) alternating layers of the same two layered media	39
Figure 2.15	Short-wavelength and long-wavelength average velocities as a function of the angle of incidence for Models A and B shown in Figure 2.14	39
Figure 2.16	Ray tracing through a ten-layered media	40
Figure 2.17	Short-wavelength and long-wavelength average velocities as a function of the angle of incidence for Model C	40
Figure 3.1	Tri-axial vibrator: T-Rex.....	50
Figure 3.2	Vertical mode of T-Rex	50
Figure 3.3	T-Rex theoretical force output.....	51
Figure 3.4	Deep downhole test setup diagram	54
Figure 3.5	Illustration of various ray paths of multilayer wave propagation.....	58
Figure 3.6	Waterfall plot of filtered P-wave receiver signals at Hanford site over the depth range of 900 to 1080 ft (270 to 324 m).....	59

Figure 3.7	P-wave acceleration signals from the reaction mass of T-Rex at the Hanford site.....	60
Figure 3.8	P-wave relative travel times and interpreted velocity profile in Borehole C4993 at Hanford site	61
Figure 3.9	P-wave receiver signals at WT-1 site, Yucca Mountain.....	62
Figure 3.10	Downhole test at Duke Cherokee site.....	62
Figure 3.11	The effect on the downhole P-wave signals of a known slope shown in Figure 3.10.....	63
Figure 3.12	Hodograph of S-wave signal in Borehole C4993 at Hanford site	64
Figure 3.13	Hodograph of filtered S-wave signal in Borehole C4993 at Hanford site.....	65
Figure 3.14	Polarization skewing, wave scattering and coupling of S-wave signal	66
Figure 4.1	5 cycles of 50-Hz P-wave drive signal to T-Rex	75
Figure 4.2	4 cycles of reversed sets of 30-Hz S-wave drive signals to T-Rex.....	75
Figure 4.3	Unfiltered P-wave acceleration signal of the reaction mass for 4 cycles of the 30-Hz sine-wave drive signal	76
Figure 4.4	Illustration of in-line and cross-line planes for S-wave generation	77
Figure 4.5	Unfiltered S-wave acceleration signals of the reaction mass excited in the forward and reverse directions with 4 cycles of a 30-Hz sine wave drive signal	78
Figure 4.6	Unfiltered weighted-sum force signal for 5 cycles of a 50-Hz sine wave drive signal	79
Figure 4.7	Unfiltered P-wave signal of lower receiver for 4 cycles of a 30-Hz sine wave drive signal.....	80
Figure 4.8	Unfiltered S-wave signal of lower in-line receiver for 4 cycles of a 30-Hz sine wave drive signal.....	80
Figure 4.9	Filtered P-wave signal of lower receiver for 4 cycles of a 30-Hz sine wave drive signal; low pass 40 Hz	81
Figure 4.10	Filtered S-wave signal of lower in-line receiver for 4 cycles of a 30-Hz sine wave drive signal; low pass 40 Hz	82
Figure 4.11	Amplitude spectrum of the unfiltered P-wave signal of the lower receiver at a depth of 1400 ft for 4 cycles of a 30-Hz sine wave drive signal; Expanded from 0 to 100 Hz.....	83
Figure 4.12	Pass band and reject band of a 40-Hz low pass filter	84
Figure 4.13	P-wave initial response of the reaction mass	84

Figure 4.14	First peak of the filtered acceleration signal of the reaction mass.....	85
Figure 4.15	Waterfall plot of unfiltered P-wave signals (370-560 ft).....	89
Figure 4.16	Waterfall plot of unfiltered P-wave signals (570-790 ft).....	90
Figure 4.17	Waterfall plot of unfiltered P-wave signals (800-980 ft).....	91
Figure 4.18	Waterfall plot of unfiltered P-wave signals (980-1400 ft).....	92
Figure 4.19	Waterfall plot of filtered P-wave signals (370-560 ft).....	93
Figure 4.20	Waterfall plot of filtered P-wave signals (570-790 ft).....	94
Figure 4.21	Waterfall plot of filtered P-wave signals (800-980 ft).....	95
Figure 4.22	Waterfall plot of filtered P-wave signals (980-1400 ft).....	96
Figure 4.23	Relative P-wave travel times and interpreted Vp Profile in Borehole C4993	97
Figure 4.24	Expanded relative P-wave travel times (300–800 ft).....	98
Figure 4.25	Expanded relative P-wave travel times (600–1100 ft).....	98
Figure 4.26	Expanded relative P-wave travel times (900–1400 ft).....	99
Figure 4.27	Comparison of P-wave velocities from downhole and suspension logging tests in Borehole C4993.....	102
Figure 4.28	Comparison of P-wave velocities from downhole and suspension logging tests in Borehole C4993 and lab test in Borehole C4998	103
Figure 4.29	Horizontal disorientation of the receiver tool.....	104
Figure 4.30	Unfiltered forward S-wave signal of lower in-line receiver (370– 475 ft).....	106
Figure 4.31	Unfiltered forward S-wave signal of lower in-line receiver (480– 540 ft).....	107
Figure 4.32	Unfiltered forward S-wave signal of lower in-line receiver (550– 660 ft).....	108
Figure 4.33	Unfiltered forward S-wave signal of lower in-line receiver (670– 760 ft).....	109
Figure 4.34	Unfiltered forward S-wave signal of lower in-line receiver (770– 870 ft).....	110
Figure 4.35	Unfiltered forward S-wave signal of lower in-line receiver (880– 990 ft).....	111
Figure 4.36	Unfiltered forward S-wave signal of lower in-line receiver (990– 1100 ft).....	112

Figure 4.37	Unfiltered forward S-wave signal of lower in-line receiver (1110–1300 ft).....	113
Figure 4.38	Filtered and rotated S-wave in-line signals (370–475 ft).....	115
Figure 4.39	Filtered and rotated S-wave in-line signals (480–540 ft)	116
Figure 4.40	Filtered and rotated S-wave in-line signals (550–660 ft).....	117
Figure 4.41	Filtered and rotated S-wave in-line signals (670–760 ft).....	118
Figure 4.42	Filtered and rotated S-wave in-line signals (770–870 ft).....	119
Figure 4.43	Filtered and rotated S-wave in-line signals (880–990 ft).....	120
Figure 4.44	Filtered and rotated S-wave in-line signals (990–1110 ft).....	121
Figure 4.45	Filtered and rotated S-wave in-line signals (1120–1300 ft).....	122
Figure 4.46	Waterfall plot of S-wave rotated in-line signals (990–1300 ft)	123
Figure 4.47	Estimation of S-wave arrival time using the P-wave arrival as a reference.....	124
Figure 4.48	Relative S-wave travel times and interpreted Vs profile in Borehole C4993	126
Figure 4.49	Expanded relative S-wave travel times (300–800 ft).....	126
Figure 4.50	Expanded relative S-wave travel times (600–1100 ft).....	127
Figure 4.51	Expanded relative S-wave travel times (900–1400 ft).....	127
Figure 4.52	Comparison of S-wave velocities between downhole and suspension logger tests in Borehole C4993	130
Figure 4.53	Comparison of S-wave velocities from downhole and suspension logging tests in Borehole C4993 and lab test at Borehole C4998	131
Figure 5.1	Illustration of a vibrator-earth system.....	134
Figure 5.2	Displacement of a SDOF system under finite sinusoidal excitation.....	137
Figure 5.3	Heaviside step function.....	137
Figure 5.4	Rectangular pulse.....	138
Figure 5.5	Causal rectangular pulse	139
Figure 5.6	Source signature and its wavelets (excitation frequency 50 Hz, natural frequency 100 Hz, duration 0.1 sec, damping ratio 25%)	140
Figure 5.7	Source signature A (excitation frequency 50 Hz, natural frequency 40 Hz, duration 0.1 sec, damping ratio 5%)	153
Figure 5.8	Source signature B (excitation frequency 50 Hz, natural frequency 40 Hz, duration 0.1 sec, damping ratio 25%)	153

Figure 5.9	Source signature C (excitation frequency 50 Hz, natural frequency 20 Hz, duration 0.1 sec, damping ratio 25%)	156
Figure 5.10	Source signature D (excitation frequency 50 Hz, natural frequency 80 Hz, duration 0.1 sec, damping ratio 25%)	156
Figure 6.1	Damped free vibration of a SDOF system with an arbitrary initial phase	171
Figure 6.2	(a) damped free sine (DFS) vibration and (b) its spectrum	174
Figure 6.3	Map of the general Equation (6.1) to DFS Equation (6.7).....	177
Figure 6.4	Map of the general Equation (6.1) to out-of-phase DFS Equation (6.7).....	178
Figure 6.5	Map of the general Equation (6.1) to DFC vibration (6.32).....	180
Figure 6.6	S-wave reference signal recorded with horizontal velocity transducer	182
Figure 6.7	Expanded unfiltered S-wave reference signal recorded with horizontal velocity transducer.....	182
Figure 6.8	Filtered S-wave reference signal recorded with horizontal velocity transducer	182
Figure 6.9	Expanded filtered S-wave reference signal recorded with horizontal velocity transducer.....	183
Figure 6.10	S-wave damping ratio measurement using velocity signal.....	183
Figure 6.11	S-wave damping ratio measurement using part of the velocity signal	184
Figure 6.12	P-wave reference signal recorded with a vertical velocity transducer	185
Figure 6.13	P-wave damping ratio measurement using velocity signal.....	185
Figure 6.14	Displacement signature of the model test (excitation frequency 50 Hz, duration 0.1 sec, damped frequency 100 Hz, damping ratio 25%).....	192
Figure 6.15	Flow chart for calculation of the source signatures	194
Figure 6.16	Velocity signature of the model test (excitation frequency 50 Hz, duration 0.1 sec, damped frequency 100 Hz, damping ratio 25%).....	197
Figure 6.17	Acceleration signature of the model test (excitation frequency 50 Hz, duration 0.1 sec, damped frequency 100 Hz, damping ratio 25%).....	199

Figure 6.18	Displacement spectrum of source signature of the model test (excitation frequency 50 Hz, duration 0.1 sec, damped frequency 100 Hz, damping ratio 25%).....	202
Figure 6.19	Displacement spectrum of sinusoidal wavelet of the model test (excitation frequency 50 Hz, duration 0.1 sec, damped frequency 100 Hz, damping ratio 25%).....	203
Figure 6.20	Displacement spectrum of transient and trailing wavelets of the model test (excitation frequency 50 Hz, duration 0.1 sec, damped frequency 100 Hz, damping ratio 25%).....	203
Figure 6.21	Displacement spectrum of twin wavelets of the model test (excitation frequency 50 Hz, duration 0.1 sec, damped frequency 100 Hz, damping ratio 25%).....	204
Figure 6.22	Velocity spectrum of source signature of the model test (excitation frequency 50 Hz, duration 0.1 sec, damped frequency 100 Hz, damping ratio 25%).....	206
Figure 6.23	Velocity spectrum of sinusoidal wavelet of the model test (excitation frequency 50 Hz, duration 0.1 sec, damped frequency 100 Hz, damping ratio 25%).....	207
Figure 6.24	Velocity spectrum of twin wavelets of the model test (excitation frequency 50 Hz, duration 0.1 sec, damped frequency 100 Hz, damping ratio 25%).....	207
Figure 6.25	Acceleration spectrum of source signature of the model test (excitation frequency 50 Hz, duration 0.1 sec, damped frequency 100 Hz, damping ratio 25%).....	210
Figure 6.26	Acceleration amplitude spectrum of sinusoidal wavelet of the model test (excitation frequency 50 Hz, duration 0.1 sec, damped frequency 100 Hz, damping ratio 25%).....	210
Figure 6.27	Acceleration spectrum of twin wavelets of the model test (excitation frequency 50 Hz, duration 0.1 sec, damped frequency 100 Hz, damping ratio 25%).....	211
Figure 7.1	Illustration of amplitude attenuation and time delay of wave propagation	215
Figure 7.2	Noise-free single wavelet response.....	217
Figure 7.3	Velocity dispersion of dual wavelets with time and depth	217
Figure 7.4	Noise-free dual wavelet response	218
Figure 7.5	Source signature and its wavelets (excitation frequency 50 Hz, natural frequency 40 Hz, duration 0.1273 sec, damping ratio 25%)	222

Figure 7.6	Energy contribution of the sinusoidal wavelet and the twin wavelets defined in Figure 7.5	223
Figure 7.7	P-wave signal of five cycles of a 50-Hz sine wave	224
Figure 7.8	The wavelet response of the P-wave signal in Figure 7.7.....	225
Figure 7.9	The low-pass filtered wavelet response of the P-wave signal in Figure 7.7	225
Figure 7.10	Amplitude spectra of a P-wave signal recorded at a depth of 111 m (370 ft) and its SDOF source signature.....	225
Figure 7.11	Amplitude spectra of a P-wave signal recorded at a depth of 291 m (970 ft) and its SDOF source signature.....	226
Figure 7.12	Hodograph and polarization of S-wave recorded on a horizontal plane.....	227
Figure 7.13	Polarization of S-wave when anisotropy is weak	228
Figure 7.14	Wavelet response pairs of S-wave components.....	229
Figure 7.15	Two components of S-wave records at a depth of 114 m (380 ft).....	229
Figure 7.16	Spectra of two components of the S-wave signal and the source signature.....	230
Figure 7.17	The wavelet response of the two components of the S-wave signal recorded at a depth of 114 m (380 ft)	230
Figure 7.18	Spike singleton indicates correct orientation	231
Figure 7.19	Multi-polarization hodograph of S-wave signal	232
Figure 7.20	Wavelet response pair for multi-polarization S-wave signal.....	233
Figure 7.21	Shifted wavelet responses of the two components of the S-wave signal.....	233
Figure 7.22	Hodograph of S-wave signal with strong anisotropy.....	234
Figure 7.23	Shifted wavelet responses of S-wave components	234
Figure 7.24	Relative time shift of wavelet responses of S-wave components	235
Figure 7.25	Relationship of local and general coordinate systems	236
Figure 7.26	Estimation of S-wave arrival time using two S-wave components	240
Figure 7.27	Synthetic source signature (excitation frequency 50 Hz, natural frequency 20 Hz, duration 0.1 sec, damping ratio 25%)	244
Figure 7.28	Synthetic signal $s(t)$	245
Figure 7.29	Amplitude spectrum of the synthetic signal $s(t)$ in Figure 7.28.....	245

Figure 7.30	Comparison of the amplitude spectra of the synthetic signal $s(t)$ and the synthetic signature $u(t)$	246
Figure 7.31	Amplitude spectrum of the synthetic signal $s(t)$ below Nyquist Frequency.....	247
Figure 7.32	Amplitude spectrum of the wavelet response in linear scale	247
Figure 7.33	Amplitude spectrum of the wavelet response in decibel scale	248
Figure 7.34	Expanded view of amplitude spectrum in Figure 7.33	248
Figure 7.35	Wavelet response when $\alpha = 0$	249
Figure 7.36	Wavelet response when $\alpha = 0.001$	249
Figure 7.37	Wavelet response when $\alpha = 0.1$	250
Figure 7.38	Wavelet response using sinusoidal wavelet when $\alpha = 0.001$	250
Figure 7.39	Wavelet response using twin wavelets when $\alpha = 0.001$	250
Figure 7.40	Wavelet response using twin wavelets when $\alpha = 0.1$	251
Figure 7.41	Spectrum of wavelet response using twin wavelets when $\alpha = 0.001$	251
Figure 7.42	Wavelet response using twin wavelets when $\alpha = 0.001$ and filtered by low pass 40 Hz.....	252
Figure 7.43	Wavelet response filtered by low pass 500 Hz.....	252
Figure 7.44	Wavelet response filtered by low pass 100 Hz.....	253
Figure 7.45	Wavelet response filtered by low pass 20 Hz.....	253
Figure 7.46	Wavelet response filtered by low pass 15 Hz.....	253
Figure 7.47	P-wave receiver signal (5 cycles of 50-Hz sine wave) at a depth of 291 m (970 ft)	254
Figure 7.48	Spectra of P-wave receiver signal (5 cycles of 50-Hz sine wave) at a depth of 291 m (970 ft) and its source signature.....	254
Figure 7.49	Spectrum of wavelet response ($\alpha = 0.1$) of P-wave receiver signal (5 cycles of 50 Hz sine wave) at a depth of 291 m (970 ft).....	255
Figure 7.50	Wavelet response of P-wave receiver signal (5 cycles of 50 Hz sine wave) at a depth of 291 m (970 ft) using source signature wavelet	255
Figure 7.51	Wavelet response of P-wave receiver signal (5 cycles of 50 Hz sine wave) at a depth of 291 m (970 ft) using sinusoidal wavelet	256
Figure 7.52	S-wave receiver signals (5 cycles of 50 Hz sine wave) at a depth of 114 m (380 ft)	256

Figure 7.53	Wavelet response of S-wave receiver signals (5 cycles of 50 Hz sine wave) at a depth of 114 m (380 ft) using source signature wavelet	256
Figure 7.54	Wavelet response of S-wave receiver signals (5 cycles of 50 Hz sine wave) at a depth of 114 m (380 ft) using sinusoidal wavelet.....	257
Figure 7.55	Wavelet response of 50-Hz P-wave receiver signals (370-515 ft)	258
Figure 7.56	Wavelet response of 50-Hz P-wave receiver signals (520-700 ft)	259
Figure 7.57	Wavelet response of 50-Hz P-wave receiver signals (700-870 ft)	260
Figure 7.58	Wavelet response of 50-Hz P-wave receiver signals (880-980 ft)	261
Figure 7.59	Wavelet response of 30-Hz P-wave receiver signals (980-1160 ft)	262
Figure 7.60	Wavelet response of 30-Hz P-wave receiver signals (1170-1400 ft)	263
Figure 7.61	Comparison of relative travel times and interpreted Vp profiles in Borehole C4993 between arrival-identification method and wavelet-response method.....	264
Figure 7.62	Wavelet response of 50-Hz forward S-wave signals of disoriented receiver (900–990 ft).....	266
Figure 7.63	Wavelet response of 30-Hz forward S-wave signals of disoriented receiver (990–1110 ft).....	267
Figure 7.64	Wavelet response of 30-Hz forward S-wave signals of disoriented receiver (1120–1300 ft).....	268
Figure 7.65	Comparison of relative travel times and interpreted Vs profiles in Borehole C4993 between arrival-identification method and wavelet-response method.....	269

Chapter 1 Introduction

1.1 BACKGROUND

The U.S. Department of Energy (DOE) and the Pacific Northwest National Laboratory (PNNL) drilled three boreholes to a depth of approximately 420 m (1400 ft) below the ground surface at the Waste Treatment and Immobilization Plant (WTP) construction site on the Hanford Site in southeastern Washington. The goal of the new boreholes was to obtain direct shear (S) and compression (P) wave velocity measurements in the subsurface to reduce uncertainty both in seismic response spectra and the design basis for the WTP. The University of Texas at Austin (UT) was selected by PNNL to collect S- and P-wave measurements over the depth range of about 110 to 420 m (360 to 1400 ft) in each of the three new boreholes identified as C4993, C4996 , and C4997 (Barnett et al, 2007; Gardner and Price , 2007).

Redpath Geophysics was contracted for the acquisition of velocity measurements in shallow alluvial sediments located from the ground surface to a depth of approximately 110 to 120 m (360 to 400 ft) using impulsive S- and P-wave seismic sources (Redpath Geophysics, 2007). In addition, the testing by Redpath Geophysics overlapped with the UT testing by about 90 m (300 ft) in the rock beneath the alluvium. As participants in the project, researchers from UT used the T-Rex tri-axial vibrator to obtain measurements below the depth of 120 m (400 ft) within basaltic and sedimentary interbeds in each of the three boreholes (Stokoe et al , 2004).

Figure 1.1 displays the generalized site which consists of alternating layers characterized by strong velocity contrast below the alluvium. The alluvium consists of the Hanford Formation H2, Hanform Formation H3, Cold Creek Unit and Ringold Formation Unit A as shown in Figure 1.1.

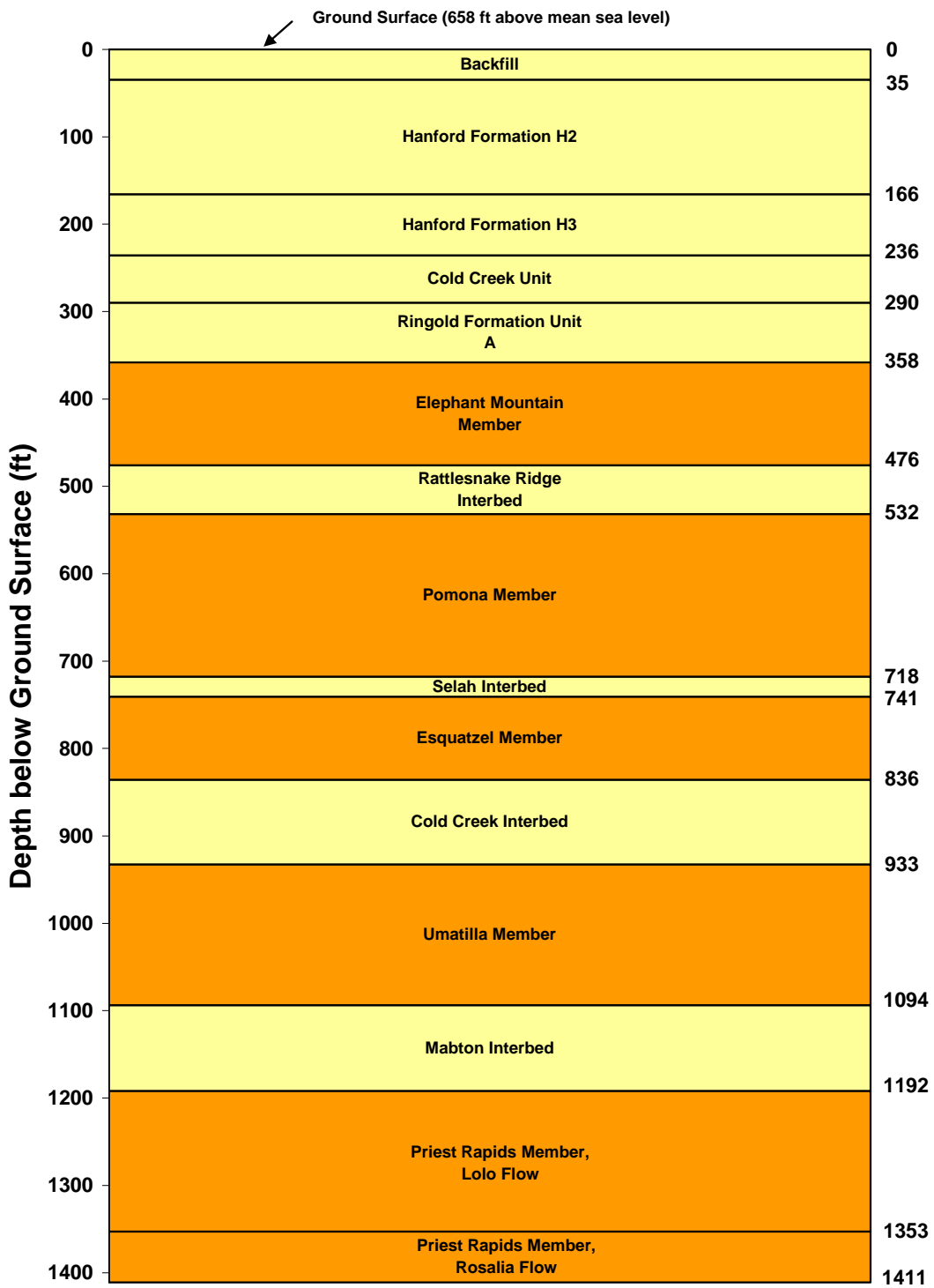


Figure 1.1 Geological stratigraphy of Borehole C4993 at Hanford WTP site

The depths used in Figure 1.1 are taken from Barnett et al. (2007) and Rohay and Brouns (2007). The alluvium is 107 m (358 ft) thick at Borehole C4993. Alternating basalt layers and sedimentary interbeds underlie the alluvium. The interbeds are both thinner and softer than the surrounding basalt layers. The wave velocities of the basalt rock layers are about twice to three times that of the interbeds. The stratigraphy is characterized by alternating strong contrast in stiffness.

The frequencies generated by a vibrator source, including the T-Rex mobile shaker, create a source signal with wavelengths greater than the thicknesses of most layers. Conventional vibratory source is a chirp sweep with a band of frequencies that vary linearly with time. Multilayer reflection and velocity dispersion contribute to poor resolution in cross-correlation of chirp sweep signals with trace data. In an effort to improve resolution, fixed-sine source signals, which are wavelets generated by a fixed excitation frequency, were also chosen for investigations to acquire data in this research. The vibratory source signal that was used was 4 to 10 cycles of a sine wave with a fixed frequency of 20, 30 or 50 Hz. This signal is a specific frequency for the fixed sine wave which is readily generated with T-Rex.

Multiple direct arrivals and reflections constitute a multi-component signal. Strong reflectivity between layer reflectors, especially thin layers, causes waveform distortion that presents challenges for travel time analysis using conventional wave identification and cross-correlation methods. Errors in travel time analysis due to these complicated factors affect the resolution of velocity profiling in that the cross correlation in the time domain is affected by the reflections. The separation of reflections and direct arrivals is a key step to obtaining more accurate travel time measurements and, hence, more accuracy and resolution in the velocity profiles for engineering purposes. Superposition of multi-cycle waveforms of multiple shifted reflections can significantly

shift cross-correlation peaks because cross-correlation relies on the shape of the waveforms, which can be distorted by reflections and lower- or higher-frequency noise. For S-wave signals, the preceding P-wave components as well as possible waves from the cable suspending the geophones further compromise cross correlation.

The difference between an impulsive source and a durational source wavelet results in much greater differences in travel time analysis. The short duration of impulsive source wavelets are of such duration that the overlap of multi-components in the receiver signal does not pose a significant problem. However, durational wavelets generated by the vibrator can display overlapping from the first break (multi-path direct arrivals) through the end of the time record (reflections, coupling of converted and/or split waves). The use of deconvolution and reflectivity coefficients may improve the resolution of the travel time analysis. Hence, the use of reflection coefficients from deconvolution requires identification of the source signature of the durational wavelets.

The velocity dispersion of different frequencies provides an advantage to using a fixed-sine source signal as opposed to using chirp sweep signals. The chirp sweep signals have a band of frequencies that velocity dispersion is of concern when site stratigraphy is characterized by alternating hard and weak rock layers. The fixed-sine source signal has at most two significant frequencies. One is the excitation frequency and the other is the damped natural frequency of the vibrator-earth system. The velocity dispersion effect of the fixed-sine source signal can be easily evaluated.

The impulse response includes velocity dispersion caused by frequency contents, but it treats the dispersion as a spread impulse instead of a separate impulse for each frequency. The impulse response is adequate for tracking group energy, but does not take into account the resolution for velocity variation when the dominant frequency content has changed or shifted during propagation. The wavelet response is the linear

combination of the impulse responses of each pure wavelet that carries a single frequency. The separation of up-going and down-going signal components from the receiver signal is more difficult for wavelet response than for the impulse response.

1.2 OBJECTIVES OF RESEARCH

The objective of this research is to find a method to improve the resolution of velocity profiling in deep downhole tests for engineering studies at sites where the geological stratigraphy exhibits strong velocity contrasts. Deep downhole testing is defined in this research as testing below a depth of 225 m (750 ft). The availability of the powerful T-Rex vibroseis enables deeper ground investigation without the use of dynamite, excavation, or other methods. The unique geological stratigraphy of the research site attenuates and reflects wave vibration energy in such a way that poses challenges to the analysis of weak and distorted signals deep within the ground. The existence of thin layers presents another difficulty for investigation methods using long wavelength sources as used in this work.

Durational source signals generally cause severe wavelet overlap, polarization change, nonlinear polarization and waveform distortion, which make the use of conventional, hand-picked, first-break techniques particularly difficult. The fixed-sine source signal is neither an impulsive wavelet nor a chirp sweep, thus the conventional impulse response method or cross-correlation technique cannot be applied in this case. An approach to source signature identification for fixed-sine source signals is presented for the acquisition of arrival and reflection coefficients. A method for in-situ measurement of damping ratio and natural frequency for the vibrator-earth system is proposed. The wavelet response technique for travel time analysis is explored and applied. The benefit of this research is then demonstrated with comparisons of the different analysis procedures at a test site in Hanford, WA.

1.3 ORGANIZATION OF DISSERTATION

Chapter 2 briefly introduces wave propagation in homogeneous anisotropic media. This introduction is followed by a discussion of how vertical velocity measurements provide an understanding of the engineering parameters (stiffness) and anisotropy. The Christoffel Equation for plane wave propagation is also presented in the chapter and use of the equation in the calculation of the difference between the phase and group velocities is discussed. The complexity of wave propagation in real earth is also discussed.

The new downhole field test procedures with a fixed sinusoidal input are introduced in Chapter 3. The method of hand-picking wave arrivals is used in this chapter to demonstrate travel time analysis for velocity profiles. Complete analysis for both P- and S-wave measurements using the new fixed-sine source are presented in detail in Chapter 4. In addition, the terminology and approaches used to develop the DeepSeis 2.1 software program are discussed. DeepSeis 2.1 was used in analyzing all travel time data collected at the Hanford site.

The characteristic of the source signal that is not directly available from field measurements because of the near-field effect is studied in Chapter 5. Source signals consist of a forced vibration followed by a free vibration. Derivations of equations for time- and frequency-domain solutions are presented to be used for signature identification in following chapters. The source signal is divided into two pure wavelets that define the analytical format of the source signature.

A method to differentiate the source signature from the field measurements is presented in Chapter 6. Determination of the damping ratio and natural frequency of the vibrator-earth system is the first step to the identification of the source signature, which is evaluated in the frequency domain. The boundary conditions between the forced

vibration and free vibration wavelets provide for complete identification of the source signature.

A discussion of how the deconvolution technique utilizes the source signature to acquire the wavelet response of the receiver signals is presented in Chapter 7. Criteria for obtaining improved receiver signals are proposed by using a specific frequency that reflects the local vibrator-earth properties. A new approach for correction of S-wave disorientation of the receiver tool is proposed. The wavelet-response method, which is implemented in the upgraded software version called DeepSeis 3.1, was developed to improve the resolution of travel time analysis. An example of the improvement is presented at the end of Chapter 7.

Summary, conclusions, and recommendations are presented in Chapter 8.

Chapter 2 Wave Propagation in Anisotropic Layered Media

2.1 INTRODUCTION

The measurement of wave velocity in the downhole method for obtaining desired engineering parameters in seismic analysis is introduced in this chapter. Factors such as anisotropy, heterogeneity, nonlinearity, mode conversion, S-wave birefringence, and S-wave splitting which affect signal quality in deep downhole testing are introduced. Wave propagation in homogeneous anisotropic media is presented as an example to demonstrate the complexity of wave propagation in real earth. Velocity dispersion due to anisotropy is one of the major sources of waveform distortion and travel-time misinterpretation.

It is also important to point out that, for the deep downhole testing considered in the research, the direction of wave propagation becomes nearly vertical because the vertical deviation of the source-receiver direction is within 5 degrees. For example, the offset of the vibratory source to Borehole C4993 is 7.5 m (25 ft), the top measurement is at a depth of 110 m (370 ft), and the deepest measurement is at 420 m (1400 ft). The vertical deviation angle of the source-receiver direction is between 1.0 to 3.9 degrees.

2.2 EFFECT OF ANISOTROPY AND HETEROGENEITY

Anisotropy describes the degree of change in material properties with direction if measured at the same location. If the properties of a material measured at the same location do not vary with direction, the material is isotropic. Heterogeneity describes the degree of variation of the material's properties with location when measured in the same direction. If the properties of a material measured in the same direction do not change with location, the material is termed homogeneous. Winterstein (1990) suggested that the

term anisotropy be constrained to indicate the variation of properties with direction in homogeneous materials as opposed to those of heterogeneous materials. Winterstein pointed out that the scale used to consider the dimension and the size of rocks is important in differentiating anisotropy from inhomogeneity. For example, locally homogeneous and anisotropic material that varies systematically on a large scale is still considered anisotropic. An inhomogeneous material with smooth variations in properties that are predictable based on the scale of the wavelengths used to probe those properties is called anisotropic instead of inhomogeneity as long as such variations do not change the symmetry properties of the material.

Velocity anisotropy represents the variation of wave velocity with direction of wave propagation in a homogeneous medium where homogeneity extends over distances on the order of or exceeding a wavelength (Winterstein, 1990). Figure 2.1 illustrates wave propagation from source point O into an isotropic medium along ray path OA. The wavefront is a locus in the wave field with the same phase angle. The wave propagation direction is the direction with the greatest phase gradient. As shown in Figure 2.1, the wavefront in an isotropic medium is circular, indicating equal velocity in all directions. The propagation direction is denoted by angle ϕ . Along the circumference of the circular wavefront, the P-wave particle motion direction, P_1 at point A, is parallel to the propagation direction. Wave propagation in an anisotropic medium is illustrated in Figure 2.2, where wave velocities vary with direction. The corresponding wavefront has an elliptical shape. The instant propagation direction is perpendicular to the tangent of the local wavefront, as denoted by θ . P-wave particle motion at point B, as denoted by P_2 in Figure 2.2, is no longer parallel to the propagation direction.

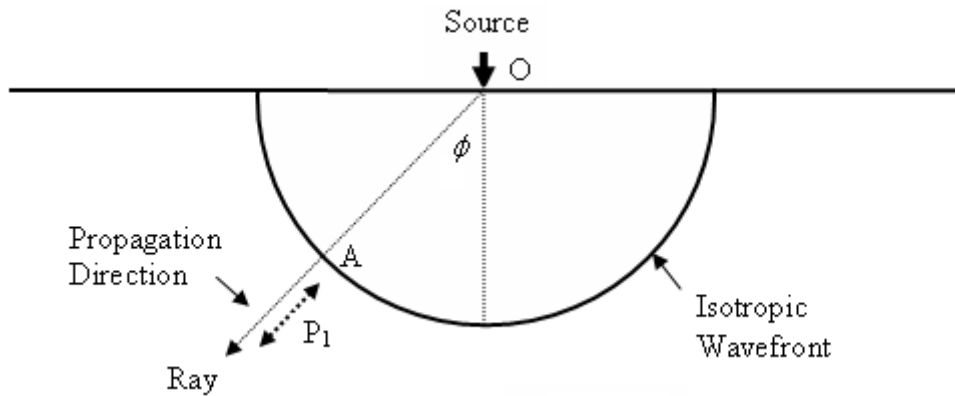


Figure 2.1 Wave propagation in an isotropic medium

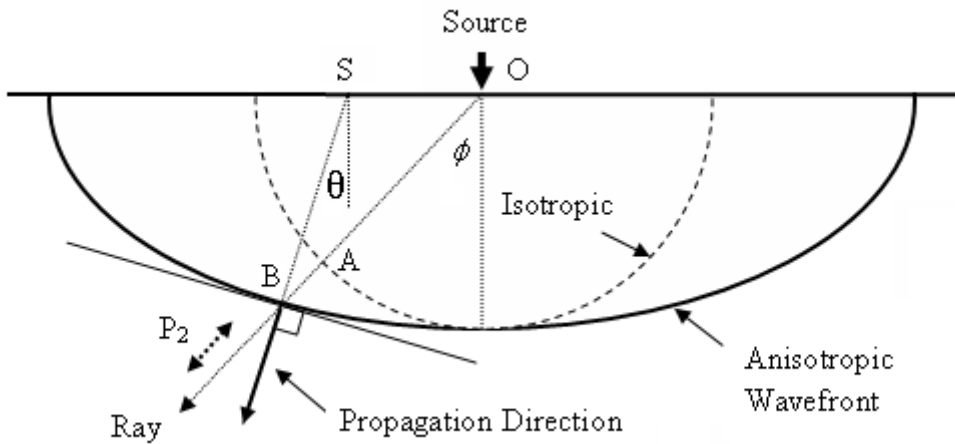


Figure 2.2 Wave propagation in anisotropic medium

Polarization is a term widely used to describe the trajectory shape and spatial orientation of particle motion. The polarization direction specifies the polarization of waves traveling along actual rays. Polarization direction is sometimes referred to as displacement direction. When particle motion is along a straight line as denoted by P_1 , the polarization is linear or the motion has polarity. Linear polarization occurs in a noise-free and perfectly elastic medium if the waves are separate. Actual polarizations can be nonlinear and of arbitrary shape. Polarization directions may vary with direction of

propagation. The source is not the sole determinant of the polarization direction, but also the medium.

Polarization of P waves in isotropic media is parallel to the direction of propagation and polarizations of S waves are perpendicular to the direction of wave propagation. Polarizations of waves in anisotropic media are generally neither perpendicular nor parallel to the direction of propagation as denoted by P_2 . When polarization of a wave in an isotropic or an anisotropic medium is either perpendicular or parallel to the propagation direction, the wave is called pure. Otherwise, it is called “quasi”, which means similar. For example, the P wave denoted by P_1 is a pure P-wave, while the P wave denoted by P_2 is a quasi-P wave, or quasi-longitudinal wave. The term “quasi” is sometimes denoted by “q”, for example qP wave. When the polarization detail is not of concern, the “quasi” or “q” is commonly dropped in the literature. If the departure of polarization of quasi waves exceeds 45 degrees from the pure polarization, then the term “quasi” is not applied (Winterstein, 1990).

An S wave has two polarizations. The S wave polarized in the vertical plane is referred to as an “SV wave”, and the one polarized in the horizontal plane is an “SH-wave”. The use of SV and SH can be confusing because their polarizations are not always vertical or horizontal during propagation because polarizations may vary. For example, in transversely isotropic medium with a tilted symmetry axis, SH-wave polarization may not always be horizontal. An SV wave and an SH wave in isotropic medium are distinguished by their plane of incidence. An SV wave lies in the plane of incidence, while an SH wave is perpendicular to it. S_1 and S_2 are generally used instead of SV and SH in anisotropic media. S_1 represents the faster S wave and S_2 the slower one for a specific wave propagation direction (Figure 2.3).

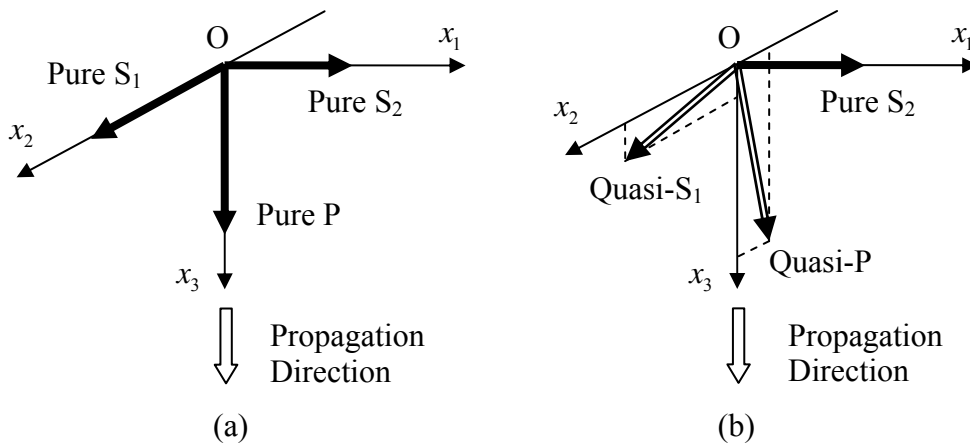


Figure 2.3 Illustration of pure and quasi polarizations

Three main factors contribute to the anisotropy in sedimentary rock (Thomsen, 1986): the first factor is intrinsic anisotropy, which is caused by the orientation of anisotropic mineral grains or the shapes of isotropic minerals; the second is thin bedding of isotropic layers, and the third is fractures or cracks.

Early problems involving anisotropy were solved by examining equivalent isotropic solutions applicable to anisotropy of stratified media for reflection seismics. Krey and Helbig (1956) determined the reflections of longitudinal waves for a small dip by considering the anisotropic material or the stratified media as isotropic because materials comprising a horizontally stratified media do not differ in the value of Poisson ratio. They found that approximating the surface of the wave using an ellipsoid resulted in significant errors. Backus (1962) studied long-wave elastic anisotropy created by horizontal layering and used the averaging technique to obtain the stiffness matrix of an effective medium that consists of many constituents within the thickness of one wavelength. The effective velocity is determined by the real-valued stiffness elements which are independent of attenuation. Berryman (1979) studied long-wave, elastic

anisotropy in transversely layered media and concluded that anisotropic effects are greatest in areas where the layering is quite thin (3-15 m or 10-50 ft) for seismic signals whose frequency range is typically below 50 Hz. Berryman (1979) considered the effects of relaxing the assumptions associated with a constant Poisson's ratio. Using the perturbation method for the near-offset test such as a deep downhole test, Berryman demonstrated that the anisotropy of P-waves is always negligible when ray path angles are nearly vertical or less than 15 degrees, while the anisotropy of S-waves caused by small angles of less than 15 degrees can still be substantial.

Thomsen (1986) introduced a critical anisotropic parameter δ (discussed in section 2.7), which is a combination of elastic parameters, and found that δ controls most anisotropic phenomena of importance in exploration geophysics. He concluded that in most cases of interest to geophysicists, the anisotropy is weak (the anisotropic parameter $\delta=10-20\%$), even though many of their constituent minerals are highly anisotropic. Thomsen drew four important conclusions from weak anisotropy equations: (1) the most common measure of anisotropy (contrasting vertical and horizontal velocities) does not adequately address problems of near-vertical P-wave propagation; (2) the definition of the most critical measure of anisotropy δ does not include the horizontal velocity and is in fact often left undetermined by experimental programs intended to measure anisotropy of rock samples; (3) the simplification of the anisotropic wave-velocity equations (elliptical anisotropy) is generally inappropriate and misleading for P- and SV-waves; and (4) estimating horizontal stress through the use of Poisson's Ratio obtained from vertical P and S velocities frequently results in significant error. These conclusions apply irrespective of the physical cause of the anisotropy.

Heterogeneity is also a factor affecting signal quality. Minor heterogeneities in materials were studied by Nair and Nemat-Nasser (1971). Gradual variations of a half

space were studied by Kluwick and Nayfeh (1979) to research heterogeneous effects caused by gradual variations of material properties. Sato et al (1998) discussed the scattering of seismic waves caused by random inhomogeneities. Particle motion surrounding the direct-wave arrival showed evidence of scattering along the propagation path from the source to the receiver. The researchers used the 3-D covariance matrix to analyze the 3-D particle motion trajectory that contains information about the types of seismic waves and their directions of travel. The P-wave should be linearly polarized in a simple medium along the direction of travel and the S-wave is polarized in the plane perpendicular to the direction of travel as illustrated in Figure 2.4. The P-wave particle motion in most cases is observed to be elliptical which indicates scattering. Scattering causes waveform distortion and travel time fluctuations.

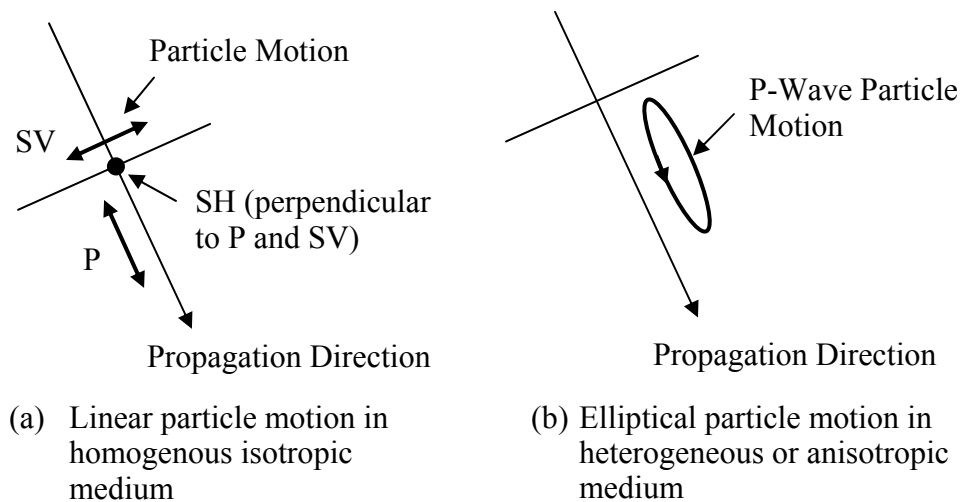


Figure 2.4 Scattering of P-wave particle motion

Intrinsic anisotropy is the anisotropy caused by small scale and especially microscopic oriented inhomogeneities but not including anisotropy caused by any succession of isotropic layers (Winterstein, 1990). Bakulin and Grechka (2003) studied

the influence of heterogeneity on intrinsic anisotropy in heterogeneous anisotropic media. Bakulin and Grechka remarked that many available measurements of in-situ anisotropy tend to be relatively contaminated by unaccounted-for heterogeneity because of the scale of measurement over a finite volume of inevitably heterogeneous rock. Bakulin and Grechka pointed out that heterogeneity and anisotropy may imitate each other, depending on the frequency of propagating waves. Seismic frequency range in seismic exploration refers to 10 to 200 Hz. A finely layered isotropic media can effectively behave as a vertically transversely isotropic media when probed by long seismic waves (Backus, 1962). Because frequency varies over the entire range of seismic frequencies, heterogeneity transitions to anisotropy and vice versa. The anisotropy that purely stems from heterogeneity, such as that produced by the Backus averaging of isotropic finely layered media, is usually weak because it is a quadratic term in the fluctuation of the relative changes from the mean values of the velocities and density. The studies concluded that the interdependence of anisotropy and heterogeneity may be ignored.

2.3 EFFECT OF NONLINEARITY

Linear wave theories assume that small-amplitude signals characterized by deformations of a solid due to elastic waves are small enough so that the linear stress-strain relationship is applicable. Linear wave theories apply only in the far field. Far field is the region where the stress and strain relationship is linear. Empirically, the distinction between the near field and the far field is frequency dependent. Baeten and Ziolkowski (1990) recommended the far field be the region more than a wavelength away from the source. Depending on the output force level of the vibrator, the far field can start from less than a wavelength away. When the maximal output force is used, the far field is assumed to start from the region a wavelength way from the vibrator. For example, P-

wave velocity near the ground surface is below 600 m/s (2000 fps), for a 50-Hz source signal, the far field of a vibratory source starts at about 12 m (40 ft).

In the near field the strains are high and the relationship between the components of the stress and strain tensors becomes nonlinear. Nonlinearity occurs in the near field, especially from explosive sources. Nonlinear elastic waves are called finite-amplitude waves in the literature. Nevertheless, the near field generates some high-frequency contents that can propagate in the far field. Although all measurements used for velocity profiling in the work come from the far field where linear wave theories apply, the signals measured in the far field can be significantly distorted by the high frequency content generated in the near field.

Nonlinear dynamic elasticity for planar and spherical waves in isotropic and compressible elastic media was studied by Bland (1969), whose primary analytical tool was the method of characteristics. The method of characteristics (Jeffrey et al, 1964) is adequate for one-dimensional wave propagation. Fine and Shield (1966) used a different approach called the straightforward perturbation method to investigate nonlinear effects of stress waves in homogeneous and isotropic solids.

Nonlinearity in the near-field media occurs in the constitutive wave propagation equations as well as in the geometrical relations between strain and displacement. The nonlinear relation between the components of the stress and strain tensors necessitates consideration of the interaction between longitudinal and transverse waves. Jones et al (1963) derived a criterion for the occurrence of a strong scattered wave from two elastic waves intersecting in a homogeneous, isotropic media. The amplitude of the scattered wave was found to be proportional to the volume of interaction. Higher harmonics and other complications arise because of the generality of the stress tensor and the interaction of P and S waves (Thompson et al, 1977; Goldberg, 1961). Higher harmonics are also

generated by a nonlinear boundary at normal incidence (Konovalov et al, 1991). Nonlinear modal interactions and energy transfer between high-frequency and low-frequency modes were studied as well (Nayfeh and Balachandran, 1994; Nayfeh, 2000).

The propagation speed of such linear waves with infinitesimally small amplitudes remains constant throughout wave propagation. However, the propagation speed of nonlinear waves with finite amplitude is not constant in cases where dissipation does not occur. Propagation speed depends on the local wave amplitude which causes crests of a wave to propagate faster than the troughs only when the coefficient of nonlinearity is positive. As a result, the wave shape becomes distorted as the wave propagates.

2.4 TRANSVERSELY ISOTROPIC MEDIUM AND MODE CONVERSION

The Saggittal plane is often used to describe a transversely isotropic medium. As shown in Figure 2.5, a coordinate system is defined with x_3 vertical along the gravitational direction, and x_1 is selected as the horizontal, which can rotate any azimuth angle ψ around x_3 . The plane defined by x_1 and x_3 is called the Sagittal plane. A transversely isotropic medium is isotropic only in any of the two axes, and the other axis is called the symmetry axis. For example, a transversely isotropic media characterized by a vertical axis of symmetry, x_3 , (TIV or VTI) is widely used to simulate sedimentary rocks. For vertical cracks, transversely isotropic media characterized by a horizontal symmetry axis x_1 or x_2 (TIH or HTI) is used (MacBeth, 2002).

If the vertical inclination angle θ in Figure 2.5 and the azimuth angle ψ are defined, the following expressions for any vector $\vec{n} = (n_1, n_2, n_3)$ are obtained:

$$n_1 = \cos \psi \sin \theta, \quad (2.1)$$

$$n_2 = \sin \psi \sin \theta, \quad (2.2)$$

$$n_3 = \cos \theta. \quad (2.3)$$

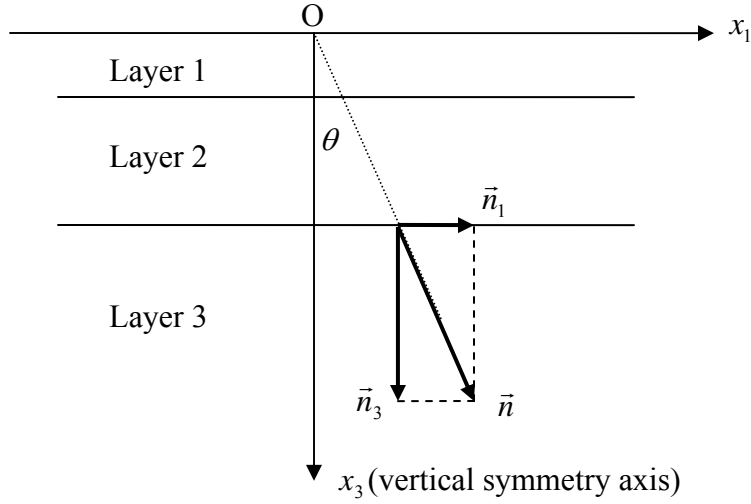


Figure 2.5 Transversely isotropic medium with a vertical symmetry axis (TIV)

When a plane wave propagating in a medium encounters a boundary, the incident wave may generate a number of reflected and transmitted waves according to the boundary condition. Generally a maximum of six wave components are possible for a flat solid boundary interfaced by two contacted solid media (Nayfeh, 1995). Snell's law (Equation 2.4) and slowness surface (see Figure 2.6) are often used to determine the number of components during reflections and refractions. Slowness surface (Musgrave, 1970) is the inverse of phase velocity surface. The dashed lines in Figures 2.6 represent the surfaces of SV waves and the solid lines represent P waves. The arrow connecting the slowness surface to the origin O is called slowness vector. The length of slowness vector represents the reciprocal of velocity values such as v_p , v_{p1} and v_{p2} . The slowness surface in anisotropic media is not circular (Figure 2.7). Slowness vectors are parallel to phase velocity vectors. The inclinations of the slowness vectors are determined according to Snell's law in Equation (2.4) as:

$$\frac{\sin \theta_p}{v_p} = \frac{\sin \theta_{p1}}{v_{p1}} = \frac{\sin \theta_{p2}}{v_{p2}} = \frac{\sin \theta_{s1}}{v_{s1}} = \frac{\sin \theta_{s2}}{v_{s2}} = a, \quad (2.4)$$

because all the arrows have the same length of projection onto the \vec{n}_1 axis, as denoted by a .

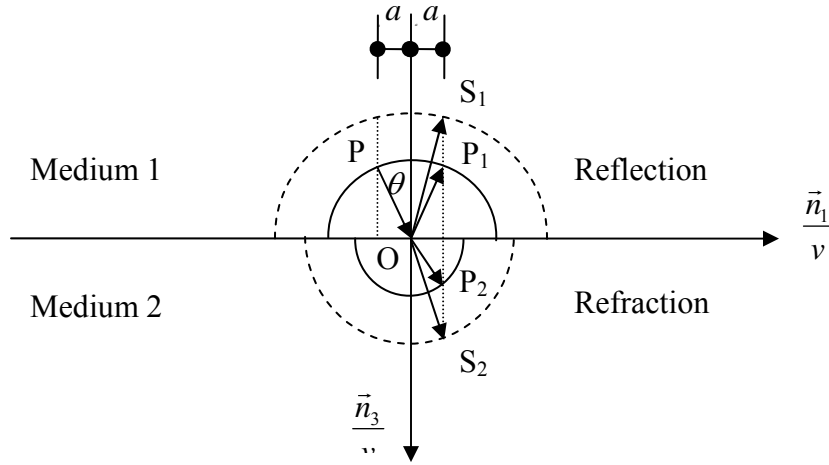


Figure 2.6 Slowness surface for an incident P-wave in isotropic medium

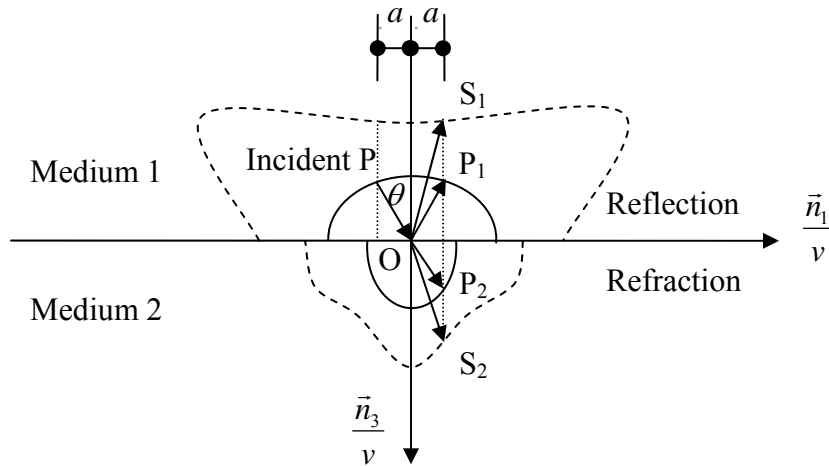


Figure 2.7 Slowness surface for an incident P-wave in anisotropic medium

Three possible modes of wave propagation in a homogeneous medium are P, SV (or S_1), and SH (or S_2) pure or quasi modes. Figure 2.8 illustrates the multiple mode conversions of an incident P wave from a source traveling through a four-layer isotropic

medium. An incident P wave or SV wave will generate reflected as well as transmitted P and SV waves.

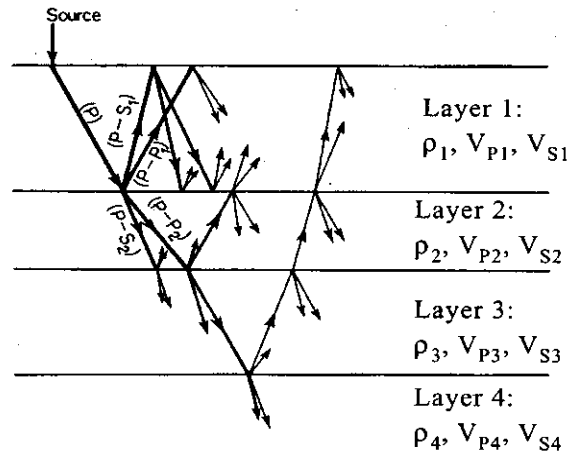


Figure 2.8 Multiple wave reflections and refractions in TIV media (from Richart et al, 1970)

As shown in Figure 2.8, half of the reflections are composed of SV waves. The adverse effect of SV waves is that, the velocity anisotropy of SV waves is about an order of magnitude greater than that of P waves (Grechka, 2001).

2.5 S-WAVE BIREFRINGENCE AND S-WAVE SPLITTING

Birefringence means double refraction (Figure 2.7), where a single incident wave refracts as two waves with different polarizations because of different velocities. An isotropic medium of geophysical interest is birefringent because the velocities of P and S wave are always different. An anisotropic medium is generally trirefringent if none of the three wave velocities (P, S_1 , and S_2 waves) are equal (Auld, 1973).

S-wave birefringence is often referred to as S waves with different polarizations traveling in a similar direction at different speeds. S-wave birefringence is a characteristic of a homogenous anisotropic medium and is used to measure anisotropy in a single homogeneous medium.

When two S-waves travel in the same direction but with different polarizations and velocities, the accumulated effects of S-wave birefringence in one or more homogeneous media will result in S-wave splitting. If the source polarization is along a natural earth polarization direction, a highly birefringent rock may have no S-wave splitting, which means the two S-waves may propagate at the same speed. The amount of splitting is measured quantitatively by the time lag between the two waves. Fractures, cracks, and fissures in typical rocks and soils can cause obvious S-wave splitting (Majer et al, 1988). Split S-waves create nonlinear polarizations if the S-waves do not completely separate.

TIV models are generally accepted for sedimentary rocks, but insufficient for describing azimuthally varying seismic signatures (Grechka, 2001). Alford (1986) studied shear data in the presence of azimuthal anisotropy, and pointed out that azimuthal anisotropy, even on the order of a few percent, cannot be ignored for shear-wave exploration because S-wave splitting due to azimuthal anisotropy can cause poor shear data quality.

2.6 RELATIONSHIP OF ENGINEERING CONSTANTS AND VERTICAL VELOCITIES

Determination of the engineering constants in the stiffness tensor for seismic site-response analyses is one of the purposes of seismic measurements. Vertical velocity measurements in the field play an important role in specifying many or all of these constants. A breakthrough from isotropic medium to anisotropic medium was made by Thomsen (1986), who first expressed anisotropy analytically using a combination of engineering elastic constants in the stiffness tensor.

In the orthogonal Cartesian system, the indices i, j, k and l below for tensor operations are assigned values 1, 2 and 3 corresponding to three axes of Cartesian coordinates (x_1, x_2, x_3) shown in Figure 2.5. The stiffness tensor c is a four-rank tensor

with 81 elements. However, the stiffness tensor has only 21 independent stiffnesses or elastic moduli, c_{ijkl} , for general anisotropy. The stress tensor, σ_{ij} , is a two-rank tensor with 9 elements; strain tensor e_{kl} is a two-rank tensor with 9 elements and displacement vector u_i is a one-rank tensor with 3 elements. The number of independent elements depends on symmetry.

The dynamic behavior of linear elastic and generally anisotropic solids satisfies the following condition:

$$\frac{\partial \sigma_{ij}}{\partial x_j} = \rho \frac{\partial^2 u_i}{\partial t^2}, \quad (2.5)$$

where: ρ is material mass density. The stress-strain relation is defined as:

$$\sigma_{ij} = c_{ijkl} e_{kl}, \quad (2.6)$$

and the strain-displacement relation is given by:

$$e_{kl} = \frac{1}{2} \left(\frac{\partial u_l}{\partial x_k} + \frac{\partial u_k}{\partial x_l} \right). \quad (2.7)$$

The stress tensor σ_{ij} and the strain tensor e_{kl} are both symmetric, each possessing 6 independent elements. The symmetry of σ_{ij} and e_{kl} results in the symmetry of the stiffness tensor, or $c_{ijkl} = c_{jikl} = c_{ijlk} = c_{jilk}$. Therefore, c_{ijkl} reduces to 36 independent elements. Further symmetry comes from the strain energy U relations given by:

$$U = \frac{1}{2} \sigma_{ij} e_{ij} = \frac{1}{2} c_{ijkl} e_{kl} e_{ij} \quad (2.8)$$

The interchange of indices kl and ij does not change the strain energy U. Thus, $c_{ijkl} = c_{klij}$, which has only 21 independent elements. The contracted index notation in Equation (2.9) is used to map the symmetric, four-rank tensor c_{ijkl} to a simplified second-rank tensor C_{ij} as shown in Equation (2.10).

$$1 \rightarrow 11, 2 \rightarrow 22, 3 \rightarrow 33, 4 \rightarrow 23, 5 \rightarrow 13, 6 \rightarrow 12. \quad (2.9)$$

$$\begin{bmatrix} \sigma_{11} \\ \sigma_{22} \\ \sigma_{33} \\ \sigma_{23} \\ \sigma_{13} \\ \sigma_{12} \end{bmatrix} = \begin{bmatrix} C_{11} & C_{12} & C_{13} & C_{14} & C_{15} & C_{16} \\ & C_{22} & C_{23} & C_{24} & C_{25} & C_{26} \\ & & C_{33} & C_{34} & C_{35} & C_{36} \\ & & & C_{44} & C_{45} & C_{46} \\ & sym & & & C_{55} & C_{56} \\ & & & & & C_{66} \end{bmatrix} \begin{bmatrix} e_{11} \\ e_{22} \\ e_{33} \\ \gamma_{23} \\ \gamma_{13} \\ \gamma_{12} \end{bmatrix} \quad (2.10)$$

where: $\gamma_{ij} = 2e_{ij}$ (2.11)

The left side of the arrows in Equation (2.9) denotes the contracted indices, while the right side stands for the tensor rank indices.

All 21 elements in the stiffness matrix in Equation (2.10) are independent of general anisotropy. The anisotropy of materials with specific symmetries exhibit fewer independent elements (Helbig, K., 1994; Nayfeh, 1995). For example, the stiffnesses for isotropic materials may be expressed as Lamé parameters λ and μ as follows:

$$c_{ijkl} = \lambda \delta_{ij} \delta_{kl} + \mu (\delta_{ik} \delta_{jl} + \delta_{il} \delta_{jk}), \quad (2.12)$$

$$C_{11} = C_{22} = C_{33} = \lambda + 2\mu, \quad (2.13)$$

$$C_{12} = C_{13} = C_{23} = \lambda, \quad (2.14)$$

and $C_{44} = C_{55} = C_{66} = \mu,$ (2.15)

where: μ is shear modulus, and λ is Lamé's constant, which is given by Young's modulus E , shear modulus μ and Poisson's ratio ν as:

$$\lambda = E - 2\mu = \frac{2\mu\nu}{1-2\nu} \quad (2.16)$$

For isotropic materials, the stiffness matrix in Equation (2.10) can also be written as:

$$c_0 = \begin{bmatrix} C_{33} & C_{33} - 2C_{44} & C_{33} - 2C_{44} & 0 & 0 & 0 \\ & C_{33} & C_{33} - 2C_{44} & 0 & 0 & 0 \\ & & C_{33} & 0 & 0 & 0 \\ & & & C_{44} & 0 & 0 \\ & sym & & & C_{44} & 0 \\ & & & & & C_{44} \end{bmatrix} \quad (2.17)$$

Substituting Equations (2.13), (2.14) and (2.15) into (2.17) yields:

$$c_0 = \begin{bmatrix} \lambda + 2\mu & \lambda & \lambda & & & \\ & \lambda + 2\mu & \lambda & & & \\ & & \lambda + 2\mu & & & \\ & & & \mu & & \\ & sym & & & \mu & \\ & & & & & \mu \end{bmatrix} \quad (2.18)$$

The vertical P- and S-wave velocities (V_P and V_S , respectively), are defined as:

$$V_P = \sqrt{C_{33} / \rho}, \quad (2.19)$$

and

$$V_S = \sqrt{C_{44} / \rho}, \quad (2.20)$$

which means that Equations (2.19) and (2.20) become:

$$C_{33} = \rho V_P^2, \quad (2.21)$$

and

$$C_{44} = \rho V_S^2. \quad (2.22)$$

The stiffness matrix c_0 for isotropic material is eventually and completely determined by substituting Equations (2.21) and (2.22) into Equation (2.17) to yield:

$$c_0 = \begin{bmatrix} \rho V_P^2 & \rho(V_P^2 - 2V_S^2) & \rho(V_P^2 - 2V_S^2) & & & \\ & \rho V_P^2 & \rho(V_P^2 - 2V_S^2) & & & \\ & & \rho V_P^2 & & & \\ & & & \rho V_S^2 & & \\ & sym & & & \rho V_S^2 & \\ & & & & & \rho V_S^2 \end{bmatrix} \quad (2.23)$$

Anisotropy of transversely isotropic material with a vertical symmetry axis (TIV) is also widely used for anisotropy of sedimentary rock. Seismic exploration using vibrators typically utilizes frequencies below 80 Hz, as a result, wavelengths in such investigations are generally in the range of a few hundred feet or longer than typical layer thicknesses. Backus (1962) studied long-wave elastic anisotropy produced by horizontal layering and concluded that waves in layered media propagate as if they were in a homogeneous, anisotropic medium in cases where the elastic wavelength is much longer than the typical layer thickness. The stiffness matrix for TIV anisotropy is:

$$c_{TIV} = \begin{bmatrix} C_{11} & C_{11} - 2C_{66} & C_{13} & 0 & 0 & 0 \\ & C_{11} & C_{13} & 0 & 0 & 0 \\ & & C_{33} & 0 & 0 & 0 \\ & & & C_{44} & 0 & 0 \\ & sym & & & C_{44} & 0 \\ & & & & & C_{66} \end{bmatrix} \quad (2.24)$$

The stiffness matrix c_{TIV} in Equation (2.24) can also be expressed a function of the vertical P- and S-wave velocities V_p and V_s , as discussed in the next section.

2.7 WAVE VELOCITIES IN ANISOTROPIC MEDIA

Group velocity and phase velocity are commonly used. Group velocity is the speed of wave energy with a wide range in frequencies traveling in a given direction from a point source. When the medium is attenuating and anisotropic, group velocity is the velocity of the wave envelope because of frequency dispersion and angular dispersion (Aki and Richards, 1980). Theoretical group velocity is defined as the differential of circular frequency with respect to wave vector (Auld, 1973). Group velocity can be measured by dividing travel distance by travel time.

Phase velocity in a homogeneous media is the speed of constant phase of a given frequency traveling in a direction normal to the wavefront. Phase velocity in attenuating

and anisotropic media is subject to frequency dispersion and angular dispersion (Futterman, 1962). The solution of the Christoffel Equation (Auld, 1973) is used to obtain phase velocity.

Group velocity and phase velocity are identical in isotropic medium, but different in anisotropic medium. To bridge the wave velocities in isotropic medium and in anisotropic medium, evaluation of anisotropy is indispensable. Based on the examination of contemporary available data and literature concerning the anisotropy of sedimentary rocks at the time, Thomsen (1986) first introduced three parameters ε , γ (not representing volume and shear strains), and δ to quantitatively describe anisotropy of a material. These parameters are given in Equations (2.25) through (2.27) as:

$$\varepsilon = \frac{C_{11} - C_{33}}{2C_{33}} \quad (2.25)$$

$$\gamma = \frac{C_{66} - C_{44}}{2C_{44}} \quad (2.26)$$

$$\delta = \frac{(C_{13} + C_{44})^2 - (C_{33} - C_{44})^2}{2C_{33}(C_{33} - C_{44})} \quad (2.27)$$

The practical evaluation and calculation methods Thomsen developed for weak anisotropy are widely considered a milestone in the study of anisotropy. He determined that most rocks have parameters ε and γ that are between 0 to 0.3 and δ in the range of -0.1 to 0.2. For layered media, $\gamma \geq 0$ and $\varepsilon - \delta \geq 0$. Berryman et al (1999) used both Monte Carlo studies and detailed analysis of Backus' equations for both two- and three-component layered media to analyze the Thomsen parameters for TIV media. They found that for finely layered media, the range of ε is:

$$-\frac{3}{8} \leq \varepsilon \leq \frac{1}{2} \left[\langle V_P^2 \rangle \langle V_P^{-2} \rangle - 1 \right] \quad (2.28)$$

where: the symbol $\langle x \rangle$ denotes the volume average of the quantity x in the layered medium under consideration. If large fluctuations occur in the Lamé parameter λ of the component layers, ε has small positive and all negative values, but δ is most likely to have positive values. The sign of δ can be either positive or negative. In constant density media, the sign of δ satisfies:

$$\text{sign}(\delta) = \text{sign}\left(\langle V_p^{-2} \rangle - \langle V_s^{-2} \rangle \left\langle \frac{V_s^2}{V_p^2} \right\rangle\right) \quad (2.29)$$

Velocity anisotropy is the variation of velocity with direction, as shown in Figure 2.9, where the relation of the phase angle, θ , to the phase velocity and the group angle, ϕ , to the group velocity is also illustrated. The phase velocity travels along the direction of the wavefront normal (shown as the wave vector in Figure 2.9), while the group velocity radiates from the point source along the ray path in Figure 2.9.

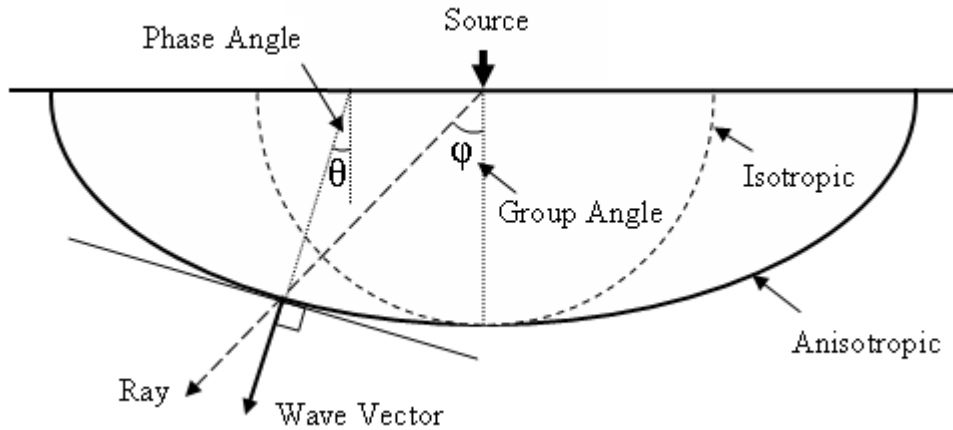


Figure 2.9 Illustration of velocity anisotropy

With help of the Thomsen parameters, the angular dispersion of phase velocity for weak anisotropy can be expressed as:

$$v_p(\theta) = V_p(1 + \delta \sin^2 \theta \cos^2 \theta + \varepsilon \sin^4 \theta) \quad (2.30)$$

$$v_{SV}(\theta) = V_s \left[1 + \frac{V_p^2}{V_s^2} (\varepsilon - \delta) \sin^2 \theta \cos^2 \theta \right] \quad (2.31)$$

and
$$v_{SH}(\theta) = V_s^2 (1 + \gamma \sin^2 \theta). \quad (2.32)$$

For arbitrary anisotropy, the velocity equations are more complicated (see Thomsen, 1986 for Equations 7 and 10) but still solvable by iterative adjustments.

Thomsen (1986) presented a conversion between group velocity and phase velocity. Equations (2.30) to (2.32) can also be used for group velocities if the phase angle θ is replaced with group angle φ when using the following relationship for the linear approximation (Thomsen, 1986):

P-wave:
$$\tan \varphi = \tan \theta [1 + 2\delta + 4(\varepsilon - \delta) \sin^2 \theta] \quad (2.33)$$

SV-wave:
$$\tan \varphi = \tan \theta \left[1 + 2 \frac{V_p^2}{V_s^2} (\varepsilon - \delta) (1 - 2 \sin^2 \theta) \right] \quad (2.34)$$

SH-wave:
$$\tan \varphi = \tan \theta (1 + 2\gamma) \quad (2.35)$$

Thomsen demonstrated that this replacement is valid for all three wave types (P, SV and SH). For near-offset VSP, the φ and θ are small. The difference between the group velocity and phase velocity is minor as shown in Figure 2.10.

Figure 2.11 is a schematic illustration of the deviation of the P-wave polarization direction P and the group direction φ from the phase direction θ in a TIV medium. The deviation of P from the phase direction is α , and the deviation of the group direction from the phase direction is $(\varphi - \theta)$. For a TIV medium where anisotropic parameters $\varepsilon = 0.2$ and $\delta = 0.1$, the maximum deviation of the polarization from the group direction ($\alpha - \varphi + \theta$) is 2 to 3 degrees (MacBeth, 2002). The deviation of measured P-wave polarization from the group direction is negligible. In other words, the measured P-wave polarization represents the unknown group direction in TIV medium.

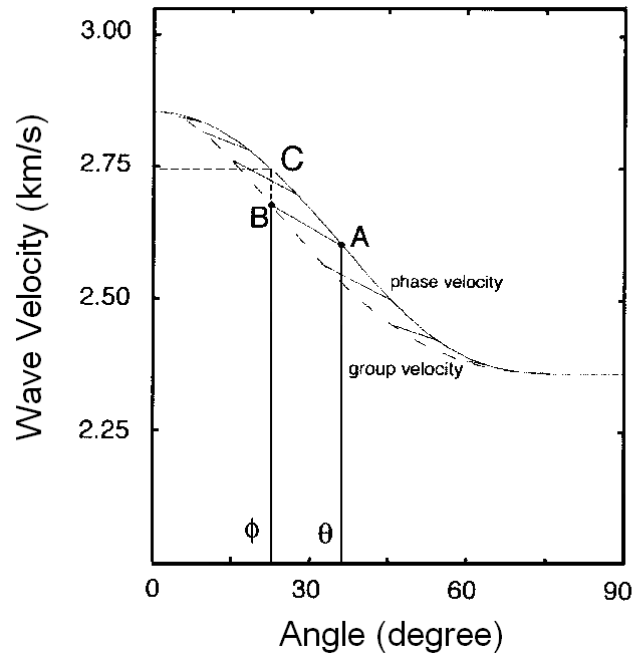


Figure 2.10 Comparison of phase velocity and group velocity (from MacBeth, 2002)

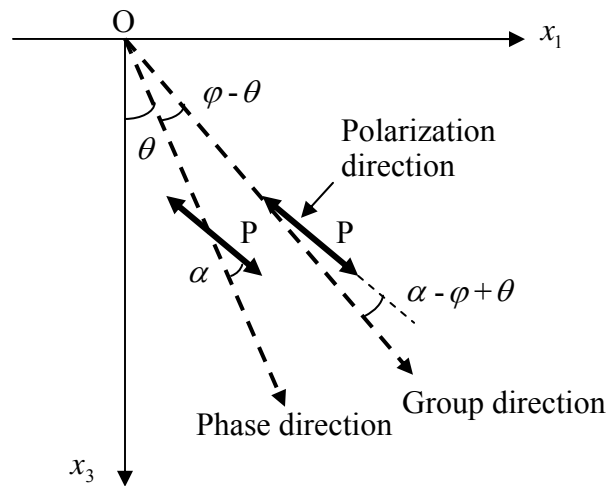


Figure 2.11 Deviation of the polarization and group direction from the phase direction (redrawn after MacBeth, 2002)

The Thomsen parameters can be measured for weak anisotropy using a single set of measurements at phase angle $\theta = 0, \frac{\pi}{4}$ and $\frac{\pi}{2}$, as shown by Equations (2.36) through (2.38):

$$\varepsilon = \frac{v_p\left(\frac{\pi}{2}\right) - V_p}{V_p} \quad (2.36)$$

$$\gamma = \frac{v_{SH}\left(\frac{\pi}{2}\right) - V_s}{V_s} \quad (2.37)$$

and

$$\delta = 4\left[\frac{v_p\left(\frac{\pi}{4}\right)}{v_p(0)} - 1\right] - \left[\frac{v_p\left(\frac{\pi}{2}\right)}{v_p(0)} - 1\right]. \quad (2.38)$$

The Thomsen parameters can also be predicted by empirical relationships with measured V_p and V_s . For example Ryan-Grigor (1998) presented the following empirical relationships for saturated shale at low and high porosities as:

$$\varepsilon = 0.2090 \frac{V_p}{V_s} - 0.2397 \quad (2.39)$$

$$\gamma = 0.4014 \frac{V_p}{V_s} - 0.5576 \quad (2.40)$$

and

$$\delta \approx \frac{\left(3.87 \frac{V_p}{V_s} - 4.54\right)^2 - \left(\left(\frac{V_p}{V_s}\right)^2 - 1\right)^2}{2\left(\left(\frac{V_p}{V_s}\right)^2 - 1\right)\left(\frac{V_p}{V_s}\right)^2}. \quad (2.41)$$

Given the Thomsen parameters ($\varepsilon, \gamma, \delta$) and the vertical velocities (V_p and V_s), the elastic stiffness matrix c_{TV} in Equation (2.24) can be completely specified using Equations (2.25) through (2.27). By substituting Equation (2.21) into Equation (2.25) one obtains:

$$C_{11} = (2\varepsilon + 1)C_{33} = (2\varepsilon + 1)\rho V_p^2 \quad (2.42)$$

By substituting Equation (2.22) into Equation (2.26), one obtains:

$$C_{66} = (2\gamma + 1)C_{44} = (2\gamma + 1)\rho V_s^2 \quad (2.43)$$

$$\begin{aligned} C_{13} &= \sqrt{2\delta C_{33}(C_{33} - C_{44}) + (C_{33} - C_{44})^2} - C_{44} \\ &= \rho \left(\sqrt{[(2\delta + 1)V_p^2 - V_s^2](V_p^2 - V_s^2)} - V_s^2 \right) \end{aligned} \quad (2.44)$$

For small δ , Equation (2.44) can be simplified as:

$$\begin{aligned} C_{13} &= \sqrt{2\delta C_{33}(C_{33} - C_{44}) + (C_{33} - C_{44})^2} - C_{44} \\ &\approx \sqrt{(2\delta C_{33})^2 + 2\delta C_{33}(C_{33} - C_{44}) + (C_{33} - C_{44})^2} - C_{44} \\ &= (2\delta + 1)C_{33} - 2C_{44} \\ &= (2\delta + 1)\rho V_p^2 - 2\rho V_s^2 \end{aligned} \quad (2.45)$$

By substituting Equations (2.42) through (2.45) into Equation (2.24), one obtains:

$$c_{TIV} = c_0 + \begin{bmatrix} 2\varepsilon\rho V_p^2 & 2\varepsilon\rho V_p^2 - 4\gamma\rho V_s^2 & 2\delta\rho V_p^2 & 0 & 0 & 0 \\ & 2\varepsilon\rho V_p^2 & 2\delta\rho V_p^2 & 0 & 0 & 0 \\ & & 0 & 0 & 0 & 0 \\ & & & 0 & 0 & 0 \\ & sym & & & 0 & 0 \\ & & & & & 2\gamma\rho V_s^2 \end{bmatrix} \quad (2.46)$$

where c_0 is defined by Equation (2.23).

2.8 WAVE PROPAGATION IN A HOMOGENEOUS MEDIUM

3-D wave propagation in 3-D general anisotropic media is more complicated to model than media with one or more symmetric axes. Sharma (2007) recently explored general anisotropy in 3D media and modeled the reflection of the elastic plane wave. He solved the inverse problem of finding the group velocity in a given direction of ray travel without using numerical differentiation. First he derived the phase direction from the

given ray direction, then used the phase direction to calculate phase velocity and group velocity. 3-D wave propagation for the deep downhole test can be reasonably simplified as 1-D (vertical) wave propagation vertically along the borehole.

The vibratory source is actually a point source. The solution of a point-source relies on the use of Green functions (Tsvankin, 2001; Cervený, 2001). When the wave propagation of concern is generally one dimensional, such as in deep downhole testing, also called near-offset vertical seismic profiling (Macbeth, 2002), or along the symmetry axis of a multilayered anisotropic medium (Nayfeh, 1995), the common practice is to approximate the far-field wavefield from a point source as an equivalent plane wave (Kennett, 1979).

Plane wave propagation in infinite homogeneous medium is described by the Christoffel Equation as follows:

$$\rho \frac{\partial^2 u_i}{\partial t^2} = c_{ijkl} \frac{\partial^2 u_l}{\partial x_j \partial x_k}. \quad (2.47)$$

where: $\vec{u} = (u_1, u_2, u_3)$ is the displacement vector or the polarization direction, and $\vec{n} = (n_1, n_2, n_3)$ is the propagation direction that satisfies $n_1^2 + n_2^2 + n_3^2 = 1$ (see Figure 2.5). The plane waveform is:

$$u_i = U_i e^{\sqrt{-1}(Kn_j x_j - \omega t)} \quad (2.48)$$

U_i is the displacement amplitude vector that also defines the polarization, and K is a scalar wave number. By substituting Equation (2.48) into Equation (2.47), the following equation is obtained:

$$\left(\frac{\omega}{K}\right)^2 U_i = \frac{c_{ijkl}}{\rho} n_j n_k U_l. \quad (2.49)$$

By defining phase velocity as:

$$v = \frac{\omega}{K} \quad (2.50)$$

and a two-rank tensor as:

$$A_{il} = \frac{c_{ijkl} n_j n_k}{\rho} \quad (2.51)$$

results in the Christoffel Equation for homogeneous linear equations as:

$$(A_{il} - v^2 \delta_{il}) U_l = 0. \quad (2.52)$$

The phase velocities, v^2 , are the eigenvalues and the displacement amplitudes U_l are the eigenvectors that are expressed as:

$$\begin{bmatrix} A_{11} - v^2 & A_{12} & A_{13} \\ A_{12} & A_{22} - v^2 & A_{23} \\ A_{13} & A_{23} & A_{33} - v^2 \end{bmatrix} \begin{pmatrix} U_1 \\ U_2 \\ U_3 \end{pmatrix} = \begin{pmatrix} 0 \\ 0 \\ 0 \end{pmatrix}. \quad (2.53)$$

The determinant is solved as

$$\begin{vmatrix} A_{11} - v^2 & A_{12} & A_{13} \\ A_{12} & A_{22} - v^2 & A_{23} \\ A_{13} & A_{23} & A_{33} - v^2 \end{vmatrix} = 0 \quad (2.54)$$

to obtain v^2 and U_l .

If the cross product of \vec{u} and \vec{n} is zero ($\vec{u} \times \vec{n} = 0$), then the polarization is directed along the propagation direction, which is a P wave. If the dot product of \vec{u} and \vec{n} is zero ($\vec{u} \cdot \vec{n} = 0$), then the polarization is directed normal to the propagation direction, which is a shear wave or S wave. Nayfeh (1995) stated that if each of the three polarization vectors is directed either along or normal to the propagation direction, then they are called pure modes of wave propagation, otherwise they are called a quasi wave.

As shown in Figure 2.3, three pure modes of wave propagation are possible only in isotropic media. In anisotropic media none of the three polarization vectors satisfies $\vec{u} \times \vec{n} = 0$. However, it is still possible to satisfy the condition of $\vec{u} \cdot \vec{n} = 0$, which

indicates that pure modes of shear waves can occur for some propagation directions in anisotropic media depending on the material symmetry.

When anisotropy results in polarization deviations, then quasi-longitudinal and quasi-shear waves can be identified using amplitude ratios. For example, Nayfeh (1995) defined normalized polarization directions with respect to the coordinate system x_i . For each eigenvalue v^2 , there is an eigenvector U_l . If the following definition is applied,

$$r_1^{(k)} = 1, \quad r_2^{(k)} = \frac{U_2^{(k)}}{U_1^{(k)}}, \quad r_3^{(k)} = \frac{U_3^{(k)}}{U_1^{(k)}}, \quad (2.55)$$

then each polarization is directed along the vector $\vec{r}^{(k)} = (r_1^{(k)}, r_2^{(k)}, r_3^{(k)})$, $k=1,2,3$. The maximal dot product value $\vec{r}^{(k)} \cdot \vec{n}$ is unity. The largest dot product value of $\vec{r}^{(k)} \cdot \vec{n}$ is associated with the largest eigenvalue, which defines the quasi-longitudinal wave, and the other two are quasi-shear waves. For pure modes, one of the dot products is unity, and it is along the propagation direction called the pure longitudinal wave; for anisotropy, the dot product is typically less than unity. If the dot products in anisotropy are not unity, then the zero value defines a single type pure mode.

2.9 VELOCITY DISPERSION

Velocity dispersion is characterized by angular dispersion and frequency dispersion. The dispersion describing velocity varying with direction is called angular dispersion. The dispersion displaying dependence of velocity on frequency is called frequency dispersion. Group velocity and phase velocity in anisotropic media are subject to angular dispersion, while in attenuating media they are subject to frequency dispersion (Futterman, 1962; Aki and Richards, 1980). The wave propagation in stratified media can be described by ray theory (Cerveny, 2001), effective medium theory (Backus, 1962), and other theories with the appropriate theory based on the scale of the wavelength to the layer spacing.

When employing the effective medium theory to consider vertically propagating waves through a horizontally layered media, if the thickness of the layers is several times greater than the incoming wavelength, then the velocity is the moderated average of the velocities of each layer which is obtained by dividing the total path length by the total travel time. If the layer thickness in horizontally layered media is only a fraction of the incoming wavelength, then these layers are considered equivalent to one homogeneous medium. The elastic stiffness in this case is the moderated average of the stiffness of each layer. The difference between the short-wavelength and long-wavelength velocities increases with the lithology contrast of the layers. However, the differences are independent of layer order.

In the stiff soil and rock tested in the research, the P- and S-wave velocities exceed 4800 m/s (16000 fps) and 2100 m/s (7000 fps), respectively. For testing with an excitation frequency of 50 Hz, the resulting wavelengths were 96 m (320 ft) and 42 m (140 ft) for P and S waves, respectively. For testing with an excitation frequency of 20 Hz, the corresponding wavelengths were 240 m (800 ft) and 105 m (350 ft) for P and S waves, respectively. As shown in Figure 1.1, these wavelengths can cover up to 7 layers, so that the effective medium theory is of concern in the research.

To better understand the effective medium theory, Marion et al (1994) examined the transition of velocity from ray theory to effective medium theory in a laboratory setting. The stratified media is a periodic media of alternating steel and plastic discs, but the volume fraction of the steel varies from test to test. The P-wave velocity of steel is 5535 m/s (18450 ft/s) and of plastic is 2487 m/s (8290 ft/s). Their densities are 7.9 g/cc and 1.21 g/cc, respectively. Experimental and theoretical studies were jointly conducted to investigate the velocity behavior in stratified media at the transition from ray theory to effective medium theory. Velocity measurements were obtained at 50 and 500 kHz. The

source was located at the bottom of the composite and the receiver was at the top in these experiments.

Figure 2.12 shows the dependence of velocity as the volume fraction of steel was varied. The upper line, indicated by “Ray theory”, is the theoretical calculations for short wavelengths (500 kHz) and the lower line, indicated by “Effective Medium”, indicates the theoretical result for long wavelengths (50 kHz). The middle lines are drawn from the theoretical result for long wavelengths (50 kHz). The middle lines are drawn from the experimental data points (shown by the small circles). Figure 2.12 indicates that, as wavelength λ increases, the experimental results gradually shift from the ray theory and to the effective medium theory.

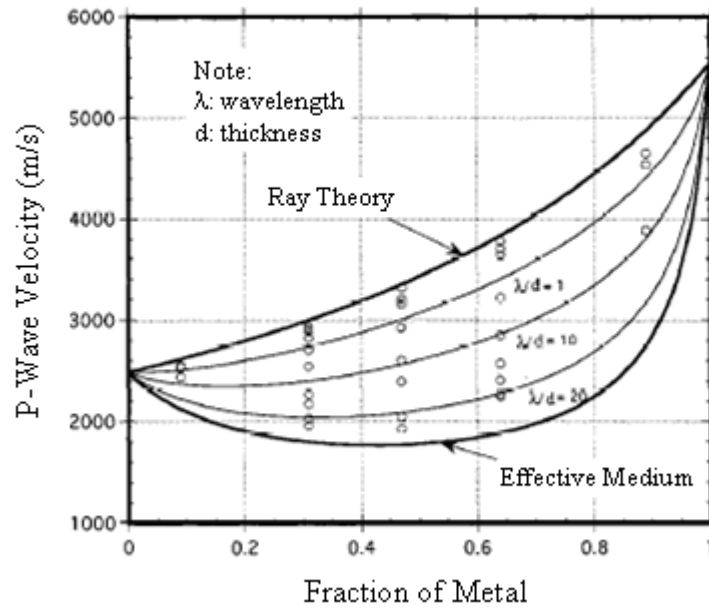


Figure 2.12 Experimentally observed velocities versus volume fraction of steel (from Marion et al, 1994)

Results displayed in Figure 2.13 confirm that velocities in stratified media not only depend on its composition, but also are controlled by the ratio of wavelength λ to the layer spacing d expressed as λ/d . The experiment indicates that a narrow transition zone with λ/d values of approximately 8 to 20 exists between the two velocities, while

the numerical calculation shows the ratio to be about 7. The solid lines denote the trend of the experimental or numerical results. The researchers mentioned that further research is needed to examine the difference between the laboratory and numerical results. They found that for plastic-steel composites, the transition from short-wavelength to long-wavelength behavior coincides with strong attenuation of the signal because of scattering and occurs over a narrow range of λ/d between 8 and 15. This transition range is almost independent of the relative fractions of steel and plastic. In addition, the scattering effect in the transition zone depends strongly upon layer order.

The thickest layer in Hanford TWP site is 61.2 m (204 ft), and the thinnest is 5.1 m (17 ft). The possible λ/d in the research varies from 1.6 to 40. In some depth range where λ/d is close to 10, the measured velocity may be very scattered, as denoted by the transition zone in Figure 2.13.

Gupta (1966) conducted similar research in materials closer in stiffness to soils. He stated that P- and S-wave propagation is dispersive in an elastic medium that is not infinite, homogeneous, and isotropic. The dispersion effects are generally minor but not negligible for the purpose of deep downhole investigations. Shorter-period body waves travel faster than longer-period body waves in propagation events normal to a layered system. Gupta (1972) further compared short-wave length and long-wave length velocities in layered media in events where propagation is not normal to the layered system. The results of his studies are presented in Figures 2.14 through 2.17. The average velocity in the figures is calculated by dividing the total ray path length by the measured travel time.

Gupta concluded that, if the probed properties of the media vary with frequency or wavelength, the results are closer to those using Snell's Law when studying shorter wavelengths that are much shorter than the thickness of layers.

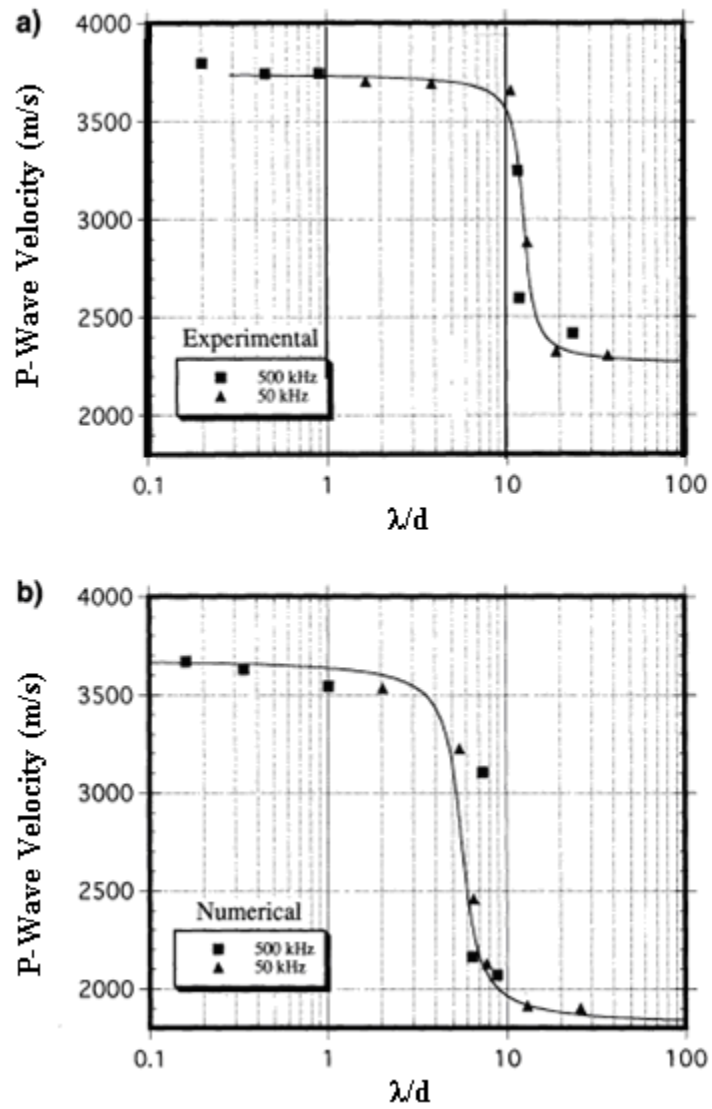
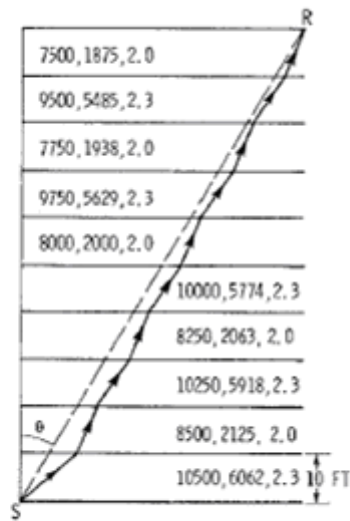


Figure 2.13 (a) Experimental velocity versus the ratio λ/d and (b) numerical simulation velocity versus the ratio λ/d (from Marion et al, 1994)



Model C

Figure 2.16 Ray tracing through a ten-layered media (from Gupta 1972). The numbers from left to right in each layer indicate P-, S-wave velocities (ft/sec) and density (g/cc), respectively

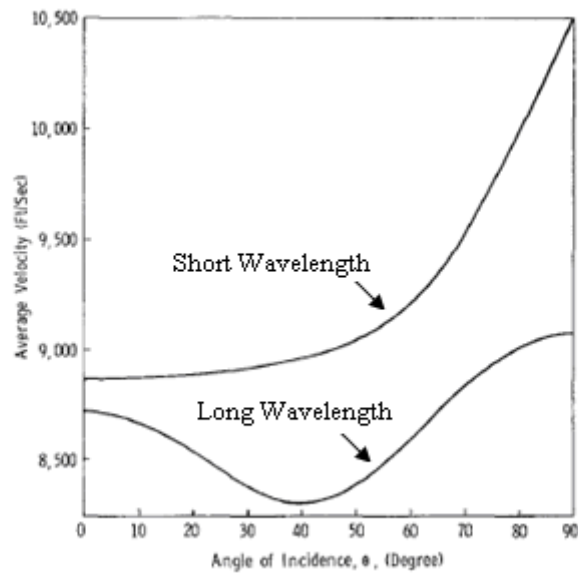


Figure 2.17 Short-wavelength and long-wavelength average velocities as a function of the angle of incidence for Model C (from Gupta, 1972)

Periodic layering for transversely isotropic media was studied by Backus (1962) as well as Folstad and Schoenberg (1992). Folstad and Schoenberg (1992) concluded that fine layering of the order of one-tenth of the smallest wavelength or less does not affect the seismic wave propagation other than causing the medium to be considered anisotropic. Anisotropy of the coarse layers increases significantly when the rapid variations in depth of velocities and density have a standard deviation approaching 0.1. The fine layers with thicknesses well below a tenth of the smallest wavelength may be replaced by more coarsely layered (thicker), homogeneous equivalent transversely isotropic layers with far fewer layers by applying the equivalent medium theory proposed by Backus (1962). If the thickness of the equivalent coarse layering is still a tenth of the smallest wavelength, no difference in travel time attenuation or pulse shape is observed once layer induced anisotropy is taken into account. However, the periodic fine layering does not accurately explain the origin of anisotropy of most transversely isotropic media (Winterstein and Paulsson, 1990).

2.10 PHASE VELOCITY SURFACE AND GROUP VELOCITY SURFACE

For a given mode (P, S_1 or S_2), a phase-velocity surface can be constructed by connecting the tips of all the phase velocity vectors of a point source embedded in a homogeneous medium. A separate phase velocity surface in isotropic medium exists for each mode where the two S-wave surfaces coincide. P-wave surface may contact one of the S-wave surfaces only in certain media (for example, tellurium dioxide) that are generally irrelevant to geophysicists' interests (Winterstein, 1990). Musgrave (1970) described the three velocity surfaces as a single surface of three sheets, one sheet for each of the three velocity eigenvalues obtained from the Christoffel equation. Crampin (1981) considered the two S-wave sheets as an analytically continuous surface because the two sheets have points in common. A point where S-wave phase velocity surfaces touch is

called S-wave singularity. Crampin (1981) distinguished three singularities: point, kiss, and line. In point singularity, phase velocity surfaces touch at a point. If the two S-wave surfaces approach tangentially and touch at some places but do not intersect, it is called kissing singularity. If S-wave surfaces intersect along a line in a transversely isotropic medium, it is called line singularity.

At points where S-wave singularity occurs, wave polarizations are impure. Phase velocity in attenuating medium is subject to frequency dispersion (Aki and Richards, 1980), hence each mode may have more than one phase velocity surfaces if the source contains more than one frequency as observed in this research. On the other hand, the three possible surfaces defined by the Christoffel equation may not always coexist if the three modes are not generated in the mean time. Theoretically, a single incidence of a plane P-wave source of a single frequency can only generate one (P-wave) phase velocity surface in an isotropic medium. However, in anisotropic medium, S-wave splitting may result in two S-wave surfaces and/or S-wave singularity. The two S-wave surfaces intersect in most cases, but along the symmetry axis the two surfaces kiss (MacBeth, 2002).

Group velocity surface can be derived by differentiation from the phase velocity surface. When the plane waves constructively interfere, the phase velocity has high curvature and the differentiation for group velocity can lead to rapid variation in polarizations that demonstrates irregular cuspidal features. For strong anisotropic medium, the cuspidal features are called cusps. Cusps only exist in the quasi-SV group velocity surface. Actual surfaces near cusps on S-wave surfaces might deviate from ray theory predictions (White, 1982). Cusps can result in two possible shear wave arrivals and earlier signal arrivals than expected (MacBeth, 2002). In isotropic medium, the group velocity surface coincides with the phase velocity surface.

This research attempts to minimize complicated polarizations caused by mode conversions, wave coupling, and S-wave singularity. P- and S-mode source signals are always generated separately and waves propagate near vertically. The three surfaces cause multiple polarizations in the receiver signals. A wavelet-response technique introduced in Chapter 7 aims at distinguishing the desired polarization from multi-polarization signals.

2.11 SUMMARY

In this chapter, background information regarding wave propagation and current theoretical developments in the exploration of seismic anisotropy and heterogeneity in real earth are presented. For most cases of interest to geophysicists, the anisotropy is weak. For P-wave velocity, most seismic anisotropy is negligible when the incident angle is vertical or within 15 degrees for a TIV medium, which is typically the case for deep downhole testing.

Frequency dispersion is of concern in anisotropic media. Waves with different frequency propagate at different speeds. Velocity dispersion leads to the variation of the source wavelet with depths if the source wavelet, such as a chirp sweep, contains different frequencies. For deep downhole test, frequency content may change with depth because of attenuation. On the other hand, if the velocities are measured by a single frequency, the measured velocity should be frequency-specific, because higher frequency results in higher measured velocity.

Effective medium theory should be used where thin layers exist. A number of layers examined in the Hanford project are much thinner than the wavelength generated by the fixed-frequency vibratory source. According to the effective medium theory, their velocity should be accordingly adjusted.

Angular dispersion is of concern when dipping layers exist. As demonstrated by Gupta (1972), both P- and S-wave velocities vary with incident angle. When the incident angle is near vertical (within 5 degrees for instance), the velocity difference between short wavelengths and long wavelengths is at a minimum.

Chapter 3 Deep Downhole Testing

3.1 INTRODUCTION

In this chapter, test equipment, procedures, and challenges in current practice in deep downhole seismic testing are introduced and discussed. Again, in the context of this research, deep downhole testing is considered to be testing at depths exceeding 225 m (750 ft).

Downhole measurements are generally categorized as near-offset vertical seismic profiling (VSP). VSP is a field survey in which seismic waves generated by a surface source are recorded by geophones located at different depths in a borehole. If the source is in the borehole and the geophones are located along a borehole or on the ground surface, the test is called a reversed or reverse VSP (Chen et al, 1990) which corresponds to an uphole test. Reversed VSP may use earthquakes or microearthquakes as a source.

VSP differs from surface surveying in that VSP records both up-going and down-going seismic waves. The effects of the borehole are negligible due to the fact that the diameter of the borehole is much smaller than the wavelength in the survey (Lee, 1987). VSP was first used in the former Soviet Union in the 1950s and afterwards used in other countries outside the Soviet Union beginning in the 1970s (Hardage, 1983; Puzirev et al, 1985). VSP has been extensively used in oil exploration, underground water resource surveys, and seismic surveys (Hardage, 2000). Based on the total number of crew months spent on land petroleum exploration from the early 1960s to the late 1980s, the use of dynamite as a source signal for VSP testing has dropped from more than 90% to 48%, while the use of vibroseis has increased from less than 10% to 49% (Baeten and Ziolkowsik, 1990). Due to the growing interest in environmental protection, the use of vibroseis is increasing.

As an impulsive seismic source for VSP tests, a dynamite explosion is destructive and introduces large nonlinear effects in the near field. The deterministic processing of data is source-dependent because the same borehole is used in successive experiments. Frequency-dependent phases tend to shift between data shots in the same place with different sources which couple with the ground. Ziolkowski and Lerwill (1979) demonstrated that frequency content shifts towards the low frequencies as the dynamite charge size increases. A trade-off exists between resolution and penetration in that a large charge has more energy and better penetration. However, the energy is concentrated in lower frequencies, therefore the resolution is decreased.

Other seismic sources were used in addition to explosives and weight-drop trucks --- for example, Dinoseis, Dynaseis, Dynageese, McCollum Vibrator, Thumper, Spring-loaded Thumper, Dynapulse, Kettle Popper, and Becker Drill (Lindsey, 1991). The seismic source Thumper (Stokoe et al, 2004) has been improved and is still used in the North America. Continental Oil Company (Conoco Inc.) developed the Vibroseis in the 1950s. It is still widely used to propagate seismic energy into the earth over an extended period of time. New land Vibroseis devices have been invented, among which are the Liquidator and T-Rex. T-Rex is the most powerful Vibroseis today for the purpose of land seismic investigation (Table 3.1).

VSP data processing methods for both impulsive sources and vibratory sources have also undergone a great deal of development while VSP equipment and testing techniques continue to undergo improvements and upgrades.

Vibrator	T-Rex	Liquidator'	Thumper
Vehicle Type	Buggy-mounted vibrator, articulated body	Buggy-mounted vibrator, articulated body	Built on Ford F650 Truck
Driving Speed	Hydraulic drive system (<15 mph)	Hydraulic drive system (<15 mph)	Highway Speeds
Total Weight	29,030 kg (64,000 lb)	29,030 kg (64,000 lb)	9980 kg (22,600 lb)
Length	9.8 m (32 ft)	9.8 m (32 ft)	7.1 m (23 ft)
Width	2.4 m (8 ft)	2.4 m (8 ft)	2.4 m (8 ft)
Height	3.2m (10.5 ft)	3.2m (10.5 ft)	2.4 m (8 ft)
Hydraulic System Pressure	207 bar (3,000 psi)	207 bar (3,000 psi)	476 bar (4000 psi)
Vibrator Pump Flow	757 l/m (200 gpm)	530 l/m (140 gpm)	151 l/m (40 gpm)
Vibration Orientations	(1) Vertical, (2) Horizontal in-line, and (3) Horizontal cross-line	(1) Vertical, and (2) Horizontal cross-line	(1) Vertical, (2) Horizontal in-line, and (3) Horizontal cross-line
Shaking Orientation Transformation	Push-button transformation of shaking orientation	Shop transformable in one day	Field transformable in about hour hours
Maximum Output Force: (1) Vertical, and (2) Shear	(1) 267 kN (60,000 lb) (2) 134 kN (30,000 lb)	(1) 89 kN (20,000 lb) (2) 89 kN (20,000 lb)	(1) 26.7 kN (6000 lb) (2) 26.7 kN (6000 lb)
Base Plate Area	4.11 m ² (44.2 ft ²)	4.34 m ² (46.7 ft ²)	0.698 m ² (7.50 ft ²)
Moving Mass: (1) Vertical, and (2) Shear	(1) 3,670 kg (8,100 lb) (2) 2,200 kg (4,850 lb)	(1) 13,475 lb (6,110 kg) (2) 13,475 lb (6,110 kg)	(1) 311 lb (140 kg) (2) 311 lb (140 kg)
Stroke (Peak to Peak): (1) Vertical, and (2) Shear	(1) 8.9 cm (3.5 in.) (2) 17.8 cm (7.0 in.)	(1) 40.6 cm (16.0 in.) (2) 40.6 cm (16.0 in.)	(1) 7.6 cm (3.0 in.) (2) 7.6 cm (3.0 in.)
Hydraulic Oil	Vegetable-based hydraulic oil	Vegetable-based hydraulic oil	Vegetable-based hydraulic oil
Special Features	(1) Cone pushing capacity (2) Hydraulic pressure take-off (3) Variable vertical hold-down force (4) Must be transported by tractor-trailer rig	(1) Optimized for low freq. (down to 0.5 Hz) (2) Cone pushing capacity (3) Hydraulic pressure take-off (4) Must be transported by tractor-trailer rig	(1) Built for high-frequency output (above 200 Hz) (2) Built for use in urban environments (3) Can be driven on highways

Table 3.1 T-Rex features (from Stokoe et al, 2004)

Thomson (1950) derived equations for wave propagation in media consisting of arbitrary numbers of flat layers. He introduced a transfer matrix, which was later referred to as a “propagator matrix” in order to describe the displacements and stresses at the

bottom of a layer with respect to those at the top of the layer. Haskell (1953) later corrected a small error in his derivation. A single matrix for the complete system can be derived from the individual matrices for any number of layers. One advantage of the propagator matrix is the correlation of the displacements and stresses at the bottom of a multilayered system to those at the top of the system. Another advantage of the propagator matrix is that the method facilitates the propagation of the boundary conditions from one boundary of the system to the other via matrix multiplications.

Some of the analytical and experimental studies dealing with VSP testing are the following. Stewart (1983, 1984) studied one-dimensional forward and inverse problems using VSP and interval velocities from travel time inversion. Gaiser et al (1984) studied anisotropic properties of near-borehole formations using P-waves. Pujol et al (1985) investigated offset vertical seismic profiling. Alford (1986) used two horizontal source components and two horizontal receiver components to rotate four-component data into other coordinate systems. Naville (1986), Nicoletis et al (1988), and Lefevre et al (1992) developed different applications for the Propagator matrix method. Tapered down-sweep and up-sweep signals were employed to reduce correlation noise (Martinez, 1987). Kommedal and Tjostheim (1989) performed a study of different methods of wavefield separation for application to VSP data. Gaiser (1990) employed six impulsive *P*-wave offset VSPs in a 663-m (2210-ft) deep well and observed strong transversely isotropic velocity variation. Lee (1990) studied inherent and crack-induced anisotropy by multi-offset VSP and well-log. Winterstein and Meadows (1991A and 1991B) explored shear-wave polarizations for depth resolution improvement. Zeng and Macbeth (1993) estimated shear-wave splitting in near-offset VSP data using algebraic processing techniques. Trantham (1994) utilized a plot sweep as a deterministic signature. Desired

impulse response and autocorrelation of vibrator pilot sweeps were used to design a deconvolution filter.

Grech et al (2002) recently performed multi-offset VSP experiments to investigate *P*-wave velocity anisotropy of the dipping shale strata and found 10% anisotropy. The currently deepest VSP was performed at a drill hole of 8.5 km depth where *P*-wave velocities dropped to about 5.5 km/s at 8.5 km depth from 6.0–6.5 km/s above 7 km depth (Rabbel et al, 2004). Digranes (1996) reported a VSP experiment in a drill hole of 12.26 km in Russia, but the measurement of VSP was between depths of 2.15 km and 6 km.

Yu et al (2006) developed a theory of crosscorrelogram migration of ghost reflections using inverse vertical seismic profile data without access to the source location and wavelet.

The VSP of this work focuses on engineering purpose that requires detailed velocity layering with measurements of every 5 to 10 ft (1.5 to 3 m) in the borehole for the complete depth range. Higher resolution for travel time analysis is required.

3.2 VIBROSEIS SOURCE

Land Vibroseises can be grouped into three different types: electro-hydraulic, electro-magnetic, and magnetic levitation. The electro-hydraulic vibrator can in principle generate any desired signal, but its major disadvantage is in the harmonic distortion because the servo valve closes discontinuously and, as a result, the fluid flow is intermittently reversed. Thus, the force applied to both the reaction mass and the base plate is discontinuous. The servo system cannot adequately correct for the amplitude and phase of these harmonic distortions because it is causal. The frequency range is restricted by the piston length and compressibility of the fluid. The velocity is restricted by the flux of the flow.

The P-wave and S-wave source signals used in this research were generated through a tri-axial vibrator T-Rex (Figure 3.1) weighing 29 tons or 64,000 lbs. T-Rex is an electro-hydraulic Vibroseis. T-Rex is capable of generating three vibration modes --- the vertical mode for P-wave shaking and two horizontal modes for S-wave shaking. The vertical theoretical force output is 60,000 lbs for frequencies between 12 and 180 Hz and the theoretical horizontal force output is 30,000 lbs for frequencies between 5 to 180 Hz (Figures 3.2 and 3.3).



Figure 3.1 Tri-axial vibrator: T-Rex (from Stokoe et al, 2004)

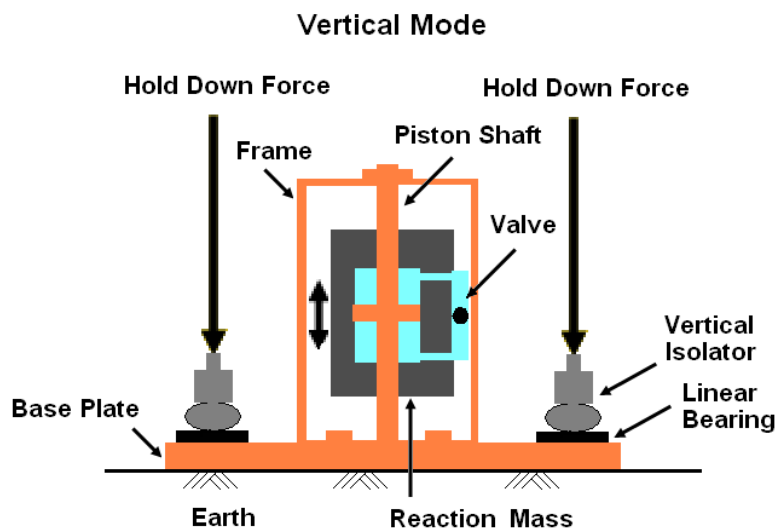


Figure 3.2 Vertical mode of T-Rex (courtesy of Brent Rosenblad)

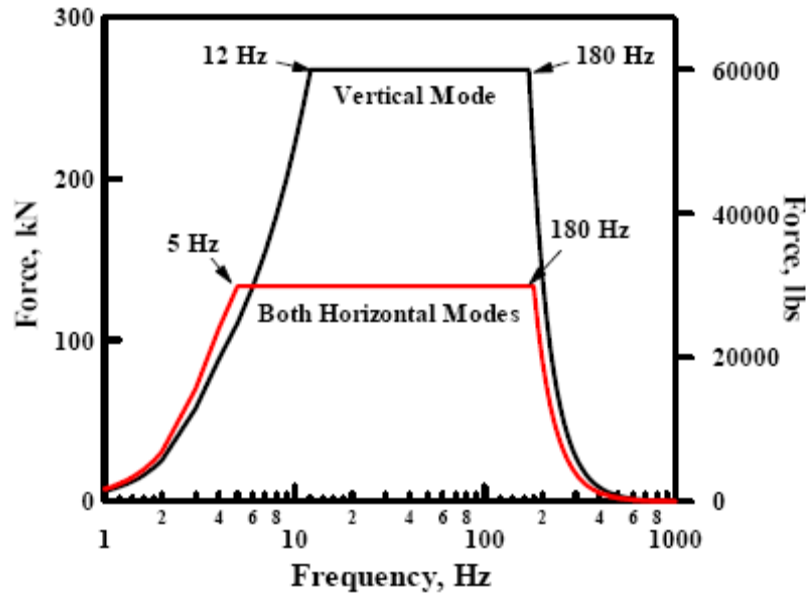


Figure 3.3 T-Rex theoretical force output (from Stokoe et al, 2004)

3.3 NONLINEAR DISTORTION IN THE VIBROSEIS SOURCE

The drive signal $q(t)$, which is a predetermined time function in the function generator, is employed for controlling the forced applied to the base plate (Baeten and Ziolkowski, 1990). The drive signal is expressed by:

$$q(t) = a(t) \sin[2\pi\theta(t)], \quad (3.1)$$

in which the function $\theta(t)$ determines the frequency of the sinusoidal excitation. The function $\theta(t)$ is a quadratic polynomial function when generating a linear chirp sweep; it is a linear function in the generation of a harmonic excitation. The amplitude function, $a(t)$, can be a linear or cosine roll-off taper function for a chirp sweep or a constant for a sinusoidal excitation. The same force must be exerted on the reaction mass in the opposite direction in order to enable T-Rex to exert a force, $f(t)$, on the base plate.

The expression of $f(t)$ is:

$$f(t) = -M_r \ddot{u}_r(t) \quad (3.2)$$

in which the mass of the reaction mass is M_r and its acceleration is $\ddot{u}_r(t)$ which can be measured. Therefore, the force on the base plate is known.

By neglecting the bending forces of the base plate, Sallas and Weber (1982) determined the ground force as:

$$g(t) = -M_r \ddot{u}_r(t) - M_b \ddot{u}_b(t) \quad (3.3)$$

where $g(t)$ is the ground force, M_b refers to the mass of the baseplate, and \ddot{u}_b is the baseplate acceleration. Equation (3.3) is called the “weighted-sum estimation” of the ground force, which assumes the baseplate a rigid body. Baeten and Ziolkowski (1990) demonstrated through field measurements that conventional rigid body assumptions regarding uniformly distributed traction and displacement directly underneath the vibrator base plate are incorrect.

The standard Vibroseis theory states that the P-wave far-field displacement is proportional to the true ground force (Miller and Pursey, 1954; Aki and Richards, 1980). Standard Vibroseis theory implies that the far-field velocity is proportional to the derivative of the true ground force when geophones are employed for obtaining velocity measurements. True ground force depends on base plate flexibility and near-field soil nonlinearity, resulting in nonuniform distribution of traction underneath the base plate.

The “weighted-sum estimation” of the ground force is widely used as a feedback signal on vibrators; for this reason, correlated Vibroseis data do not contain zero phase wavelets. Smoothing and causal correction (delay) in the feedback system causes the weighted-sum signal to differ from the pilot sweep or drive signal. The true ground force differs from the force estimated from the weighted sum acceleration because of the true traction involving the bending of the base plate and the nonlinearity of the soil beneath it.

Two sources of nonlinearity occur with the use of Vibroseis sources. First, the travel time is occasionally correlated with the driving force level, which means the travel

time changes as driving force level increases. Martin and Jack (1990) attribute this correlation to possible changes from the physical soil properties of the near-surface layers. As the amplitude of the vibrations increase, the near-surface soil layers become softer and have a lower velocity. The second nonlinear problem is the harmonic distortion of the outgoing waveforms. Two general viewpoints regarding this issue are found in the literature. One states that nonlinearity stems from the vicinity of the base plate, but accumulates as the wave propagates in the far field (Dimitriu, 1990). The other viewpoint states that the near-source zone is primarily responsible for the harmonic distortion beyond which the waves remain essentially linear (Jeffrey, 1996). No matter the sources of the nonlinearity, it does exist in the measurements.

Lebedev et al (2004) built a contact-nonlinearity model to explain the nonlinearity. The model approximates the thin layer between the base plate and the soil with large deformations as a nonlinear oscillating spring. The contact spring determines the rigidity of the contact. They conclude that the harmonic distortion originates from the contact-nonlinearity or from the difference in the restoring force between the compression and tension phases of the structurally inhomogeneous media.

Finite amplitude waves in the near field generate higher harmonics and other complications due to the interaction of P and S waves (Thompson et al, 1977; Goldberg, 1961), the existence of a nonlinear boundary (Konovalov et al, 1991), or nonlinear modal interactions and energy transfer between high-frequency and low-frequency modes (Nayfeh and Balachandran, 1994; Nayfeh, 2000).

The adverse effect of the nonlinear distortion on the travel time analysis is significant for chirp sweep signals. To reduce the nonlinear distortion to the minimum, this work used a sinusoidal drive signal that has a fixed single frequency, called fixed-

sine signal. A new method is developed to identify the source signature of the fixed-sine source signal.

3.4 FIELD TEST CONFIGURATION AND TEST PROCEDURES

Figure 3.4 shows field test setup that was used for Borehole C4993 at Hanford Waste Treatment Project site. The results from measurements in this borehole are used as examples of the measurements and signal processing in this work. T-Rex was located on the ground surface 7.5 m (25 ft) away from the borehole with its longitudinal axis tangential to a circle centered at the borehole.

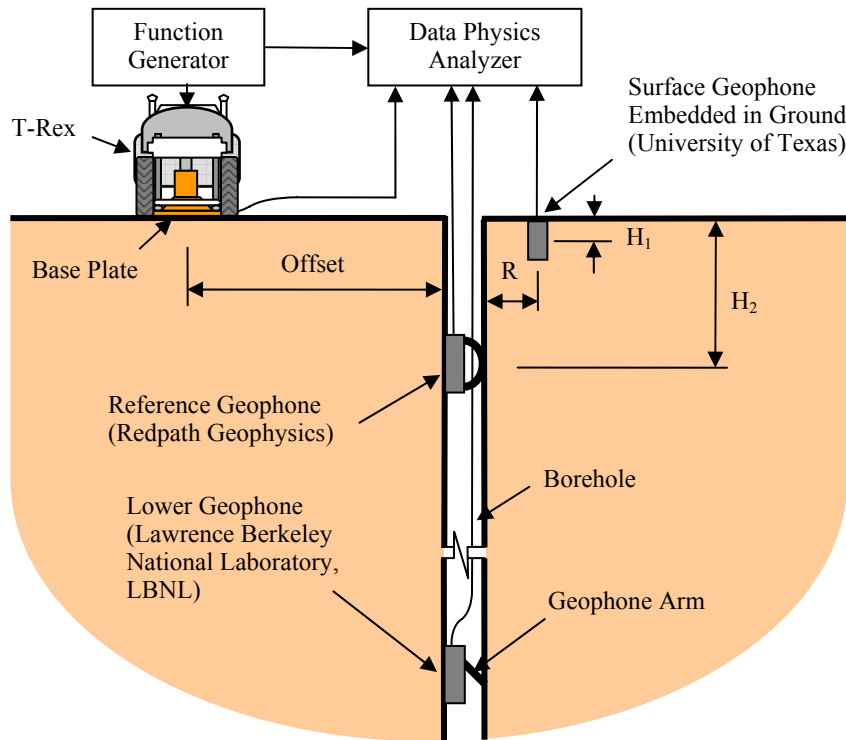


Figure 3.4 Deep downhole test setup diagram

All P- and S-wave measurements were performed using the Lawrence Berkeley National Laboratory (LBNL) 3-D wireline geophone as the at-depth borehole receiver,

which is called the lower receiver. A hoist was used to move the lower geophone along the borehole and vary the depths traveled by this device.

In addition to the LBNL 3-D geophone, a 3-D geophone from Redpath Geophysics was fixed at a depth of 6 m (20 ft) and a 3-D geophone from the University of Texas was embedded near the borehole at about 0.45m (1.5 ft) below the ground surface.

The drive signal used to control the motion of T-Rex is defined by a given number of cycles of a fixed sine signal at a fixed frequency. The drive signal was generated by a function generator and dispatched to T-Rex in order to excite the reaction mass. The base plate of T-Rex transmitted the vibration energy from the reaction mass to the ground surface.

The recorded time series of the base plate motion is called the input signal. When the base plate moves only in the vertical direction, then the input signal is called a P-wave. Only one mode of P-wave motion (vertical) was generated. The initial force was normally set to allow the base plate to initially move downward and compress the soil underneath the plate.

When the base plate moves in the horizontal direction, then the input signal is called an S-wave. As discussed further in section 4.3.4, two modes of S-wave vibrations can be generated; one is along the longitudinal axis of T-Rex, called the in-line S-wave; the other is along the transverse axis, called the cross-line S-wave. T-Rex is usually oriented in such a way that either the longitudinal or the transverse axis is tangential to a circle centered at the borehole. Each mode of S-wave shaking has two initial orientations; one is called forward motion and the other is called reversed motion, which is characterized by a 180-degree phase difference from the forward motion. In the

measurements at Borehole C4993, only one mode of S-wave shaking was used and this mode was driven in both the forward and reverse motions (directions).

All signals during the test were recorded by a Data Physics Analyzer, which was connected to a laptop for synchronized monitoring. Signals that were recorded include the drive signal, reaction mass and base plate acceleration signals, surface geophone receiver signals as well as signals from the reference and lower geophones.

Whenever the lower geophone was moved and fixed at a given depth, three tests were performed separately in any sequence, namely the P-wave, forward S-wave, and reversed S-wave tests. Each test corresponded to a unique vibration mode of T-Rex. Each test for a fixed lower geophone depth was repeated multiple times in the same mode so as to permit signal averaging in the time domain. Signal averaging was performed using approximately 3 to 15 averages, with 5 or 10 averages typically used.

After completing all the three tests, the lower geophone was moved to a new depth and the procedures described above were repeated until all measurements over the depth range were performed. For example, measurements in Borehole C4993 at the Hanford site were performed over the depth range of 110m (370 ft) to 420 m (1400 ft) (Figure 3.4), typically at 3m (10 ft) intervals. However, in some interbeds, 1.5m (5 ft) depth intervals were used, while below about 360m (1200 ft), depth intervals of 6m (20 ft) were used.

Measurements using this method and procedures were also performed at the Yucca Mountain Site in Nevada. In this case, the measurements were accelerated by replacing the single 3-D lower geophone mentioned above with five identical 3-D lower geophones. These geophones are called the LBNL 5-level receivers and were secured at 3m intervals along a cable, which permitted relocating the receivers along the borehole. For each vibration mode of T-Rex, five depths within a 15 m (50 ft) depth range were

simultaneously measured. The LBNL GeoRes was used to record all the 3-D signals of each of the 5 geophones at the Yucca Mountain Site.

3.5 TRAVEL TIMES OF MULTI-COMPONENT SIGNAL

Travel times have two definitions as discussed by Cerveny (2001). The first definition is ray-theory travel times and the other is first-arrival travel times. Ray-theory travel times are calculated along the rays of such individual elementary waves as direct waves, reflected waves, converted waves, and multiply-reflected waves. Ray-theory travel times consider multi-path travel. First-arrival travel times are the travel times of the first arrival of the complete wave field at a specified receiver position. First-arrival travel times are the properties of the complete wave field, regardless of what type of wave that arrives first. It is not related to the amplitudes of the wave field unless it coincides with the ray-theory travel time.

The main features of deep downhole analysis are multilayer reflections, multi-ray-path, angular and frequency dispersion, waveform scattering and coupling, and low signal-to-noise ratio (Figure 3.5). These features pose a challenge to the consistency of first-arrival travel times. Ray-theory travel times were used in this work.

Vertical wave propagation is chosen in this work because it increases the signal-to-noise ratio as well as permits vibration energy to reach greater depths. The T-Rex vibratory source is located very close to the borehole. The offset of T-Rex to the borehole is about 6 to 12m (20 to 40 ft), while the depth of the borehole is about 600 m (2000 ft).

The motion can be considered as many energy fluxes, each propagating along a ray path. Energy flux is defined as the kinetic energy crossing unit surface in unit time (Auld, 1973). The motion at receiver R is the superposition of many energy fluxes from different ray paths, including direct and reflected ray paths. The direct ray paths have no reflections in that the direct ray path arrives directly from the source to the receiver

without reflecting from the layer boundaries throughout the course of propagation, such as ray paths c and d. The reflected arrivals have one or more reflections, such as ray paths e, f, and g. The travel times of different energy fluxes from the source to the receiver typically are not the same, which constitute a multi-component signal at the receiver.

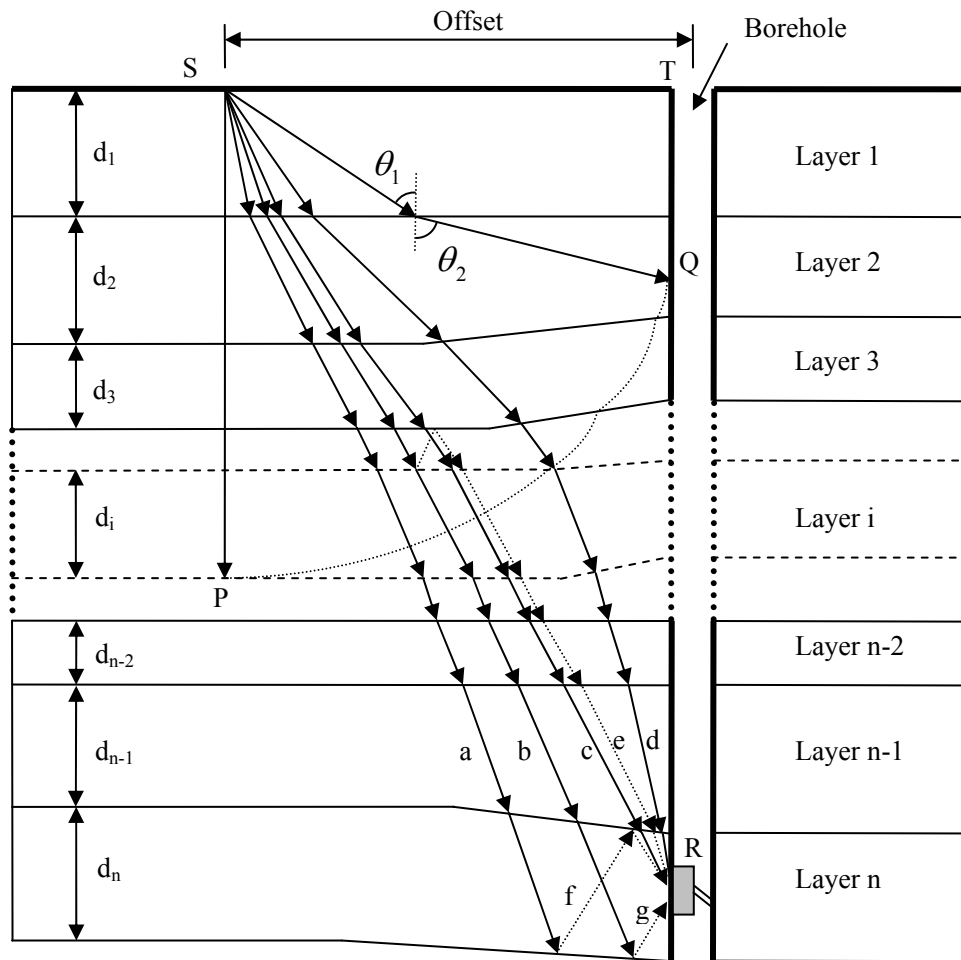


Figure 3.5 Illustration of various ray paths of multilayer wave propagation

At deep depths where the incident angles are much smaller than 15 degrees (which is the depth of 93.3 m or 311 ft in the tests at Hanford with a 7.5m or 25 ft offset),

all ray paths that reach the receiver can be approximated as a ray beam that is a straight line connecting the source, S, and the receiver, R.

The signal at the receiver is considered a superposition of direct waves of both P and S waves, reflected waves of both P and S waves, coupled waveforms, correlated noise (for example, waves from the cable that have similar frequency as the desired signals), and white noise. Several approaches are used for travel time analysis. The most commonly used approaches are arrival-identification method (hand picked), deconvolution, cross-correlation, wavelet transform, and time-frequency domain analysis. Figure 3.6 displays an application of the arrival-identification method, which uses the first-arrival travel times of a pre-selected point on the waveform. The first peak marked by a small circle is used as the wave arrival-identification for the P wave.

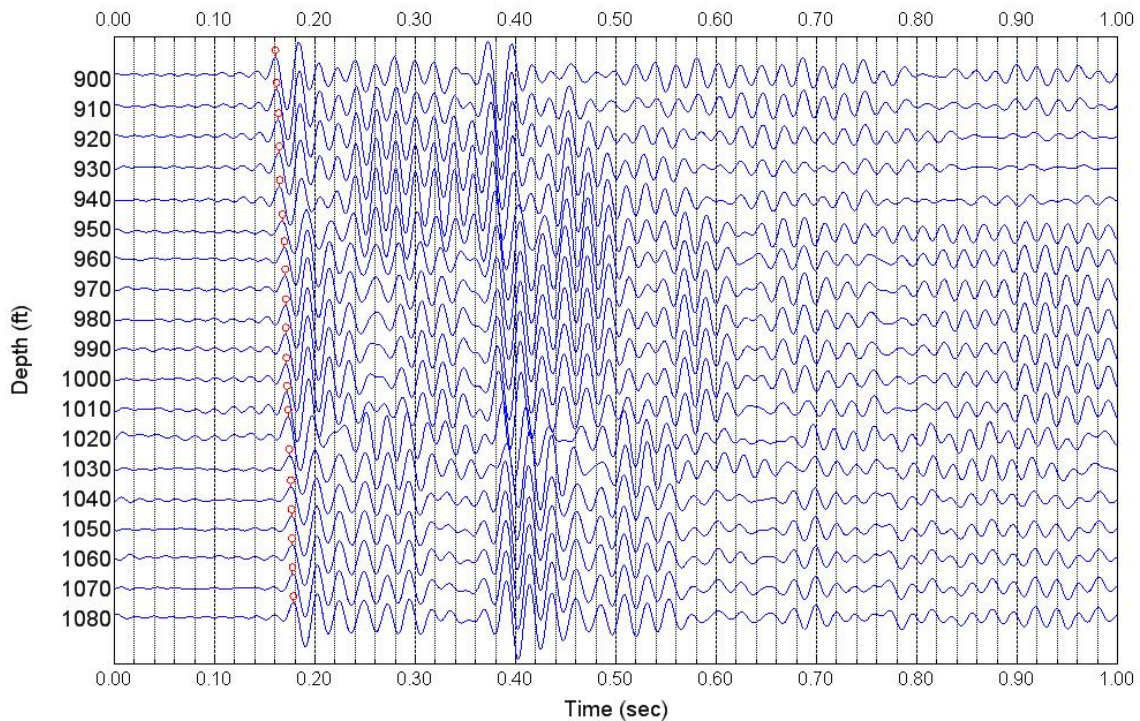


Figure 3.6 Waterfall plot of filtered P-wave receiver signals at Hanford site over the depth range of 900 to 1080 ft (270-324 m)

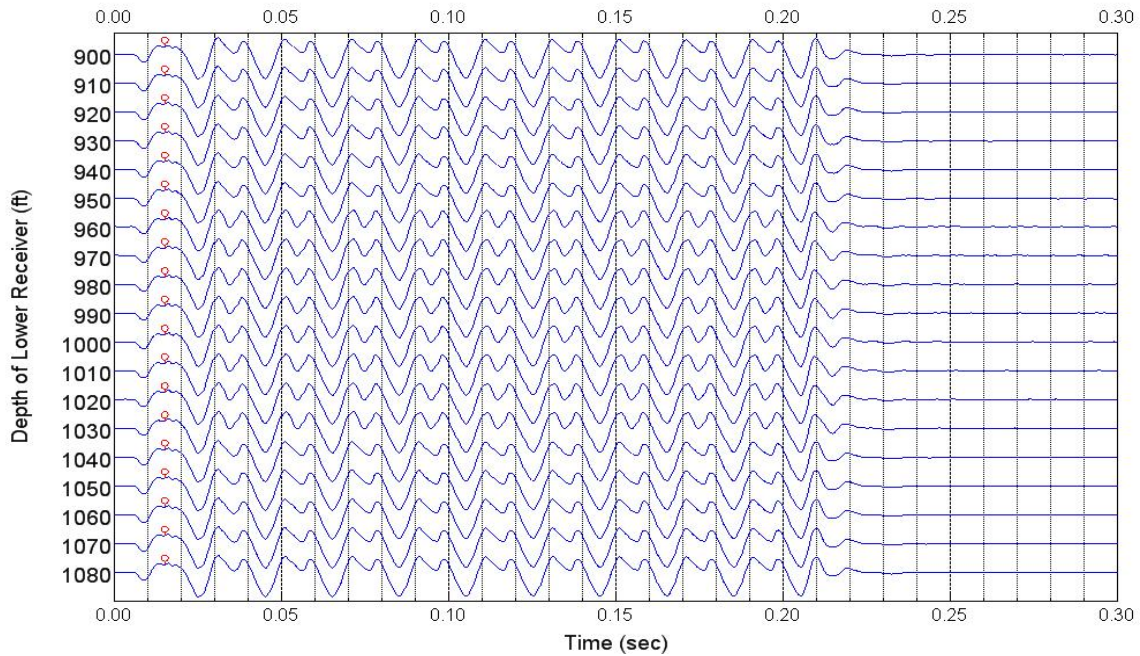


Figure 3.7 P-wave acceleration signals from the reaction mass of T-Rex at the Hanford site

Measurements of travel times at each depth were obtained using different source signals as references. One problem that was found is the different references can give trigger times that may not be perfectly aligned. Figure 3.7 is an example of the trigger times corresponding to the receiver signals in Figure 3.6. As a result, relative travel times were used, which means that arrival times are subtracted from the corresponding trigger times.

The slopes of linear segments of the travel time versus depth plot are considered to represent the phase velocity. Figure 3.8 is an example of such a plot and the travel times of each layer can be plotted as a straight line if the layer is homogeneous and isotropic. Once the velocity profile is completed, engineering constants can be obtained using the method introduced in Chapter 2.

The analysis of travel times becomes complicated when soil or rock layers demonstrate strong anisotropy or stiffness contrast. Figure 3.9 shows distortion of the first peaks (marked by small circles) caused by reflections or other possible factors such as anisotropy, scattering and coupling, heterogeneity, and fractures. The impact of these factors and the analyses to minimize their effects are the thrust of this research.

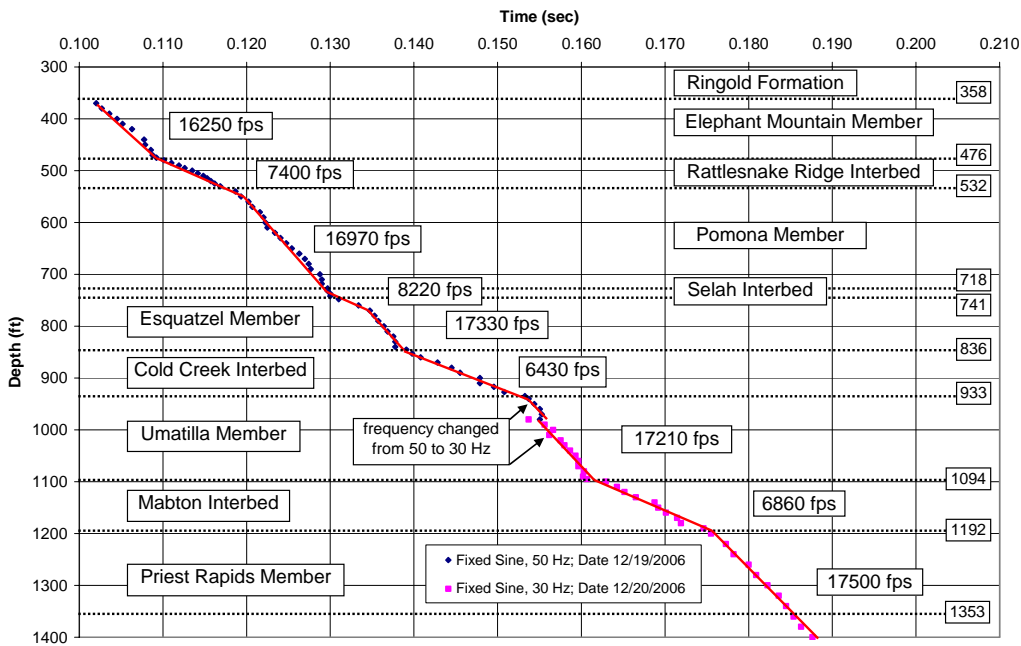


Figure 3.8 P-wave relative travel times and interpreted velocity profile in Borehole C4993 at Hanford site

Figure 3.10 is a shallow downhole test at Duke Cherokee site with a sledge hammer used to generate the source signal. The same source signal was applied to the receiver signals at all the depths. The bottom of the borehole is located on an incline slope. As shown in Figure 3.11, starting from a depth of about 5 m (15 ft), an additional peak gradually emerged between the first arrival and the first trough.

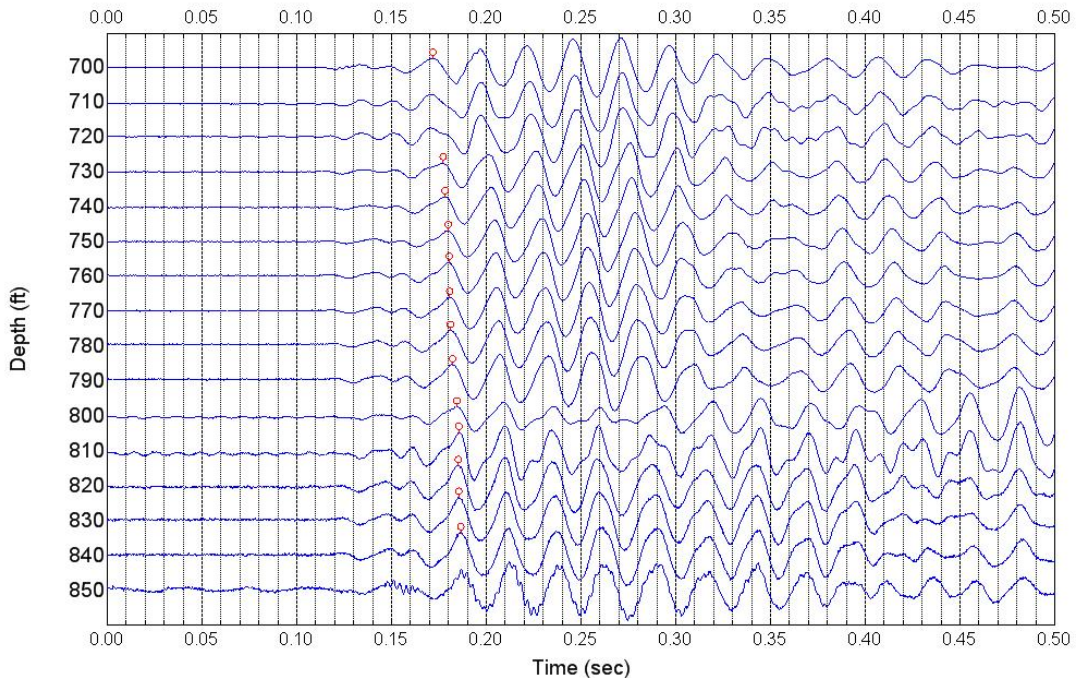


Figure 3.9 P-wave receiver signals at WT-1 site, Yucca Mountain, NV

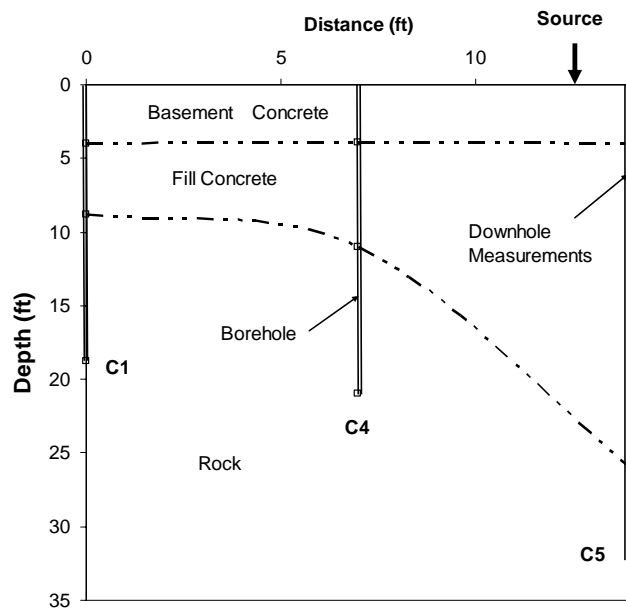


Figure 3.10 Downhole test at Duke Cherokee site (Courtesy of Minjae Jung)

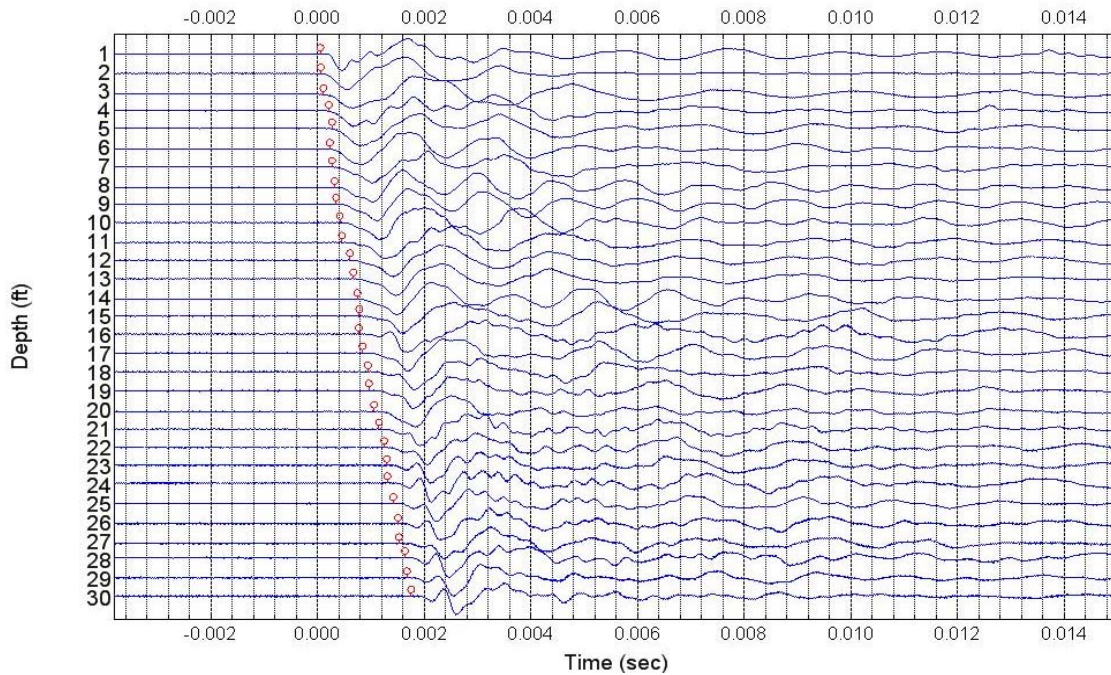


Figure 3.11 The effect on the downhole P-wave signals of a known slope shown in Figure 3.10

3.6 S-WAVE ORIENTATION AND COMPOSITION

All boreholes are vertical. The length of the receiver tool is a few times the diameter of the boreholes. The deviation of the receiver tool from the vertical line due to the roughness of borehole walls is negligible. Therefore, P-wave signals were considered directly measured from the vertical geophone. However, the receiver tool attached to a cable was prone to horizontal twisting each time the receiver was mounted to the borehole thereby adversely affecting the orientation of horizontal geophones. During the test, the alignment of two horizontal geophones - namely the S_1 (in-line component) and the S_2 (cross-line or X-line component) - to the vibration orientation is not completely assured. Figure 3.12 shows the hodograph of S-wave signal at a depth of 380 ft (114 m). The vibration orientation is about 46 degree. The two components S_1 and S_2 have 180

degree phase shift. To track the same phase of the S-wave signal for travel time analysis, a common practice is to correct the disorientation of the receiver tool and retrieve the S-wave signal in the corrected direction of shaking. The drive signal is 5 cycles of 50-Hz sine wave. Figure 3.13 is the filtered hodograph of the S-wave in Figure 3.12. The filter is an 80-Hz low-pass filter. The straight line denotes the rotated in-line direction, which indicates that the strongest horizontal motion is characterized by a 46 degrees angle to the in-line geophone orientation. The angles vary along the borehole with depth because of unavoidable twisting of the cables from which the geophones are mounted.

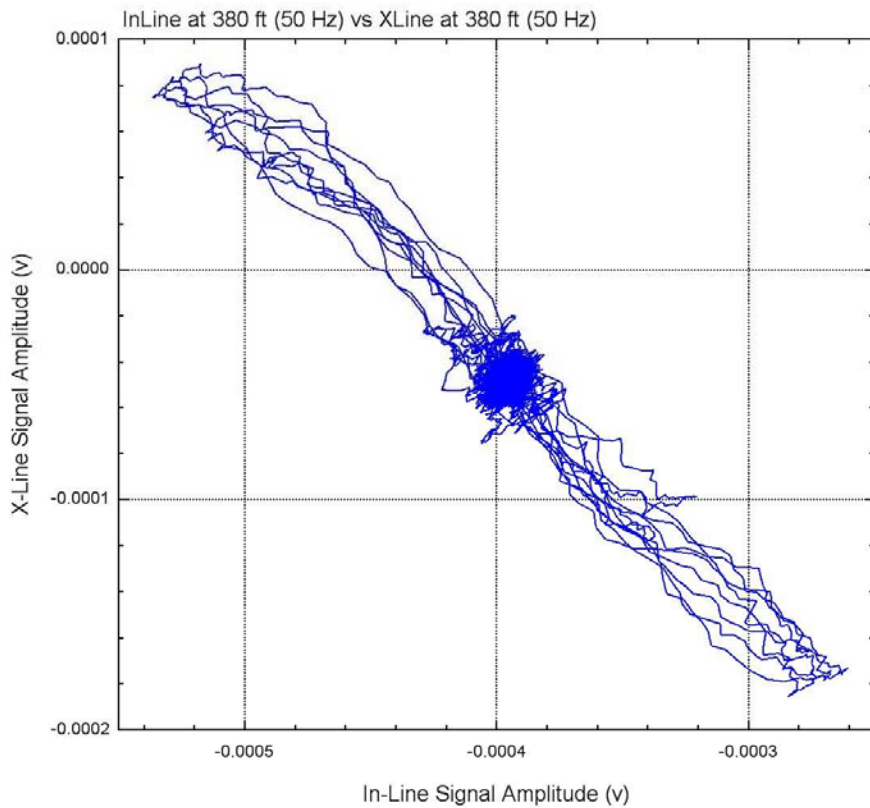


Figure 3.12 Hodograph of S-wave signal in Borehole C4993 at Hanford site

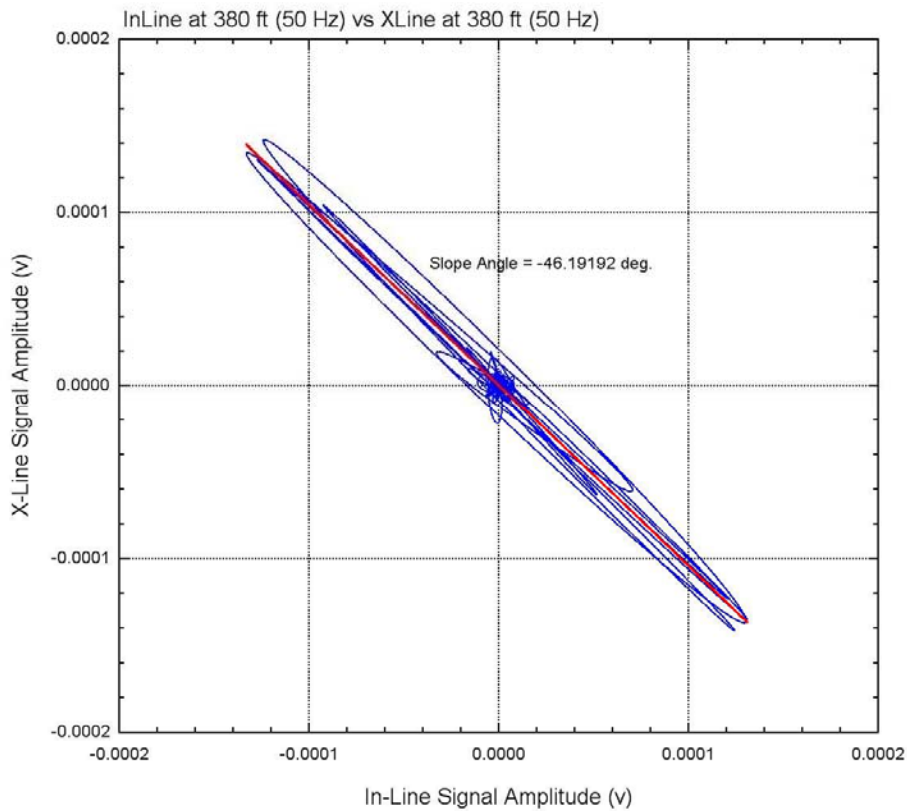


Figure 3.13 Hodograph of filtered S-wave signal in Borehole C4993 at Hanford site

The variation in geophone orientation requires correction. Failure to correct variations in geophone orientation will result in phase or time shifts in recorded signals. There are a few methods in the literature to correct the disorientation. One correction is to track the particle motion alignment by inspection (Oye et al, 2005). This method works when signal-to-noise ratio is high because it is sensitive to noise and preceding P-wave and SV-wave arrivals. Another method for the correction is the maximum energy method by Di Siena et al (1984) using P-wave arrivals. The most common method is the eigenvector analysis of the covariance matrix (Kanasewich, 1981; Esmersoy, 1984; Daley et al, 1988). Strong anisotropy and polarization skewing pose a challenge to all of these methods. A trend line was used to obtain the strongest direction of the S-wave motion,

which is called the rotated in-line orientation. The recorded in-line and x-line signals were then projected onto the rotated in-line orientation in order to reproduce S-wave signals at each depth that are aligned to the T-Rex shaking orientation. Strong anisotropy, multi-polarization and polarization skewing pose a challenge to all of these methods when signal-to-noise is low at significant depths. Only when the polarization skewing, wave scattering and coupling effect (Figure 3.14) are eliminated from the time series can the rotated in-line orientation be correctly recovered. A new method using wavelet response is proposed in Chapter 6 to solve this problem.

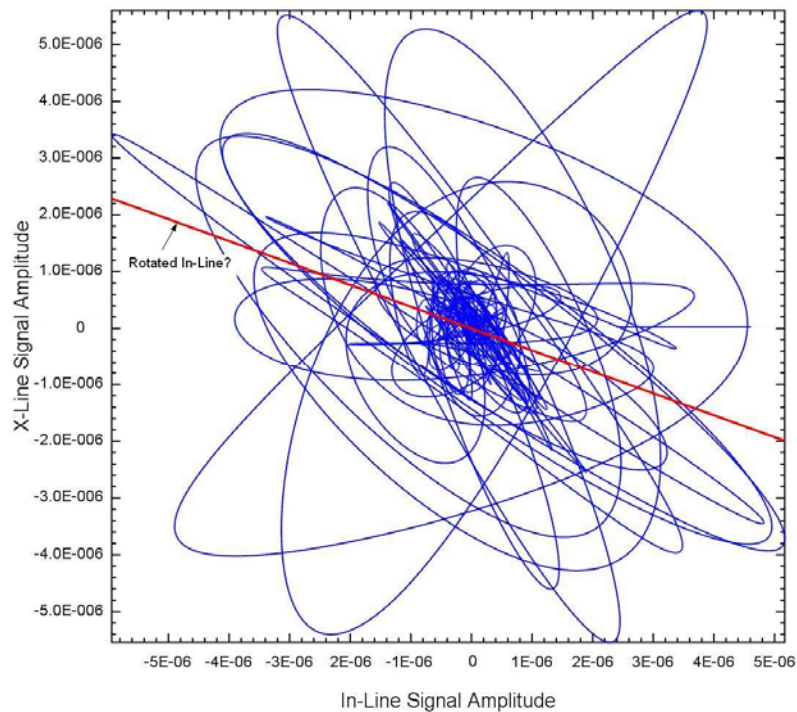


Figure 3.14 Polarization skewing, wave scattering and coupling of S-wave signal

3.7 SUMMARY

In this chapter, the vibratory source equipment and the procedures for field testing are discussed. Complicated conditions caused the underground stratigraphy of the real

earth add to the difficulty in obtaining high quality signals. As discussed in the following chapters, the signal quality can be improved by customizing the excitation frequency of the vibrator to the damped natural frequency of the earth-vibrator system. A proper increase in the excitation duration of the source signal also contributes to the quality of the receiver signal.

The arrival-identification method is also discussed in this chapter and an example of a travel-time analysis is presented. This method is vulnerable to waveform distortions. Other conventional travel time analyses almost universally focus on impulsive sources or chirp sweeps. No data processing technique is available in the literature regarding the trace data generated by durational harmonic source wavelet. This approach and lack of analysis technique call for the development of a new technique in signal processing, namely the wavelet response technique as discussed in the following chapters.

Chapter 4 Simplified Analysis of Downhole Measurements

4.1 INTRODUCTION

To assist in the analysis of deep downhole seismic measurements using T-Rex and a fixed-sine wavelet as described in Chapter 3, a computer program called DeepSeis 2.1 was developed. The primary functions of the software are as follows:

1. Read any data files or time records in ASCII format. Data files can be recorded with any number of description header lines, in any number of rows or columns for any number of traces in one file. The program provides an interface to script useful information from raw data saved in the various formats of different recording equipments. To avoid data contamination, the program always directly reads the raw data file throughout the data processing process.
2. Filter signals in time domain or frequency domain. Raw data records can be averaged or stacked, and time shift between each shot can be aligned. Disorientation of S-wave components can be corrected.
3. Visualize signals with interactive graphic user interface. Signals can be displayed individually or grouped in panels, or in waterfall format. For example, this program permits comparison of the filtered and unfiltered signals, the in-line and x-line signals, the forward and reverse signals, and the P-wave and S-wave signals.
4. Pick travel time interactively using a mouse pointer or using keyboard. The paneled plot and the waterfall plot can be switched alternatively to track wave identifications or amplitude variations.
5. Create travel time or velocity profiles.

One example of using DeepSeis 2.1 is presented in this chapter. Testing was conducted using the setup shown in Figure 3.4. An example set of data from one borehole at the Hanford site is shown.

4.2 BRIEF BACKGROUND OF CONVENTIONAL ANALYSES

Conventional VSP and the deep downhole test commonly assume that the source and receiver are on the same vertical line perpendicular to horizontal layers. On the other hand, in offset VSP tests, the ray deviation is located significantly from a vertical line, thereby requiring moveout corrections and migration of trace data.

Conventional VSP processing is divided into five processing sequences (Mari et al, 1999). The first sequence includes correlation, correction for signature variations, tool rotation and borehole deviation, editing inaccurate records, and sorting into 3D components. The second sequence comprises selection of the first arrival times. The third sequence is characterized by wave separation of up-going and down-going P and S waves. The third sequence is deconvolution of up-going waves by down-going waves. The fourth sequence consists of flattening the deconvolved up-going waves. The fifth sequence is the production of the stacked VSP trace.

An impulse response of the earth is generally preferred for travel time analysis. For a source signal $f(t)$, if $e(t)$ is the impulse response of a linear system, then the displacement response, $u(t)$, at the receiver satisfies:

$$u(t) = f(t) * e(t) \quad (4.1)$$

where the asterisk “*” denotes convolution.

If the source signal is available, deconvolution is used to get the impulse response as:

$$e(t) = FFT^{-1} \left\{ \frac{FFT\{u(t)\}}{FFT\{f(t)\}} \right\} \quad (4.2)$$

where FFT denotes Fast Fourier Transform, and FFT^{-1} denotes inverse FFT.

If the source signal is unavailable, one approach to obtaining an impulse, $\delta(t)$, is trying to find an inverse filter $l(t)$ such that:

$$l(t) * f(t) \approx \delta(t). \quad (4.3)$$

Application of the inverse filter to Equation (4.1) yields:

$$l(t) * u(t) = l(t) * f(t) * e(t) \approx \delta(t) * e(t) = e(t). \quad (4.4)$$

Unfortunately, an inverse filter is not always available. As an alternative, a chirp sweep $f(t)$ is used in the conventional VSP, the autocorrelation of which results in a zero-phase wavelet that is similar to an impulse $\delta(t)$. The autocorrelation can be expressed as:

$$f(t) \otimes f(t) \approx \delta(t) \quad (4.5)$$

where the symbol “ \otimes ” denotes correlation.

It is assumed (Brotz et al, 1987; Bickel, 1982) that the cross-correlation of the chirp sweep $f(t)$ with receiver signal $u(t)$ would result in the impulse response $e(t)$ that can be expressed as:

$$f(t) \otimes u(t) = f(t) \otimes f(t) * e(t) \propto e(t) \quad (4.6)$$

where the symbol “ \propto ” denotes proportional with a constant scale. In the frequency domain, if the following is defined:

$$E(\omega) = FFT\{e(t)\}, U(\omega) = FFT\{u(t)\}, F(\omega) = FFT\{f(t)\} \quad (4.7)$$

one obtains (Baeten et al, 1990):

$$F(\omega)U(\omega) = \bar{F}(\omega)F(\omega)E(\omega) = |F(\omega)|^2 E(\omega) \quad (4.8)$$

where: $\bar{F}(\omega)$ denotes the conjugate of $F(\omega)$.

A chirp sweep is capable of keeping the power spectrum $|F(\omega)|^2$ constant over a given bandwidth. The impulse response within this bandwidth can be recovered from:

$$E(\omega) = \frac{F(\omega)U(\omega)}{|F(\omega)|^2} \quad (4.9)$$

The terms minimum phase, maximum phase, and zero phase generally refer to a system, a signal, or a filter in the literature. These terms and concepts are critical to the correct interpretation of signal processing.

A linear and time-invariant system and its inverse are both causal and stable, so that the system is considered minimum-phase (Oppenheim and Schaffer, 1975; Cambois, 2000). The energy of a minimum-phase system (for example, an airgun shot or a dynamite blast) is as close to time zero (trigger time) as possible, but the energy can not precede the trigger time because a minimum-phase signal must be causal. The inverse of the minimum-phase is also causal. Mari et al (1999) defines the minimum and maximum phase signals as follows. The z-transform of a wavelet $s(t)$ can be expressed as the product of multiple doublets as:

$$S(z) = \sum_{i=0}^N s_i z^i = C \prod_k (1 + b_k z) \quad (4.10)$$

where: $1 + b_k z$ is the k-th doublet and C is a normalization constant. If $|b_k| < 1$ for all k, the signal S(z) is called the minimum phase, and S(z) is invertible because the doublet is invertible and stable. If $|b_k| > 1$ for all k, then S(z) is maximum phase.

A minimum phase filter has a phase spectrum $\phi(\omega)$ which is the Hilbert transform of the amplitude spectrum $|A(\omega)|$, or:

$$\phi(\omega) = HT \{ \ln(|A(\omega)|) \} \quad (4.11)$$

where HT is the Hilbert transform. A minimum phase filter is causal and causally invertible.

An autocorrelation function, which has the largest central amplitude at time zero, is called a zero-phase wavelet (Berkhout, 1984). The Continental Oil Company recommended using zero-phase deconvolution on Vibroseis data in the 1970s. However, Baeten and Ziolkowski (1990) concluded that the Vibroseis source signature was not

zero-phase after they analyzed the mechanism of the Vibroseis vibration and then modeled it analytically and compared with field test results.

The weighted sum signal of the ground force of the vibrators is generally used as the feedback signal, while the chirp sweep is widely used as the drive signal. This is partly due to the effectiveness of the predictive deconvolution for a chirp sweep that assumes a zero phase Klauder (pilot sweep) wavelet. In addition, the recording instruments, attenuation, ghosts, reverberations, and other types of multiple reflections are minimum-phase components. The convolution of the zero-phase Klauder wavelet with minimum-phase components results in a mixed phase seismic wavelet. The Klauder wavelet is converted to its minimum-phase equivalent in order to avoid a mixed phase wavelet for a spiking deconvolution (Cambois, 2000; Robinson and Saggaf, 2001; and Brittle et al, 2001). However, this solution still assumes that the zero-phase Klauder wavelet represents the Vibroseis source signature, which conflicts with the results by Baeten and Ziolkowski (1990) who concluded the correlated Vibroseis data does not contain a zero phase wavelet.

On the other hand, the conventional predictive deconvolution is challenged because it assumes that the reflectivity of the earth is statistically white, the data is noise free, and the seismic wavelet is minimum phase. Mewhort (2002) redeems the use of predictive deconvolution on Vibroseis data as a violation of the minimum phase assumption because the source signature is constant phase. Mewhort (2002) concluded that the results from the minimum-phase Vibroseis deconvolution are superior to zero-phase deconvolution, though both displayed residual phase errors.

Correlation with a matched filter produces a degraded result in the presence of significant noise (Mari, 1999). Cross-correlation is sensitive to waveform distortions as a result of noise and correlated waveforms such as multi-path arrivals, reflections, S-wave

birefringe, and S-wave splitting. When the signal to noise ratio is low, the cross-correlation deteriorates. Generalized cross-correlation algorithms have been widely used to filter signals in a frequency window before correlation (Ching et al, 1999; Hero and Schwartz, 1985).

The multi-component signal poses a challenge to current wavelet transform and time-frequency signal analysis. Okaya et al (1992) used Fourier frequency-uncorrelated time transformation (short time Fourier transform) to suppress and reduce resonance-induced energy through vibrator-to-ground coupling. Wei and Bi (2005) divided a signal into a number of segments and estimated the desired parameters for computing the modified local polynomial time-frequency transform in each segment from polynomial Fourier transform in the frequency domain.

Jiang et al (2006) proposed a time-frequency cross-correlation algorithm based on wavelet transform to extract reflections from the trace data. Their method proved appropriate for removing ambient noise and extracting reflected sweeps from the trace data. Eigenimage discrete wavelet transform is used for multi-scale geophysical data analysis by Droujine (2006) to improve the scale resolution when non-stationary noise spans most wavelet scales.

Without assuming weak anisotropy, Ursin and Stovas (2006) derived approximations for travel time and travel time squared for multiple transmitted, reflected, and converted quasi-P-quasi-SV-waves, or multiple transmitted, reflected SH-waves in a layered transversely isotropic medium using the Taylor series approximations in slowness.

Svenningsen and Jacobsen (2007) presented a novel method to recover and retrieve information on absolute S-wave velocities from receiver functions. They

calculated the half-space S-wave velocity from the horizontal slowness and the angle of surface particle motion for an incident P wave using a suite of filter-parameters.

The drive signal used in this research is a fixed-sine wavelet as discussed in Chapter 3. Different from a chirp sweep, an inverse filter as described by Equation (4.3) is not available, and an autocorrelation of a fixed-sine wavelet as described by Equation (4.5) is far from an impulse $\delta(t)$. The hand-picked arrival-identification method is used for this simplified travel time analysis before the more complex wavelet-response analysis is introduced in Chapter 7.

4.3 EXPLANATION OF TERMINOLOGY USED IN DEEPSEIS 2.1

4.3.1 Record or signal

The recorded and sampled time series of analog voltage from a geophone or an accelerometer is called a record. A signal generally refers to a raw record, a processed record, or any designed or generated (as by function generator) time series. The magnitude of any signals related to the downhole test is by default denoted in voltage. All signal amplitudes (y-axis for time series, both axes for hodograph) in the figures in this chapter, if not otherwise explicitly labeled, are denoted in volts.

All figures for time series are shown with the y axis scaled independently in order to improve legibility for each trace (gain-normalized). This makes the figures more legible in cases where the amplitude varies from trace to trace (large when close to the surface, small at depth).

4.3.2 Input signal or drive signal

An independent fixed sine wave with a frequency of 50 Hz, 30 Hz or 20 Hz was sent from a function generator to T-Rex at each measurement depth. This signal is called the Input Signal to T-Rex, or the T-Rex Drive Signal. The input signal was a perfect sine

wave comprising of either 5 cycles of 50 Hz or 4 cycles of 30 or 20 Hz. A 50-Hz drive signal is shown in Figure 4.1. Input signals of all measurements were aligned so that they all commenced at the same instant, which is called time zero, and was marked as time zero (at $t = 0$) on all recorded signals.

The input signal was sent to T-Rex anywhere from three to 15 times to allow signal averaging of the compression and shear waves in the time domain. In addition, the polarity of the drive signal for the shear wave was then reversed and the whole process was repeated to allow another averaged shear wave signal with reversed polarity to be recorded at the same depth. A set of 30-Hz S-wave drive signals is shown in Figure 4.2.

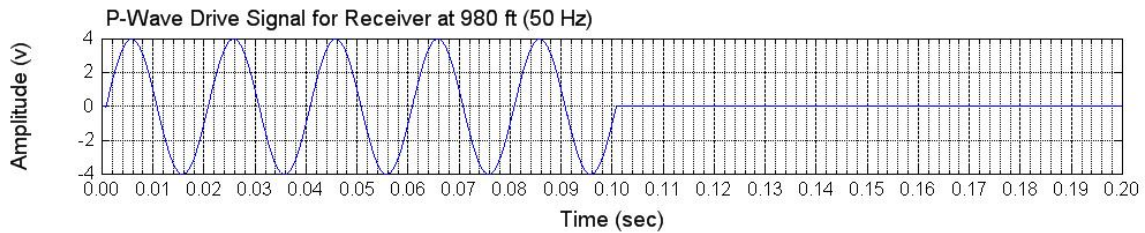


Figure 4.1 5 cycles of 50-Hz P-wave drive signal to T-Rex

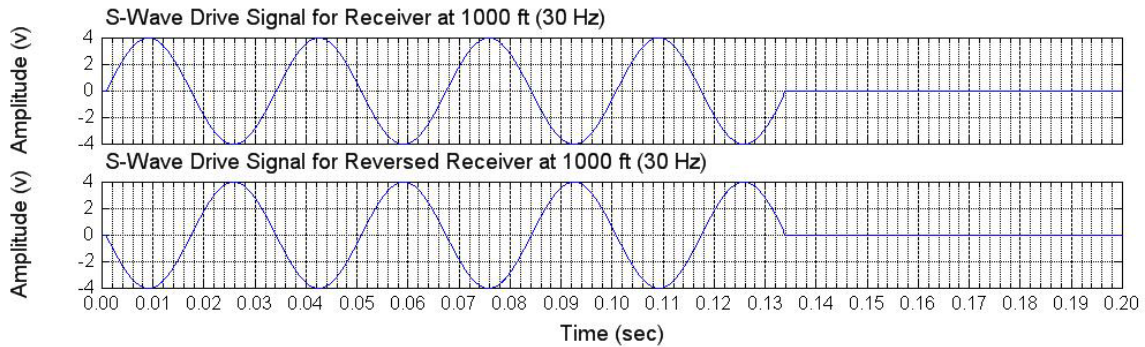


Figure 4.2 4 cycles of reversed sets of 30-Hz S-wave drive signals to T-Rex

4.3.3 Reaction mass acceleration in vertical shaking

The vertical output force of T-Rex that was used to generate compression waves was transmitted to the ground surface by the square base plate located on the bottom of

T-Rex. The base plate directly contacted the ground surface. The acceleration of the reaction mass that loads the base plate was recorded by a vertical accelerometer on the reaction mass. An example of the reaction mass output signal is presented in Figure 4.3.

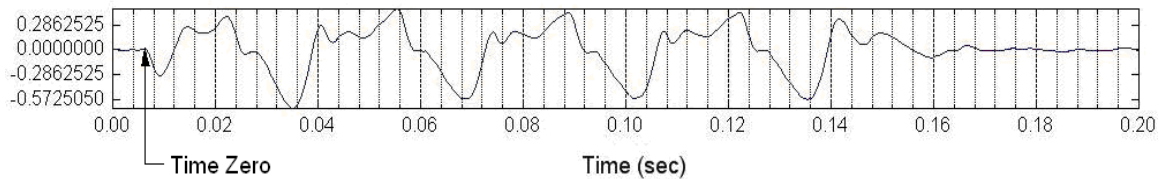


Figure 4.3 Unfiltered P-wave acceleration signal of the reaction mass for 4 cycles of the 30-Hz sine-wave drive signal

4.3.4 In-line and cross-line (x-line)

Two ways to position the vibrator are illustrated in the Figure 4.4. Figure 4.4 (a) displays the most common plane layout of the vibrator relative to the borehole. Regardless of the orientation of the vibrator, the vertical section crossing both the center line of the vibrator and the borehole is called the in-line plane or in-line direction,. The plane perpendicular to the in-line section is called the cross-line plane or cross-line direction. Figure 4.4 (b) shows the layout of T-Rex used in this research. During shaking for the generation of shear waves, the base plate was moving perpendicular to a radial line between the base plate and borehole as shown in Figure 4.4b. The radial line is called the cross-line (x-line) direction, while the tangential line, which represents the direction of the base plate, is called the in-line direction.

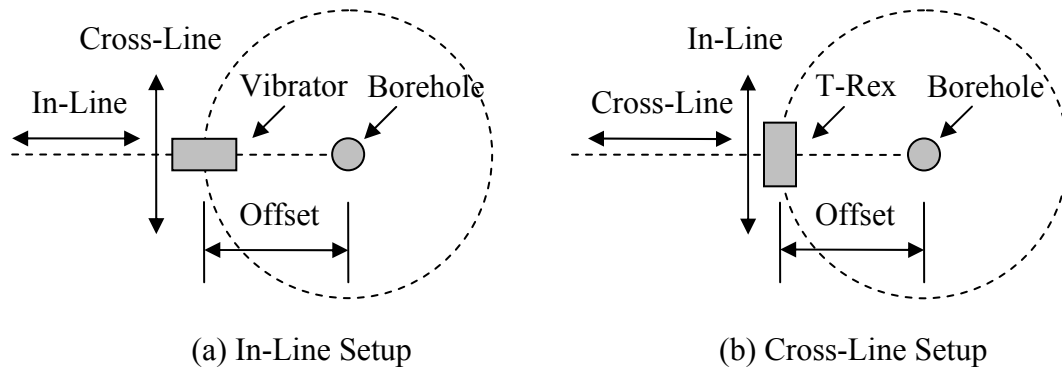


Figure 4.4 Illustration of in-line and cross-line planes for S-wave generation

4.3.5 Forward signal and reverse signal

The horizontal in-line direction in Figure 4.4 (b) has two orientations - the forward direction and its opposite, namely the reverse direction. Specifically for shear wave generation, the initial horizontal direction in which T-Rex is excited is called the forward direction. The opposite initial direction of excitation as a result of reversing the polarity of the drive signal to T-Rex is called the reverse direction. The forward and reverse motions should be out of phase or have a 180-degree in-phase difference. An example of these two records is shown in Figure 4.2 for the drive signal.

4.3.6 Reaction mass acceleration in horizontal shaking

The horizontal output force of T-Rex was transmitted to the ground surface by the square base plate located on the bottom of T-Rex. The acceleration of the reaction mass that loads the base plate was recorded by a horizontal accelerometer on the reaction mass during horizontal shaking. An example of the reaction mass output signal is presented in Figure 4.5. The top graph represents the forward initial motion while the lower graph represents the reverse input motion.

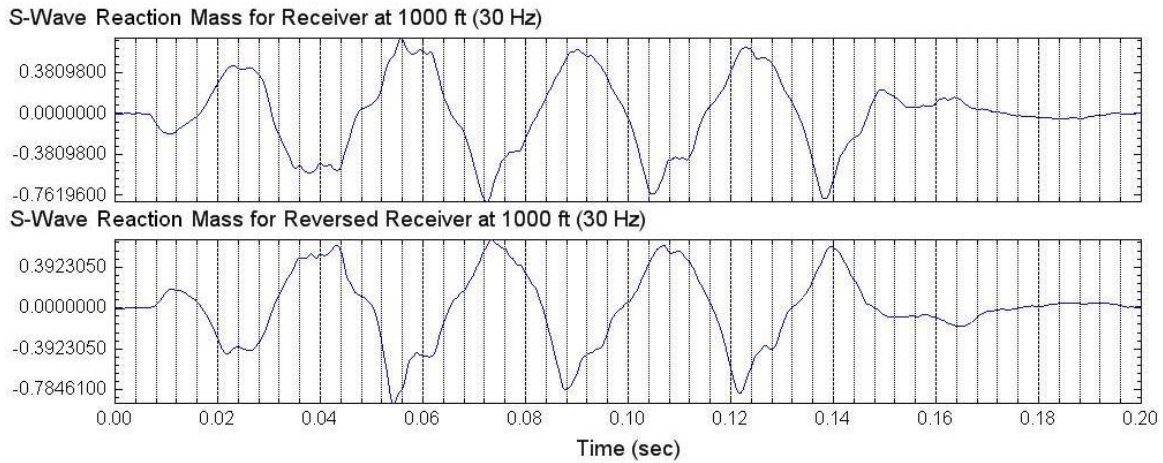


Figure 4.5 Unfiltered S-wave acceleration signals of the reaction mass excited in the forward and reverse directions with 4 cycles of a 30-Hz sine wave drive signal

4.3.7 Weighted-sum force signal

As defined by Equation (3.3), the weighted-sum force signal is the weighted average of the accelerations of the reaction mass and the baseplate when their corresponding masses are used for weights. Figure 4.6a shows that the P-wave weighted-sum signal is smoother than P-wave acceleration signal of the reaction mass in Figure 4.3, but slightly shifted upward. The S-wave weighted-sum signals shown in Figures 4.6 b and c are not significantly improved over that of the acceleration of the reaction mass shown in Figure 4.5.

As the feedback signal of the Vibroseis, the weighted-sum signal better represents the ground force signal than does the acceleration of the reaction mass. However, as a reference for the trigger time or time zero, the acceleration of the reaction mass is preferred because the trigger time of the weight-sum signal is averaged.

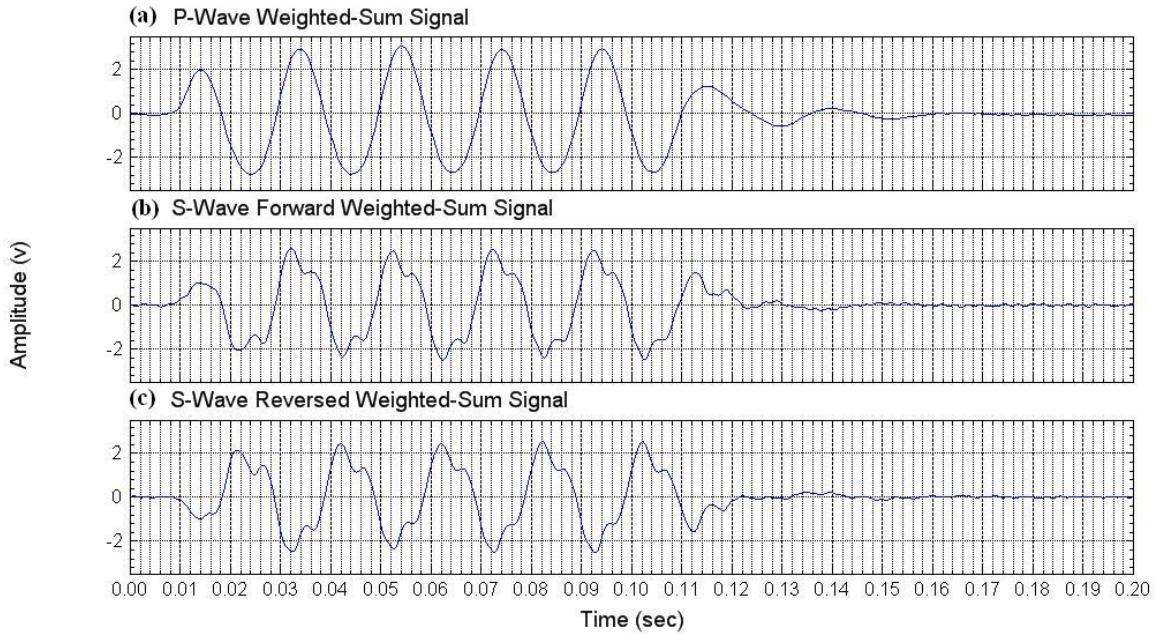


Figure 4.6 Unfiltered weighted-sum force signal for 5 cycles of a 50-Hz sine wave drive signal

4.3.8 Unfiltered signals

Unfiltered signals are the averaged original time series directly recorded with the Data Physics Analyzer. They are the averaged outputs of the reaction mass accelerometer or the receiver geophones from the 50-Hz, 30-Hz or 20-Hz input signal. The average amplitude of the unfiltered signal over the record length may not be zero because of the non-zero initial voltage. Figure 4.7 shows that, the average amplitude of the unfiltered P-wave signal of the lower receiver at a depth of 1400 ft is less than zero. Figure 4.8 shows that, the average amplitude of the unfiltered S-wave signal is also less than zero. If an unfiltered signal is not stationary, its average value displays a trend or variation with time. Only the fluctuation of the waves is of concern. The trend of each signal was removed to obtain a zero average, so that in waterfall plots showing signal fluctuations

versus scaled depth intervals, the center line (average) of each signal is located exactly at each depth location.

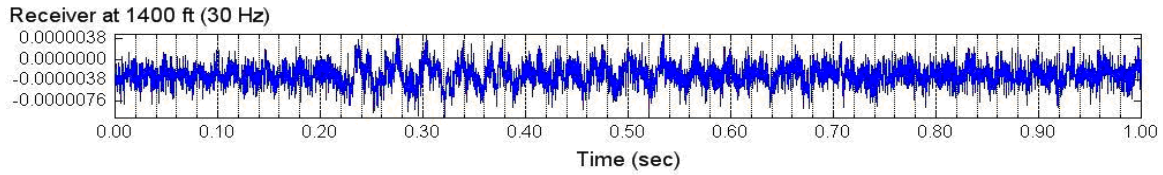


Figure 4.7 Unfiltered P-wave signal of lower receiver for 4 cycles of a 30-Hz sine wave drive signal

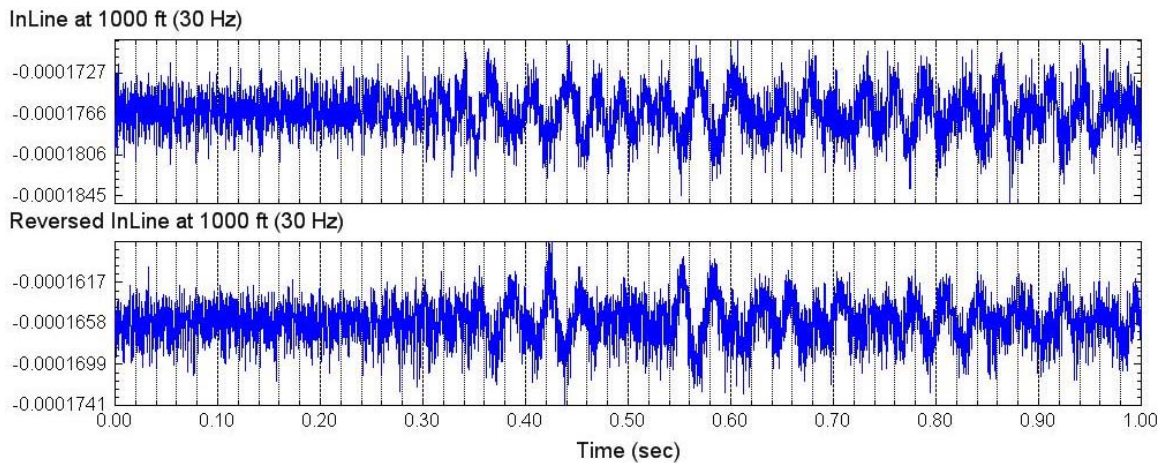


Figure 4.8 Unfiltered S-wave signal of lower in-line receiver for 4 cycles of a 30-Hz sine wave drive signal

4.3.9 Filters and filtered signals

Filters were used in processing the unfiltered signals in this research using DeepSeis 2.1. A filter is a transfer function that modifies magnitudes and phases of the signal. A low-pass filter is a filter that attenuates or removes undesired high frequencies. The filtered signal is then smoother, thereby facilitating identification of the input signal transmitted through the geologic column. Unfiltered signals in the time domain are transformed into the frequency domain using the discrete Fast Fourier Transform (FFT).

A low-pass filter is applied by multiplying filter coefficients with both the real and imaginary parts of the frequency magnitudes to obtain a modified frequency response. Then the inverse FFT is applied to the modified frequency response to obtain a filtered signal in the time domain. Figure 4.9 displays the filtered P-wave signal from Figure 4.7. Figure 4.10 is the filtered S-wave signal from Figure 4.8. The open symbols on the waveforms in Figures 4.9 and 4.10 identify wave points on the waveforms that were used to determine the relative travel times discussed in later sections.

The exact same filtering was performed on all signals with a given fixed frequency in this research. Therefore, any minor shifting in the time domain due to the filtering is the same for each fixed-frequency signal. As a result, the relative travel times determined herein are unaffected by this filtering. As noted above, the wave-arrival identification on the filtered waveform is denoted by a symbol added to the waveform (the small circle at $t \sim 0.21$ sec in Figure 4.9 and the triangles at $t \sim 0.37$ sec in Figure 4.10)

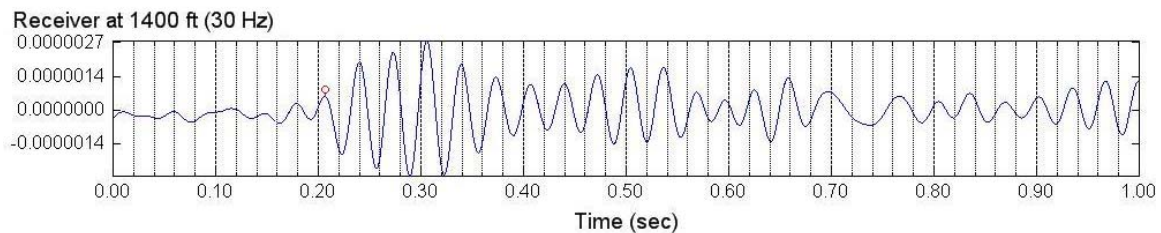


Figure 4.9 Filtered P-wave signal of lower receiver for 4 cycles of a 30-Hz sine wave drive signal; low pass 40 Hz

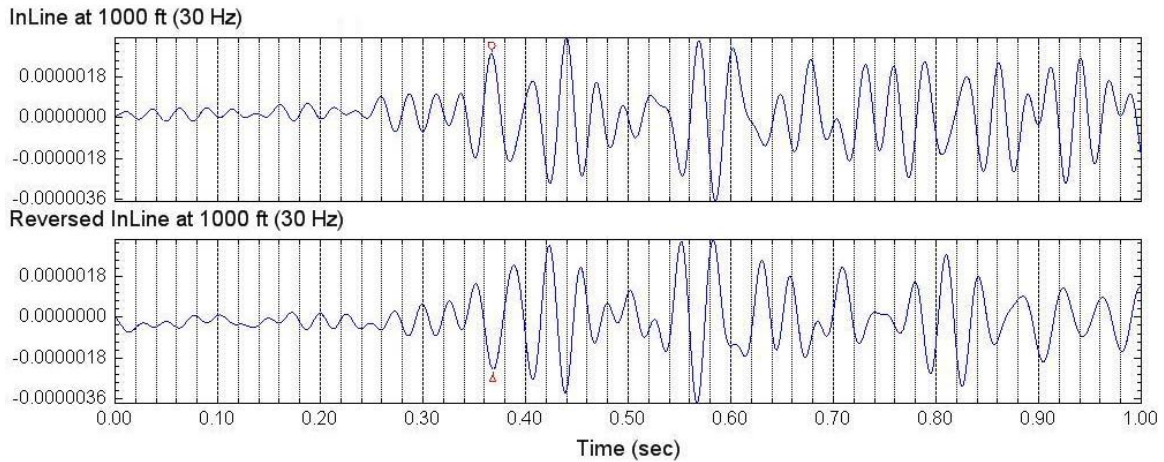


Figure 4.10 Filtered S-wave signal of lower in-line receiver for 4 cycles of a 30-Hz sine wave drive signal; low pass 40 Hz

4.3.10 Pass band and low pass filter

According to signal-processing convention, the “pass band” of a filter refers to the band of frequencies that lie within three decibels (a factor of two) of the peak magnitude. The “stop band” or “reject band” comprises all other frequencies. The word “band” refers to a frequency range. The frequency corresponding to three decibels of the peak value is called the “cut-off” frequency. A “low pass” filter applies to a pass band of a filter in the frequency range between zero and the cut-off frequency.

Unfiltered signals are all considered digital discrete time series whose frequency domain is also discrete. Figure 4.11 shows the amplitude spectrum of the P-wave signal when the input signal is a 30-Hz sine wave. As demonstrated in the figure, the largest magnitude in the spectrum is the frequency near 30 Hz except for the 60-Hz noise peak. Because the 60-Hz noise has a dominant contribution in the unfiltered signal, it must be filtered or removed in order to retrieve and view the desired measurement of the 30-Hz input signal.

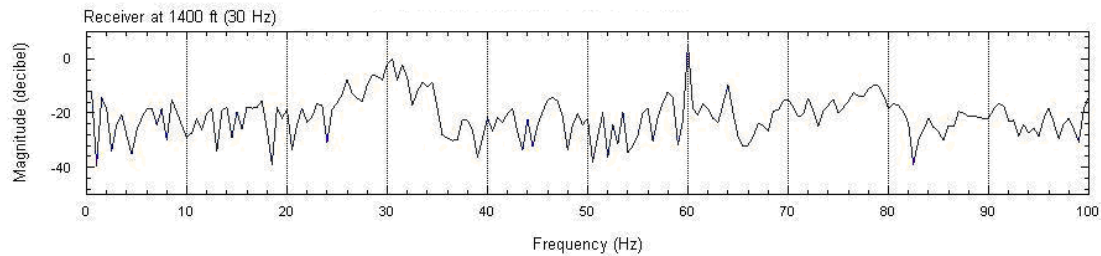


Figure 4.11 Amplitude spectrum of the unfiltered P-wave signal of the lower receiver at a depth of 1400 ft for 4 cycles of a 30-Hz sine wave drive signal; Expanded from 0 to 100 Hz

A discrete filter in the frequency domain is shown in Figure 4.12. This filter is applicable to these discrete time series. The pass band is 0 to 40 Hz while the reject band is 50 Hz to the Nyquist frequency, which is half of the sampling frequency (the sampling rate used in this research is 0.00012207 sec). A transitional band exists between 40 Hz and 50 Hz, which is a cubic spline curve or a straight line in this work.

A transitional band is selected if the magnitude of the reject band is not negligible compared with the magnitude of the desired dominant frequency. For example, in Figure 4.11, if the pass band is 0 to 32 Hz, then a transitional band of 32 to 40 Hz significantly improves the filtered signal. If the contribution of the reject band to the spectrum (or energy) is negligible, an ideal filter makes little difference compared to a transitional filter. For example, if the pass band is 0 to 40 Hz, no significant difference is observed between a transitional filter and an ideal filter. If a general trough (near 39 Hz) follows the peak of the signal energy (near 30 Hz), a cut-off frequency (40 Hz) is chosen near the trough and an ideal filter is used. Otherwise, a transitional filter is used.

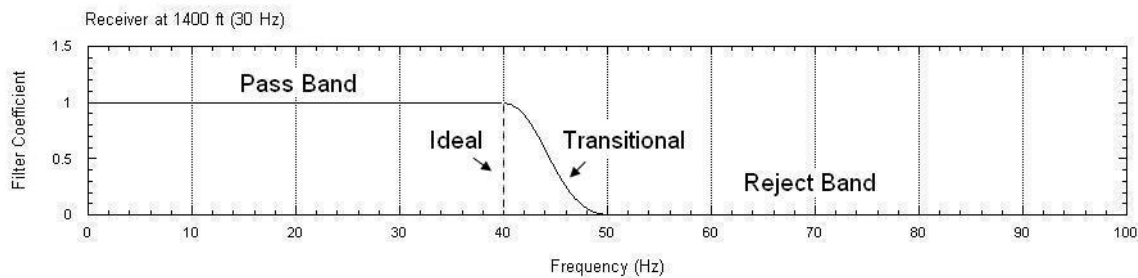


Figure 4.12 Pass band and reject band of a 40-Hz low pass filter

4.3.11 Time shift

The acceleration of the reaction mass, as shown in Figure 4.3 is prone to distortion when the initial state of the T-Rex mass is inconsistent, or the soil below the base plate is nonlinearly loaded. In this research, it was found that even if the drive signal is always aligned to zero time, the reaction mass initial response may be shifted from zero time, which is called a time shift. The denoted first-arrival in Figure 4.13 is the optimal point for wave-arrival identification. However, this point is not reliable because of the nonlinear initial response of the reaction mass, which may produce different first arrival times for the reaction mass and receivers even if the drive signals are exactly aligned.

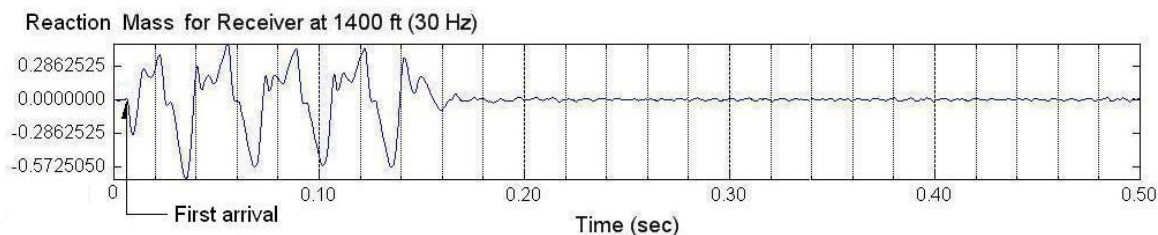


Figure 4.13 P-wave initial response of the reaction mass

Figure 4.14 is used to further explain the unreliability of the first arrival (or first movement of the reaction mass) and the transient effect on both frequency and magnitude. The filter is a 40-Hz low-pass filter (shown in Figure 4.12) that removes all

frequencies higher than 40 Hz. The first arrival point (or “first break”) in Figure 4.13 no longer exists in Figure 4.14 because it may originally contain transient frequencies that are higher than 30 Hz. On the other hand, a low pass filter in the frequency domain is equivalent to a convolution of a sinc-function with the corresponding time series. If the cutoff frequency is too close to the desired frequency, the moving average effect of the convolution will also cause the time shift near the first break. The amplitude of the first peak denoted by the small circle in Figure 4.14 is smaller than that of other peaks because of the transient state of the reaction mass before the steady state is reached. It was found in the research that this first peak is a relatively consistent timing point to use in evaluating the relative travel times of P waves.

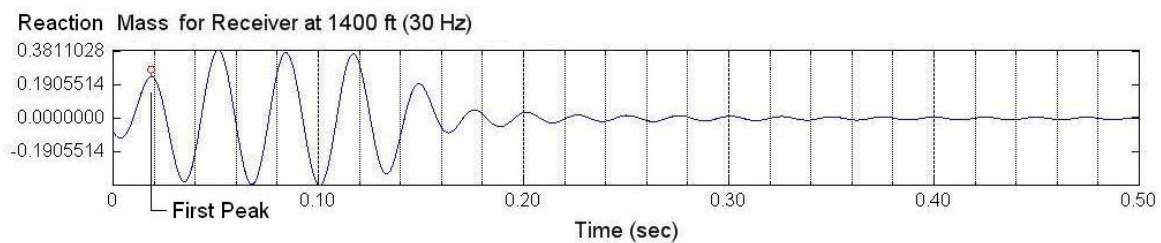


Figure 4.14 First peak of the filtered acceleration signal of the reaction mass

Further analysis confirmed that different non-causal low pass filters for the 30-Hz signal in Figure 4.13 will shift the first arrival and first trough, but only slightly shift the first peak. When the transient state extends to the first peak, other peaks and troughs that are in steady state remain unchanged and perfectly aligned. The shift of the first arrival is systematically backward (time is less) and stable because the desired 30-Hz signal remains dominant. Steady-state peaks of output signals display no time shift if the input signals do not demonstrate a time shift. A low-pass filter proved superior to other approaches (for example, Butterworth filter) in tracking the desired fixed frequencies in this research.

Nevertheless, steady state peaks and troughs do not always serve as an appropriate reference for wave-arrival identification because of reflection waves that come into the direct signal and distort the steady state peaks and troughs. As a compromise and for convenience, the first-arrival wave identification method is replaced with the first peak or first trough of the waveform for the reaction mass acceleration and other receiver signals in the analysis using DeepSeis 2.1. Little shifting is observed from the steady state of the desired signal frequency (for example 30 Hz) and less interference is seen from the reflections.

As an alternative to the non-causal filter, a Butterworth filter may secure the first arrival as being stationary, but proved inadequate if the frequency of the dominant noise (60-Hz noise in Figure 4.11 with larger magnitude than the desired signal at 30 Hz) is very close to that of the signal, and even more so for the filtering of the 60-Hz noise from the 50-Hz signal, which was used in much of this work. If the noise can not be significantly attenuated or removed, it will shift the first arrival as well as the steady-state peaks and troughs, and the shift is irregular because it is controlled by the noise. On the other hand the low-pass filter can remove undesired 60-Hz noise completely and track the desired frequency effectively. Therefore, the low-pass filter was used herein in all analysis with DeepSeis 2.1.

4.3.12 Relative travel times

Relative travel times refer to the time intervals between the same points on the waveforms of the reaction mass and receivers (lower receiver or reference receiver). The time on each filtered waveform used to determine the relative travel time is denoted by a small symbol that has been added to all waveforms. Examples are shown in Figures 4.9, 4.10, and 4.14 by the small circles or triangles. These points representing times are not

the wave arrivals but are the same point on the waveform from one measurement depth to the next. These points are called herein: “wave-arrival identifications”.

4.3.13 Long lever arm and short lever arm

The lower borehole geophone from Lawrence Berkeley National Laboratory (LBNL) was fixed to the borehole wall at a depth by rotating the pivoting lever arm attached to the geophone tool (see Figure 3.4). As the lever arm rotated outward, the geophone tool came into contact with the borehole wall. Two lengths of lever arms were used, namely a longer lever arm and the shorter lever arm. Because of irregularities in the borehole diameter (Gardner and Price, 2007), the longer lever arm was used to avoid inadequate contact with the borehole wall in regions where washouts would have substantially increased the borehole diameter. Both longer and shorter arms were used at depths 1240 and 1260 ft in borehole C4993 and no significant difference was found in the lower receiver output with the different level arms. For all other depths, only the longer lever arm was used.

4.3.14 Reference receiver

The reference receiver is the receiver that was consistently fixed at a depth of 6.6 m (22 ft) in Borehole C4993 while the lower 3-D receiver of LBNL (see next section) was moved downward or upward along the borehole (see Figure 3.4). During comparison of the responses of the longer arm and shorter arm lower receiver, the same reference receiver was used but its depth was changed to 5.1 m (17 ft).

4.3.15 Lower receiver

The lower receiver is the LBNL 3-D receiver with three orthogonal geophones in the tool, one for P wave and two for S waves (see Figure 3.4). It was positioned lower

than the location of the reference receiver, and was moved along the borehole for measurements at different depths.

4.4 WATERFALL PLOTS OF UNFILTERED AND FILTERED P-WAVE RECORDS

Figures 4.15 to 4.18 are waterfall plots of unfiltered P-wave signals of the vertical receiver in Borehole C4993. The drive signal used in recording the records in Figures 4.15 to 4.17 is 5 cycles of a 50-Hz sine wave. The drive signal used in the records in Figure 4.18 is 4 cycles of a 30-Hz sine wave.

Observation of the unfiltered P-waveforms in Figures 4.15 to 4.18 makes clear that the unfiltered waveforms facilitate identification of the initial portion of the P waveform over depths from 370 ft (the starting depth in these tests) to a depth of approximately 980 ft. However, tracking the initial portion of the waveform below this depth is difficult.

One benefit of DeepSeis 2.1 is the filtering of the fixed-frequency waveform. This benefit is seen when viewing the filtered signals of the unfiltered records. The filtered signals are presented in Figures 4.19 to 4.22. A 60-Hz low-pass filter was applied to all 50-Hz P-wave records, and a 40-Hz low-pass filter was used to 30-Hz P-wave records. The initial portion of the waveform in these figures is also identified by the open circle on each waveform. Clearly, the filtered signals are excellent and the fixed-sine signal generation with T-Rex works well in deep downhole profiling for seismic engineering purposes.

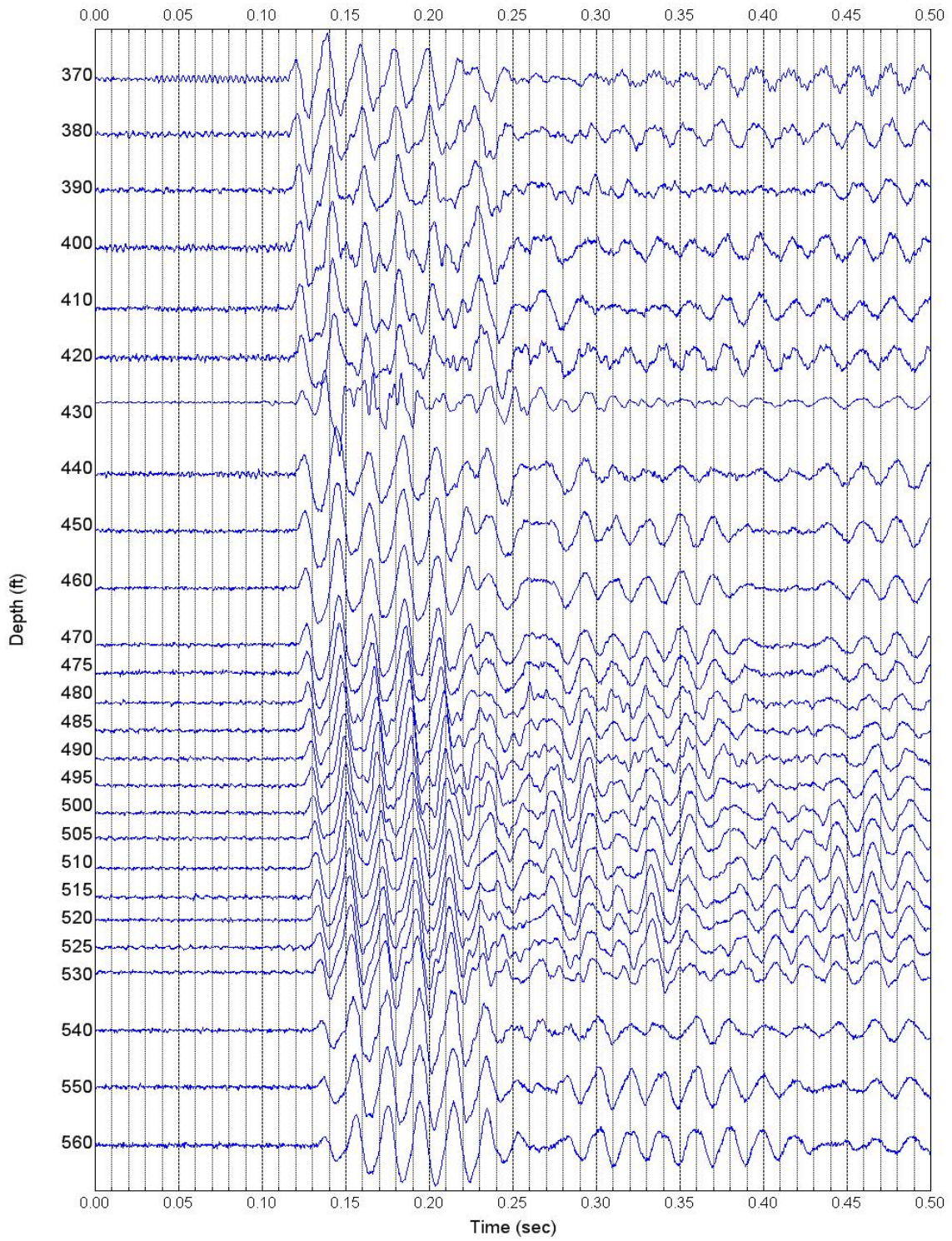


Figure 4.15 Waterfall plot of unfiltered P-wave signals (370-560 ft)

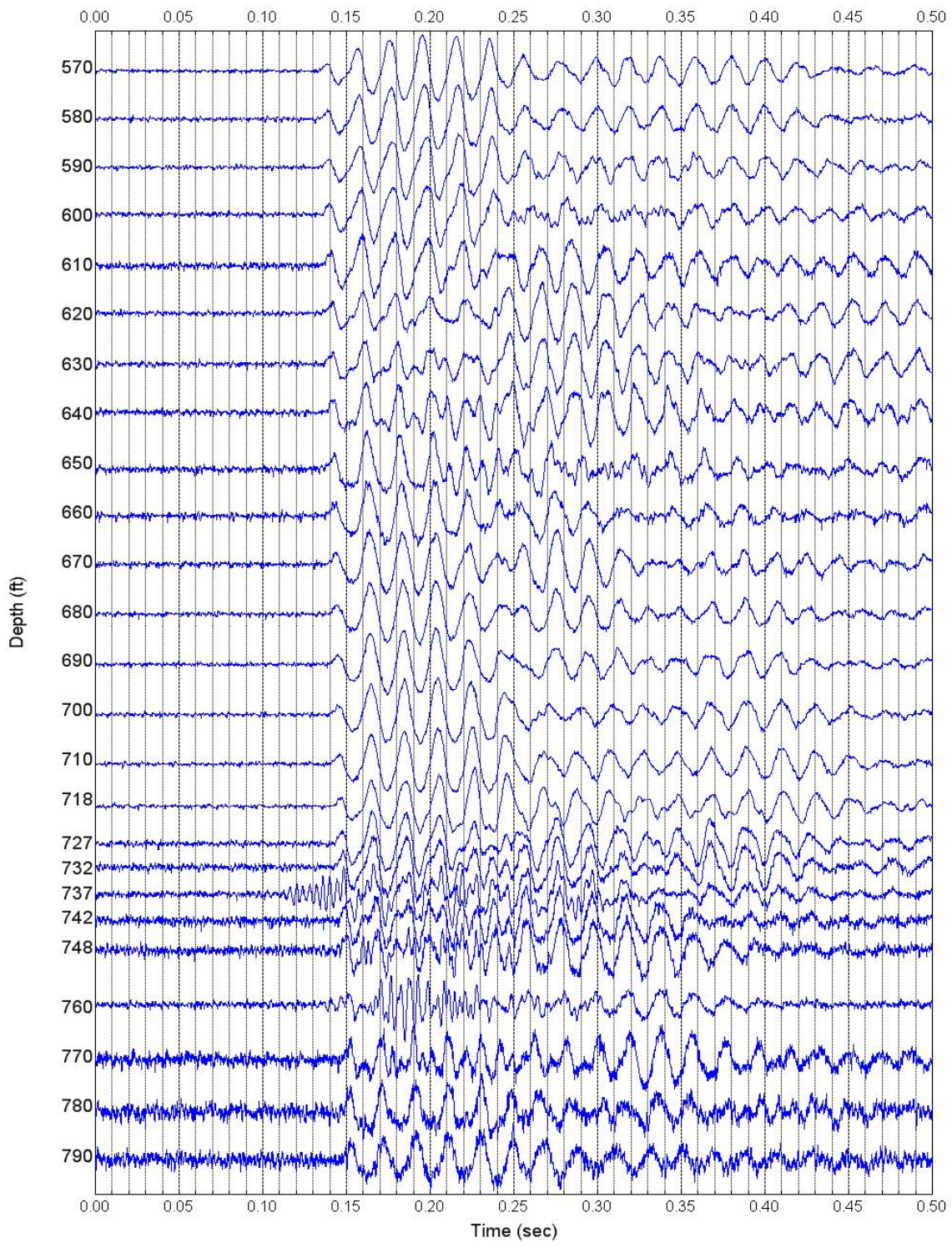


Figure 4.16 Waterfall plot of unfiltered P-wave signals (570-790 ft)

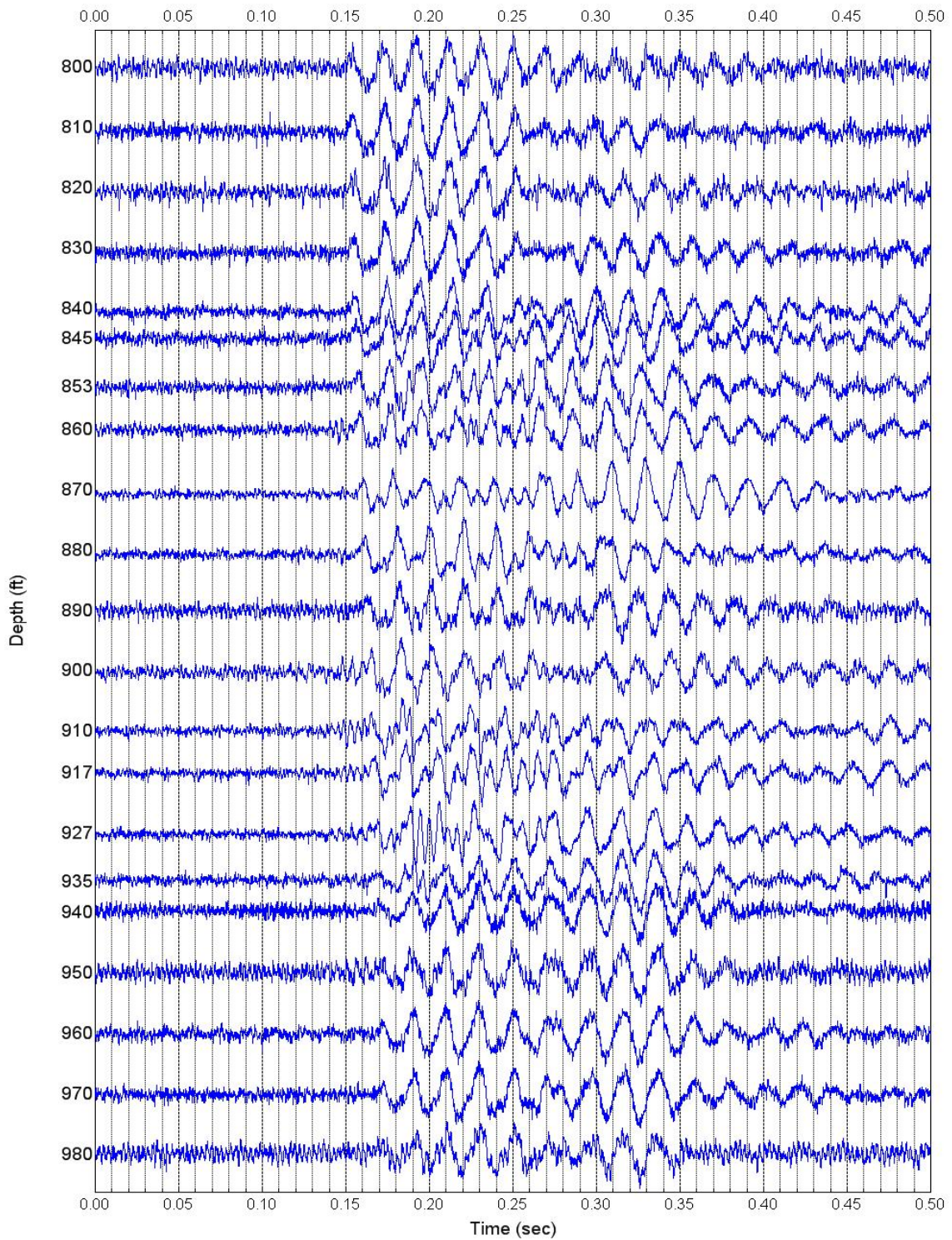


Figure 4.17 Waterfall plot of unfiltered P-wave signals (800-980 ft)

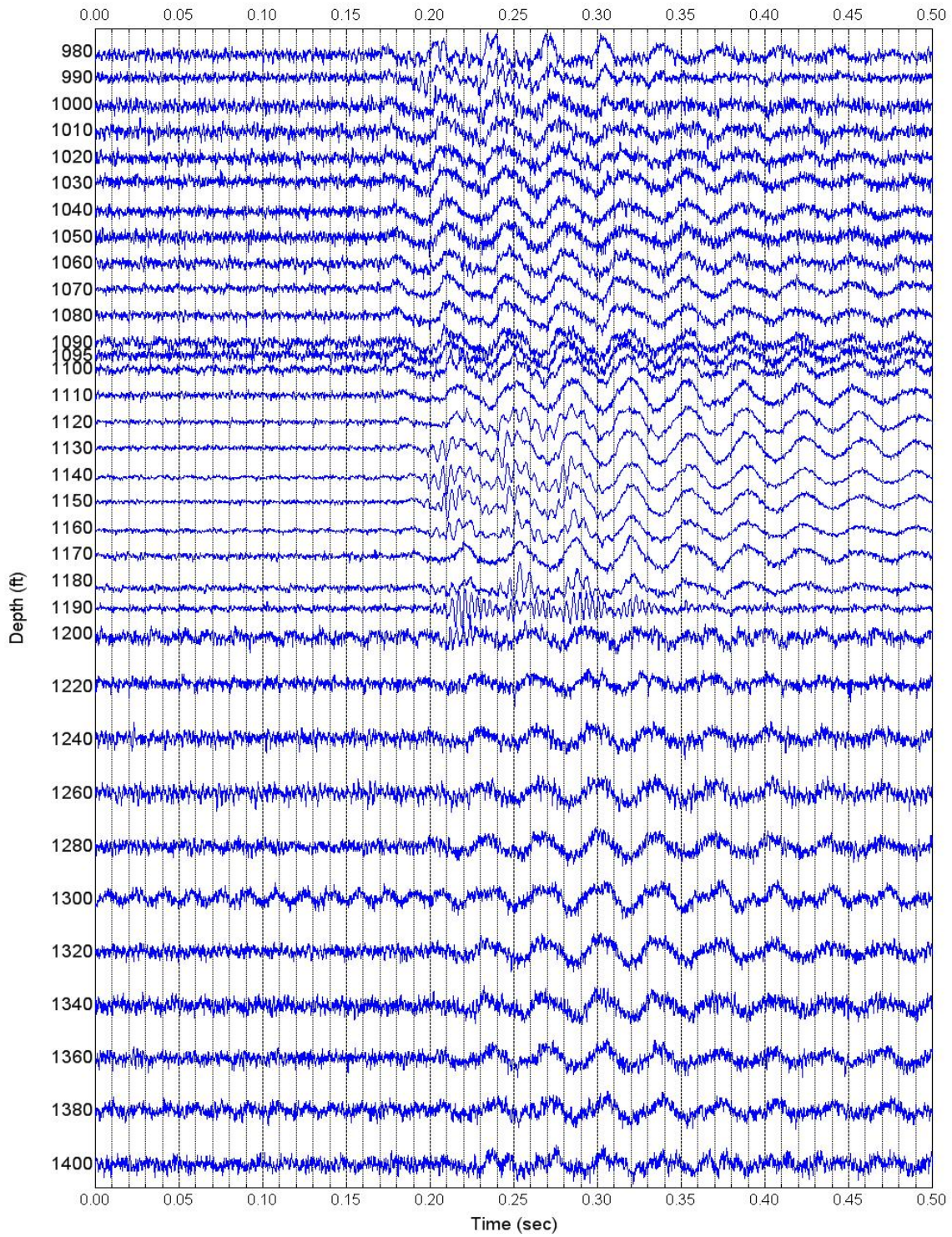


Figure 4.18 Waterfall plot of unfiltered P-wave signals (980-1400 ft)

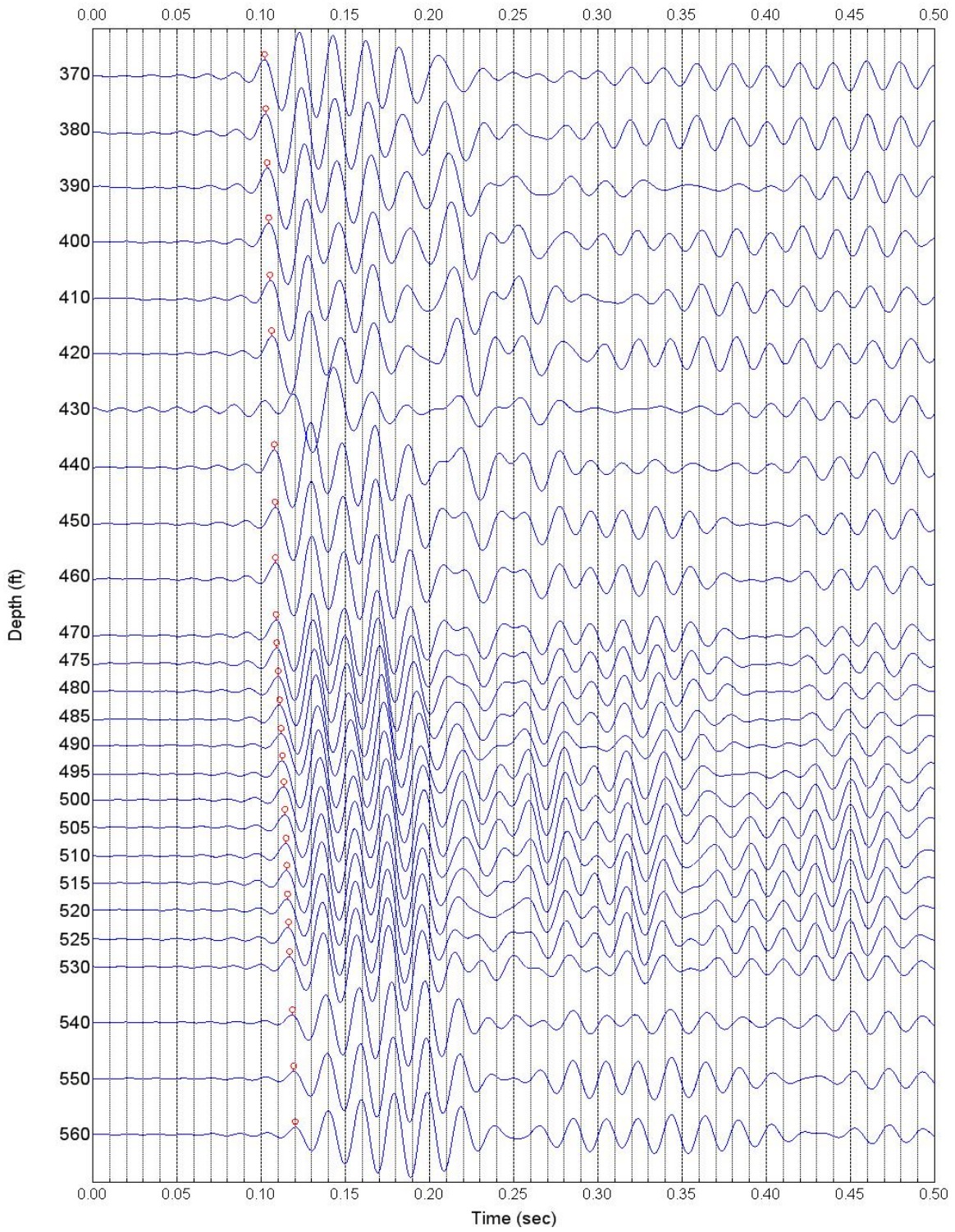


Figure 4.19 Waterfall plot of filtered P-wave signals (370-560 ft)

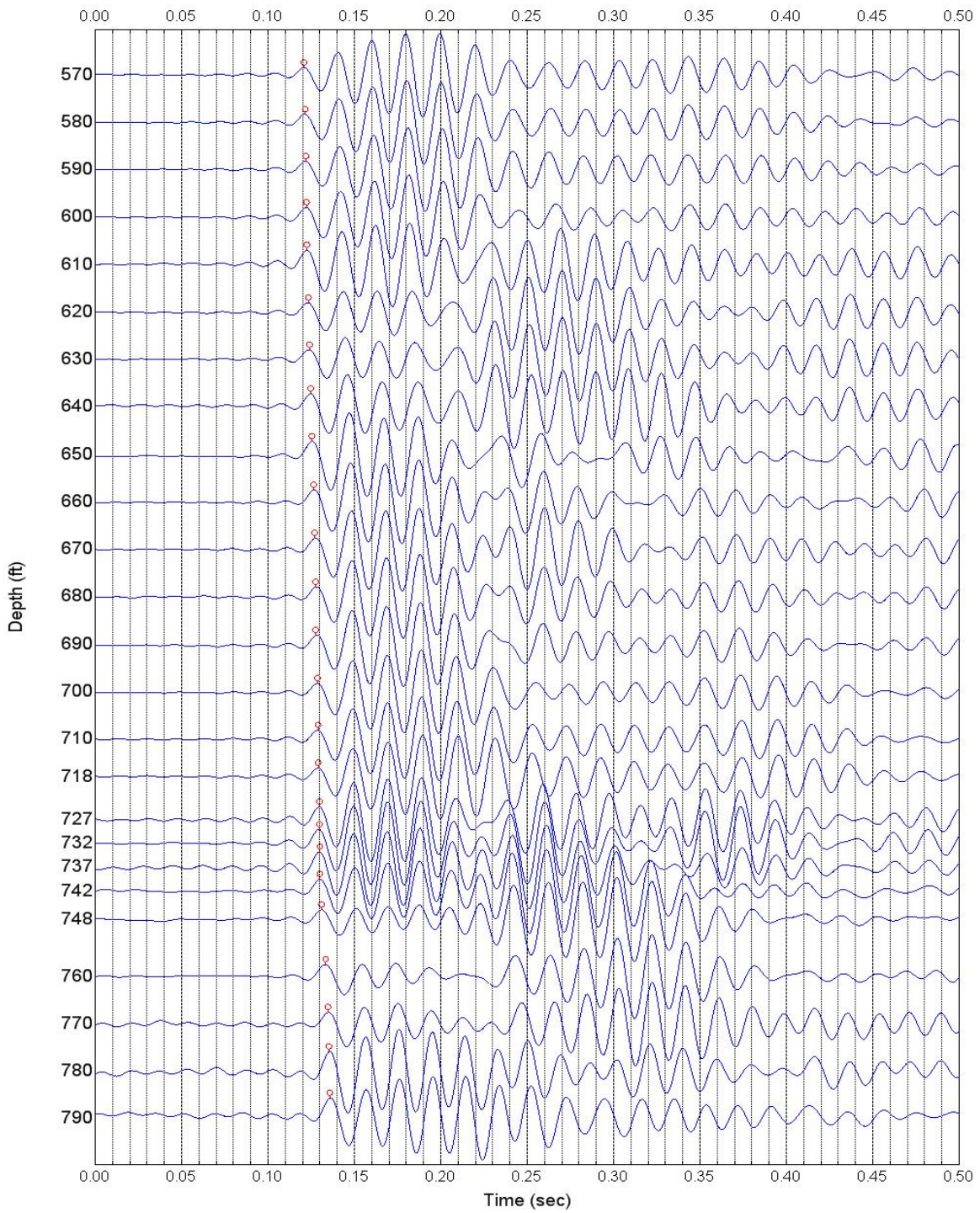


Figure 4.20 Waterfall plot of filtered P-wave signals (570-790 ft)

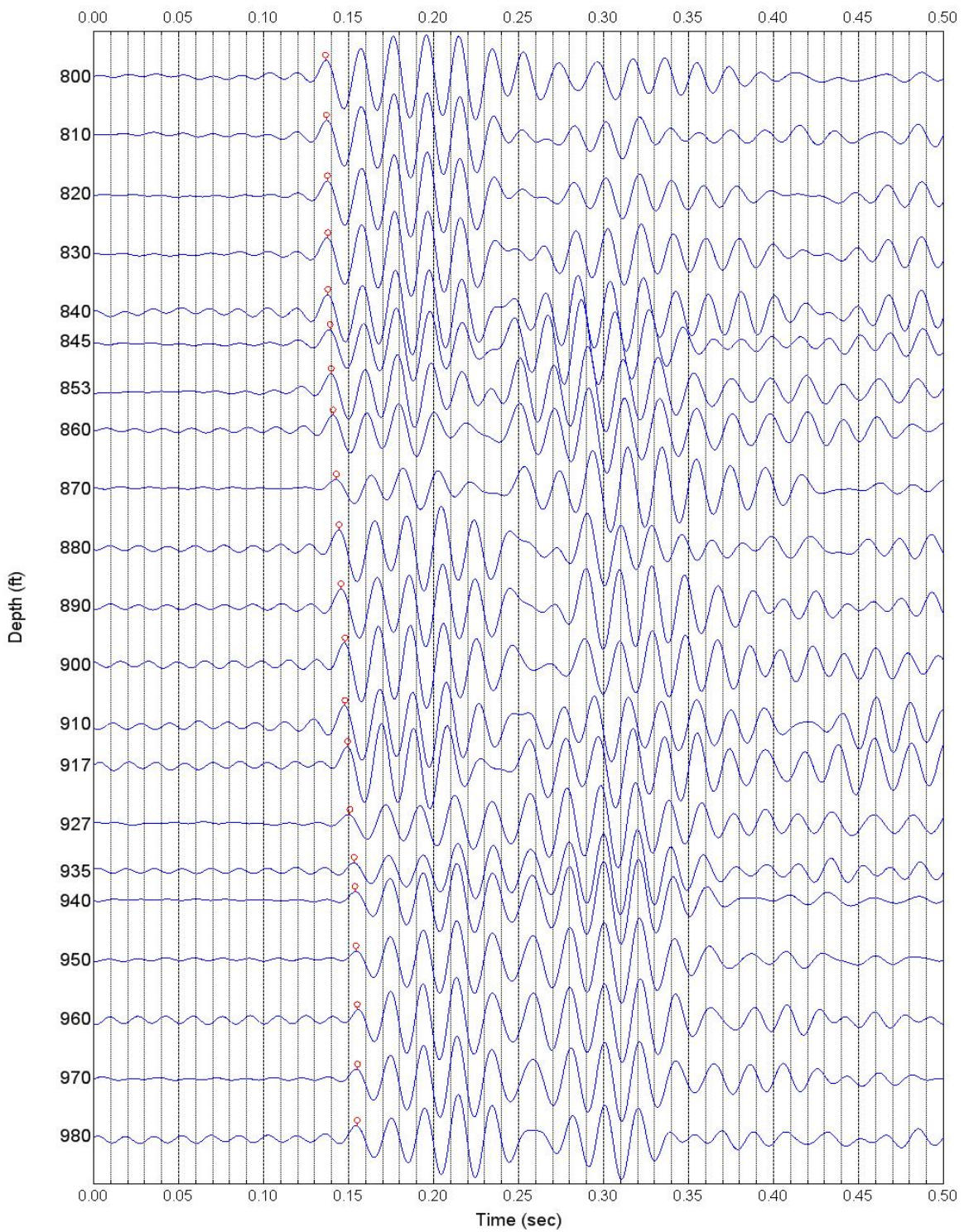


Figure 4.21 Waterfall plot of filtered P-wave signals (800-980 ft)

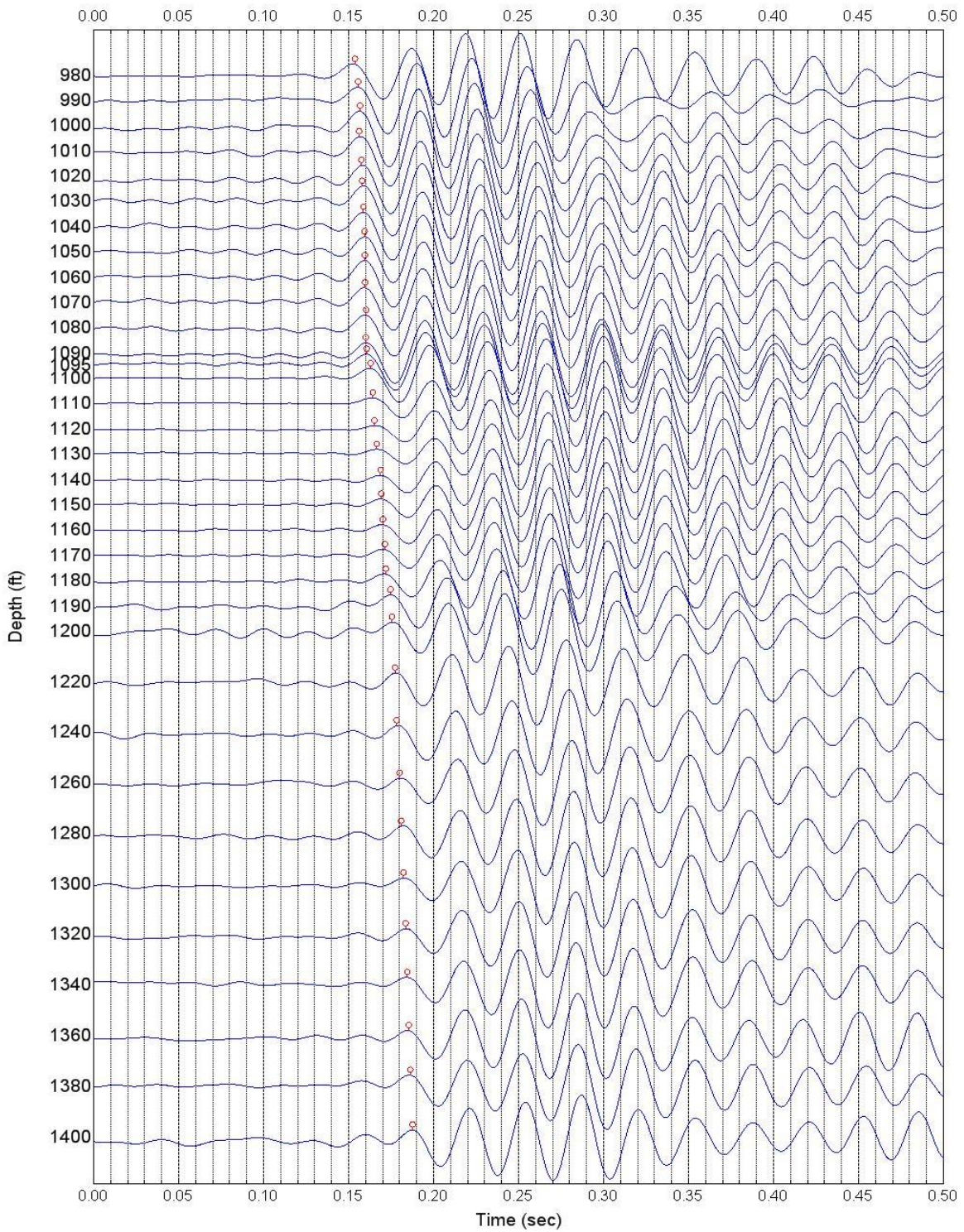


Figure 4.22 Waterfall plot of filtered P-wave signals (980-1400 ft)

4.5 RELATIVE P-WAVE TRAVEL TIMES AND INTERPRETED Vp PROFILE

All relative P-wave travel times determined by the open circles in the waterfall plots of the filtered P-wave signals for Borehole C4993 at the Hanford site are shown in Figure 4.23. Expanded plots of the relative P-wave travel times are shown in Figures 4.24 to 4.26. The interpreted Vp values of each layer or sub-layers are given by the inverse of the slopes of the solid lines through the relative times in these figures. The values of Vp are presented in the boxes next to the solid lines. Clearly, reasonable correlations exist between the layering and velocities. It should be noted that the geologic profile with the depths of the layer boundaries were known before the data were analyzed. However, fitting the straight lines through the data was done based on the data and not the layer boundaries.

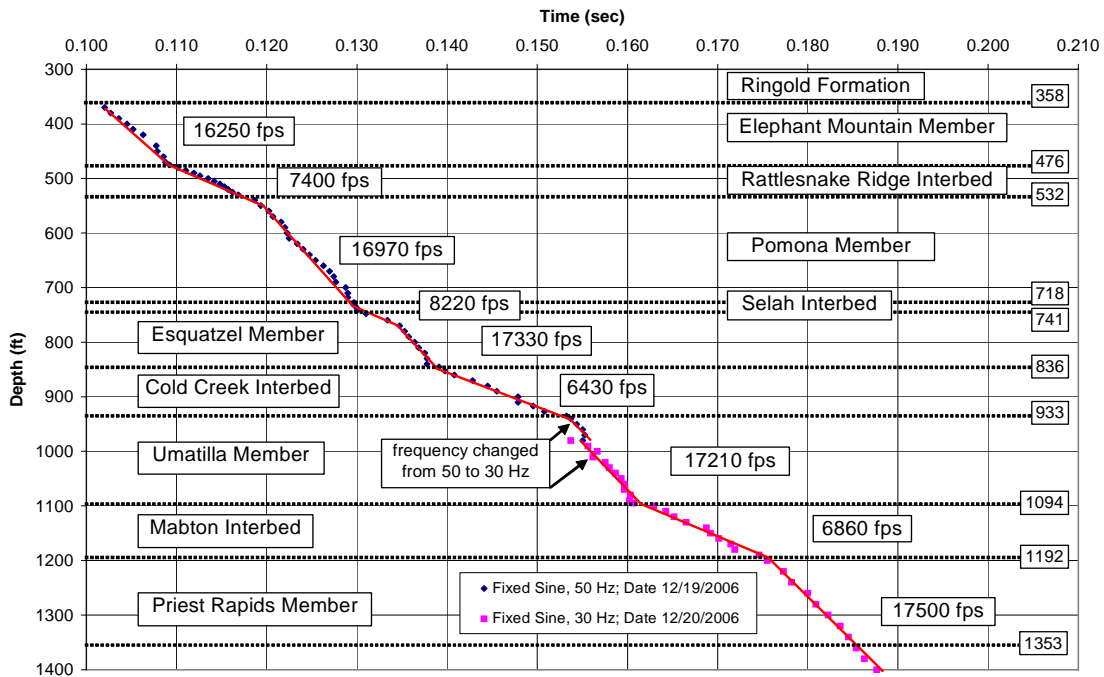


Figure 4.23 Relative P-wave travel times and interpreted Vp Profile in Borehole C4993

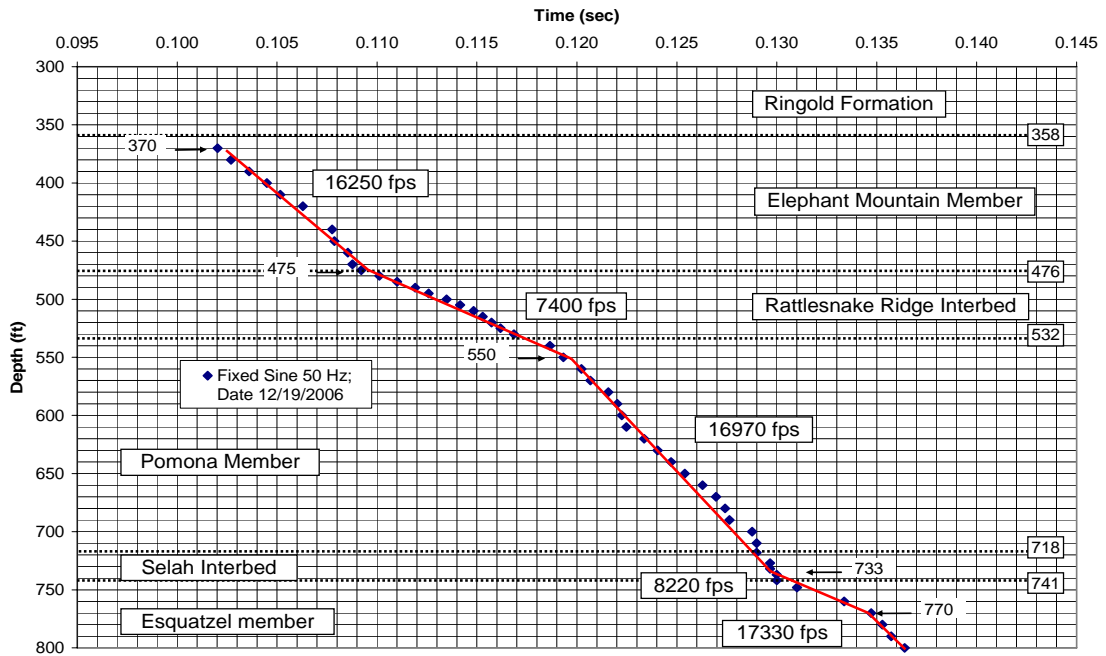


Figure 4.24 Expanded relative P-wave travel times (300–800 ft)

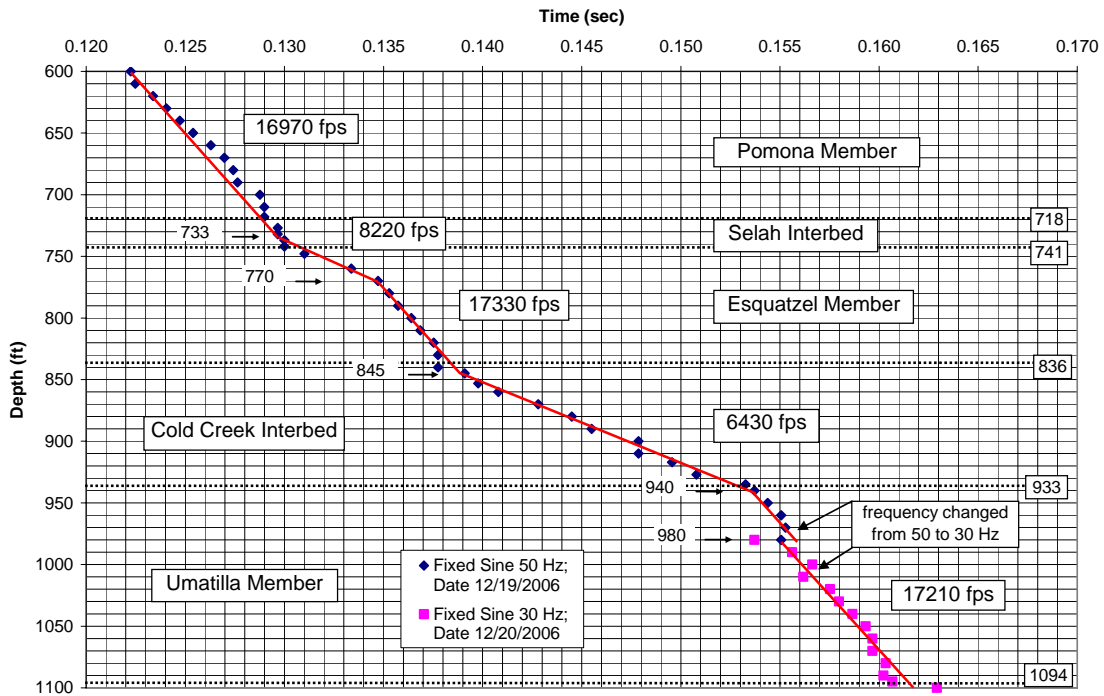


Figure 4.25 Expanded relative P-wave travel times (600–1100 ft)

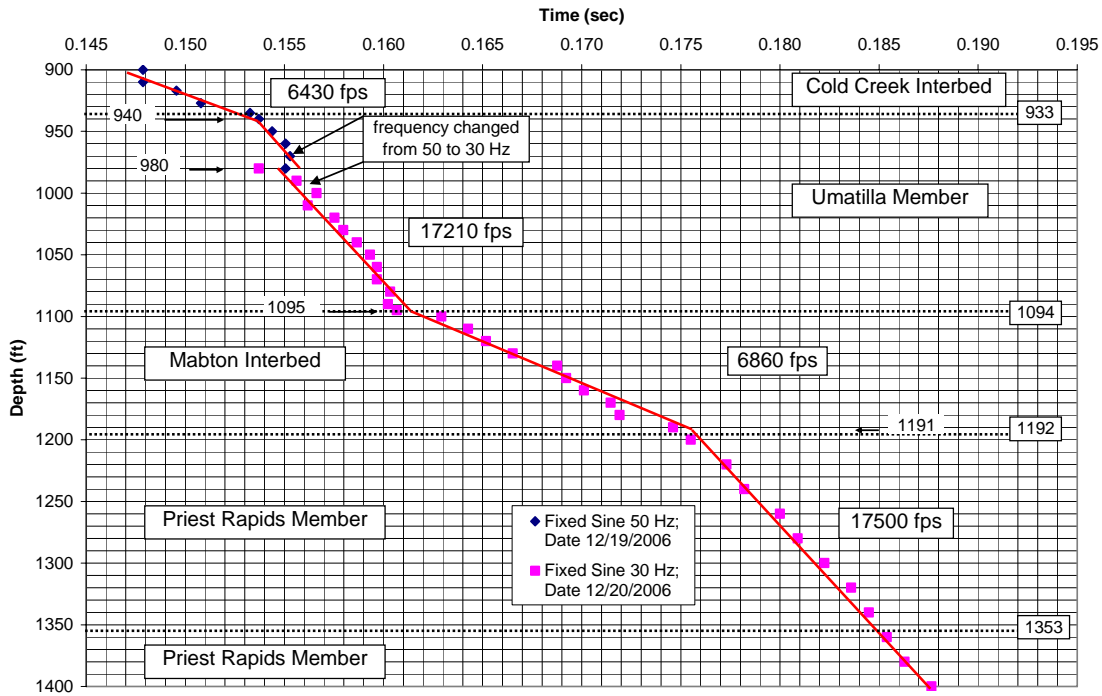


Figure 4.26 Expanded relative P-wave travel times (900–1400 ft)

As seen from the expanded travel time figures in Figures 4.24 to 4.26, some measured points deviate from the straight line near the layer boundaries. For example, the data points between depths of 195 to 215 m (650 to 718 ft) exhibit a flatter slope than the straight line, and then become steeper near the boundary. It is believed that the reflections shifted the wave arrival-identification points on the waveforms from the direct arrival times. When fitting a straight line through the data points, an overall trend was considered, and engineering judgment was applied to discount the local, unreasonable data points. The wavelet-response method is developed and presented in Chapter 7 to reduce the waveform distortions caused by the reflections, and improve the resolution of the travel time analysis.

An independent check on the downhole V_p values was also available at this site. Independent P-wave velocities were measured in Borehole C4993 with the P-S suspension logger by GeoVision Geophysical Services. The V_p profiles from both methods are compared in Figure 4.27. Five important results are apparent. First, the overall comparison between the two methods is quite good. Second, the average P-wave velocities in three of the four interbeds (Rattlesnake Ridge, Cold Creek and Mabton) agree well. Third, the P-wave velocities of the thin Selah interbeds (6.9 m or 23 ft thick) at an average depth of about 219 m (730 ft) does not agree well. Fourth, the P-wave velocities in the basalt layers measured by the suspension logger are generally 10% above those measured by the downhole tests. Fifth, the suspension logger captures the variations in P-wave velocities within the basalt layers and interbeds and near the boundaries while the downhole test does not.

It should be noted that the frequency dispersion effect may contribute to the velocity differences between the downhole and suspension logging tests in basalt layers. The source signal generated by the OYO Model 170 Suspension Logging Probe, which was used for the suspension logging tests, is between 500 and 5000 Hz, while the frequency of a vibratory source (T-Rex) is between 20 and 50 Hz. Suspension logging uses much shorter wavelengths (for example, 3000 Hz for P waves and 1000 Hz for S-waves in soft rock or stiff soils) than does the downhole test (20 ~ 50 Hz). As discussed in Chapter 2, tests with higher frequencies yield somewhat higher velocities than do tests with lower frequencies due to frequency dispersion. The generally higher velocities in basalt layers measured by the suspension logger may be affected by the much higher frequencies used in the suspension logging tests.

On the other hand, it appears that both the frequency dispersion effect and the effective medium theory contribute to the velocity differences between the downhole test

and suspension logging test in the interbeds as well as the basalt layers. The P-wave velocities of the interbeds measured by downhole tests match with those by the suspension logger. The frequency dispersion effect on the interbeds is possible to be counteracted by the effect from the effective medium theory discussed in Chapter 2. The downhole test used much longer wavelengths than the thickness of the thin interbed layers. The measured velocity of the thin layers is actually the weighted average of the velocities of all layers within a wavelength. For measurements in an interbed, part of the basalts within the thickness of a wavelength is covered and measured as an equivalent interbed. Similarly, the wavelength is also longer than some of the basalt layers, where measured velocities may be underestimated because of the thin layers covered within a wavelength from the measurement depths.

The measured velocities vary with testing frequencies. For the purpose of seismic hazard analysis, a test frequency closer to the dominant earthquake frequency is preferred. Typically earthquake frequencies that cause strong ground motions are much lower than 30 Hz. The frequency of the vibratory source is much closer to the earthquake dominant frequencies than that of the suspension logging test. Therefore, the velocities measured using downhole tests should be more representative for site response analysis.

Velocities measured in laboratory tests using samples from Borehole C4998 are presented in Figure 4.28. The stratigraphy at Borehole C4998 is similar to that at Borehole C4993. Laboratory results are available only for the basalt layers. The velocities show some variability because the samples represent localized conditions, but generally the laboratory results agree with the measurements by the downhole and suspension logging tests.

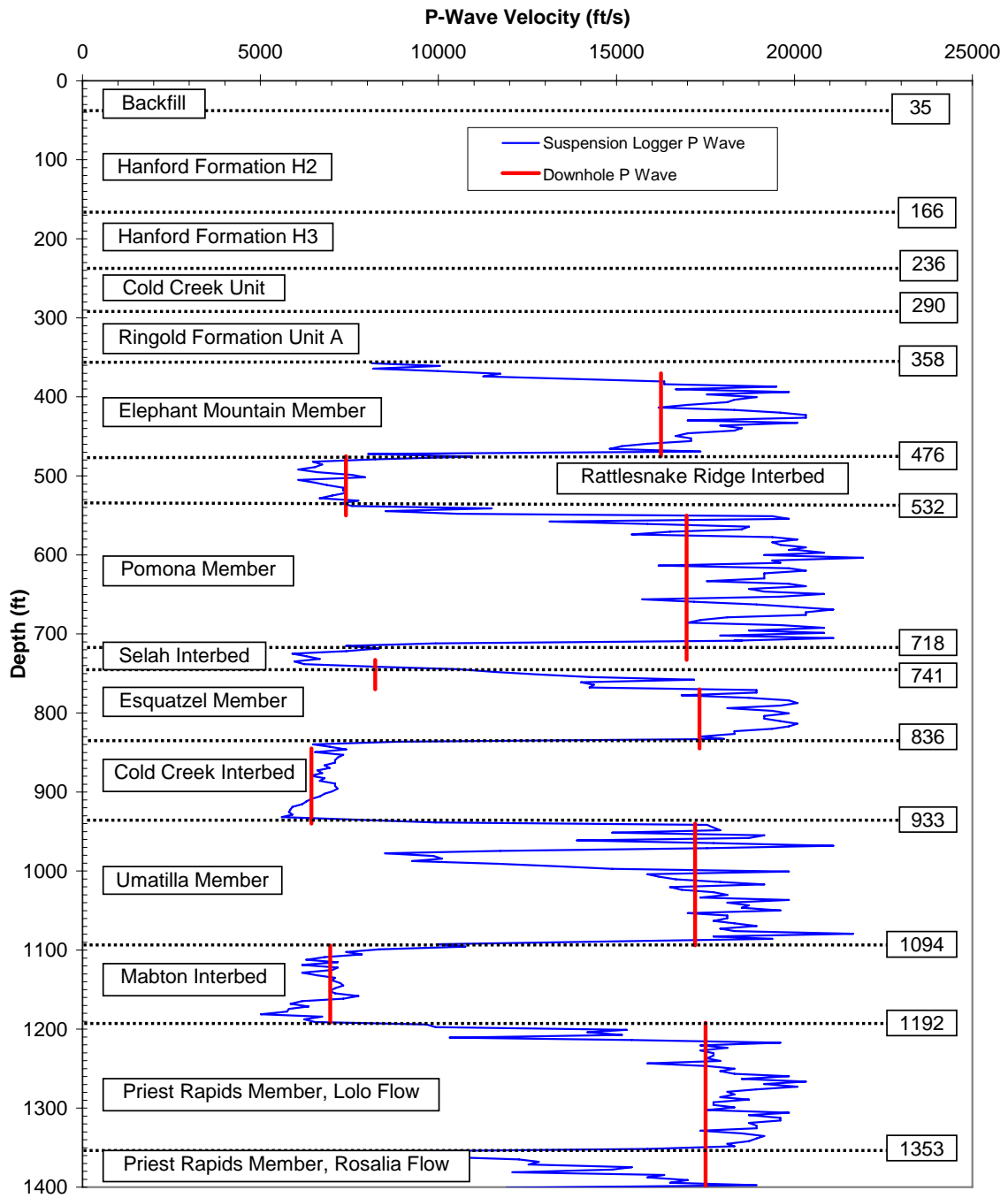


Figure 4.27 Comparison of P-wave velocities from downhole and suspension logging tests in Borehole C4993

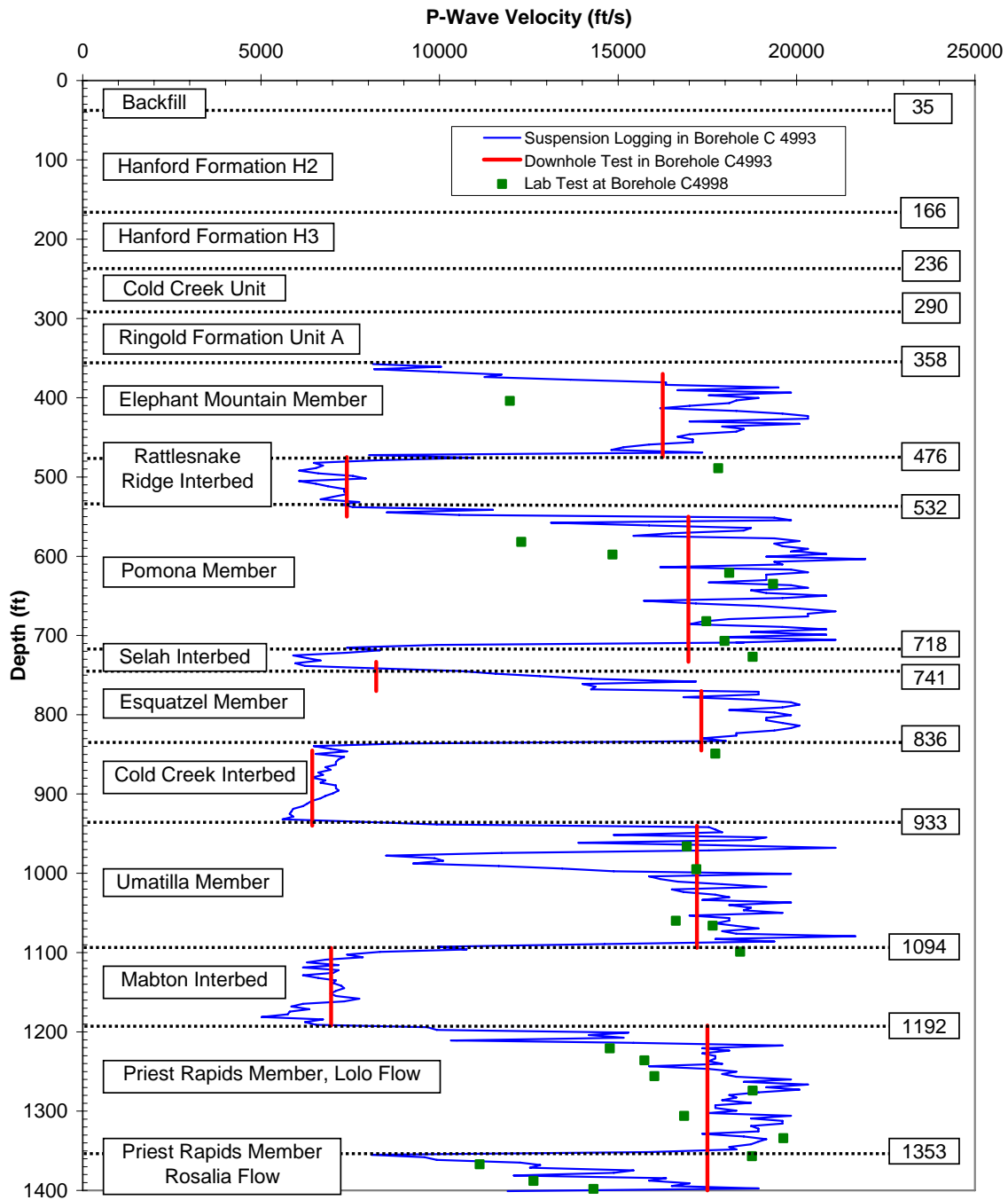


Figure 4.28 Comparison of P-wave velocities from downhole and suspension logging tests in Borehole C4993 and lab test in Borehole C4998

4.6 UNFILTERED S-WAVE FORWARD IN-LINE RECORDS

The orientation of both in-line and cross-line receivers is uncontrolled. As shown in Figure 4.29, the in-line receiver is expected to be aligned with the in-line shaking direction, but its actual orientation is unknown because of the unknown twisting angle, θ , of the cable suspending the receiver tool. Therefore, the signal recorded by the in-line receiver is not necessarily the motion in the in-line plane. To obtain the motion in the in-line plane, or the rotated in-line motion, correction for disorientation is performed using both the in-line and cross-line signals.

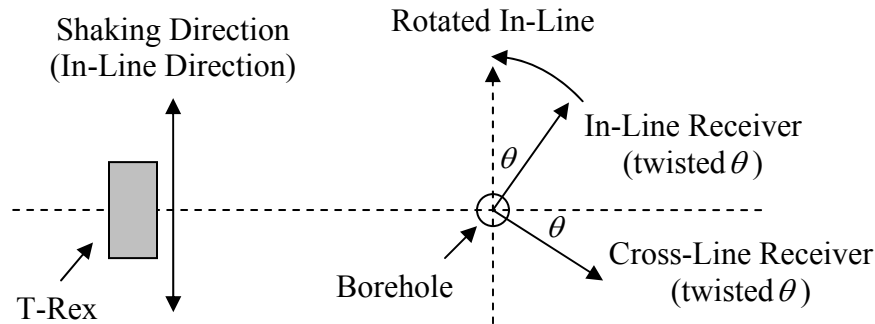


Figure 4.29 Horizontal disorientation of the receiver tool

The horizontal S-wave shaking is comprised of two initial orientations along the in-line direction in Figure 4.4(b). One orientation is called forward, and the other called reverse. Figures 4.30 to 4.37 present the unfiltered S-wave signals produced only by forward shaking. The reversed S-wave signals, which are similar to the forward S-wave signals except a 180-degree phase difference, are not shown. For each forward shaking, the horizontal motion is recorded simultaneously by two orthogonal components of the lower horizontal receiver, namely the in-line receiver and the cross-line receiver. Figures 4.30 to 4.37 present the signals recorded only by the in-line receiver. The signals recorded by the cross-line receiver are similar.

By viewing the records in Figures 4.30 to 4.37, it can be seen that an arrival point on the waveform can not be tracked consistently from the in-line signals with depth and the records are difficult to interpret below 297 m (990 ft). The disorientation is corrected and shown in the next section.

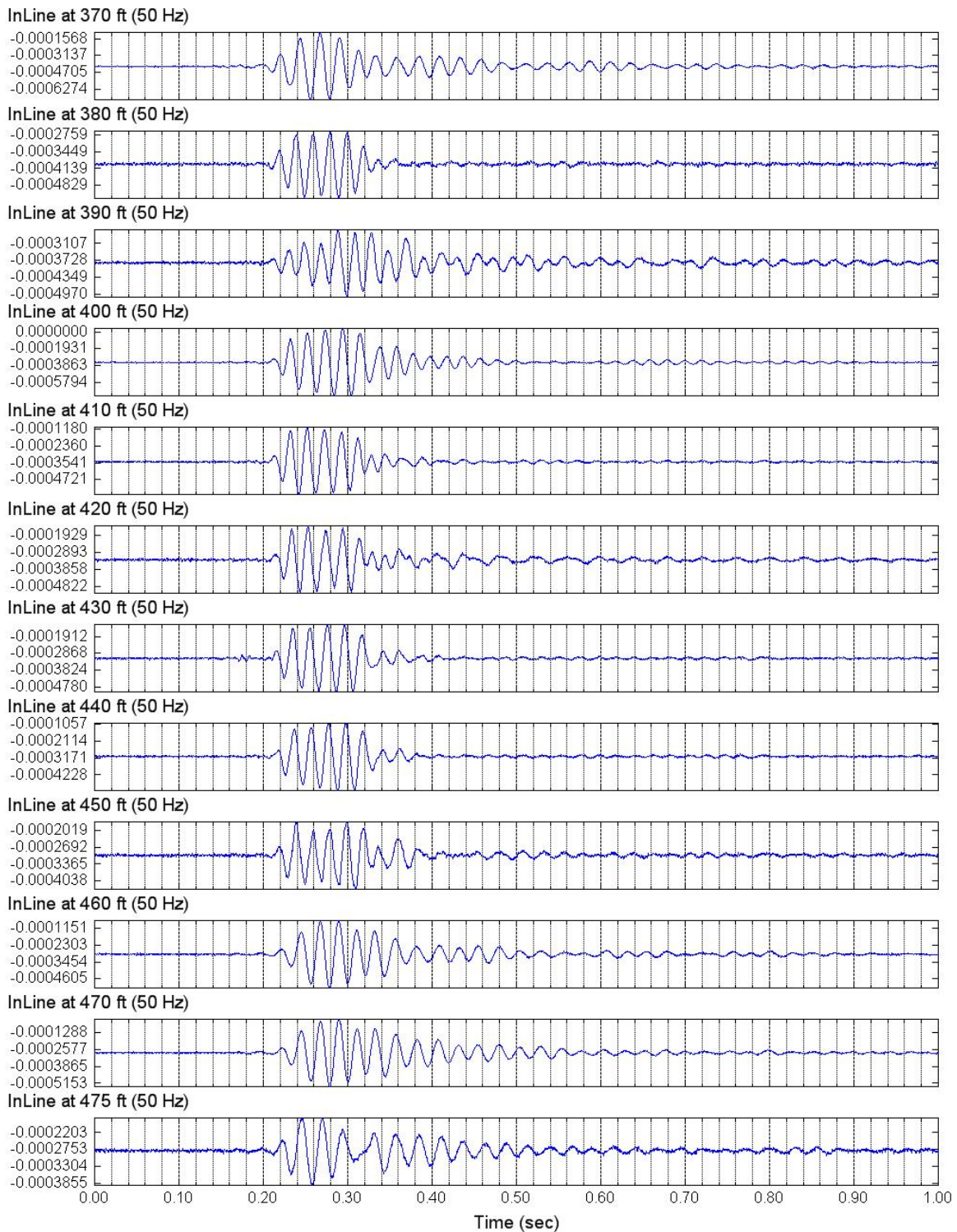


Figure 4.30 Unfiltered forward S-wave signal of lower in-line receiver (370 – 475 ft)

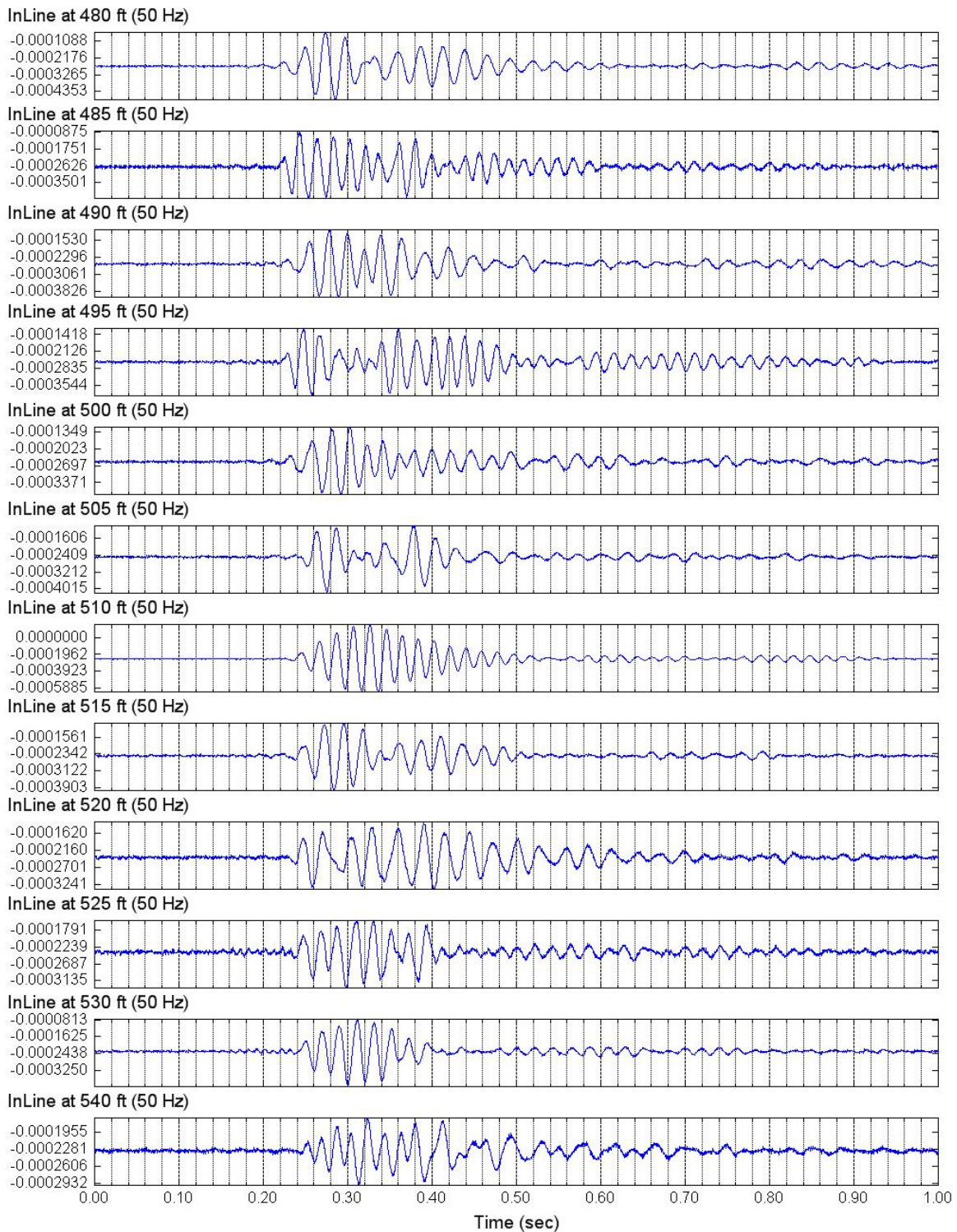


Figure 4.31 Unfiltered forward S-wave signal of lower in-line receiver (480 – 540 ft)

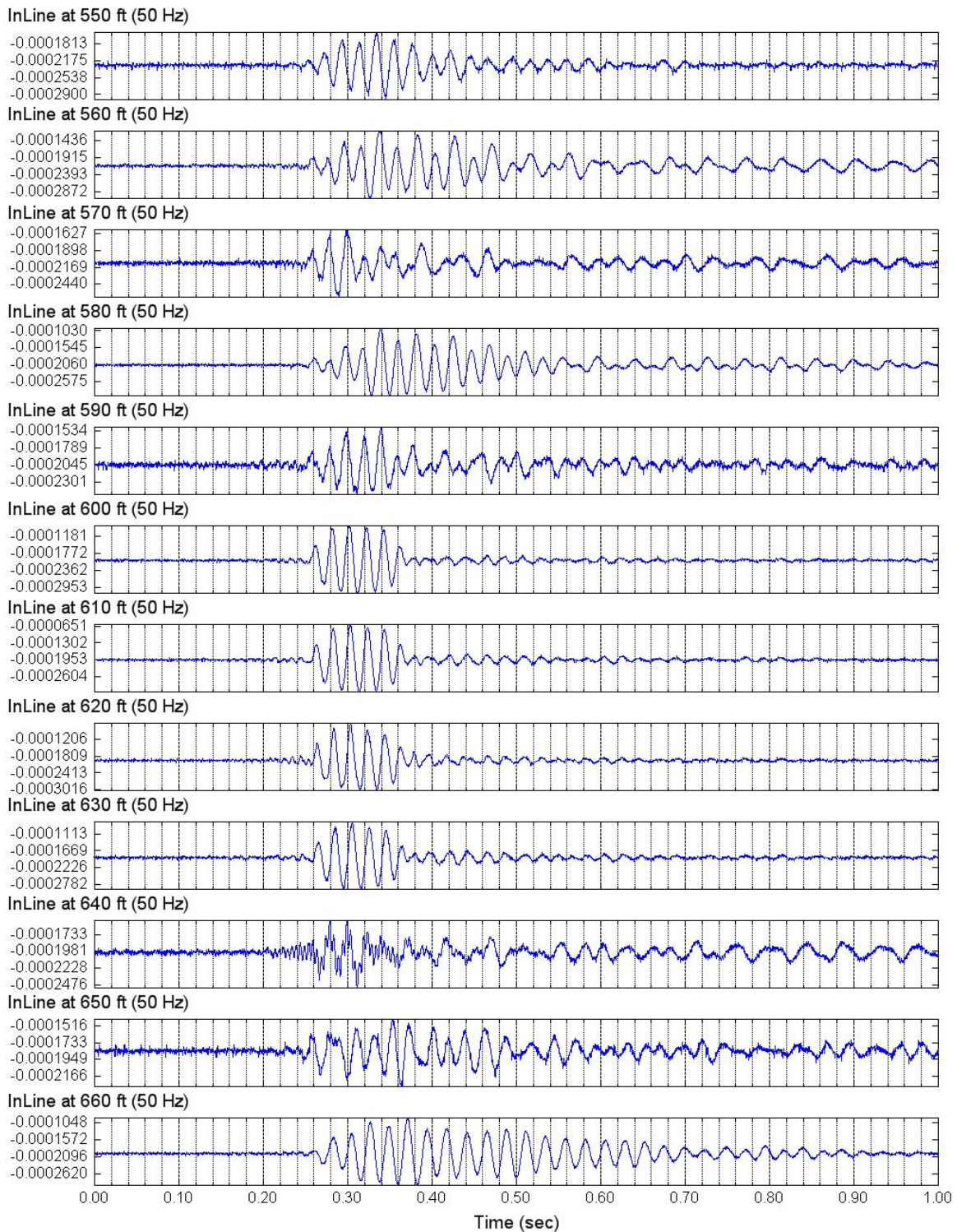


Figure 4.32 Unfiltered forward S-wave signal of lower in-line receiver (550 – 660 ft)

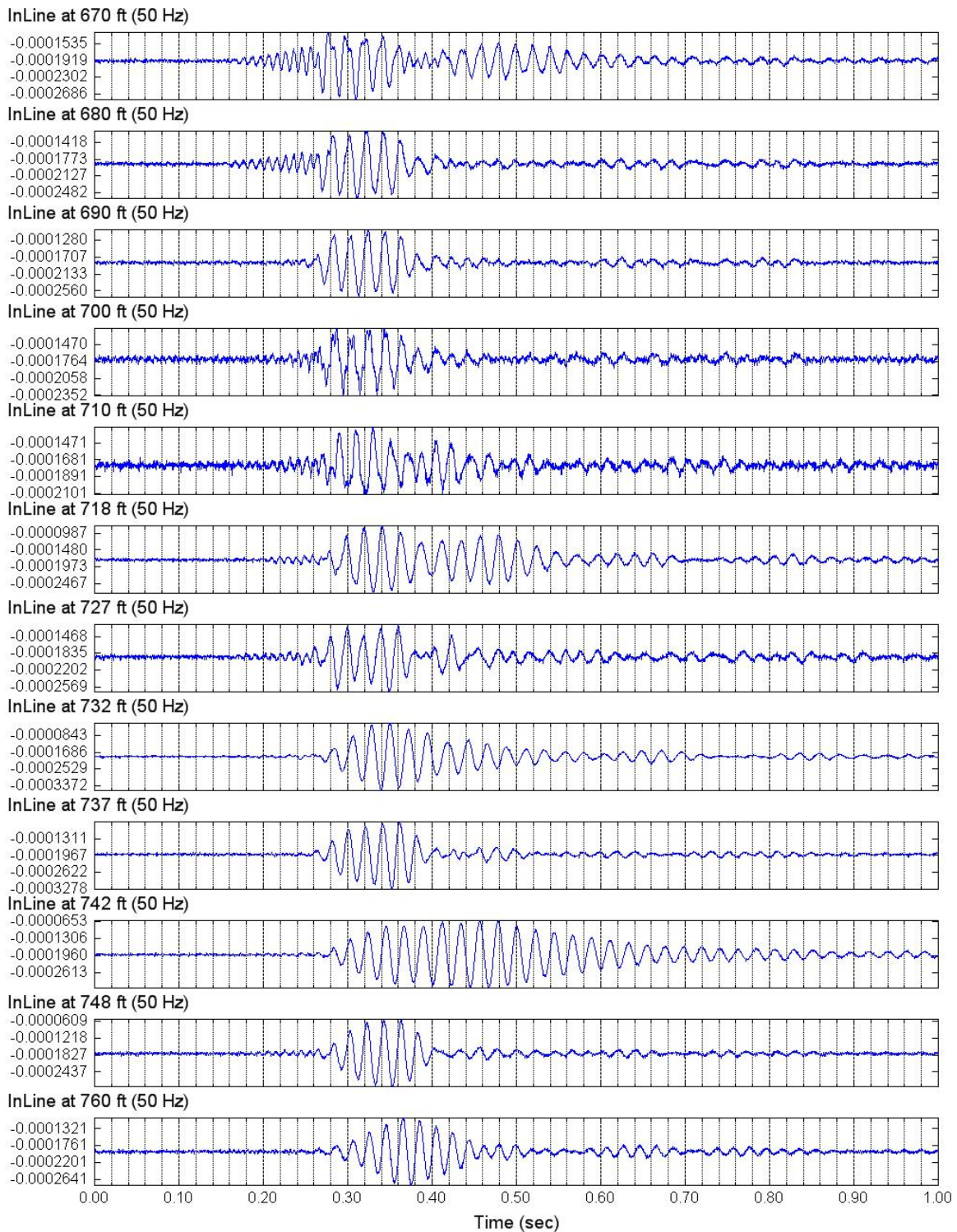


Figure 4.33 Unfiltered forward S-wave signal of lower in-line receiver (670 – 760 ft)

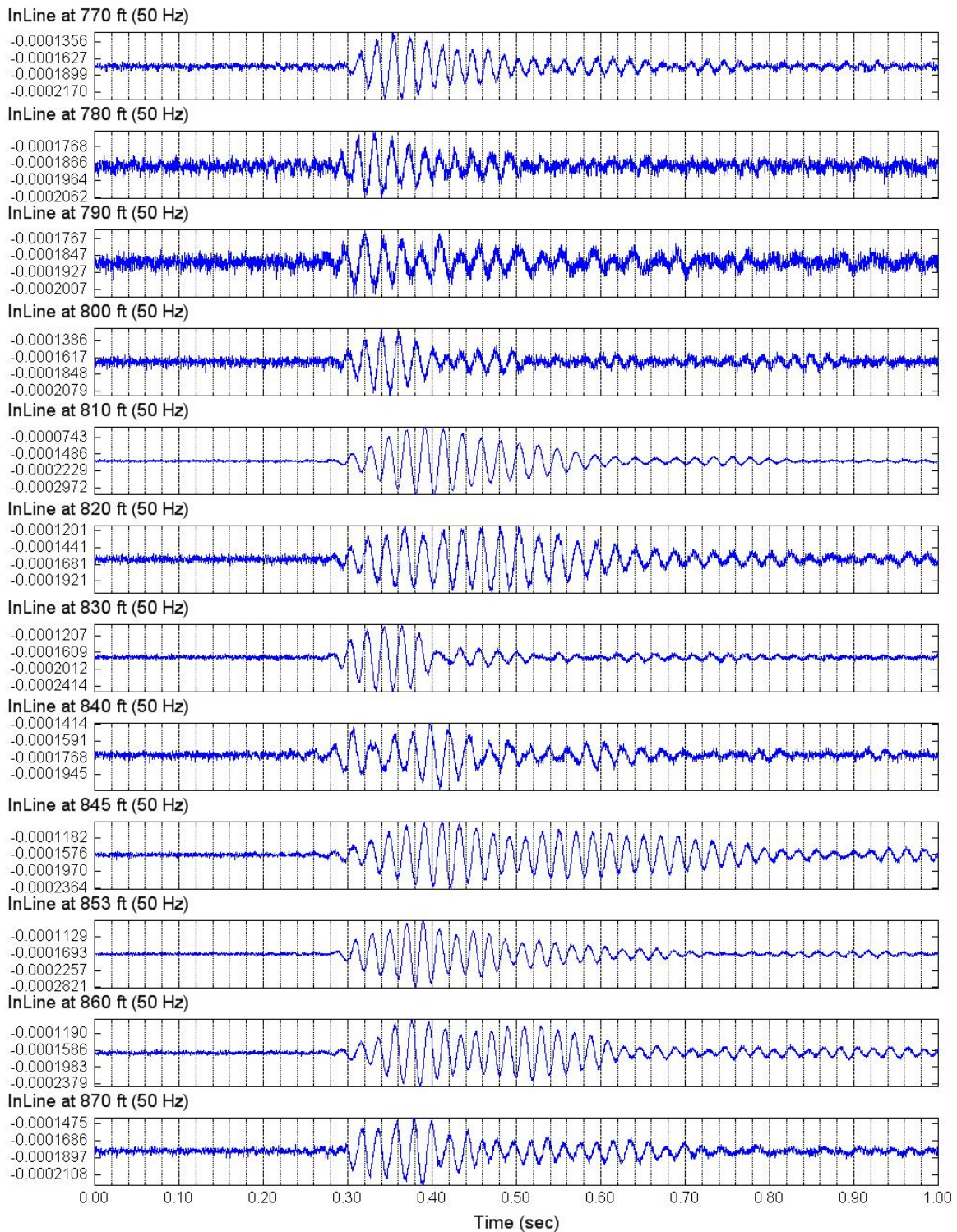


Figure 4.34 Unfiltered forward S-wave signal of lower in-line receiver (770 – 870 ft)

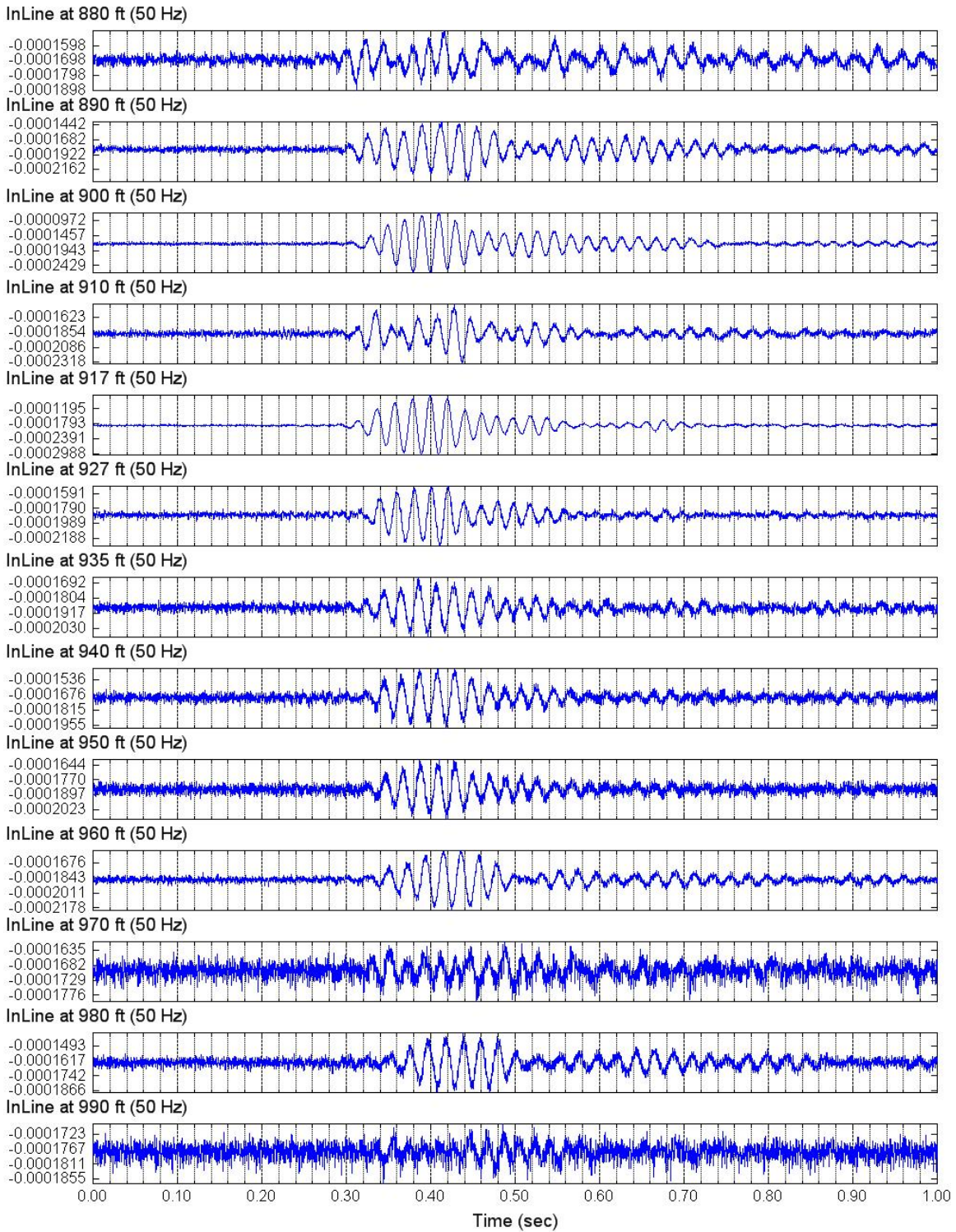


Figure 4.35 Unfiltered forward S-wave signal of lower in-line receiver (880 – 990 ft)

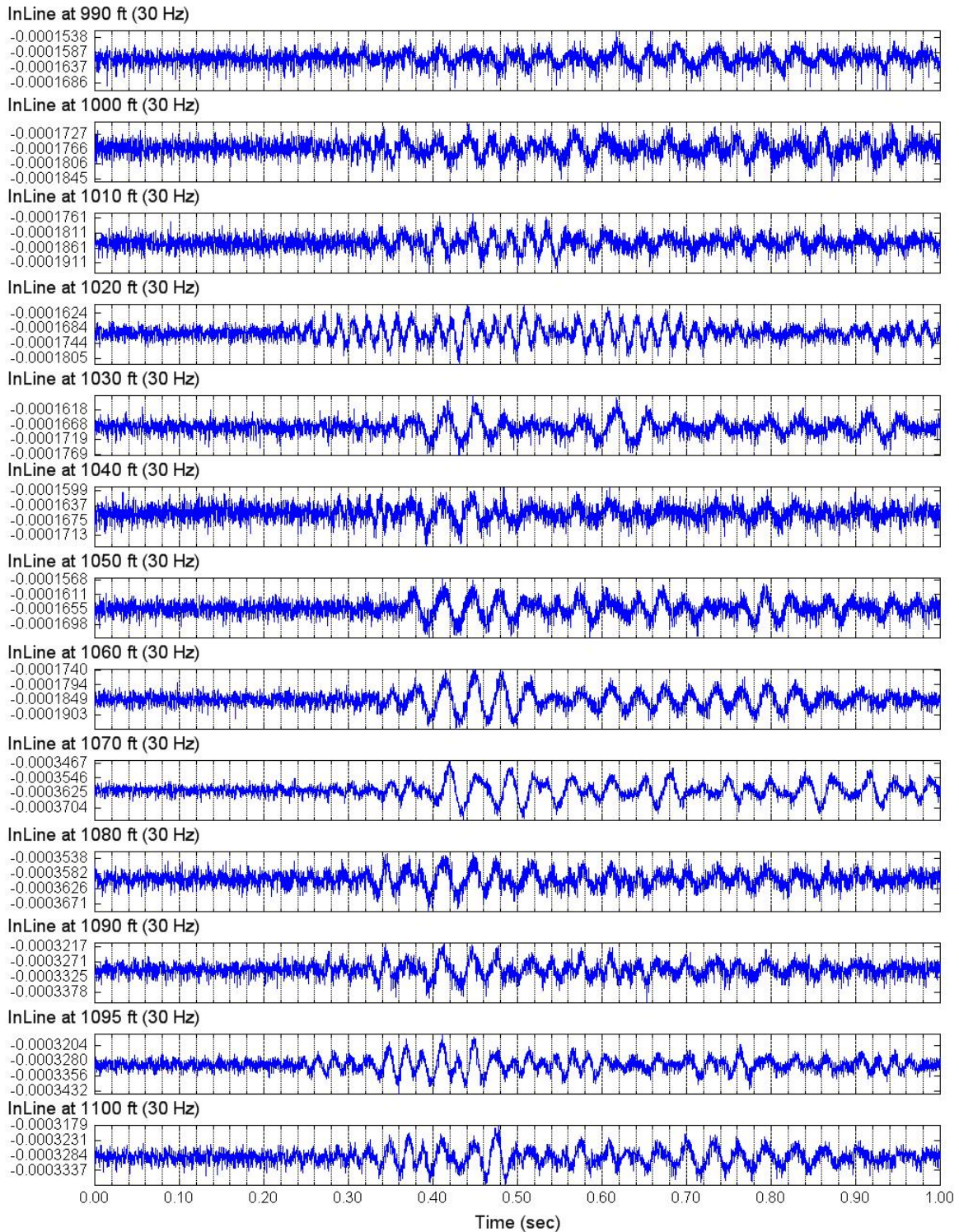


Figure 4.36 Unfiltered forward S-wave signal of lower in-line receiver (990 – 1100 ft)

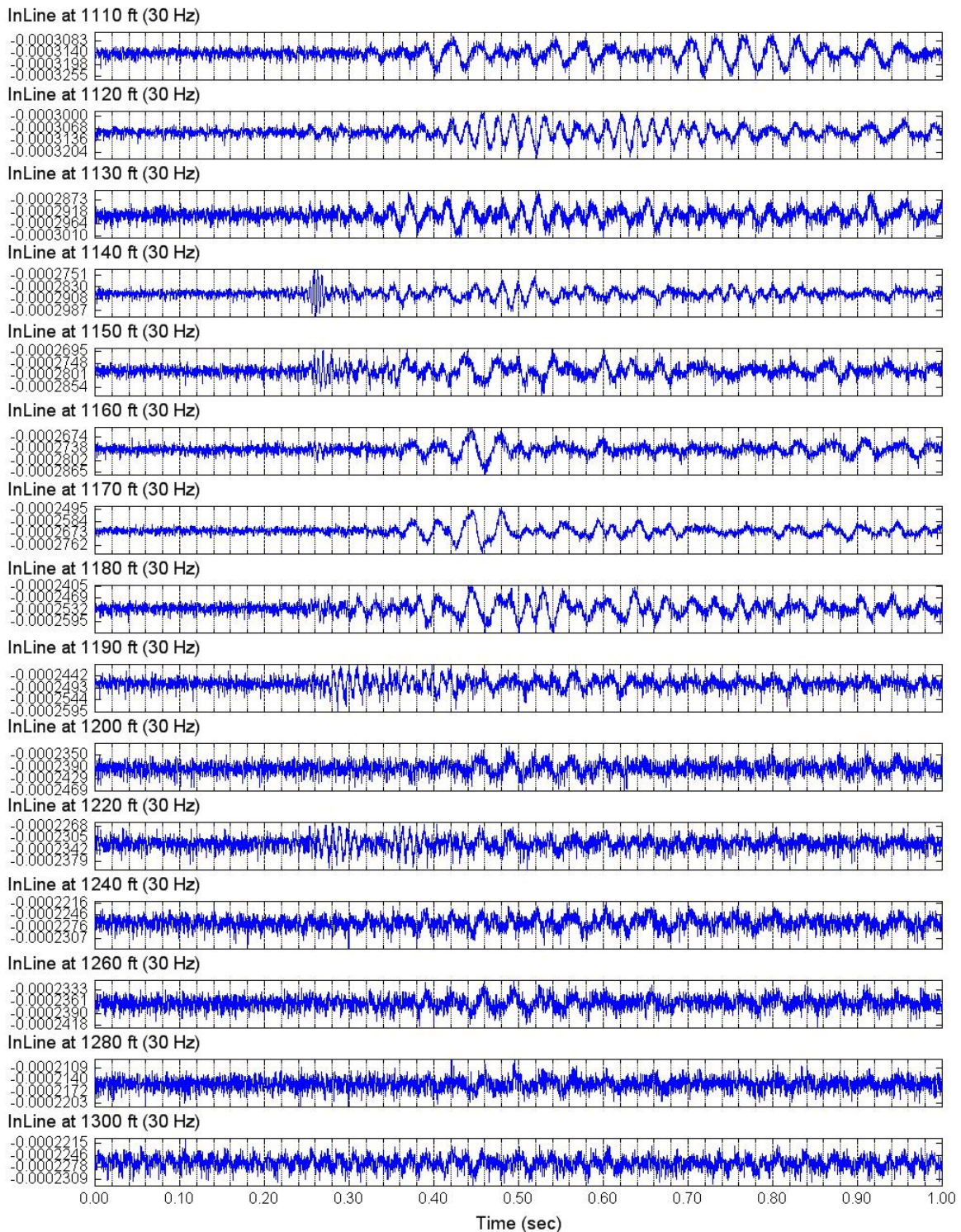


Figure 4.37 Unfiltered forward S-wave signal of lower in-line receiver (1110 – 1300 ft)

4.7 FILTERED AND ROTATED S-WAVE IN-LINE SIGNALS

Each panel shown in Figures 4.38 to 4.45 presents the filtered and rotated in-line signals from both the forward and reverse shaking. The forward shaking is marked by a small circle while the reverse shaking is marked by a small triangle. The small circles or triangles denote the waveform identifications that present the same waveform traveling in the downward direction. After correction for disorientation as shown in Figures 4.38 to 4.45, the S-wave arrival identifications are followed using the rotated in-line signals. The butterfly pattern produced by the forward and reverse rotated-in-line signals is useful for identifying the arrival times.

At significant depths when the signal-to-noise ratio is low, the S-wave signals interfere with multiple-path S-wave arrivals as well as preceding P-wave and possible SV-wave signals. Superposition of multiple waveforms results in phase shifts and waveform distortions that make the tracking of the same waveform very difficult as shown in Figure 4.46. When the wave identifications can no longer be tracked in the S-wave waterfall plots, the combination of waterfall plots of P-wave and S-wave signals are appropriate for predicting and estimating the S-wave arrival times using empirical Poisson's ratio values. Figure 4.47 demonstrates the use of the relative time interval between P-wave and S-wave arrivals in the deepest range of this profile.

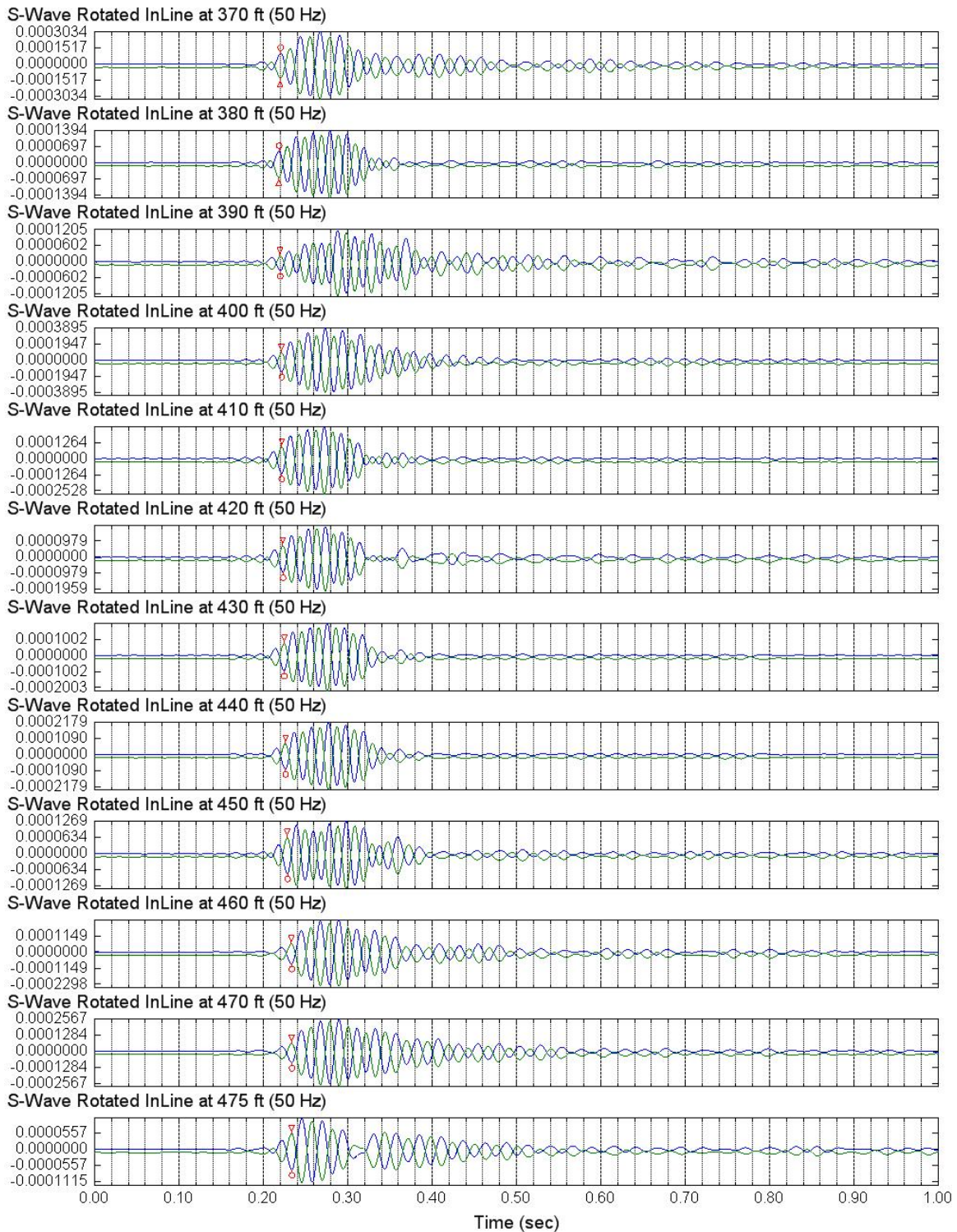


Figure 4.38 Filtered and rotated S-wave in-line signals (370 – 475 ft)

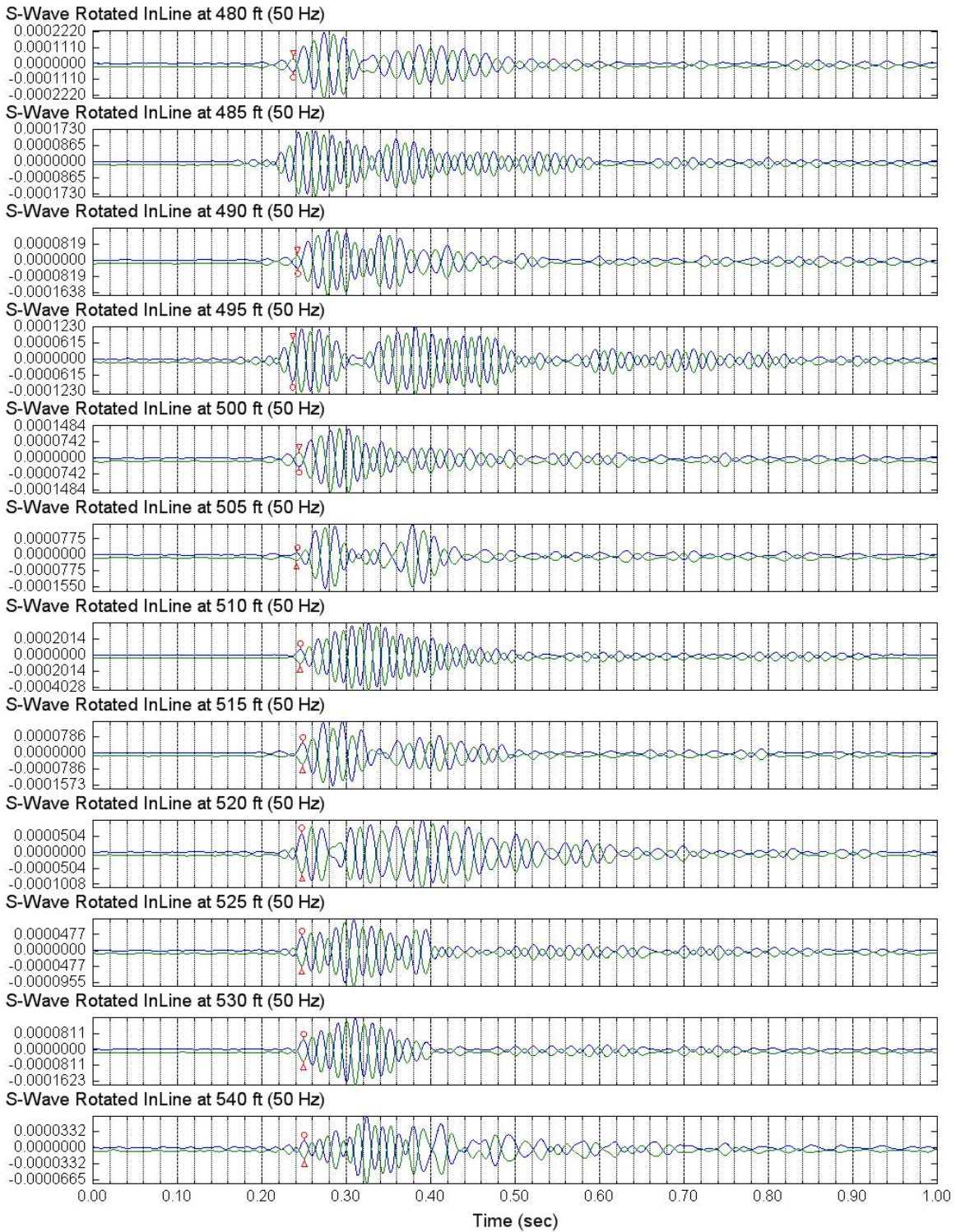


Figure 4.39 Filtered and rotated S-wave in-line signals (480 – 540 ft)

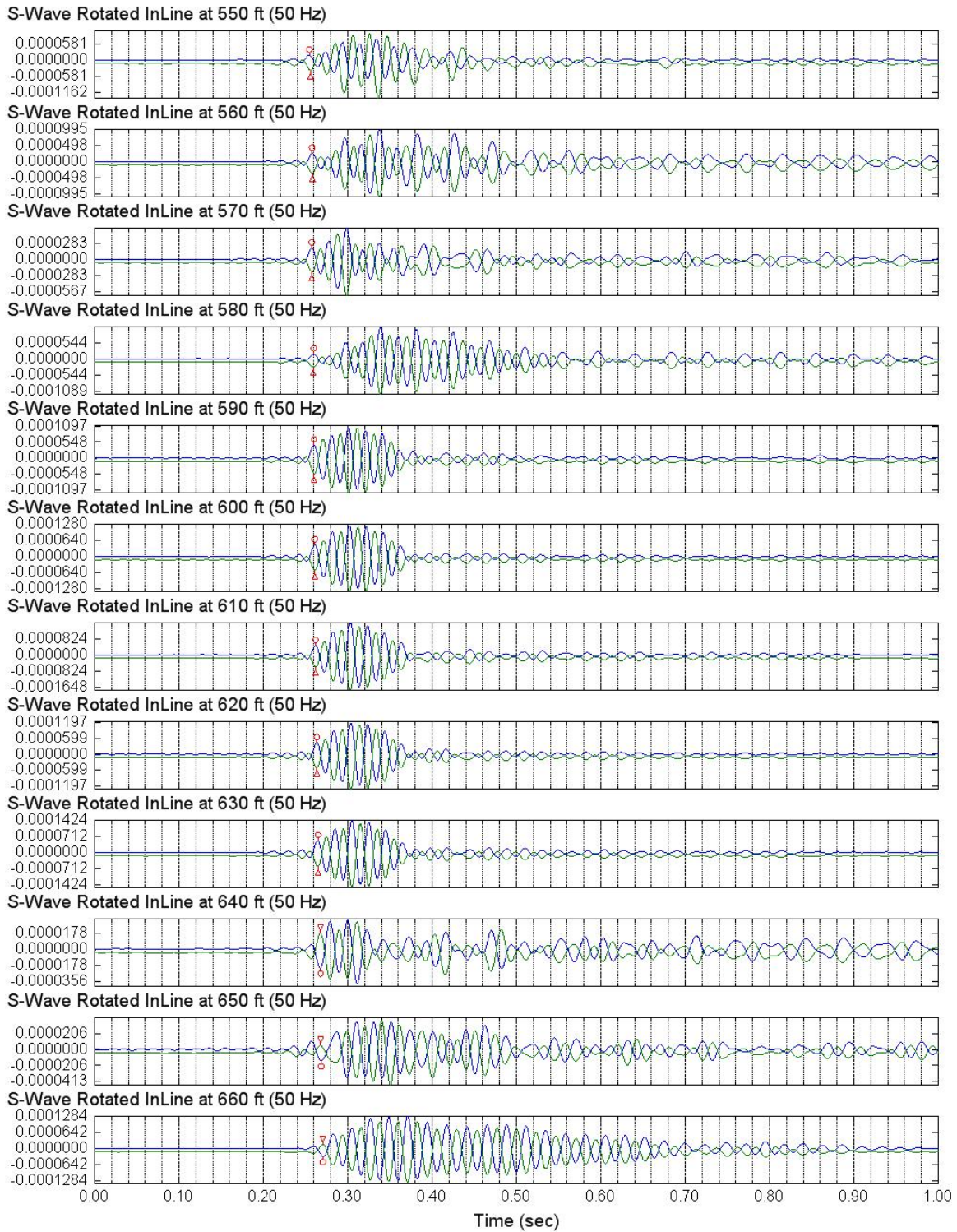


Figure 4.40 Filtered and rotated S-wave in-line signals (550 – 660 ft)

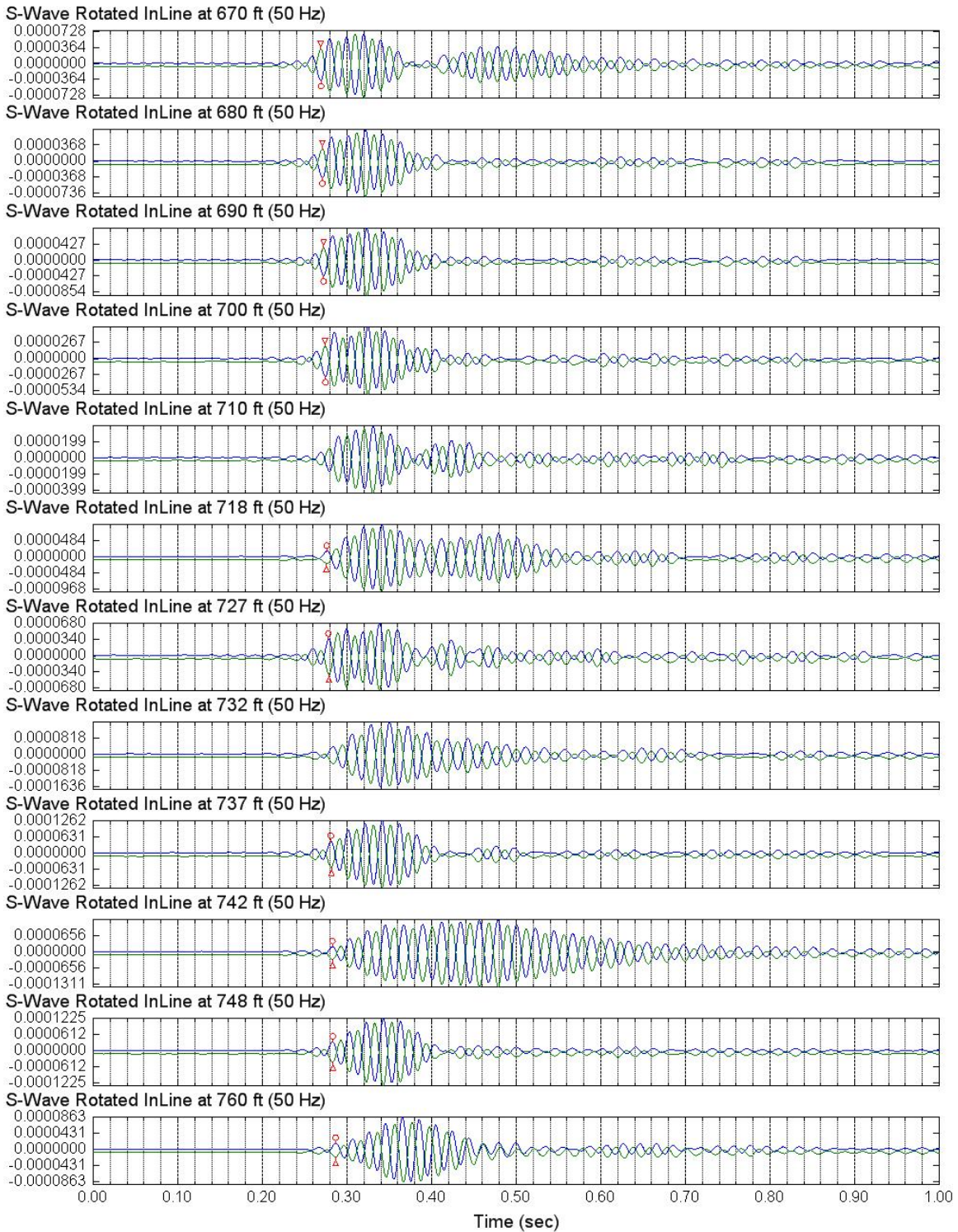


Figure 4.41 Filtered and rotated S-wave in-line signals (670 – 760 ft)

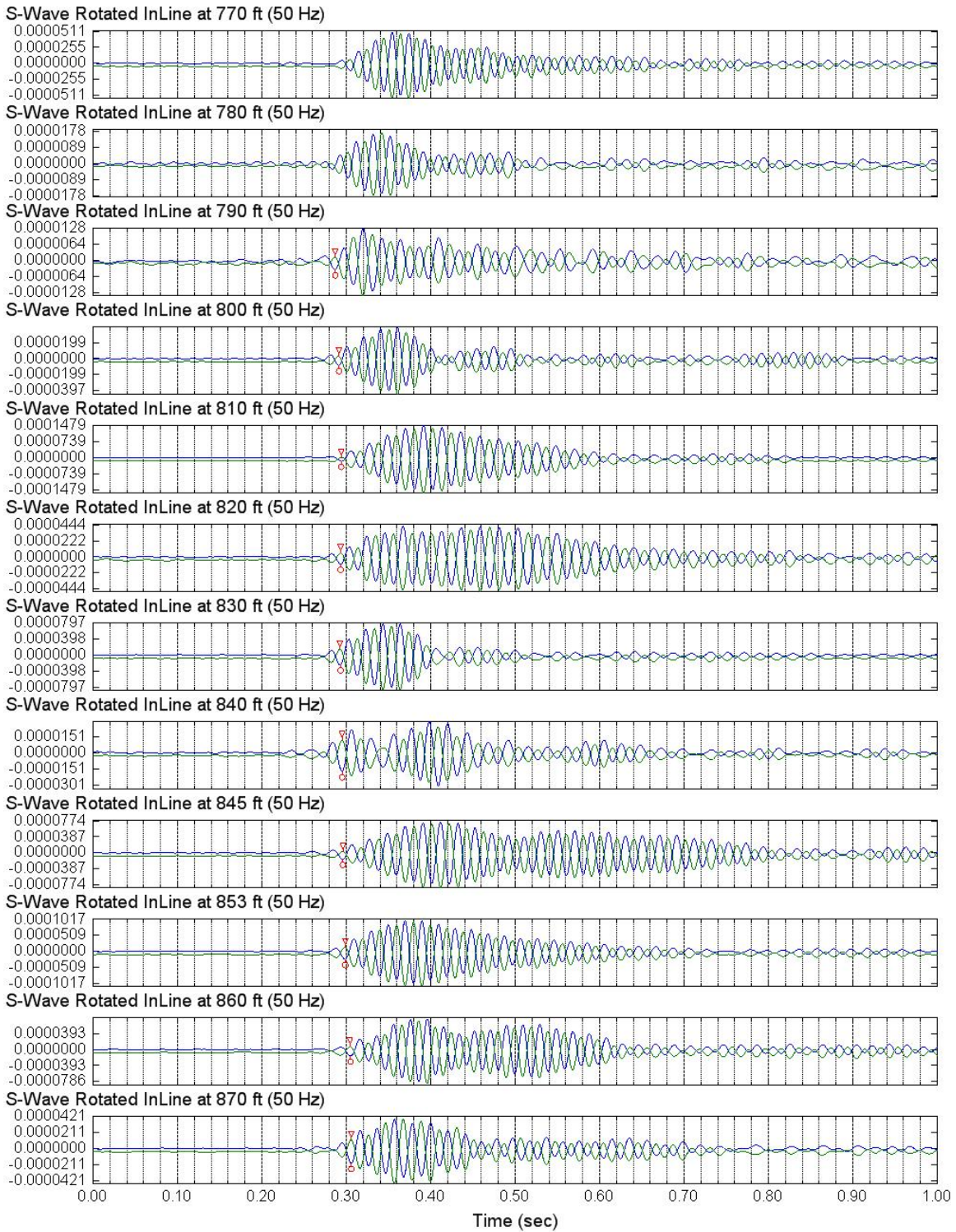


Figure 4.42 Filtered and rotated S-wave in-line signals (770 – 870 ft)

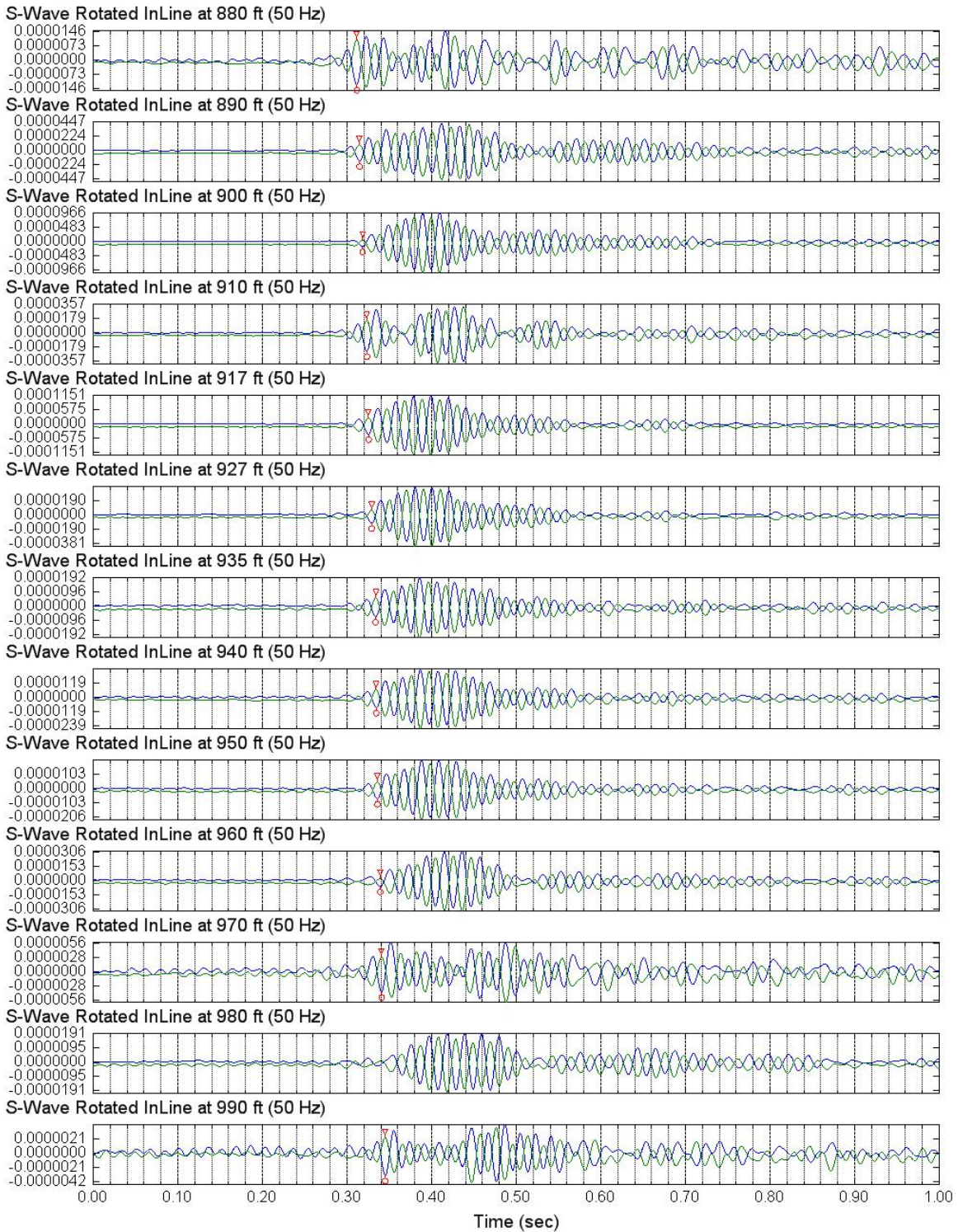


Figure 4.43 Filtered and rotated S-wave in-line signals (880 – 990 ft)

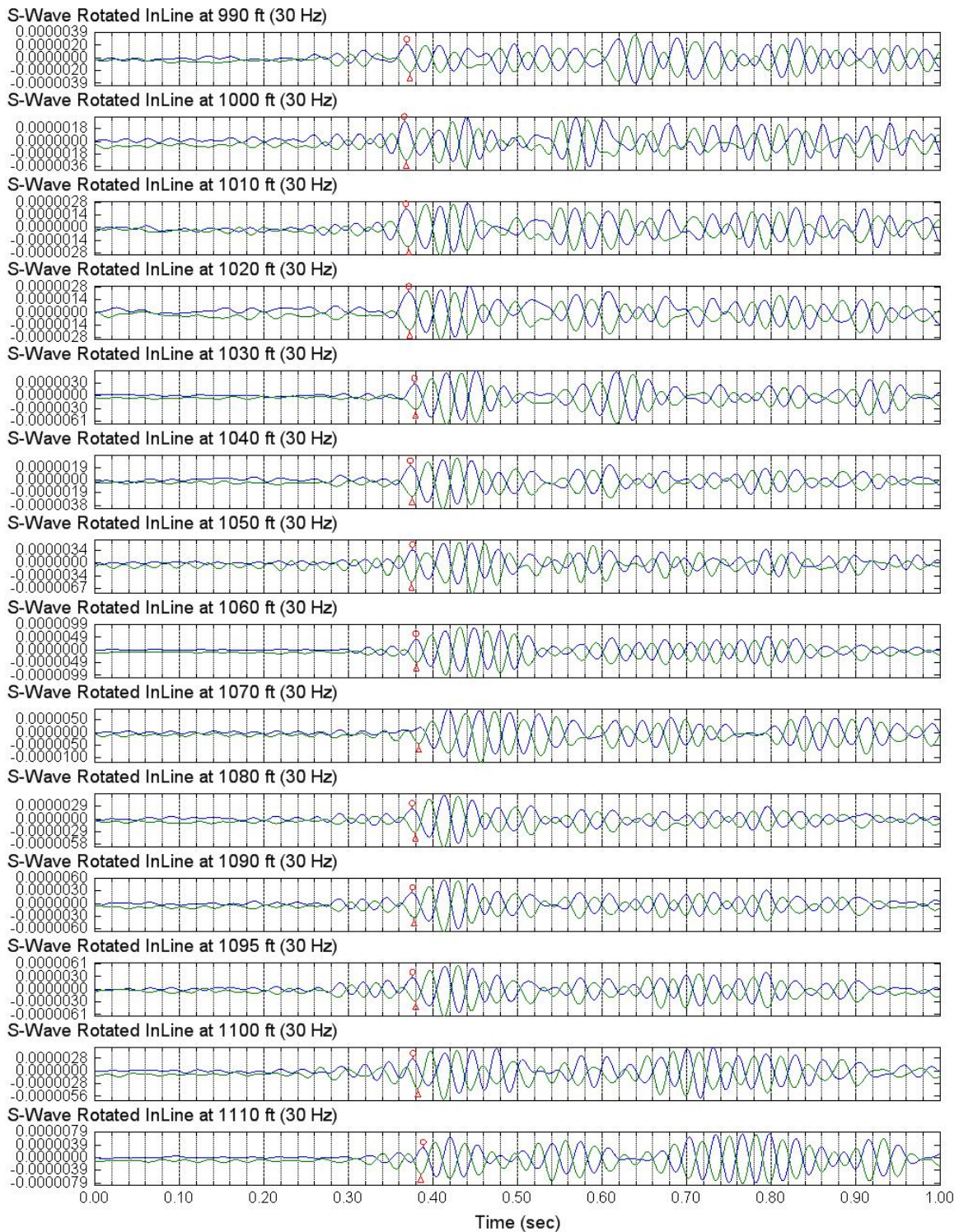


Figure 4.44 Filtered and rotated S-wave in-line signals (990 – 1110 ft)

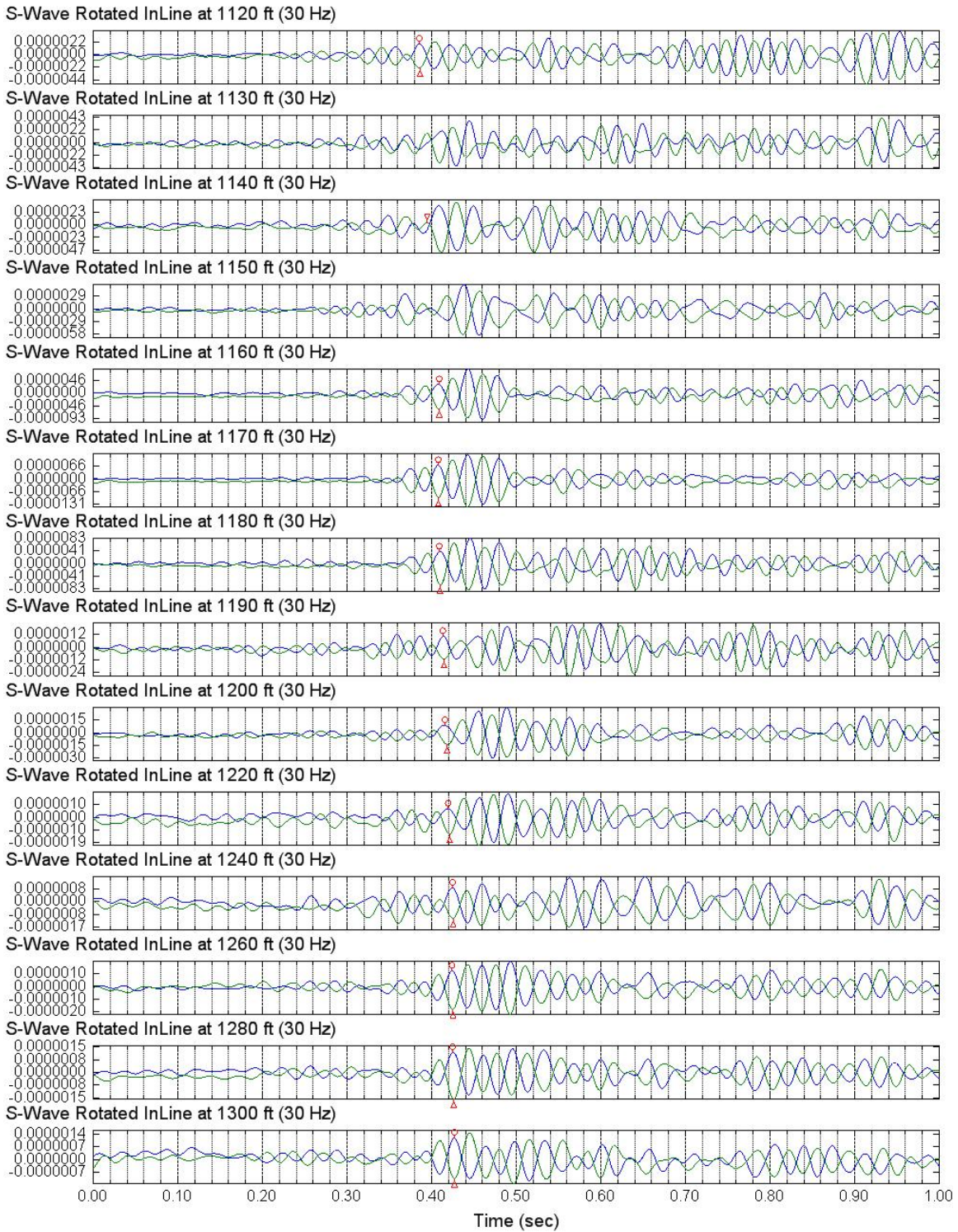


Figure 4.45 Filtered and rotated S-wave in-line signals (1120 – 1300 ft)

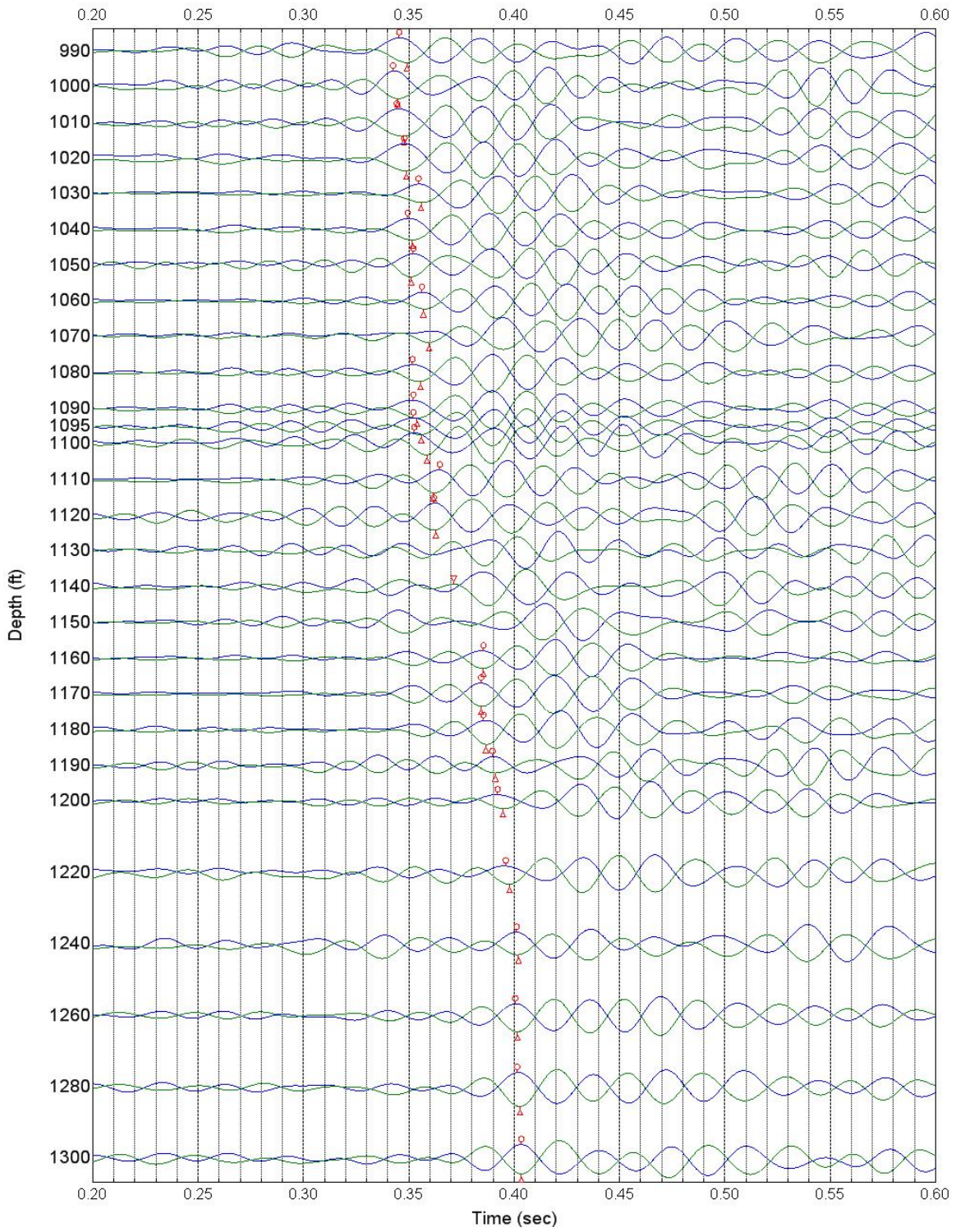


Figure 4.46 Waterfall plot of S-wave rotated in-line signals (990 – 1300 ft)

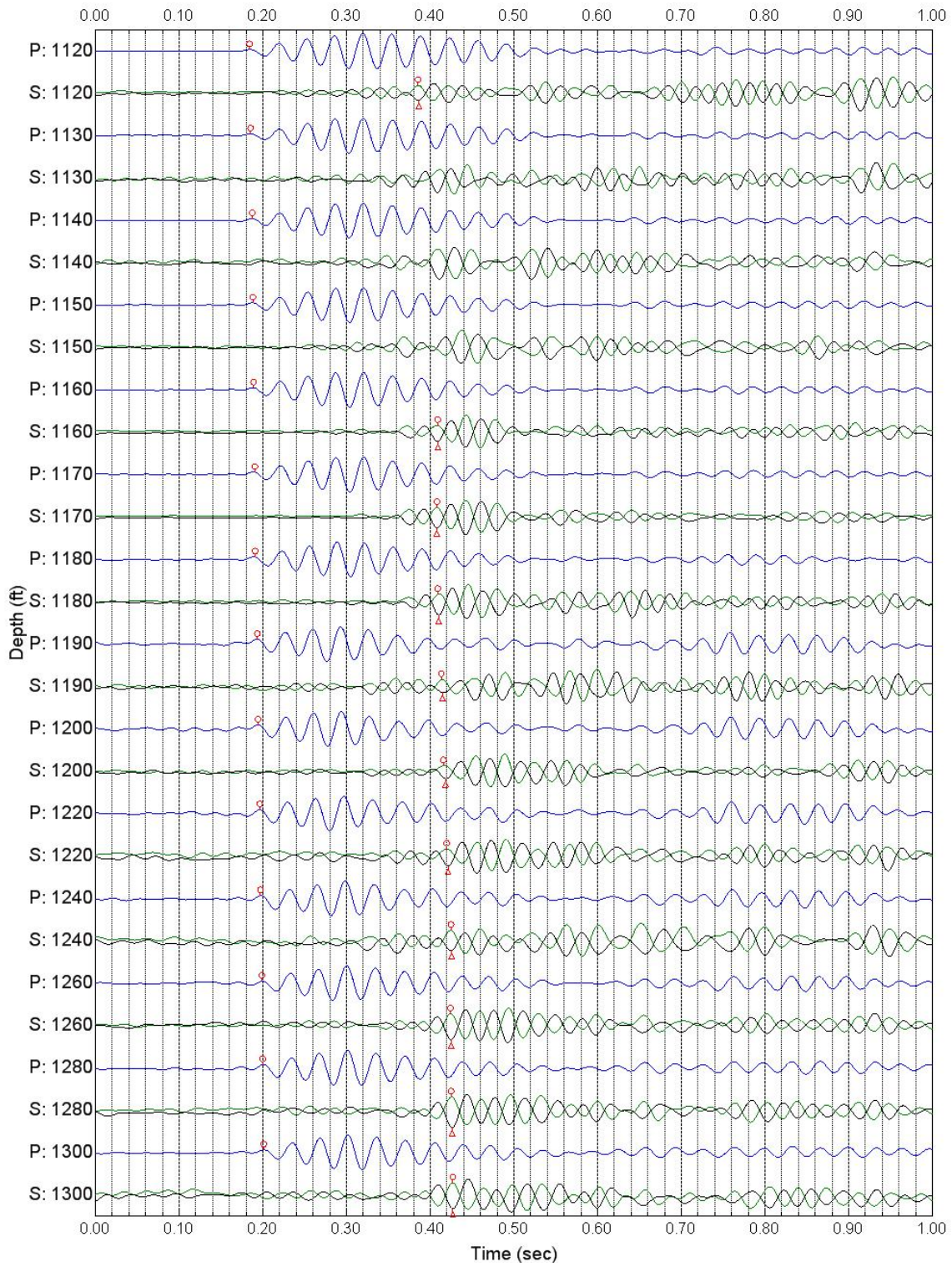


Figure 4.47 Estimation of S-wave arrival time using the P-wave arrival as a reference

4.8 RELATIVE S-WAVE TRAVEL TIMES AND INTERPRETED VS PROFILE

All relative S-wave travel times determined by the open circles or triangles in the waterfall plots of the filtered and rotated S-wave signals for Borehole C4993 at Hanford are shown in Figure 4.48. Expanded plots of the relative S-wave travel times are shown in Figures 4.49 to 4.51. The interpreted Vs values of each layer or sub-layers are given by the inverse of the slopes of the solid lines through the relative times in these figures. The values of Vs are presented in the boxes next to the solid lines. Clearly, reasonable correlations exist between the layering and velocities. As with P-wave velocity profiles discussed in Section 4.5, the geologic profile with the depths of the layer boundaries were known before the data were analyzed. However, fitting the straight lines through the data was done based on the data and not the layer boundaries. Obviously, the S-wave travel times exhibit more scattered than the P-wave travel times, especially at depths below 300 m (1000 ft) because of the added difficulty in distinguishing S-wave arrivals from preceding P, SV and coupled waveforms in the travel time records.

As seen from expanded Figures 4.49 to 4.51, some measured points are not shown. For example, some measurement points between depths of 330 to 360 m (1100 to 1200 ft) are not shown but travel-time records were taken. These data points demonstrated strong scattering and multi-polarizations, a reasonable rotated in-line direction is not even available. When fitting a straight line for the data points, an overall trend was considered, and engineering judgment was applied. The wavelet-response method is developed and presented in Chapter 7 to correct the disorientation of the receiver tool at these depths.

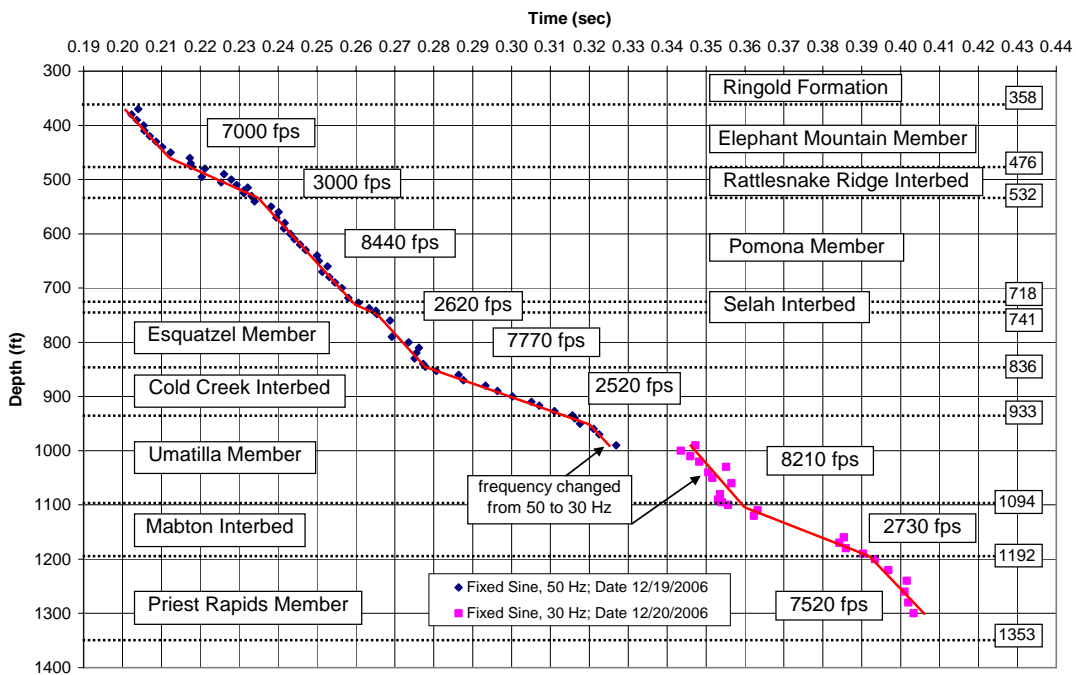


Figure 4.48 Relative S-wave travel times and interpreted Vs profile in Borehole C4993

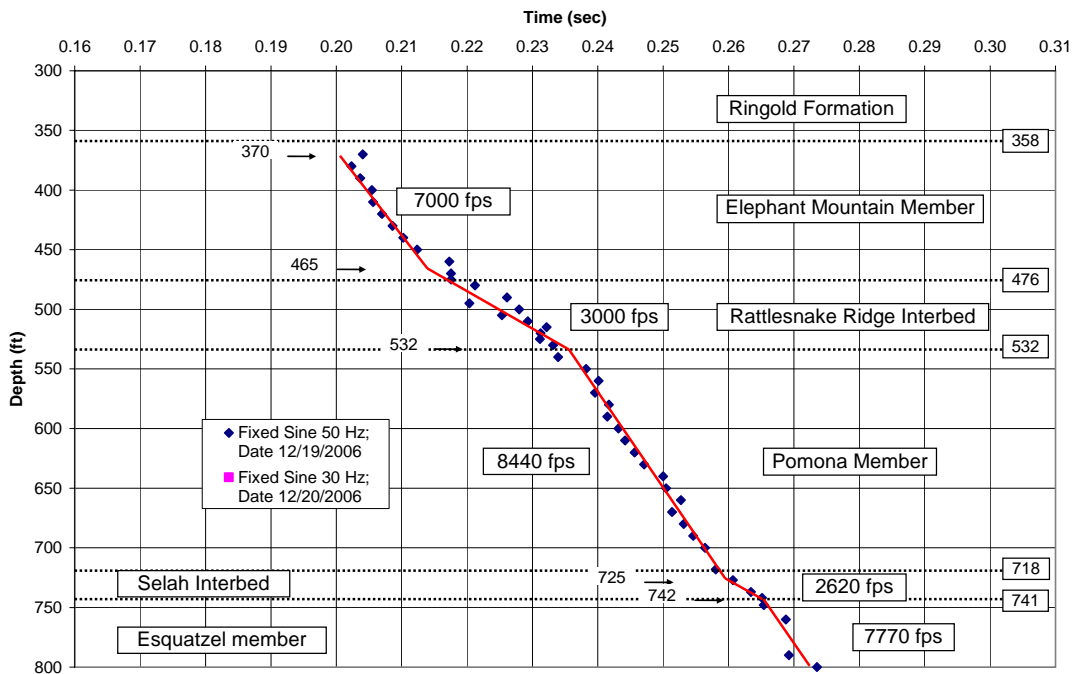


Figure 4.49 Expanded relative S-wave travel times (300 – 800 ft)

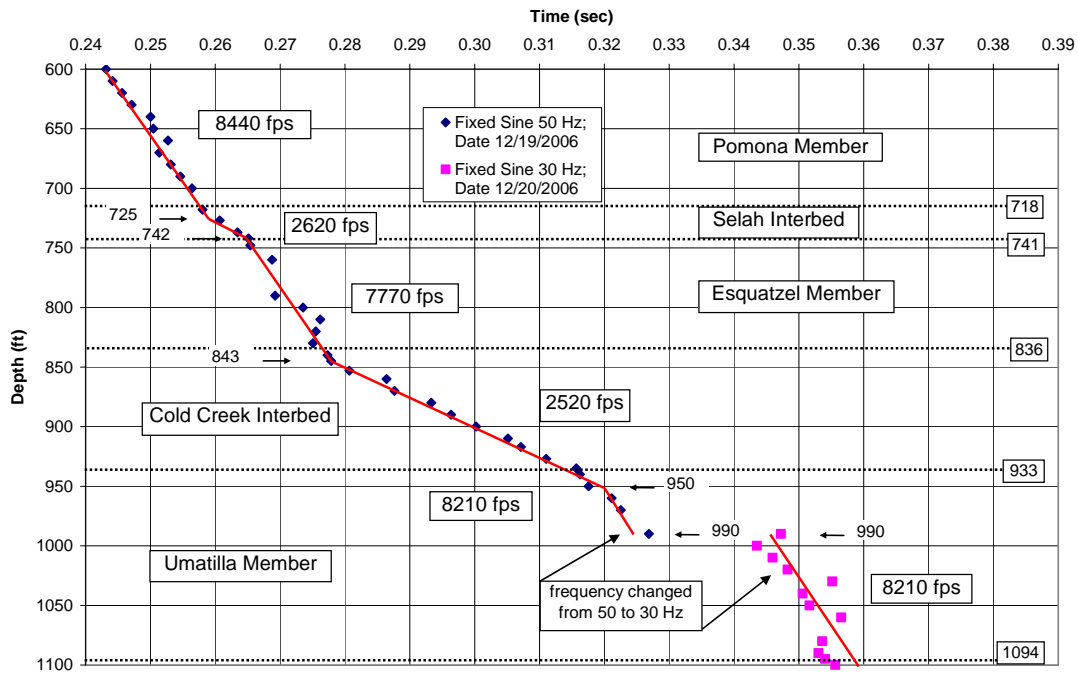


Figure 4.50 Expanded relative S-wave travel times (600 – 1100 ft)

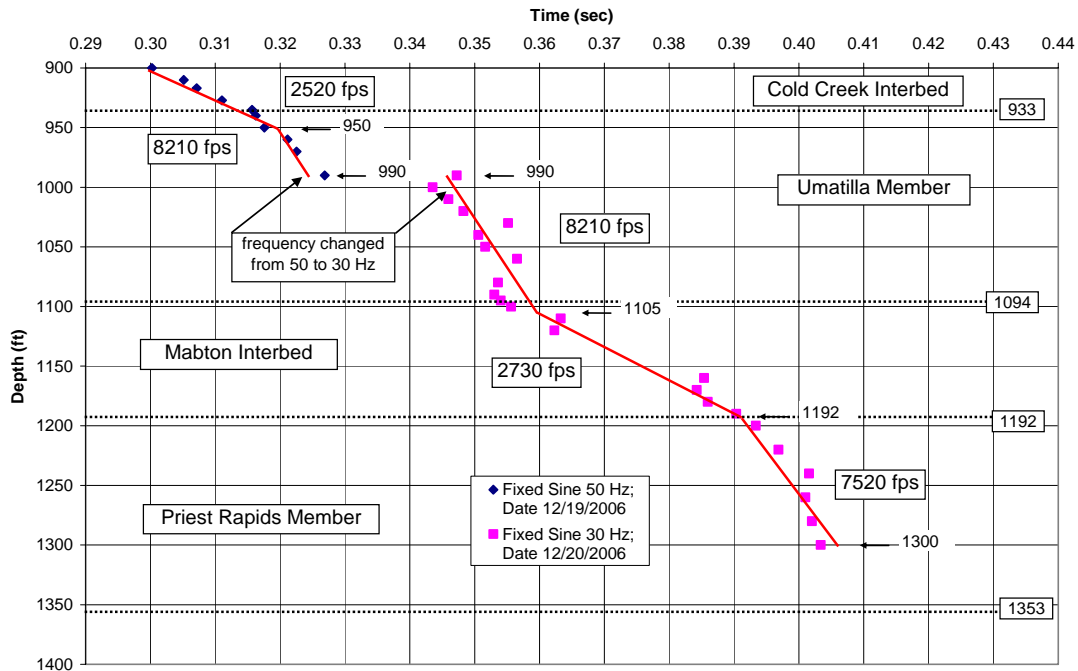


Figure 4.51 Expanded relative S-wave travel times (900 – 1400 ft)

An independent check on the downhole V_s values was also available at this site. Independent S-wave velocities were measured in Borehole C4993 with the P-S suspension logger by GeoVision Geophysical Services. The V_s profiles from both methods are compared in Figure 4.52. The overall comparison between the two methods is quite good. The average S wave velocities in the interbeds agree very well, but the S-wave velocities in the basalt layers measured by suspension logging are generally about 20% higher than those measured by the downhole tests. It should be noted that the suspension logger captures the variations in S-wave velocities within the basalt layers and interbeds and near the boundaries but the downhole test does not have the same resolution at these depths.

Both the frequency dispersion effects and the effective medium theory on P-wave velocities may also apply to S-wave velocities. The frequency dispersion effect may play a role in the velocity differences between the downhole and suspension logging tests in the basalt layers. The generally higher velocities in the basalt layers measured by suspension logging test may be affected by the much higher frequencies used in suspension logging than downhole tests.

Both the frequency dispersion effect and the effective medium theory may also justify the velocity differences between the downhole test and suspension logging test in interbeds. The S-wave velocities of the interbeds measured by downhole tests match with those by the suspension logger. The frequency dispersion effect on the interbeds could be counteracted by the effect from the effective medium theory discussed in Chapter 2. The downhole test used much longer wavelengths than the thickness of the thin interbed layers. The measured velocity of the thin layers measured by the downhole test should be lower than the suspension logger, as is true for the velocity in the basalt layer. The measured velocity in the interbeds is actually the volume-weighted average of the

velocities of all layers within a wavelength. The measurements in an interbed could be a result of an equivalent layer that covers part of the basalt layers within the thickness of a wavelength.

The S-wave velocities measured on intact specimens in laboratory tests are compared in Figure 4.53 with the downhole and suspension logging measurements. The V_s values of the basalt that were measured in the laboratory agree well with those from the suspension logging tests. Typical samples for laboratory test have higher quality than the field samples, and the laboratory test results generally overestimate the field velocities in rock. It is reasonable to suspect that, the velocities measured by the suspension logging test might also overestimate the field conditions as they closely agree with the laboratory results.

The S-wave velocities measured in the laboratory with the samples in the interbeds may confirm the effective medium theory. The downhole S-wave velocity in an interbed are higher than the laboratory test results because of the basalt layers within a wavelength of the interbed.

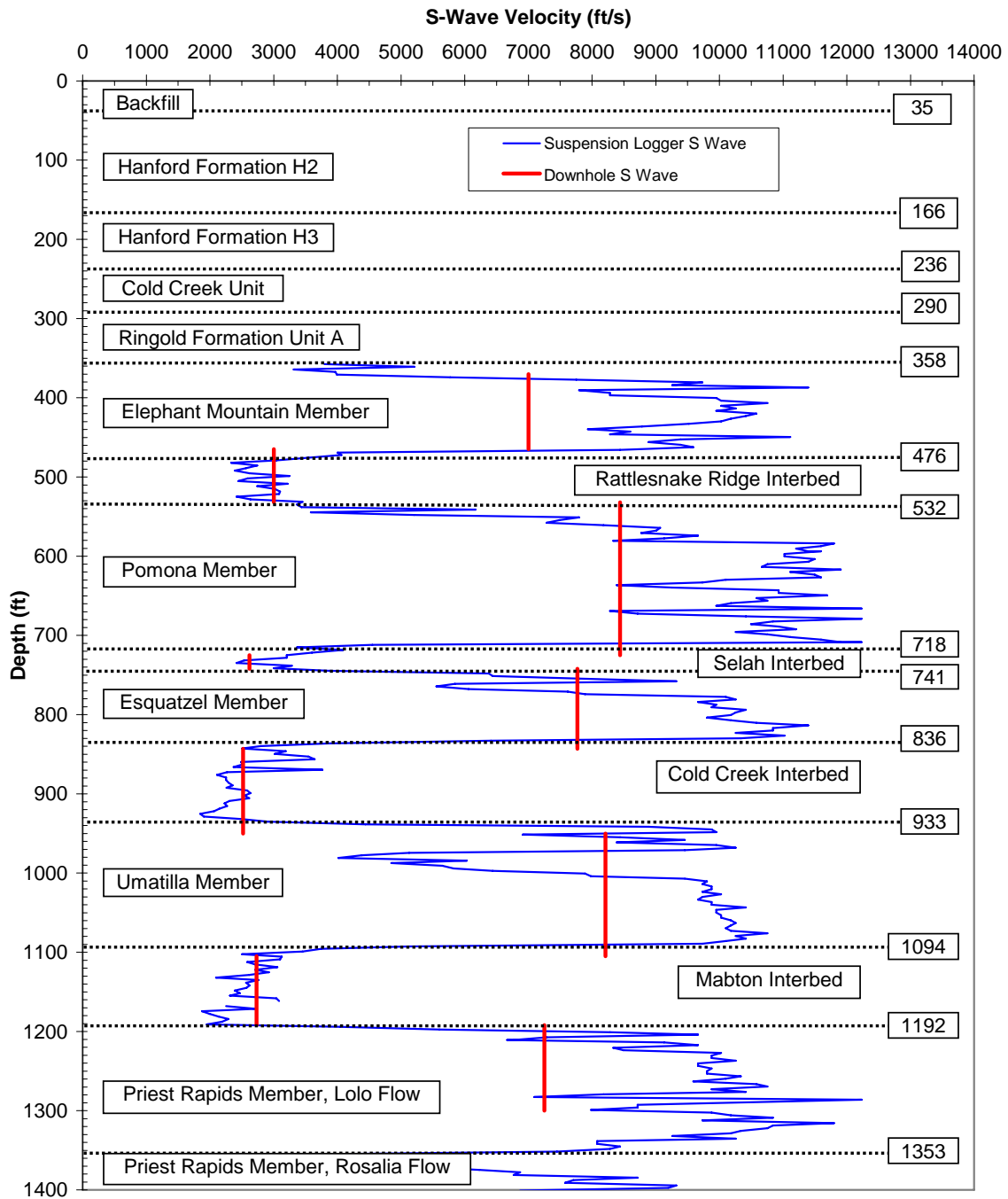


Figure 4.52 Comparison of S-wave velocities between downhole and suspension logger tests in Borehole C4993

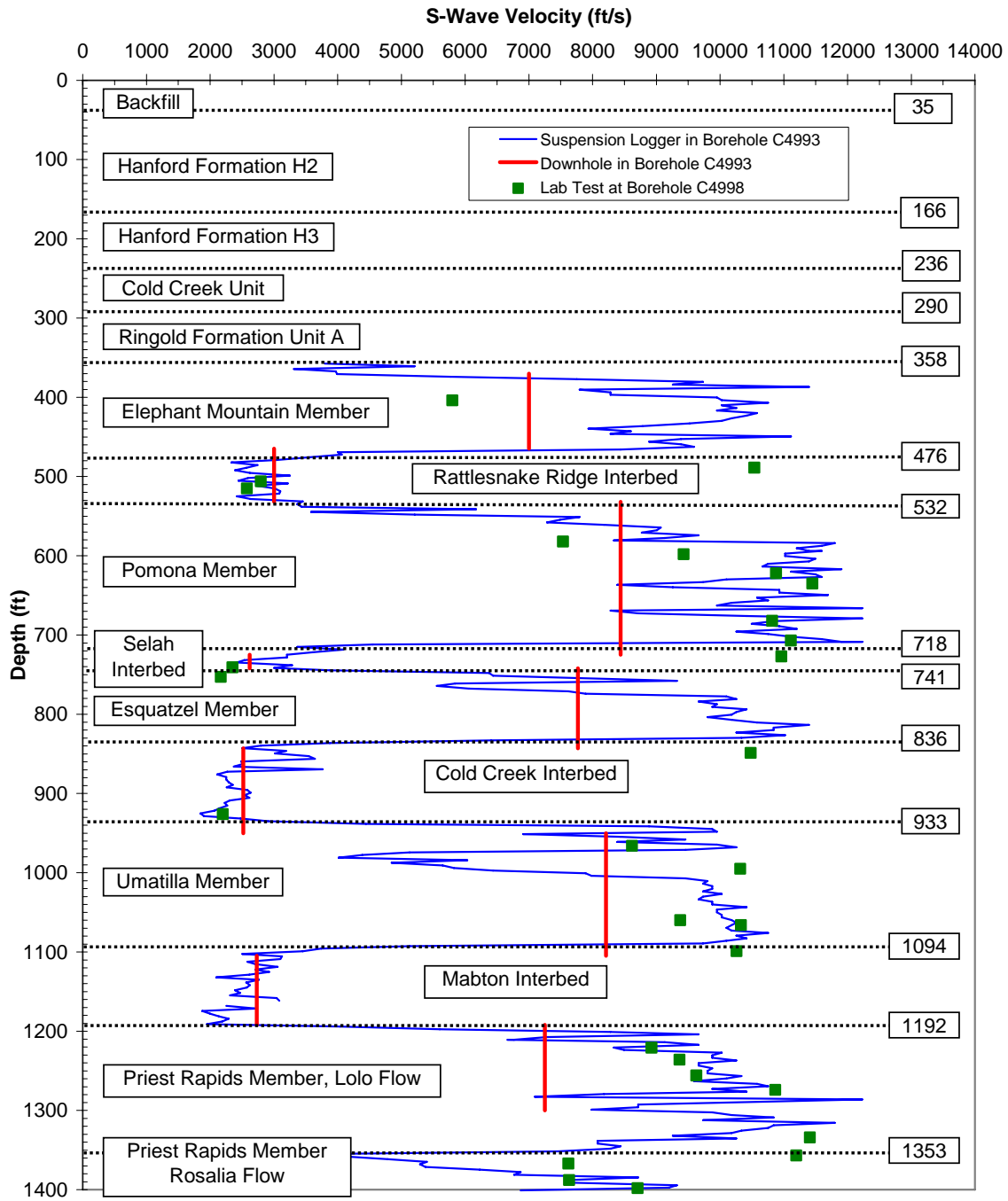


Figure 4.53 Comparison of S-wave velocities from downhole and suspension logging tests in Borehole C4993 and lab test at Borehole C4998

4.9 SUMMARY

To minimize the effect of frequency dispersion in deep downhole testing, a new source signal called the fixed-sine wavelet is used in this research as opposed to a conventional chirp sweep. The downhole test data from a real project with strong layer contrasts are processed using software called DeepSeis 2.1 that was developed for use with T-Rex as a fixed-sine source. The test data are presented as an example of the travel-time analysis that can be performed with DeepSeis 2.1. High-frequency noise is low-pass filtered after the time series are transformed into the frequency domain using fast Fourier transform. Travel times are hand-picked directly on filtered waveforms. Waterfall plots are used to track wave identifications. Disorientation of the receiver tool is corrected for S-wave signals to obtain a rotated in-line signal, a critical aspect in deep downhole testing.

The effect of frequency dispersion may play a role in the travel times of the basalt layers. Both P- and S-wave velocities measured by downhole tests in the basalt layers are lower than those measured by the suspension logger. The difference may be justified by the effect of frequency dispersion, which states that velocity measured with higher frequencies is greater than that measured with lower frequencies (Gupta, 1972).

Effective medium theory (Backus, 1962) may also be a factor in the travel time analysis of the thin interbeds. The surrounding basalt layers are much thicker than the interbeds. The effective medium theory may have little effect in the basalt layers. The thin interbeds are characterized by thicknesses much less than the wavelengths of the test frequencies. The downhole test is supposed to overestimate the measured wave velocity of the interbeds due to the effective medium theory. However, compared with the velocity measured by the suspension logger, the overestimation could be counteracted by the effect of frequency dispersion.

Strong contrasts in layer stiffnesses between basalt and interbed layers results in significant boundary reflections that heavily distort waveforms within the first cycle of the waveform. It is clearly seen that waveforms are more distorted near the boundaries or in thin layers.

For vibratory source, the effect of effective medium theory on thin layers and the strong reflection at reflectors could compromise a clear identification of the velocity profile near the boundary using travel times. Travel times near the boundaries exhibit fluctuations and disruptions that cause difficulty in determination of a distinct velocity value.

Signal-to-noise ratio is low for deep downhole signals. Wave arrivals of signals below 1000 ft are more difficult to identify. P-wave signals have less waveform distortion than S-wave signals because the prescribed capability of source energy for P wave is almost double that for S-wave.

Chapter 5 Characteristics of Vibratory Source

5.1 INTRODUCTION

The seismic source used in this research is T-Rex, a controlled vibratory source. A vibratory source can be modeled by several components connected in series with multiple degrees of freedom (Lebedev and Beresnev, 2004). However, if consider the imaginary boundary between the near-field and far-field earth as an equivalent ground surface, the displacement of the equivalent ground surface can be simulated by the response of a single-degree-of-freedom (SDOF) system (see Figure 5.1) regardless how many internal degrees of freedom for equivalent excitation force. In this chapter, the fixed-sine vibratory source is modeled as an equivalent SDOF system in terms of far-field seismic measurements in the earth as performed in this work. The source signature is also defined.

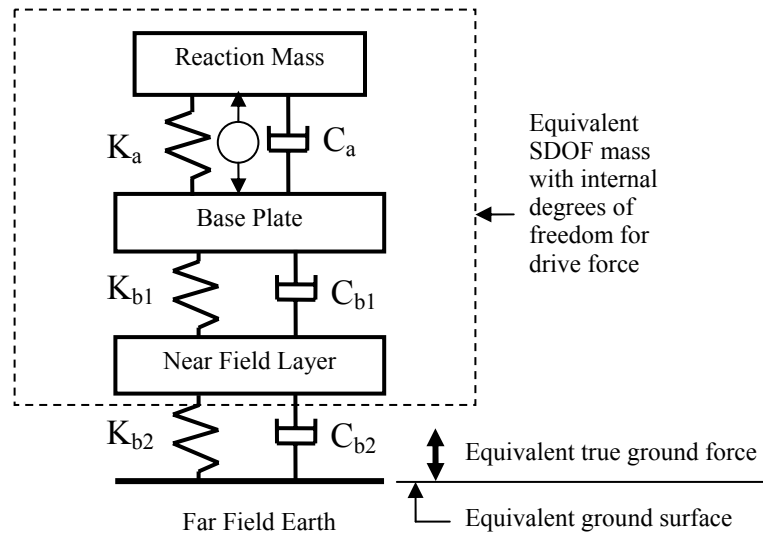


Figure 5.1 Illustration of a vibrator-earth system (adapted from Lebedev and Beresnev, 2004)

Standard Vibroseis theory states that the P-wave, far-field displacement is proportional to the true ground force (Miller and Pursey, 1954; Aki and Richards, 1980). The theory is based on results of Miller and Pursey (1954), who studied seismic radiation from a piston source on the surface of an elastic half space. The true ground force is equal to the traction underneath the baseplate integrated over the baseplate area. The traction is distributed non-uniformly, and cannot be represented directly by the base plate acceleration or reaction mass acceleration. The weighted sum estimation of the ground force may be unreliable because of the bending of the baseplate (Baeten and Ziolkowski, 1990; Martin and Jack, 1990). The travel time depends on amplitude and phase of the source wavelet, while the source waveform is subject to distortion during propagation (Walker, 1995; Jeffreys, 1996). In the literature, various models and assumptions are used to simulate the true ground force or extract the source signature (Hero and Schwartz, 1985; Baeten and Ziolkowski, 1990); Ching et al, 1999; Cambois, 2000; Robinson and Saggaf, 2001; Brittle et al, 2001; Mewhort, 2002). Conventional processing of Vibroseis data assumes that the signal forced into the ground by the Vibroseis is equal to the predetermined drive signal or pilot sweep. Baeten and Ziolkowski (1990) extensively studied the source effect and modeled the Vibroseis source signal. They found large errors for conventional assumptions in both the amplitude and phase of the estimated signal.

Waveform distortion occurs not only during propagation, but also at the vibrator itself. Source spectrum control has been studied by many authors (Lerwill, 1981; Sallas and Weber, 1982; Sallas, 1984; Jeffrey and Martin, 2003; Bagaini, 2006). Walker (1995) proposed a method to describe harmonic distortion and baseplate vibration observed in experiments. Lebedev and Beresnev (2004) studied the linear and nonlinear oscillations of the vibrator and improved previous SDOF models for the vibrator-earth system by

adding a thin layer of earth under the base plate to the SDOF system. The simulation model proposed by Lebedev and Beresnev quantitatively described the nonlinearity of the contact between the base plate and the ground, near-field soil. They concluded that contact nonlinearity does not lead to dependence of wave travel times on the amplitude of the force applied to the ground.

Conventional drive signals used in the field are linear chirp sweeps. In this research, both chirp sweeps and fixed-sine drive signals were used. Fixed-sine drive signal is a predetermined sinusoidal signal with duration of a few cycles at a single frequency of the Vibroseis. Extensive and intensive studies have examined chirp sweeps as a source signal, but no source identification technique is found in the literature using the fixed-sine source wavelet as the vibrator source. The analysis of the fixed-sine source signature is presented in this work.

5.2 SOURCE SIGNATURE MODEL

A source-signature model for fixed-sine excitation based on the characteristic of the Vibroseis vibration is presented in this chapter. Using a fixed-sine excitation force signal as the drive signal greatly simplifies the identification of the Vibroseis source signature. By analyzing the characteristics of the far field velocity signal, the source signature is modeled and analytically identified through methods formulated in this work.

Regardless of the complication posed by the nonlinear near-field effect and the interaction of the vibrator system, the far-field displacement and velocity are distinguished by a sinusoidal excitation of a SDOF system (see Figure 5.2). This is based on observation of the filtered far-field signals, and verified by spectral match in later chapters. However, this source signature model does not require that the vibrator-earth system be a SDOF system. The vibrator-earth system may be much complicated than a SDOF system, but its far-field signals coincide with the responses to a SDOF system.

Hence, the far-field signals can be regarded as generated from an equivalent SDOF system. The source signature is back-calculated directly from the measured far-field displacement or velocity signals instead of from any assumed models of the true ground force.

In this chapter, the source signature model for displacement is introduced as a background for the normalized source signatures of displacement, velocity and acceleration in next chapter.

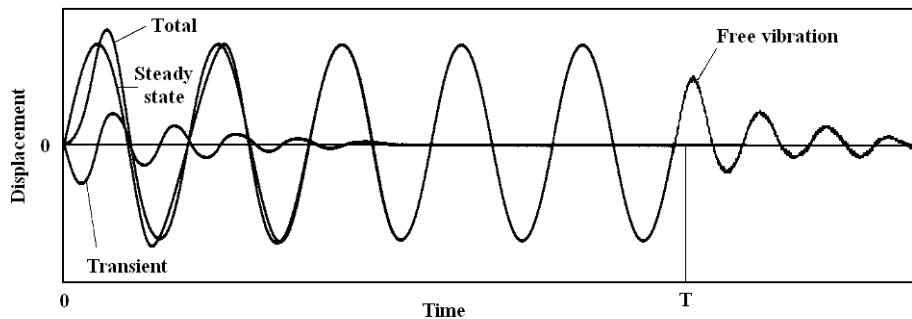


Figure 5.2 Displacement of a SDOF system under finite sinusoidal excitation (adapted from Kramer, 1996)

If the Heaviside step function or unit step function $U(t)$ (in Figure 5.3) is defined as:

$$U(t) = \begin{cases} 0 & t < 0 \\ 1 & t \geq 0 \end{cases}, \quad (5.1)$$

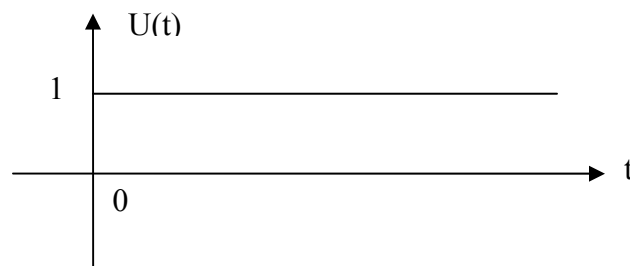


Figure 5.3 Heaviside step function

then the sinusoidal excitation of a SDOF system is

$$m\ddot{u} + c\dot{u} + ku = [U(t) - U(t-T)]Q \sin(\omega t + \psi) \quad (5.2)$$

where: m is the mass of the system, u is the displacement of the mass, c is the damping, and k is the stiffness. Q is the constant excitation force amplitude, ω is the sinusoidal excitation frequency, ψ is the initial phase of excitation and T is the duration of the excitation force. T is exclusively used to denote the excitation duration, which can be a whole number of cycles of the drive signal, or any time interval. The factor $[U(t) - U(t-T)]$ denotes that the excitation duration is from $t = 0$ to $t = T$. A signal that exists significantly only for a finite time interval is called a wavelet. The key feature of a source signal is called a source signature which refers to the solution to Equation (5.2) in this work.

To illustrate the source of singular frequencies for deconvolution discussed in Chapter 7, the rectangular pulse $P(t)$ as shown in Figure 5.4 is also used as an alternative way to present a finite time interval $[U(t) - U(t-T)]$. This rectangular pulse $P(t)$ is defined as:

$$P(t) = U\left(t + \frac{T}{2}\right) - U\left(t - \frac{T}{2}\right) = \begin{cases} 0 & |t| > \frac{T}{2} \\ 1 & |t| \leq \frac{T}{2} \end{cases} \quad (5.3)$$

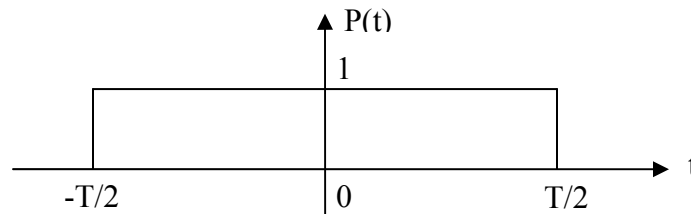


Figure 5.4 Rectangular pulse

Shifting a half duration (or $\frac{T}{2}$) to the right for the rectangular pulse in Figure 5.4 results in a causal pulse defined by

$$P(t - \frac{T}{2}) = U(t) - U(t - T) = \begin{cases} 0 & t < 0 \text{ or } t > T \\ 1 & \text{otherwise} \end{cases} \quad (5.4)$$

and shown in Figure 5.5.

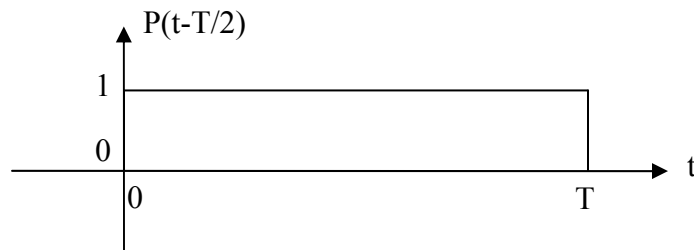


Figure 5.5 Causal rectangular pulse

The use of rectangular pulse instead of step function for Equation (5.2) gives

$$m\ddot{u} + c\dot{u} + ku = P(t - \frac{T}{2})Q \sin(\omega t + \psi) . \quad (5.5)$$

Equation (5.5) consists of two equations: the damped forced vibration described by Equation (5.6) and the damped free vibration described by Equation (5.7).

$$m\ddot{u} + c\dot{u} + ku = Q \sin(\omega t + \psi) \quad (0 \leq t \leq T) \quad (5.6)$$

$$m\ddot{u} + c\dot{u} + ku = 0 \quad (t > T) \quad (5.7)$$

The solution of Equation (5.6) without time domain restraints is the superposition of the particular solution, $u_p(t)$, for the steady-state vibration and the complementary solution, $u_c(t)$, for the transient vibration. Figure 5.6 illustrates their relative relationship, where $u_I(t)$ and $u_{II}(t)$ denote the corresponding time restraint equivalents to $u_p(t)$ and $u_c(t)$, respectively, and $u_{III}(t)$ denotes the solution to Equation (5.7). As shown in Figure 5.6, the source signature is the superposition of the subsequent three vibrations,

namely, the harmonic vibration, the transient vibration and the free vibration. For convenience, three wavelets are named after the vibrations: the sinusoidal wavelet, the transient wavelet, and the trailing wavelet.

The sinusoidal wavelet corresponds to the sinusoidal excitation force. It is a single frequency sine wave but truncated to the excitation duration T . The frequency of the sinusoidal wavelet is equal to the excitation frequency.

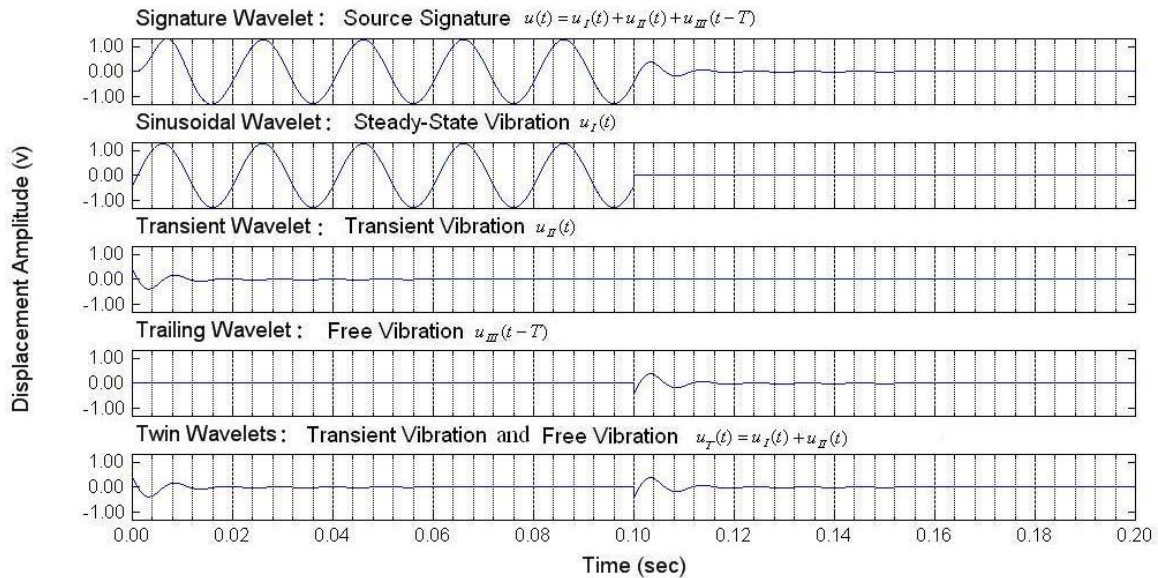


Figure 5.6 Source signature and its wavelets (excitation frequency 50 Hz, natural frequency 100 Hz, duration 0.1 sec, damping ratio 25%)

The transient wavelet is the transient response of the system. The trailing wavelet is the damped free vibration of the system. Both the transient and the trailing wavelets have the same carrier frequency, which is the damped frequency of the vibrator-earth system. For convenience, the transient and trailing wavelet as a whole is called the twin wavelets.

If a wavelet has only one single carrier frequency, it is called a pure wavelet. Both the sinusoidal wavelets and the twin wavelets are pure wavelets of different carrier

frequencies. When the carrier frequencies of the sinusoidal wavelet and the twin wavelets are equal, the combination of the two pure wavelets is termed a U-wavelet herein, which is also a pure wavelet but the union of the sinusoidal wavelet and the twin wavelets. Each pure wavelet has a single carrier frequency. The advantage of pure wavelets is that there is no dispersion within a wavelet because each pure wavelet carries only one frequency. The frequency content of a pure wavelet remains stable during propagation. It is subject to amplitude attenuation. The envelope shape of each pure wavelet also remains relatively stable during propagation, especially for the sinusoidal wavelet.

5.3 DAMPED FORCED VIBRATION

The undamped natural circular frequency, ω_0 , the damping ratio, ξ , the damped natural circular frequency, ω_d , and tuning ratio, β , are defined for a SDOF system as (Kramer, 1996; Chopra, 1995):

$$\omega_0 = \sqrt{\frac{k}{m}} \quad (5.8)$$

$$\xi = \frac{c}{2m\omega_0} \quad (5.9)$$

$$\omega_d = \omega_0 \sqrt{1 - \xi^2} \quad (5.10)$$

$$\beta = \frac{\omega}{\omega_0} \quad (5.11)$$

After dividing by m and using the relationships expressed in Equations (5.8) and (5.9), Equation (5.6) becomes:

$$\ddot{u} + 2\xi\omega_0\dot{u} + \omega_0^2u = \frac{Q}{m}\sin(\omega t + \psi). \quad (5.12)$$

5.2.1 Solution of steady-state vibration

The particular solution of Equation (5.12) is:

$$u_p(t) = C_1 \sin(\omega t - \varphi) + C_2 \cos(\omega t - \varphi), \quad (5.13)$$

where: C_1 , C_2 and φ are constants to be determined.

$$\dot{u}_p(t) = C_1 \omega \cos(\omega t - \varphi) - C_2 \omega \sin(\omega t - \varphi), \quad (5.14)$$

$$\ddot{u}_p(t) = -C_1 \omega^2 \sin(\omega t - \varphi) - C_2 \omega^2 \cos(\omega t - \varphi), \quad (5.15)$$

By using $u = u_p(t)$ and substituting Equations (5.13), (5.14) and (5.15) into Equation (5.12), one obtains:

$$\begin{aligned} & (C_1 \omega_0^2 - C_1 \omega^2 - 2\xi \omega_0 \omega C_2) \sin(\omega t - \varphi) \\ & + (C_2 \omega_0^2 - C_2 \omega^2 + 2\xi \omega_0 \omega C_1) \cos(\omega t - \varphi) = \frac{Q}{m} \sin(\omega t + \psi) \end{aligned} \quad (5.16)$$

At the instances where $\omega t - \varphi = n\pi$ (n is any integer), one obtains:

$$\sin(\omega t - \varphi) = 0, \quad (5.17)$$

$$\cos(\omega t - \varphi) = (-1)^n, \quad (5.18)$$

and $\sin(\omega t + \psi) = (-1)^n \sin(\varphi + \psi) \quad (5.19)$

By substituting Equations (5.17) through (5.19) into Equation (5.16), one obtains:

$$C_2 \omega_0^2 - C_2 \omega^2 + 2\xi \omega_0 \omega C_1 = \frac{Q}{m} \sin(\varphi + \psi) \quad (5.20)$$

At the instances where $\omega t - \varphi = n\pi + \frac{\pi}{2}$ (n is any integer), one obtains:

$$\sin(\omega t - \varphi) = (-1)^n, \quad (5.21)$$

$$\cos(\omega t - \varphi) = 0, \quad (5.22)$$

and $\sin \omega t = (-1)^n \cos(\varphi + \psi) \quad (5.23)$

By substituting Equations (5.21) through (5.23) into Equation (5.16), one obtains:

$$C_1\omega_0^2 - C_1\varpi^2 - 2\xi\omega_0\varpi C_2 = \frac{Q}{m} \cos(\varphi + \psi) \quad (5.24)$$

Combination of the Equation (5.20) and (5.24) yields:

$$C_1 = \frac{Q}{m} \frac{(2\xi\omega_0\varpi) \sin(\varphi + \psi) + (\omega_0^2 - \varpi^2) \cos(\varphi + \psi)}{(2\xi\omega_0\varpi)^2 + (\omega_0^2 - \varpi^2)^2} \quad (5.25)$$

and

$$C_2 = \frac{Q}{m} \frac{(-2\xi\omega_0\varpi) \cos(\varphi + \psi) + (\omega_0^2 - \varpi^2) \sin(\varphi + \psi)}{(2\xi\omega_0\varpi)^2 + (\omega_0^2 - \varpi^2)^2} \quad (5.26)$$

The use of Equations (5.8) and (5.11) simplifies Equations (5.25) and (5.26) as:

$$C_1 = \frac{Q}{k} \frac{(1 - \beta^2) \cos(\varphi + \psi) + 2\xi\beta \sin(\varphi + \psi)}{(1 - \beta^2)^2 + (2\xi\beta)^2} \quad (5.27)$$

and

$$C_2 = \frac{Q}{k} \frac{(1 - \beta^2) \sin(\varphi + \psi) - 2\xi\beta \cos(\varphi + \psi)}{(1 - \beta^2)^2 + (2\xi\beta)^2} \quad (5.28)$$

Equation (5.13) becomes:

$$u_p(t) = \frac{Q}{k} \frac{1}{(1 - \beta^2)^2 + (2\xi\beta)^2} [(1 - \beta^2) \sin(\varpi t + \psi) - 2\xi\beta \cos(\varpi t + \psi)] \quad (5.29)$$

The constant φ does not appear in Equation (5.29), which implies the phase shift φ can be arbitrary. Without loss of generality, by assuming $\varphi = 0$ in the Equations (5.13), (5.27) and (5.28), one obtains the particular solution as:

$$u_p(t) = C_1 \sin \varpi t + C_2 \cos \varpi t \quad (5.30)$$

where

$$C_1 = \frac{Q}{k} \frac{(1 - \beta^2) \cos \psi + 2\xi\beta \sin \psi}{(1 - \beta^2)^2 + (2\xi\beta)^2} \quad (5.31)$$

and

$$C_2 = \frac{Q}{k} \frac{(1 - \beta^2) \sin \psi - 2\xi\beta \cos \psi}{(1 - \beta^2)^2 + (2\xi\beta)^2} \quad (5.32)$$

Equation (5.30) can also be expressed as:

$$u_p(t) = A_I U(t) \sin[\varpi(t - t_I)] \quad (5.33)$$

where:

$$A_I = \frac{Q}{k\sqrt{(1 - \beta^2)^2 + (2\xi\beta)^2}} \quad (5.34)$$

$$t_I = \frac{1}{\varpi} [\arctan\left(\frac{2\xi\beta}{1 - \beta^2}\right) - \psi + n\pi], \quad n \text{ is integer} \quad (5.35)$$

The value of t_I in Equation (5.35) is not unique between $[-\pi, \pi]$ because computing the arc tangent for y/x in order to convert the Cartesian coordinates of a point (x, y) to polar coordinates, the value is such that the conventional arc tangent operator will yield

$$-\frac{\pi}{2} \leq \arctan\left(\frac{y}{x}\right) \leq \frac{\pi}{2}. \quad (5.36)$$

The unique conversion from the Cartesian coordinates of a point (x, y) to the polar coordinates results in a new function $\arctan 2(y, x)$ which yields:

$$-\pi \leq \arctan 2(y, x) \leq \pi \quad (5.37)$$

Equation (5.35) thus becomes:

$$t_I = \frac{1}{\varpi} [\arctan 2(2\xi\beta, 1 - \beta^2) - \psi] \quad (5.38)$$

The drive signal determined by a sine wave in practice lasts a finite time interval T . T is typically a whole number of cycles of the exciting sinusoidal function.

The displacement function, $u_I(t)$, denotes the steady-state motion of a finite time interval, which is truncated from $u_p(t)$ in Equation (5.33). The displacement function, $u_I(t)$, is called the sinusoidal wavelet:

$$\begin{aligned} u_I(t) &= u_p(t)[U(t) - U(t - T)] \\ &= A_I[U(t) - U(t - T)]\sin[\varpi(t - t_I)] \end{aligned} \quad (5.39)$$

For the sinusoidal wavelet to start at zero amplitude when $t = 0$, t_i must be zero in Equation (5.39). Letting $t_i = 0$ in Equation (5.38) gives

$$\psi = \arctan 2(2\xi\beta, 1 - \beta^2) \quad (5.40)$$

Therefore, the sinusoidal wavelet (not the total motion) starts at zero amplitude if and only if the initial phase, ψ , of the excitation force satisfies equation (5.40). However, a vibratory source is supposed to always start from static state or zero initial force, that is, at $t = 0$, the following is true:

$$\psi = 0 \quad (5.41)$$

Substituting Equation (5.41) to Equations (5.31) and (5.32) leads to (Chopra, 1995):

$$C_1 = \frac{Q}{k} \frac{1 - \beta^2}{(1 - \beta^2)^2 + (2\xi\beta)^2} \quad (5.42)$$

$$C_2 = \frac{Q}{k} \frac{-2\xi\beta}{(1 - \beta^2)^2 + (2\xi\beta)^2} \quad (5.43)$$

5.2.2 Solution of transient vibration

The complementary solution of Equation (5.12) is:

$$u_c(t) = e^{-\xi\omega_0 t} (C_3 \sin \omega_d t + C_4 \cos \omega_d t), \quad (5.44)$$

where: C_3 and C_4 are coefficients subject to initial conditions of the complete solution of forced vibration Equation (5.12). Equation (5.12) can be obtained by combining the particular and complementary solutions, or:

$$u_f(t) = u_p(t) + u_c(t). \quad (5.45)$$

Using Equations (5.30) and (5.44), the following is obtained:

$$u_f(t) = C_1 \sin \omega t + C_2 \cos \omega t + e^{-\xi\omega_0 t} (C_3 \sin \omega_d t + C_4 \cos \omega_d t), \quad (5.46)$$

where: C_1 and C_2 are given by (5.31) and (5.32), respectively.

During each test, T-Rex starts from zero initial displacement and zero initial velocity. Substituting $t = 0$ and $u_f(0) = 0$ into Equation (5.46) provides $C_4 = -C_2$ or

$$C_4 = \frac{Q}{k} \frac{2\xi\beta \cos\psi - (1 - \beta^2) \sin\psi}{(1 - \beta^2)^2 + (2\xi\beta)^2} \quad (5.47)$$

The velocity solution can be obtained from Equation (5.46):

$$\begin{aligned} \dot{u}_f(t) = & \varpi(C_1 \cos \varpi t - C_2 \sin \varpi t) \\ & + \omega_d e^{-\xi\omega_0 t} (C_3 \cos \omega_d t - C_4 \sin \omega_d t) \\ & - \xi\omega_0 e^{-\xi\omega_0 t} (C_3 \sin \omega_d t + C_4 \cos \omega_d t) \end{aligned} \quad (5.48)$$

Substituting $t = 0$ and $\dot{u}_f(0) = 0$ into Equation (5.48) obtains:

$$C_3 = \frac{\xi\omega_0}{\omega_d} C_4 - \frac{\varpi}{\omega_d} C_1 \quad (5.49)$$

Equations (5.31) and (5.47) are used to obtain:

$$C_3 = \frac{Q}{k} \frac{1}{\sqrt{1 - \xi^2}} \frac{\beta(\beta^2 + 2\xi^2 - 1) \cos\psi - \xi(1 + \beta^2) \sin\psi}{(1 - \beta^2)^2 + (2\xi\beta)^2} \quad (5.50)$$

when $\psi = 0$:

$$C_3 = \frac{Q}{k} \frac{\varpi}{\omega_d} \frac{\beta^2 + 2\xi^2 - 1}{(1 - \beta^2)^2 + (2\xi\beta)^2} \quad (5.51)$$

The transient motion Equation (5.44) becomes:

$$\begin{aligned} u_c(t) = & \frac{Q}{k} \frac{1}{(1 - \beta^2)^2 + (2\xi\beta)^2} e^{-\xi\omega_0 t} \\ & \cdot \left\{ \frac{\omega_0}{\omega_d} [\beta(\beta^2 + 2\xi^2 - 1) \cos\psi - \xi(1 + \beta^2) \sin\psi] \sin \omega_d t \right. \\ & \left. + [2\xi\beta \cos\psi - (1 - \beta^2) \sin\psi] \cos \omega_d t \right\} \end{aligned} \quad (5.52)$$

Equation (5.52) can be expressed as:

$$u_c(t) = A_{II} e^{-\xi\omega_0 t} U(t) \sin[\omega_d(t - t_{II})] \quad (5.53)$$

$$A_{II} = \sqrt{C_3^2 + C_4^2} \quad (5.54)$$

$$t_{II} = \frac{1}{\omega_d} \arctan 2(-C_4, C_3) \quad (5.55)$$

Where: C_3 and C_4 are determined from Equations (5.50) and (5.47), respectively.

when $\psi = 0$, Equation (5.52) becomes:

$$u_c(t) = \frac{Q}{k} \frac{1}{(1-\beta^2)^2 + (2\xi\beta)^2} e^{-\xi\omega_0 t} \cdot \left[\frac{\overline{\omega}}{\omega_d} (\beta^2 + 2\xi^2 - 1) \sin \omega_d t + 2\xi\beta \cos \omega_d t \right] \quad (5.56)$$

And Equations (5.54) and (5.55) becomes:

$$A_{II} = \frac{Q}{k} \sqrt{\frac{(\frac{\overline{\omega}}{\omega_d})^2 (\beta^2 + 2\xi^2 - 1)^2 + (2\xi\beta)^2}{(1-\beta^2)^2 + (2\xi\beta)^2}} \quad (5.57)$$

$$\text{and} \quad t_{II} = \frac{1}{\omega_d} \arctan 2[-2\xi\beta, \frac{\overline{\omega}}{\omega_d} (\beta^2 + 2\xi^2 - 1)] \quad (5.58)$$

The transient motion of finite time interval, $u_{II}(t)$, is a truncated sine wave from $u_c(t)$.

$u_{II}(t)$ is called transient wavelet:

$$\begin{aligned} u_{II}(t) &= u_c(t)[U(t) - U(t-T)] \\ &= A_{II} e^{-\xi\omega_0 t} [U(t) - U(t-T)] \sin[\omega_d(t - t_{II})] \end{aligned} \quad (5.59)$$

The actual transient motion continues after the termination of the excitation force at $t = T$.

The part of the transient motion after time T is called residual transient motion, $u_{II}^{(r)}(t)$,

which is:

$$u_{II}^{(r)}(t) = u_c(t)U(t-T) = A_{II} e^{-\xi\omega_0 t} U(t-T) \sin[\omega_d(t - t_{II})] \quad (5.60)$$

Clearly,

$$u_c(t) = u_{II}(t) + u_{II}^{(r)}(t) \quad (5.61)$$

5.2.3 Solution of damped forced vibration

The solution of the damped forced vibration Equation (5.12) is the superposition of the steady-state motion and the transient motion, or:

$$u_f(t) = u_p(t) + u_c(t). \quad (5.62)$$

The solution to the forced vibration with finite time interval excitation is

$$u_f(t) = u_I(t) + u_{II}(t) \quad (5.63)$$

5.4 DAMPED FREE VIBRATION

T-Rex motion during damped free vibration satisfies:

$$m\ddot{u} + c\dot{u} + ku = 0. \quad (5.64)$$

The solution to Equation (5.64) is similar to Equation (5.44), except that the coefficients C_3 and C_4 are no longer given by Equations (5.47) and (5.50) because of different initial conditions. To avoid confusion, C_5 and C_6 are used instead as follows:

$$u_{III}(t) = e^{-\xi\omega_0 t} U(t) (C_5 \sin \omega_d t + C_6 \cos \omega_d t) \quad (5.65)$$

$$\begin{aligned} \dot{u}_{III}(t) &= \omega_d e^{-\xi\omega_0 t} U(t) (C_5 \cos \omega_d t - C_6 \sin \omega_d t) \\ &\quad - \xi\omega_0 e^{-\xi\omega_0 t} U(t) (C_5 \sin \omega_d t + C_6 \cos \omega_d t) \end{aligned} \quad (5.66)$$

Considering that the damped free vibration follows immediately after the forced vibration, the time origin of $u_{III}(t)$ should be at time T . On the other hand, the initial condition is bound by the steady-state at time $t = T$ when damped free vibration starts with initial displacement u_0 and initial velocity \dot{u}_0 at $t = T$ as follows:

$$\begin{aligned} u_0 &= u_{III}(0) = u_p(T) + u_c(T) \\ &= A_I \sin[\varpi(T - t_I)] + A_{II} e^{-\xi\omega_0 T} \sin[\omega_d(T - t_{II})] \end{aligned} \quad (5.67)$$

$$\begin{aligned} \dot{u}_0 &= \dot{u}_{III}(0) = \dot{u}_p(T) + \dot{u}_c(T) \\ &= A_I \varpi \cos[\varpi(T - t_I)] \\ &\quad + A_{II} e^{-\xi\omega_0 T} \{ \omega_d \cos[\omega_d(T - t_{II})] - \xi\omega_0 \sin[\omega_d(T - t_{II})] \} \end{aligned} \quad (5.68)$$

Substituting Equations (5.67) and (5.68) into Equations (5.65) and (5.66) gives:

$$C_5 = \frac{\dot{u}_0 + \xi\omega_0 u_0}{\omega_d}, \quad C_6 = u_0 \quad (5.69)$$

The damped free vibration solution is:

$$u_{III}(t) = e^{-\xi\omega_0 t} U(t) \left(\frac{\dot{u}_0 + \xi\omega_0 u_0}{\omega_d} \sin \omega_d t + u_0 \cos \omega_d t \right) \quad (5.70)$$

An alternative way to present (5.70) is:

$$u_{III}(t) = A_{III} e^{-\xi\omega_0 t} U(t) \sin[\omega_d(t - t_{III})] \quad (5.71)$$

$$A_{III} = \sqrt{\left(\frac{\dot{u}_0 + \xi\omega_0 u_0}{\omega_d} \right)^2 + u_0^2} \quad (5.72)$$

$$t_{III} = \frac{1}{\omega_d} \arctan 2 \left(-u_0, \frac{\dot{u}_0 + \xi\omega_0 u_0}{\omega_d} \right) \quad (5.73)$$

In Equation (5.71), $u_{III}(t)$ is called a trailing wavelet. $u_{III}(t)$ actually starts right after the excitation duration T . Hence $u_{III}(t - T)$ is also called a trailing wavelet.

The initial condition of the trailing wavelet is comprised of two parts: the first part corresponding to the termination of the steady-state force, which is called the steady-state transitional motion $u_{III}^{(s)}(t)$ herein, and the second part corresponding to the continuation of the transient motion, which is the residual transient motion. The first part includes:

$$u_0^{(s)} = u_{III}^{(s)}(0) = u_p(T) = A_I \sin[\varpi(T - t_I)], \quad (5.74)$$

and
$$\dot{u}_0^{(s)} = \dot{u}_{III}^{(s)}(0) = \dot{u}_p(T) = A_I \varpi \cos[\varpi(T - t_I)]. \quad (5.75)$$

Substituting Equations (5.74) and (5.75) into Equations (5.65) and (5.66) gives:

$$C_5 = \frac{\dot{u}_0^{(s)} + \xi\omega_0 u_0^{(s)}}{\omega_d}, \quad C_6 = u_0^{(s)} \quad (5.76)$$

The steady-state transitional motion is:

$$u_{III}^{(s)}(t) = e^{-\xi\omega_0 t} U(t) \left(\frac{\dot{u}_0^{(s)} + \xi\omega_0 u_0^{(s)}}{\omega_d} \sin \omega_d t + u_0^{(s)} \cos \omega_d t \right) \quad (5.77)$$

As an alternative to (5.70), the trailing wavelet $u_{III}(t)$ is also the superposition of the residual transient motion $u_{II}^{(r)}(t)$ defined in Equation (5.60), and the steady-state transitional motion $u_{III}^{(s)}(t)$ defined in Equation (5.77). The trailing wavelet $u_{III}(t)$ can be expressed as:

$$u_{III}(t) = u_{II}^{(r)}(t) + u_{III}^{(s)}(t - T) \quad (5.78)$$

The transient wavelet and the trailing wavelet always occur subsequently, so that the superposition of the transient wavelet $u_{II}(t)$ and the trailing wavelet $u_{III}(t - T)$ is called twin wavelets and expressed as:

$$u_T(t) = u_{II}(t) + u_{III}(t - T) \quad (5.79)$$

The same twin wavelets can also be regarded as the superposition of the transient motion and the steady-state transitional motion:

$$u_T(t) = u_c(t) + u_{III}^{(s)}(t - T) \quad (5.80)$$

5.5 SOURCE SIGNATURE

A high quality source signal is a signal with the least waveform distortion and least undesired concurrent signals. Analysis of the source signature characteristics improves the source signal in the field test. A source signature is defined by:

$$u(t) = u_I(t) + u_{II}(t) + u_{III}(t - T), \quad (5.81)$$

or

$$u(t) = u_I(t) + u_c(t) + u_{III}^{(s)}(t - T), \quad (5.82)$$

where: $u_I(t)$, $u_{II}(t)$ and $u_{III}(t)$ are defined by Equations (5.39), (5.59) and (5.71), respectively. $u_c(t)$ and $u_{III}^{(s)}(t - T)$ are defined by Equations (5.53) and (5.77), respectively. The source signature start time is assumed to be always at time zero. Source

signature Equations (5.81) and (5.82) are identical. By default, the Equation (5.81) is implied as the source signature.

The first term of the source signature is the sinusoidal wavelet:

$$u(t) = u_I(t) \quad (5.83)$$

The second term of the source signature is the transient wavelet:

$$u(t) = u_{II}(t) \quad (5.84)$$

The third term of the source signature is the trailing wavelet:

$$u(t) = u_{III}(t) \text{ or } u(t-T) = u_{III}(t-T) \quad (5.85)$$

The combination of the second and the third terms is the twin wavelets:

$$u(t) = u_{II}(t) + u_{III}(t-T) \quad (5.86)$$

When the sinusoidal and twin wavelets have the same carrier frequency, the source signature is called the U-wavelet:

$$\begin{aligned} u(t) = & A_I [U(t) - U(t-T)] \sin[\omega_d(t-t_I)] \\ & + A_{II} e^{-\xi\omega_0 t} [U(t) - U(t-T)] \sin[\omega_d(t-t_{II})] \\ & + A_{III} e^{-\xi\omega_0(t-T)} U(t-T) \sin[\omega_d(t-T-t_{III})] \end{aligned} \quad (5.87)$$

When the sinusoidal and twin wavelets have different frequencies, the source signature is characterized by two wavelets separately, namely the sinusoidal wavelet and the twin wavelets.

A source signal can be a source signature with any or all transformations such as amplitude scaling, frequency scaling, time or phase shifting. Considering that the main concern of velocity profiling is in the relative travel time, for convenience, the source signal is regarded as simply the shifted version of the source signature. For example, a source signal corresponding to Equation (5.81) starting at time t_0 is:

$$w(t) = u(t-t_0) \quad (5.88)$$

where t_0 is the actual initial shaking time of the recorded time series. It can be negative, zero or positive depending on what time origin is configured to use for the time series when recording. Most of the tests were recorded from time zero. However, the drive signals for some tests started at negative or positive time values.

Actually only relative travel times between traces are used regardless of the value of the source signal initial time (t_0). For convenience, assume $t_0 = 0$ if not specifically redefined.

The source signature in Equation (5.81) or Equation (5.82) is strongly correlated to the damping ratio and natural frequency of the vibrator-earth system. Figures 5.7 and 5.8 show how the damping ratio significantly affects the quality of the source signature when other conditions are the same. For low system damping in Figure 5.7, the source signature with a damping ratio 5% has a much longer trailing wavelet than with a damping ratio 25%. The “Transient Motion” in Figure 5.7 and other figures later in this chapter refers to $u_c(t)$ in Equation (5.82). The part of “Transient Motion” before time T, which corresponds to 0 to 0.1 sec in Figure 5.7, is called the “Transient wavelet” denoted by $u_H(t)$ in Equation (5.59). The rest part of “Transient Motion” after time T is called the residual transient motion, $u_H^{(r)}(t)$ defined by Equation (5.60).

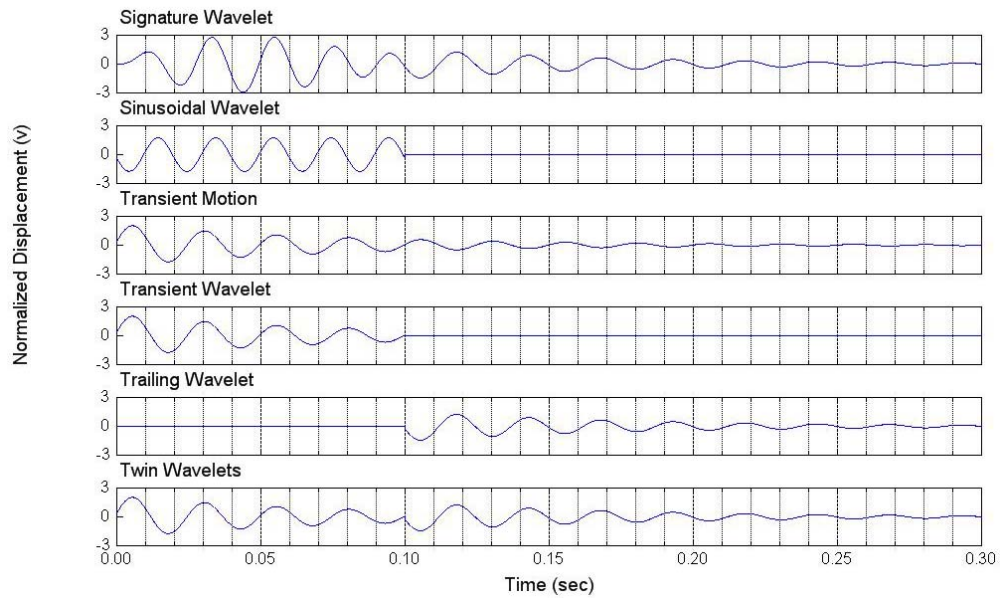


Figure 5.7 Source signature A (excitation frequency 50 Hz, natural frequency 40 Hz, duration 0.1 sec, damping ratio 5%)

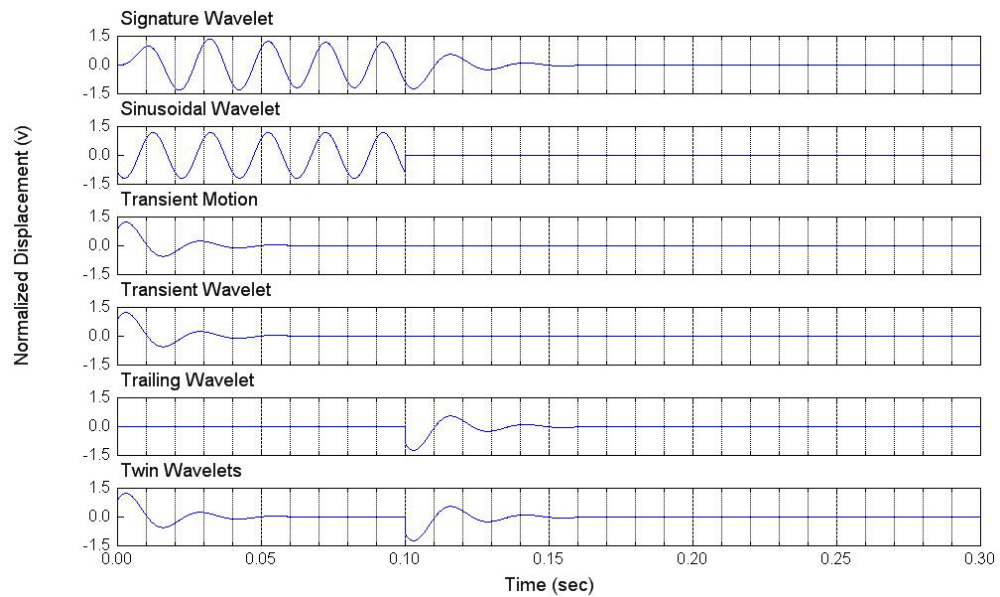


Figure 5.8 Source signature B (excitation frequency 50 Hz, natural frequency 40 Hz, duration 0.1 sec, damping ratio 25%)

Two initial conditions for the signature model should be clarified. As shown in Figure 5.7, the first initial condition is at the start-up of the test ($t = 0$). Both the sinusoidal wavelet and the transient wavelet may have initial displacements, but the sum of the two displacements should be zero, which is the initial condition of the vibration or the signature wavelet. The second initial condition is at the end of the excitation ($t = T$) when the free vibration starts. The initial condition of the free vibration comprises of two parts: the contribution of the steady-state vibration and that of the transient vibration. If the transient vibration is considered as continuing after the end of excitation, the free vibration wavelet should exclude the contribution of the transient vibration. The actual transient vibration continues anyway after the end of excitation. However, the transient vibration merges into the free vibration. There are two approaches to define the wavelets. First, to avoid the truncation of the transient vibration into two time intervals, as a compromise, the free vibration should be decomposed into two components: one corresponds to the transient vibration, and the other to the steady-state vibration. The approach only uses the free vibration caused by the termination of the steady-state vibration for trailing wavelet. The second approach is to avoid the decomposition of the free vibration into two components, but truncate the transient vibration into two segments separated at time T . Both approaches will result in the same twin wavelets, though the twin wavelets may not be smooth or even not continuous at time T .

Figures 5.9 and 5.10 demonstrate how the natural frequency of the vibrator-earth system can affect the quality of the source signature. The system with a higher natural frequency than the excitation frequency produces a better waveform shape than the system with the natural frequency of the system lower than the exciting frequency (Figure 5.9). The higher natural frequency leads to a higher damped natural frequency, which is the carrier frequency of the twin wavelets. As a result, the twin wavelets

propagate faster than the sinusoidal wavelet (Gupta, 1972). The first breaks of propagating waves are dominated by the undesired twin wavelets, and later at greater depths, are dominated by the sinusoidal wavelet due to attenuation and diminishing of the twin wavelets.

As long as there is a frequency difference between the sinusoidal wavelet and the twin wavelets, a relative time shift exists between them during propagation. The time shift will distort the waveforms associated with first breaks or first wave identifications. In order to avoid the frequency difference and the relative time shift, the excitation frequency should be equal to or close to the damped natural frequency. The earth underneath the base plate becomes softer and softer with each repetition of the tests at each depth so that the damping ratio of the vibrator-earth system steadily increases. Thus the excitation frequency should be accordingly adjusted.

These comparisons indicate that the best excitation frequency should be determined by the in-situ earth condition in order to generate a high-quality source signal. A method is proposed in Chapter 6 for field measurement of the natural frequency and damping ratio of the vibrator-earth system in the vicinity of the borehole.

The source signature corresponding to the velocity and acceleration records is discussed in Chapter 6.

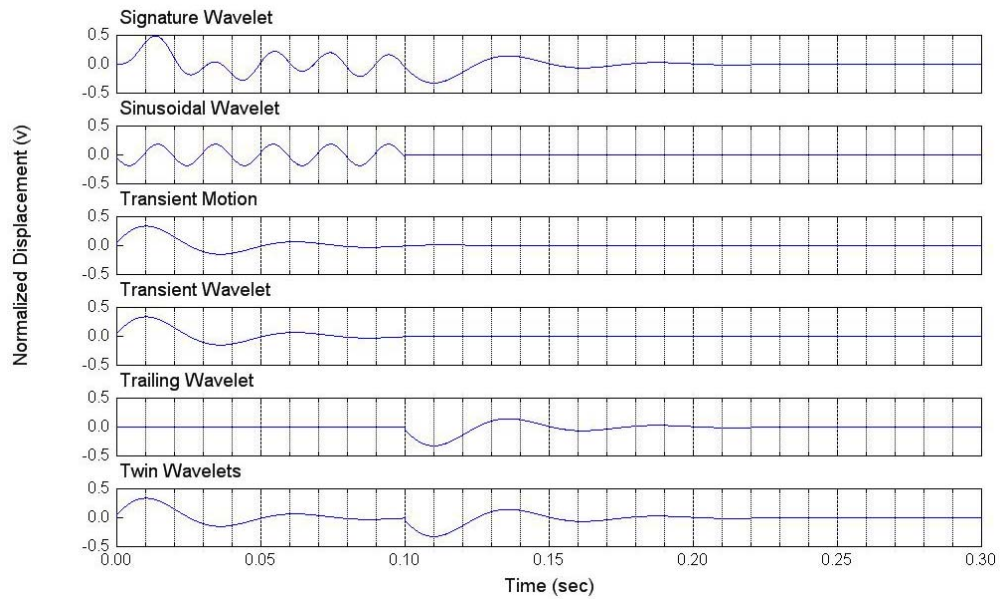


Figure 5.9 Source signature C (excitation frequency 50 Hz, natural frequency 20 Hz, duration 0.1 sec, damping ratio 25%)

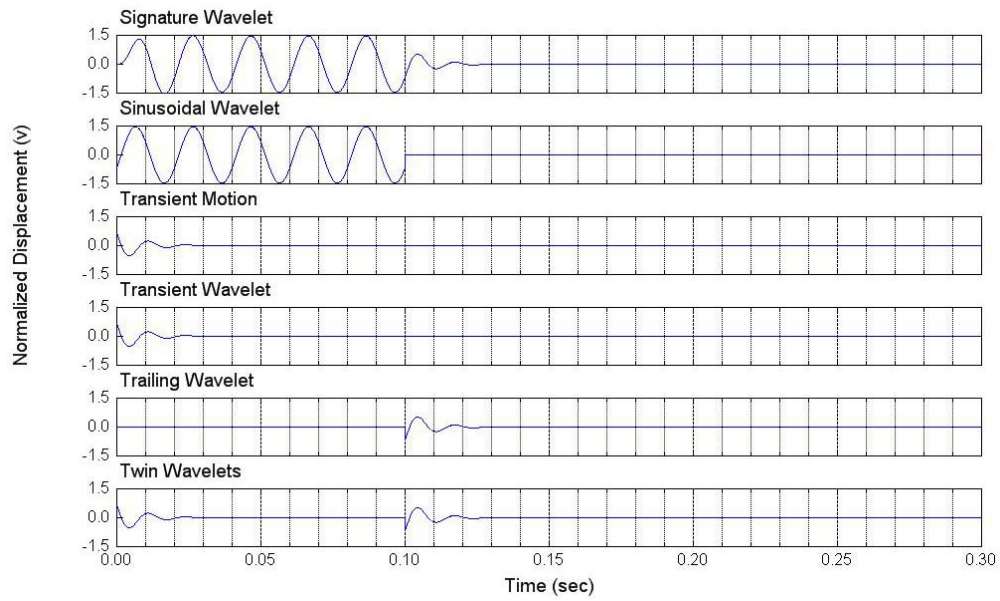


Figure 5.10 Source signature D (excitation frequency 50 Hz, natural frequency 80 Hz, duration 0.1 sec, damping ratio 25%)

5.6 FOURIER TRANSFORM OF SOURCE SIGNATURE

This section deals extensively with the Fourier integrals and their applications for deriving the frequency response of the source signature. Some of the basic equations (Equations 5.89 to 5.93) discussed in Papoulis (1962) are presented here as a reference for ongoing derivations. All the time series and frequency series in integration herein, whether discrete or continuous, are understood to have finite energy (Boggess and Narcowich, 2001).

5.6.1 Basic equations for Fourier transform

The notation $\hat{F}\{\cdot\}$ is used throughout this work to denote the Fourier transform. For any time series $x(t)$, its Fourier transform $X(\omega)$ is the following:

$$X(\omega) = \hat{F}\{x(t)\} = \int_{-\infty}^{+\infty} x(t)e^{-j\omega t} dt . \quad (5.89)$$

The inverse Fourier transform is defined as:

$$x(t) = \hat{F}^{-1}\{X(\omega)\} = \frac{1}{2\pi} \int_{-\infty}^{+\infty} X(\omega)e^{j\omega t} d\omega , \quad (5.90)$$

where \hat{F}^{-1} denotes inverse Fourier transform.

A time delay t_0 for any time series $x(t)$ will result in a phase shift ωt_0 in the frequency domain, or:

$$\hat{F}\{x(t-t_0)\} = \hat{F}\{x(t)\}e^{-j\omega t_0} \quad (5.91)$$

If $h(t)$ is the convolution of $f(t)$ and $g(t)$, then the definition of convolution is:

$$h(t) = f(t) * g(t) = \int_{-\infty}^{+\infty} f(y)g(t-y)dy , \quad (5.92)$$

where the asterisk “*” denotes the convolution. Any asterisk in the place of an operator rather than a superscript denotes the convolution operation throughout the dissertation.

The Fourier transform of the product of any two functions $f(t)$ and $g(t)$ is the convolution of their Fourier transforms, as shown in Equation (5.93), where the dot “ \cdot ” (largely omitted) denotes a multiplication.

$$\hat{F}\{f(t) \cdot g(t)\} = \frac{1}{2\pi} \hat{F}\{f(t)\} * \hat{F}\{g(t)\}. \quad (5.93)$$

5.6.2 Fourier transform of sinusoidal wavelet

The sinusoidal wavelet $u_I(t)$ is the motion caused by the truncated harmonic excitation, which is divided into two parts, $u_{I,a}(t)$ and $u_{I,b}(t)$ as follows:

$$\begin{aligned} u_I(t) &= A_I[U(t) - U(t-T)]\sin[\varpi(t-t_I)] \\ &= A_I U(t)\sin[\varpi(t-t_I)] - A_I U(t-T)\sin[\varpi(t-t_I)] \\ &= u_{I,a}(t) - u_{I,b}(t) \end{aligned} \quad (5.94)$$

where:
$$u_{I,a}(t) = A_I U(t)\sin[\varpi(t-t_I)] \quad (5.95)$$

$$u_{I,b}(t) = A_I U(t-T)\sin[\varpi(t-t_I)] \quad (5.96)$$

The Fourier transform of Equation (5.94) thus can also be divided into two parts associated with Equations (5.95) and (5.96). The first part is the Fourier transform of Equation (5.95), or

$$\begin{aligned}
F_{I,a}(\omega) &= \hat{F}\{u_{I,a}(t)\} \\
&= \frac{A_I}{2\pi} \hat{F}\{U(t)\} * \hat{F}\{\sin[\varpi(t-t_I)]\} \\
&= \frac{A_I}{2\pi} \left\{ \frac{1}{j\omega} + \pi\delta(\omega) \right\} * \left\{ e^{-j\omega t_I} j\pi[\delta(\omega+\varpi) - \delta(\omega-\varpi)] \right\} \\
&= \frac{jA_I}{2} \int \left[\frac{1}{j(\omega-y)} + \pi\delta(\omega-y) \right] e^{-jy t_I} [\delta(y+\varpi) - \delta(y-\varpi)] dy \\
&= \frac{jA_I}{2} \left[\frac{e^{j\varpi t_I}}{j(\omega+\varpi)} - \frac{e^{-j\varpi t_I}}{j(\omega-\varpi)} \right] \\
&\quad + \frac{jA_I}{2} [\delta(\omega+\varpi)(e^{-j\omega t_I} + e^{j\varpi t_I}) - \delta(\omega-\varpi)(e^{-j\omega t_I} + e^{-j\varpi t_I})] \\
&= \frac{A_I}{\omega^2 - \varpi^2} [j\omega \sin(\varpi t_I) - \varpi \cos(\varpi t_I)] \\
&\quad + \frac{jA_I}{2} [\delta(\omega+\varpi)(e^{-j\omega t_I} + e^{j\varpi t_I}) - \delta(\omega-\varpi)(e^{-j\omega t_I} + e^{-j\varpi t_I})]
\end{aligned} \tag{5.97}$$

The second part is the Fourier transform of Equation (5.96), which can be obtained by converting Equation (5.96) into an equivalent format as Equation (5.95) and then using Equation (5.97). Let $\tau = t - T$ and substitute it into Equation (5.96), thereby obtaining

$$\begin{aligned}
u_{I,b}(\tau) &= u_{I,b}(t-T) \\
&= A_I U(t-T) \sin[\varpi(t-t_I)] \\
&= A_I U(\tau) \sin[\varpi(\tau - (t_I - T))]
\end{aligned} \tag{5.98}$$

The only difference between Equations (5.98) and (5.95) is the initial phase angle. Thus the two have the same format for spectrum as Equation (5.97), where t_I is replaced with $(t_I - T)$ as:

$$\begin{aligned}
F_{I,b}(\omega) &= \hat{F}\{u_{I,b}(\tau)\} \\
&= \frac{A_I}{2\pi} \hat{F}\{U(\tau)\} * \hat{F}\{\sin[\varpi(\tau - (t_I - T))]\} \\
&= \frac{A_I}{\omega^2 - \varpi^2} [j\omega \sin(\varpi(t_I - T)) - \varpi \cos(\varpi(t_I - T))] \\
&\quad + \frac{jA_I}{2} [\delta(\omega + \varpi)(e^{-j\omega(t_I - T)} + e^{j\varpi(t_I - T)}) \\
&\quad - \frac{jA_I}{2} [\delta(\omega - \varpi)(e^{-j\omega(t_I - T)} + e^{-j\varpi(t_I - T)})]
\end{aligned} \tag{5.99}$$

The spectrum of Equation (5.94) is the combination of the two parts:

$$\begin{aligned}
F_I(\omega) &= \hat{F}\{u_I(t)\} = \hat{F}\{u_{I,a}(t)\} - \hat{F}\{u_{I,b}(t)\} \\
&= F_{I,a}(\omega) - F_{I,b}(\omega) \\
&= \frac{A_I}{\omega^2 - \varpi^2} [j\omega \sin(\varpi t_I) - \varpi \cos(\varpi t_I)] \\
&\quad + \frac{jA_I}{2} [\delta(\omega + \varpi)(e^{-j\omega t_I} + e^{j\varpi t_I}) - \delta(\omega - \varpi)(e^{-j\omega t_I} + e^{-j\varpi t_I})] \\
&\quad - \frac{A_I}{\omega^2 - \varpi^2} [j\omega \sin(\varpi(t_I - T)) - \varpi \cos(\varpi(t_I - T))] \\
&\quad - \frac{jA_I}{2} [\delta(\omega + \varpi)(e^{-j\omega(t_I - T)} + e^{j\varpi(t_I - T)}) \\
&\quad \quad - \delta(\omega - \varpi)(e^{-j\omega(t_I - T)} + e^{-j\varpi(t_I - T)})]
\end{aligned} \tag{5.100}$$

where: $F_{I,a}(\omega)$ is defined by Equation (5.97), and $F_{I,b}(\omega)$ by Equation (5.99).

An alternative way to derive the Fourier transform of Equation (5.94) is using the rectangular pulse $P(t)$ in Figure 5.4 in place of $U(t)-U(t-T)$, which results in:

$$u_I(t) = A_I \sin[\varpi(t - t_I)]P(t - \frac{T}{2}). \tag{5.101}$$

The spectrum of the rectangular pulse $P(t)$ is called the sinc-function (Papoulis 1962), which is:

$$\hat{F}\{P(t)\} = \frac{2 \sin(\omega T / 2)}{\omega}, \tag{5.102}$$

$$\text{or} \quad \hat{F}\left\{P\left(t - \frac{T}{2}\right)\right\} = \frac{2 \sin(\omega T / 2)}{\omega} e^{-j\omega T / 2}, \quad (5.103)$$

The spectrum of Equation (5.101) is:

$$\begin{aligned} F_I(\omega) &= \hat{F}\{u_I(t)\} \\ &= \frac{1}{2\pi} \hat{F}\{A_I \sin[\varpi(t - t_I)]\} * \hat{F}\left\{P\left(t - \frac{T}{2}\right)\right\} \\ &= \frac{A_I}{2\pi} \{e^{-j\omega t_I} j\pi[\delta(\omega + \varpi) - \delta(\omega - \varpi)]\} * \left\{e^{-j\omega T / 2} \frac{2 \sin(\omega T / 2)}{\omega}\right\} \\ &= \frac{jA_I}{2} e^{-j\omega T / 2} \left\{e^{-j\varpi(T/2 - t_I)} \frac{\sin[(\omega + \varpi)T / 2]}{\omega + \varpi} \right. \\ &\quad \left. - e^{j\varpi(T/2 - t_I)} \frac{\sin[(\omega - \varpi)T / 2]}{\omega - \varpi}\right\} \end{aligned} \quad (5.104)$$

5.6.3 Fourier transform of transient wavelet

The transient motion in Equation (5.59) or:

$$u_{II}(t) = A_{II} e^{-\xi\omega_0 t} [U(t) - U(t - T)] \sin[\omega_d(t - t_{II})] \quad (5.105)$$

is the subtraction of the two parts shown in Equation (5.106). $u_c(t)$ is the vibration from time zero to infinity. In $u_{II}^{(r)}(t)$, the vibration starts from the end of excitation time T and goes until infinity. This can be expressed as:

$$\begin{aligned} u_{II}(t) &= A_{II} e^{-\xi\omega_0 t} [U(t) - U(t - T)] \sin[\omega_d(t - t_{II})] \\ &= A_{II} e^{-\xi\omega_0 t} U(t) \sin[\omega_d(t - t_{II})] \\ &\quad - A_{II} e^{-\xi\omega_0 t} U(t - T) \sin[\omega_d(t - t_{II})] \\ &= u_c(t) - u_{II}^{(r)}(t) \end{aligned} \quad (5.106)$$

where:

$$u_c(t) = A_{II} e^{-\xi\omega_0 t} U(t) \sin[\omega_d(t - t_{II})] \quad (5.107)$$

$$u_{II}^{(r)}(t) = A_{II} e^{-\xi\omega_0 t} U(t - T) \sin[\omega_d(t - t_{II})] \quad (5.108)$$

The Fourier transform of the transient vibration $u_{II}(t)$ is also the subtraction of the following two items:

$$\begin{aligned} F_{II}(\omega) &= \hat{F}\{u_c(t)\} - \hat{F}\{u_{II}^{(r)}(t)\} \\ &= F_{II,a}(\omega) - F_{II,b}(\omega) \end{aligned} \quad (5.109)$$

The first item of Equation (5.109) is Fourier transform of the whole transient vibration:

$$\begin{aligned} F_{II,a}(\omega) &= \hat{F}\{u_c(t)\} \\ &= \frac{A_{II}}{2\pi} \hat{F}\{e^{-\xi\omega_0 t} U(t)\} * \hat{F}\{\sin[\omega_d(t-t_{II})]\} \\ &= \frac{A_{II}}{2\pi} \left(\frac{1}{\xi\omega_0 + j\omega} \right) * \{e^{-j\omega t_{II}} j\pi[\delta(\omega + \omega_d) - \delta(\omega - \omega_d)]\} \\ &= \frac{jA_{II}}{2} \left\{ \int \frac{e^{-jy t_{II}} \delta(y + \omega_d)}{\xi\omega_0 + j(\omega - y)} dy - \int \frac{e^{-jy t_{II}} \delta(y - \omega_d)}{\xi\omega_0 + j(\omega - y)} dy \right\} \\ &= \frac{jA_{II}}{2} \left[\frac{e^{j\omega_d t_{II}}}{\xi\omega_0 + j(\omega + \omega_d)} - \frac{e^{-j\omega_d t_{II}}}{\xi\omega_0 + j(\omega - \omega_d)} \right] \end{aligned} \quad (5.110)$$

A correlation between the trailing vibration in Equation (5.107) and the complete vibration Equation (5.108) simplifies the second term. Let $\tau = t - T$ or $t = \tau + T$, then Equation (5.108) becomes:

$$\begin{aligned} u_{II}^{(r)}(t) &= A_{II} e^{-\xi\omega_0 t} U(t-T) \sin[\omega_d(t-t_{II})] \\ &= A_{II} e^{-\xi\omega_0(\tau+T)} U(\tau) \sin[\omega_d(\tau+T-t_{II})] \\ &= e^{-\xi\omega_0 T} A_{II} e^{-\xi\omega_0 \tau} U(\tau) \sin\{\omega_d[\tau - (t_{II} - T)]\} \\ &= e^{-\xi\omega_0 T} \bar{u}_c(\tau) \\ &= e^{-\xi\omega_0 T} \bar{u}_c(t-T) \end{aligned} \quad (5.111a)$$

$$\text{where:} \quad \bar{u}_c(\tau) = A_{II} e^{-\xi\omega_0 \tau} U(\tau) \sin\{\omega_d[\tau - (t_{II} - T)]\}. \quad (5.111b)$$

The only difference between $\bar{u}_c(t)$ and $u_c(t)$ is the T time shift of the sine function. As Equation (5.111a) indicates, the trailing vibration is an amplitude-scaled and time-shifted

version of the complete vibration. Following the same procedures as shown by Equation (5.110), one obtains:

$$\begin{aligned}
\bar{F}_{II,a}(\omega) &= \hat{F}\{\bar{u}_c(t)\} \\
&= \frac{A_{II}}{2\pi} \hat{F}\{e^{-\xi\omega_0 t} U(t)\} * \hat{F}\{\sin[\omega_d(t - (t_{II} - T))]\} \\
&= \frac{jA_{II}}{2} \left[\frac{e^{j\omega_d(t_{II} - T)}}{\xi\omega_0 + j(\omega + \omega_d)} - \frac{e^{-j\omega_d(t_{II} - T)}}{\xi\omega_0 + j(\omega - \omega_d)} \right]
\end{aligned} \tag{5.112}$$

The second item is obtained from Equations (5.111a) and (5.112) as:

$$\begin{aligned}
F_{II,b}(\omega) &= \hat{F}\{u_{II}^{(r)}(t)\} \\
&= e^{-\xi\omega_0 T} \hat{F}\{\bar{u}_c(t - T)\} \\
&= e^{-\xi\omega_0 T} e^{-j\omega T} \hat{F}\{\bar{u}_c(t)\} \\
&= e^{-\xi\omega_0 T} e^{-j\omega T} \bar{F}_{II,a}(\omega) \\
&= e^{-\xi\omega_0 T} e^{-j\omega T} \frac{jA_{II}}{2} \left[\frac{e^{j\omega_d(t_{II} - T)}}{\xi\omega_0 + j(\omega + \omega_d)} - \frac{e^{-j\omega_d(t_{II} - T)}}{\xi\omega_0 + j(\omega - \omega_d)} \right]
\end{aligned} \tag{5.113}$$

By substituting Equations (5.110) and (5.113) into Equation (5.109), the spectrum of the transient vibration becomes:

$$\begin{aligned}
F_{II}(\omega) &= F_{II,a}(\omega) - F_{II,b}(\omega) \\
&= \frac{jA_{II}}{2} \left[\frac{e^{j\omega_d t_{II}}}{\xi\omega_0 + j(\omega + \omega_d)} - \frac{e^{-j\omega_d t_{II}}}{\xi\omega_0 + j(\omega - \omega_d)} \right] \\
&\quad - e^{-\xi\omega_0 T} e^{-j\omega T} \frac{jA_{II}}{2} \left[\frac{e^{j\omega_d(t_{II} - T)}}{\xi\omega_0 + j(\omega + \omega_d)} - \frac{e^{-j\omega_d(t_{II} - T)}}{\xi\omega_0 + j(\omega - \omega_d)} \right]
\end{aligned} \tag{5.114}$$

5.6.4 Fourier transform of trailing wavelet

The Fourier transform of the free vibration Equation (5.71) is

$$F_{III}(\omega) = \hat{F}\{u_{III}(t)\} = \frac{jA_{III}}{2} \left[\frac{e^{j\omega_d t_{III}}}{\xi\omega_0 + j(\omega + \omega_d)} - \frac{e^{-j\omega_d t_{III}}}{\xi\omega_0 + j(\omega - \omega_d)} \right] \tag{5.115}$$

The trigonometric form of Equation (5.115) is:

$$F_{III}(\omega) = \hat{F}\{u_{III}(t)\} = A_{III} \frac{\omega_d \cos(\omega_d t_{III}) - (\xi\omega_0 + j\omega) \sin(\omega_d t_{III})}{(\xi\omega_0 + j\omega)^2 + \omega_d^2} \quad (5.116)$$

By accounting for the time shift T, one obtains:

$$\begin{aligned} F_{III,T}(\omega) &= \hat{F}\{u_{III}(t-T)\} = e^{-j\omega T} \hat{F}\{u_{III}(t)\} \\ &= \frac{jA_{III}}{2} e^{-j\omega T} \left[\frac{e^{j\omega_d t_{III}}}{\xi\omega_0 + j(\omega + \omega_d)} - \frac{e^{-j\omega_d t_{III}}}{\xi\omega_0 + j(\omega - \omega_d)} \right] \end{aligned} \quad (5.117)$$

If only consider the trailing vibration caused by the inertia of the sinusoidal (steady-state) wavelet $u_{III}^{(s)}(t)$, one obtains:

$$F_{III}^{(s)}(\omega) = \hat{F}\{u_{III}^{(s)}(t)\} \quad (5.118)$$

$$\text{and} \quad F_{III,T}^{(s)}(\omega) = \hat{F}\{u_{III}^{(s)}(t-T)\} \quad (5.119)$$

Equations (5.118) and (5.119) have exactly the same format as Equations (5.116) and (5.117), respectively.

5.6.5 Spectrum of the source signature

The spectrum of the source signature Equation (5.81) is:

$$\begin{aligned} F(\omega) &= \hat{F}\{u(t)\} \\ &= \hat{F}\{u_I(t)\} + \hat{F}\{u_{II}(t)\} + \hat{F}\{u_{III}(t-T)\} \end{aligned} \quad (5.120a)$$

The spectrum of the source signature Equation (5.82) is:

$$\begin{aligned} F(\omega) &= \hat{F}\{u(t)\} \\ &= \hat{F}\{u_I(t)\} + \hat{F}\{u_c(t)\} + \hat{F}\{u_{III}^{(s)}(t-T)\} \end{aligned} \quad (5.120b)$$

Equation (5.120a) can be written as:

$$F(\omega) = F_I(\omega) + F_{II}(\omega) + F_{III,T}(\omega) \quad (5.121a)$$

where: $F_I(\omega)$, $F_{II}(\omega)$, $F_{III,T}(\omega)$ are defined by Equations (5.104), (5.114) and (5.118), respectively.

Equation (5.120b) can be written as:

$$F(\omega) = F_I(\omega) + F_{II,a}(\omega) + F_{III,T}^{(s)}(\omega) \quad (5.121b)$$

where: $F_I(\omega)$, $F_{II,a}(\omega)$, $F_{III,T}^{(s)}(\omega)$ are defined by Equations (5.104), (5.110) and (5.119), respectively.

The use of twin wavelets defined in Equations (5.79) and (5.80) can combine the spectra of the source signature in Equations (5.121a) and (5.121b). If define the spectrum of the twin wavelets $F_{II,III}(\omega)$ as:

$$\begin{aligned} F_{II,III}(\omega) &= \hat{F}\{u_T(t)\} \\ &= F_{II}(\omega) + F_{III,T}(\omega) \\ &= F_{II,a}(\omega) + F_{III,T}^{(s)}(\omega) \end{aligned} \quad (5.122)$$

Then the spectrum of the source signature is:

$$F(\omega) = F_I(\omega) + F_{II,III}(\omega). \quad (5.123)$$

A source signal can exhibit any delay in the records as

$$w(t) = u(t - t_0). \quad (5.124)$$

The spectrum of the delayed source signal defined by Equation (5.122) is

$$\begin{aligned} W(\omega) &= \hat{F}\{w(t)\} \\ &= \hat{F}\{u(t - t_0)\} \\ &= e^{-j\omega t_0} \hat{F}\{u(t)\} \\ &= e^{-j\omega t_0} F(\omega) \end{aligned} \quad (5.125)$$

The spectra of source signatures corresponding to velocity and acceleration outputs are described in Chapter 6.

5.7 SUMMARY

The displacement solutions of a SDOF system under sinusoidal excitation in a finite time interval are derived in this chapter. This system is used to represent vibratory

source in deep downhole testing. However, Three wavelets corresponding to the three displacement solutions are defined as the components of the source signature. The successful derivations of the spectra of the three wavelets as well as the source signature confirm that the source signature is identifiable in the frequency domain as well as in the time domain. The analytical identification of the source signature advances the use of deterministic deconvolution for source wavelet extraction, which is an important technique to reduce waveform distortion.

As shown in Chapter 2, different frequencies may travel at different speeds due to velocity dispersion in anisotropic medium. One approach to improve signal quality is to reduce the frequency content in the source signature. Fixed-sine drive signal has much less velocity dispersion concern because of less frequency content. The waveform of the source signature produced by fixed-sine excitation varies with the frequency of the sinusoidal excitation and the damped natural frequency of the vibrator-earth system. For deep downhole testing, an optimal source excitation frequency can now be determined with this solution to give the best-quality source wavelet. This excitation frequency should be close to the in-situ damped natural frequency of the vibrator-earth system, otherwise it should be distinctly higher or lower to reduce waveform distortion. The excitation frequency should be higher than the damped natural frequency when wave identification method is used, in that the higher frequency travels faster than the lower one.

To decide the better excitation frequency to use, one must first measure locally the in-situ damped natural frequency. When the test is repeated, the earth beneath the vibrator could become softer, and the variation of in-situ damped natural frequency with time would change so that this frequency should also be tracked. Due to the different

values of the damped natural frequency for P- and S-wave shaking modes, different excitation frequencies should be applied to P- and S-wave vibration.

In this chapter, fundamental equations are presented for use in the next two chapters where normalized source signatures are identified and the wavelet response method is explored.

Chapter 6 Identification of Source Signature

6.1 INTRODUCTION

Ziolkowski (1980) defined a point source as a source whose maximum dimension is small compared with the shortest wavelength of the useful radiation it generates. Vibratory source is a point source in terms of his definition. His definition of the point source is in the space domain. For the purpose of differentiating between an impulsive point source and a point source with finite time duration of at least 100 ms, the former is herein called the impulsive source and the latter is called the durational source in this work.

Identification of source signature and extraction of source wavelet have a long history in the literature. Various assumptions were made to advance an impulse response for travel time analysis. This chapter introduces a deterministic source wavelet that is back calculated from the far-field signal recorded in the field test.

6.1.1 Impulsive source wavelet

The method used by Robinson (1957) and Rice (1962) requires that the impulse response be stationary, white and consist of a random sequence of impulses. The source wavelet must also be minimum-phase and have the same shape throughout the seismogram with no absorption. The critical reflection theorem (Fokkema et al, 1987) does not require assumptions about the distribution of the reflection coefficients, but it does require that critical reflections occur at the boundary of the lower half space under the stack of layers. Ziolkowski et al (1987) used this theorem for the extraction of the dynamite wavelet on real data.

6.1.2 Scalable source wavelet

Ziolkowski (1980) introduced a source scaling law for wavelet deconvolution from a point source in a homogeneous, isotropic medium. The source scaling law requires that two different seismograms be generated from each source-receiver pair with the source and the receiver remaining at the same locations. The source used to generate one seismogram is scaled to generate the second seismogram. The scaling relationship between the two source signatures permits the earth impulse response to be extracted from the seismograms without any of the usual assumptions about phases. The scaling law requires that the source elastic radiation possess spherical symmetry, such as a buried explosion or a single air or water gun. It does not apply to surface sources. The scaling law is unsuitable for application if the absorption is not convolutional or not approximated by a convolutional model.

6.1.3 Mixed-delay source wavelet

Tygel and Hubral (1987) studied transient waves in layered media from a pressure response for reflection seismogram at certain depths below the ground surface. Tygel et al (1991) employed evanescent wavefields of the point-source seismogram to extract a mixed-delay source wavelet. The researchers assumed that the seismic shot record describes the pressure, velocity, or amplitude response to a point source emanating from a horizontally layered acoustic medium. They used the plane-wave decomposition method, which transforms a point-source seismogram from a time-space domain into a frequency-ray parameter domain. The researchers made no assumptions about the velocity distribution in the layered medium. Critical reflections were not required for the extraction of source wavelets.

6.1.4 Source wavelet array

Loveridge et al (1984) used a marine source array and studied the effects of marine source array directivity on seismic data and source signature deconvolution. Loewenthal et al (1985) performed the 1-D acoustic wavelet estimation using an impedance type technique. The medium above the receivers as well as measurements of both field and normal derivatives were all assumed to be known. Based on analogous assumptions, Weglein and Secret (1990) presented a method of calculating the total wavelet of a point-source or point-source array for an arbitrary inhomogeneous multidimensional acoustic or elastic earth. This method relied only on the incident wave and effectively filtered the scattered energy from the integral. A surface integral over the data and its normal derivative were required in order to produce the wavelet estimation. The derivative of the field required two separate vertical samplings of the field by using an Eulerian approximation. The Lippmann-Schwinger equation and Green's theorem were used to determine the wavelet.

6.1.5 Source wavelet in this work

Based on the source signature derived from a modeled SDOF system in Chapter 5, an equivalent SDOF system is introduced in this chapter that is back calculated from the far-field signal. The far-field signal is correlated with the vibrator-earth system, but not necessarily identical to any of the directly measured signals from the vibrator or in the near field. Observation of both the vibrator and the far-field signals reveals that, even though any or all of the recorded signals directly from the vibrator are heavily distorted, the far-field signal is still featured and can be mapped by the motion of an ideal SDOF system. Most of the waveform distortions caused by the near-field effect do not survive in the far field.

Therefore, in this work all far-field signals are regarded as generated from the same equivalent SDOF system that is calibrated by a reference receiver in the proper far field but still reasonably near the vibrator. This approach does not affect the velocity profile in that the absolute travel times from the vibrator to the receiver are not used; rather, the relative delay in travel times between receivers or traces is sufficient for calculation of velocities. This method for identification of source signature avoids the internal mechanism of the vibrator-earth system and the controversial near field effect as long as the system is causal. All the source signatures in this context are defined as the signatures of the equivalent SDOF system.

6.2 LOGARITHMIC DECREMENT METHOD FOR DAMPING RATIO

The damping ratio can be evaluated from the SDOF damped free vibration of a system or from Equation (5.71), which is:

$$u_{III}(t) = A_{III} e^{-\xi \omega_0 t} U(t) \sin[\omega_d (t - t_{III})]. \quad (6.1)$$

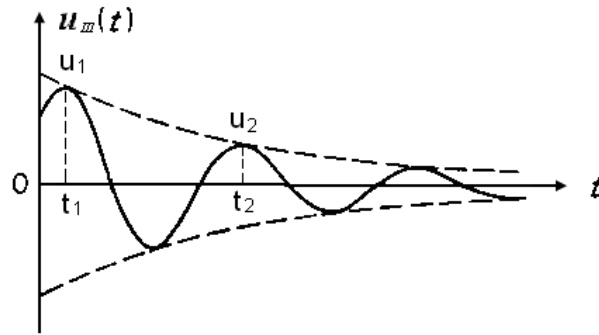


Figure 6.1 Damped free vibration of a SDOF system with an arbitrary initial phase

According to Figure 6.1, peak amplitudes u_n of Equation (6.1) are as follows:

$$u_n = u_0 e^{-\xi \omega_0 t_n}, \quad n = 1, 2, 3 \dots \quad (6.2)$$

The logarithmic decrement δ is defined as:

$$\delta = \ln\left(\frac{u_n}{u_{n+1}}\right), \quad (6.3)$$

and the damped natural period T_d as:

$$T_d = t_{n+1} - t_n = \frac{2\pi}{\omega_d}. \quad (6.4)$$

By substituting Equation (6.2) into Equation (6.3) and using Equation (6.4), one obtains:

$$\delta = \xi\omega_0 T_d = 2\pi\xi \frac{\omega_0}{\omega_d} = \frac{2\pi\xi}{\sqrt{1-\xi^2}} \quad (6.5)$$

or

$$\xi = \frac{\delta}{\sqrt{4\pi^2 + \delta^2}}. \quad (6.6)$$

By measuring the period from the time-domain records, one obtains the approximate damped natural frequency ω_d .

Noise present in the measurement significantly affects the calculated damping ratio as defined in this method, especially when the signal-to-noise ratio is low. The average of the first three peaks is used in this method; however, noise is unavoidable. Hence the spectrum method is introduced and recommended as an improvement.

6.3 SPECTRAL ANALYSIS METHOD FOR DAMPING RATIO

The use of the marginal median discrete Fourier transform to estimate the sinusoidal frequency in impulsive noise and the Gaussian-noise environment was recently explored by Djurovic (2007). The frequency grid near the true frequency and an interpolation technique are used. Djurovic derives the expression for the marginal-median discrete Fourier transform of the sinusoidal signal in the neighborhood of the exact frequency and proposes two specific displacement techniques in order to achieve an accurate estimation of the frequency displaced from the frequency grid.

In this chapter, a different approach than Djurovic's is used to estimate the natural frequency of the vibrator-earth system. This approach is solved albeit with great effort from the SDOF damped free vibration. First, the theoretical amplitude spectrum of the damped free vibration is derived. The theoretical damping ratio and damped natural frequency are expressed as a function of the featured amplitudes. Second, the damped free vibration segment of a measured signal is located. The reference signal in the far field but close to the vibrator is used to avoid interference from reflections that carry the frequencies other than the damped natural frequency. Third, the spectra of the theoretical damped free vibration and the measured damped free vibration are compared and matched in order to obtain the values of damping ratio and damped natural frequency.

Before commencing study of the general Equation (6.1), a simplified equation called the damped free sine (DFS) equation is introduced as:

$$\bar{u}(\tau) = \bar{A} e^{-\xi\omega_0\tau} U(\tau) \sin(\omega_d \tau) \quad (6.7)$$

where: $\bar{u}(\tau)$ is a displacement, velocity or acceleration time series. The initial amplitude \bar{A} corresponds to $\tau = 0$. Regardless of the initial phase, the displacement, velocity, and acceleration time series of a damped free vibration can all be mapped onto the DFS equation by phase shifting and amplitude scaling. This feature is demonstrated later in this chapter.

The Fourier transform of DFS Equation (6.7) is

$$\begin{aligned} F_d(\omega) &= \hat{F}\{\bar{u}(\tau)\} \\ &= \frac{\bar{A}\omega_d}{(\xi\omega_0 + j\omega)^2 + \omega_d^2} \\ &= \frac{\bar{A}\omega_d(\xi^2\omega_0^2 + \omega_d^2 - \omega^2) - j\bar{A}\omega_d(2\xi\omega\omega_0)}{(\xi^2\omega_0^2 + \omega_d^2 - \omega^2)^2 + (2\xi\omega\omega_0)^2} \end{aligned} \quad (6.8)$$

The amplitude spectrum of Equation (6.8) as shown in Figure 6.2(b) is:

$$\begin{aligned}
A(\omega) &= |F_d(\omega)| \\
&= \left| \frac{\bar{A} \omega_d}{(\xi \omega_0 + j\omega)^2 + \omega_d^2} \right| \\
&= \frac{|\bar{A}| \omega_d}{\sqrt{(\xi^2 \omega_0^2 + \omega_d^2 - \omega^2)^2 + (2\xi \omega \omega_0)^2}}
\end{aligned} \tag{6.9}$$

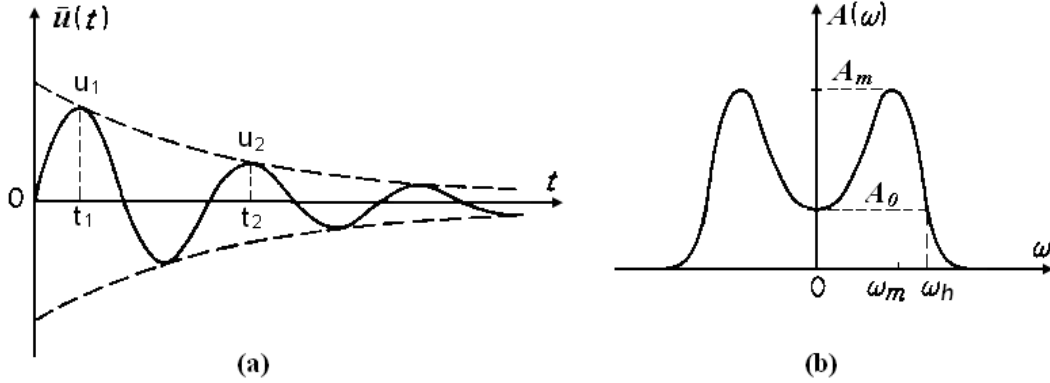


Figure 6.2 (a) damped free sine (DFS) vibration and (b) its spectrum

The peak or trough extreme values of $A(\omega)$ seen in Figure 6.2 (b) are given by:

$$\frac{dA(\omega)}{d\omega} = \frac{2|\bar{A}|\omega_d\omega[\omega_d^2 - \xi^2\omega_0^2 - \omega^2]}{[(\xi^2\omega_0^2 + \omega_d^2 - \omega^2)^2 + (2\xi\omega\omega_0)^2]^{\frac{3}{2}}} = 0, \tag{6.10}$$

Two extreme values can be obtained; the relative minimum value, A_0 , at $\omega = 0$ and the relative maximum value, A_m , at $\omega = \omega_m$. By substituting $\omega = 0$ into Equation (6.9), one obtains the relative minimum value as:

$$\begin{aligned}
A_0 &= |F_d(0)| = \frac{|\bar{A}| \omega_d}{(\xi \omega_0)^2 + \omega_d^2} \\
&= \frac{|\bar{A}| \sqrt{1 - \xi^2}}{\omega_0}
\end{aligned} \tag{6.11}$$

Upon rearranging Equation (6.11), the measurement of damping ratio is attained as:

$$\xi = \sqrt{1 - \left(\frac{A_0 \omega_0}{|\bar{A}|}\right)^2}. \quad (6.12)$$

Equation (6.12) involves prior knowledge of ω_0 and \bar{A} , which is not feasible due to the variation of the near field earth condition that constitutes part of the SDOF system. The relative maximum value or the peak amplitude, A_m , of the spectrum curve in Figure (6.2) can also be obtained from Equation (6.10), as shown in Equations (6.13) and (6.14).

$$\omega_m = \omega_0 \sqrt{1 - 2\xi^2}. \quad (6.13)$$

$$A_m = A(\omega_m) = |F_d(\omega_m)| = \frac{|\bar{A}|}{2\xi\omega_0} \quad (6.14)$$

Using Equations (6.11) and (6.14) to cancel ω_0 and \bar{A} in Equation (6.12), the damping ratio ξ as the function of the ratio of the two extreme values is obtained as:

$$\xi = \frac{\sqrt{2}}{2} \sqrt{1 \pm \sqrt{1 - \left(\frac{A_0}{A_m}\right)^2}} \quad (6.15)$$

The plus sign in Equation (6.15) yields a damping ratio value $\xi > 0.7$, while a typical under-damped free vibration has $\xi < 0.7$ or:

$$\xi = \frac{\sqrt{2}}{2} \sqrt{1 - \sqrt{1 - \left(\frac{A_0}{A_m}\right)^2}} \quad (6.16)$$

where A_0 and A_m are evaluated from the amplitude spectrum curve in Figure (6.2b).

The field condition may appear as a nonlinear vibration system. A convenient approach to verifying nonlinearity is the hillside frequency, ω_h , which has the same spectrum amplitude value A_0 as at zero frequency in Figure (6.2b), that is:

$$|F_d(\omega_h)| = |F_d(0)| = A_0 \quad (6.17)$$

A linear SDOF system is characterized by (Papoulis, 1962):

$$\omega_h = \sqrt{2}\omega_m. \quad (6.18)$$

Otherwise, the system is nonlinear or characterized by high noise. White noise has high frequencies which tend to spread from below the hillside frequency to the Nyquist frequency.

Once the damping ratio is available from Equations (6.16), the natural frequency ω_0 can be obtained from Equation (6.13) as:

$$\omega_0 = \frac{\omega_m}{\sqrt{1-2\xi^2}} \quad (6.19)$$

The damped natural frequency can be obtained from Equation (5.10) as:

$$\omega_d = \omega_0\sqrt{1-\xi^2} \quad (6.20)$$

The tuning ratio, β , can be obtained by Equation (5.11) as:

$$\beta = \frac{\varpi}{\omega_0}, \quad (6.21)$$

where: ϖ is any constant excitation frequency obtained in the field tests.

6.3.1 Measurement of damping ratio using displacement signal

The displacement Equation (6.1) presents an initial phase which can be shifted and mapped onto the DFS Equation (6.7) so that Equation (6.16) can be used for the damping ratio. Figure (6.3) demonstrates two cases in mapping Equation (6.1) to the DFS Equation (6.7). Figures (6.3a) and (6.3b) both use the nearest zero amplitude point (indicated by $\tau = 0$); the former $t_{III} \geq 0$ and in the latter $t_{III} < 0$. The phase shift is indicated by mapping t to τ by Equations (6.22) or (6.23) is:

$$\tau = t - t_{III} \quad (6.22)$$

$$t = \tau + t_{III} \quad (6.23)$$

By substituting Equation (6.23) into Equation (6.1), one obtains:

$$\begin{aligned}
 u_{III}(t) &= A_{III} e^{-\xi\omega_0 t} U(t) \sin[\omega_d(t - t_{III})] \\
 &= A_{III} e^{-\xi\omega_0(t_{III} + \tau)} U(t_{III} + \tau) \sin(\omega_d \tau) \\
 &= e^{-\xi\omega_0 t_{III}} A_{III} e^{-\xi\omega_0 \tau} U(t_{III} + \tau) \sin(\omega_d \tau)
 \end{aligned} \tag{6.24}$$

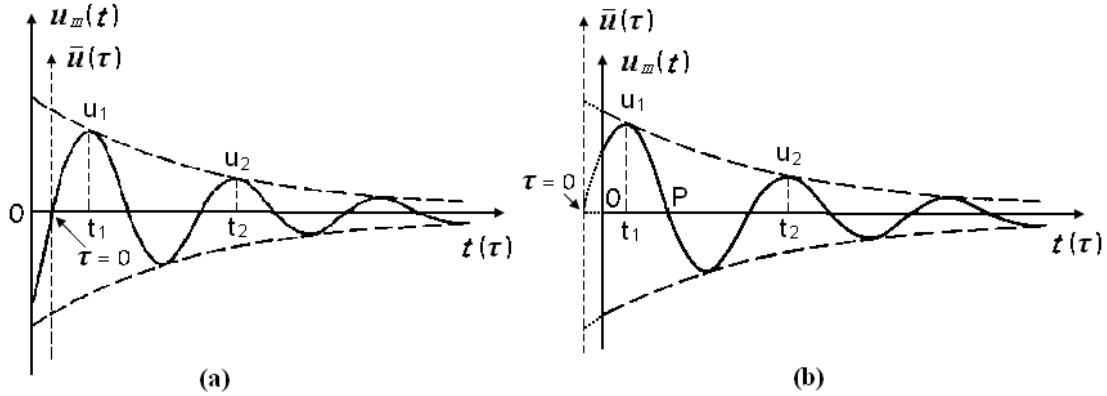


Figure 6.3 Map of the general Equation (6.1) to DFS Equation (6.7)

As indicated in Figure (6.3a), when $t_{III} \geq 0$, the time corresponding to $\tau < 0$ is removed for an exact mapping. Doing so is equivalent to multiplying Equation (6.24) by a step function $U(\tau)$:

$$\begin{aligned}
 u(\tau) &= u_{III}(t)U(\tau) \\
 &= e^{-\xi\omega_0 t_{III}} A_{III} e^{-\xi\omega_0 \tau} U(t_{III} + \tau)U(\tau) \sin(\omega_d \tau) \\
 &= e^{-\xi\omega_0 t_{III}} A_{III} e^{-\xi\omega_0 \tau} U(\tau) \sin(\omega_d \tau) \\
 &= \bar{A} e^{-\xi\omega_0 \tau} U(\tau) \sin(\omega_d \tau)
 \end{aligned} \tag{6.25}$$

$$\text{where: } \bar{A} = e^{-\xi\omega_0 t_{III}} A_{III} \tag{6.26}$$

As indicated in Figure (6.3b), when $t_{III} < 0$, the damped free vibration is extended backward to the near zero amplitude point at $\tau = 0$. The extrapolation is equivalent to the union of Equation (6.24) and $U(\tau)$ as:

$$\begin{aligned}
u(\tau) &= u_{III}(t) \cup U(\tau) \\
&= e^{-\xi\omega_0 t_{III}} A_{III} e^{-\xi\omega_0 \tau} \sin(\omega_d \tau) [U(t_{III} + \tau) \cup U(\tau)] \\
&= e^{-\xi\omega_0 t_{III}} A_{III} e^{-\xi\omega_0 \tau} U(\tau) \sin(\omega_d \tau) \\
&= \bar{A} e^{-\xi\omega_0 \tau} U(\tau) \sin(\omega_d \tau)
\end{aligned} \tag{6.27}$$

where: $\bar{A} = e^{-\xi\omega_0 t_{III}} A_{III}$, the same as Equation (6.26).

However, this extrapolation method needs prior estimation of the period of the free vibration (for example, by estimating from the time series) so that the origin at $\tau = 0$ can be located by extending a half cycle backward from point P. In order to avoid the inconvenience of performing this extrapolation, an alternative method is presented as shown in Figure (6.4).

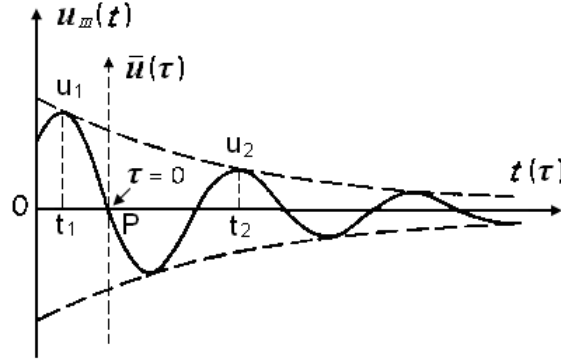


Figure 6.4 Map of the general Equation (6.1) to out-of-phase DFS Equation (6.7)

Assigning point P as the new origin using Equations (6.28a) and (6.28b) as:

$$\tau = t - \left(\frac{\pi}{\omega_d} + t_{III} \right) \tag{6.28a}$$

$$t = \tau + \left(\frac{\pi}{\omega_d} + t_{III} \right) \tag{6.28b}$$

The derivation procedures are similar to those presented in Equation (6.24) as follows:

$$\begin{aligned}
u_{III}(t) &= A_{III} e^{-\xi\omega_0 t} U(t) \sin[\omega_d(t - t_{III})] \\
&= -A_{III} e^{-\xi\omega_0 t} U(t) \sin[\omega_d(t - t_{III}) - \pi] \\
&= -A_{III} e^{-\xi\omega_0 t} U(t) \sin[\omega_d(t - (\frac{\pi}{\omega_d} + t_{III}))] \\
&= -A_{III} e^{-\xi\omega_0(\frac{\pi}{\omega_d} + t_{III} + \tau)} U(\frac{\pi}{\omega_d} + t_{III} + \tau) \sin(\omega_d \tau) \\
&= -e^{-\xi\omega_0(\frac{\pi}{\omega_d} + t_{III})} A_{III} e^{-\xi\omega_0 \tau} U(\frac{\pi}{\omega_d} + t_{III} + \tau) \sin(\omega_d \tau)
\end{aligned} \tag{6.29}$$

By removing signals for $\tau < 0$, one obtains:

$$\begin{aligned}
u(\tau) &= u_{III}(t)U(\tau) \\
&= -e^{-\xi\omega_0(\frac{\pi}{\omega_d} + t_{III})} A_{III} e^{-\xi\omega_0 \tau} U(\frac{\pi}{\omega_d} + t_{III} + \tau)U(\tau) \sin(\omega_d \tau) \\
&= -e^{-\xi\omega_0(\frac{\pi}{\omega_d} + t_{III})} A_{III} e^{-\xi\omega_0 \tau} U(\tau) \sin(\omega_d \tau) \\
&= \bar{A} e^{-\xi\omega_0 \tau} U(\tau) \sin(\omega_d \tau)
\end{aligned} \tag{6.30}$$

where:
$$\bar{A} = -e^{-\xi\omega_0(\frac{\pi}{\omega_d} + t_{III})} A_{III} \tag{6.31}$$

Equations (6.25), (6.27), and (6.30) all map to the same DFS Equation (6.7). Thus the damping Equation (6.16) is applicable for all these cases.

The general free vibration Equation (6.1) may also be mapped to the damped free cosine (DFC) Equation (6.32) as shown in Figure 6.5.

$$\bar{u}(\tau) = \bar{A} e^{-\xi\omega_0 \tau} U(\tau) \cos(\omega_d \tau) \tag{6.32}$$

The procedures to map Equation (6.1) onto DFC Equation (6.32) are essentially the same as onto the DFS equation. Generally speaking, the DFS equation is preferable because the peak amplitude values of a time series experience more noise and distortion than does the zero amplitude point. Thus the identification of the origin of DFC (at peak amplitude) may be more prone to error than of the origin of DFS (at zero amplitude).

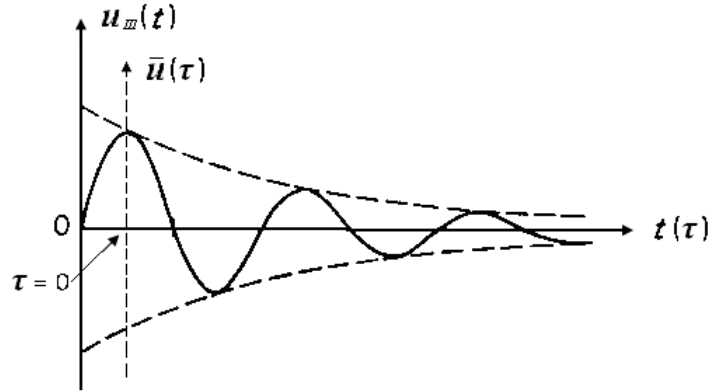


Figure 6.5 Map of the general Equation (6.1) to DFC vibration (6.32)

6.3.2 Measurement of damping ratio using velocity signal

The velocity signal is the derivative of Equation (6.1) and is expressed as:

$$\begin{aligned}
 \dot{u}_{III}(t) &= -A_{III} e^{-\xi\omega_0 t} U(t) \{ \xi\omega_0 \sin[\omega_d(t-t_{III})] - \omega_d \cos[\omega_d(t-t_{III})] \} \\
 &= -A_{III} e^{-\xi\omega_0 t} U(t) \sqrt{(\xi\omega_0)^2 + \omega_d^2} \sin[\omega_d(t-t_{III}-t_v)] \\
 &= -\omega_0 A_{III} e^{-\xi\omega_0 t} U(t) \sin[\omega_d(t-t_{III}-t_v)]
 \end{aligned} \tag{6.33}$$

where:

$$t_v = \frac{1}{\omega_d} \arctan 2(\omega_d, \xi\omega_0) \tag{6.34}$$

By shifting the phase using $\tau = t - t_{III} - t_v$ and following similar procedures as Equation (6.24), the following is obtained:

$$\begin{aligned}
 \dot{u}_{III}(t) &= -\omega_0 A_{III} e^{-\xi\omega_0 t} U(t) \sin[\omega_d(t-t_{III}-t_v)] \\
 &= -\omega_0 e^{-\xi\omega_0(t_{III}+t_v)} A_{III} e^{-\xi\omega_0 \tau} U(\tau+t_{III}+t_v) \sin(\omega_d \tau)
 \end{aligned} \tag{6.35}$$

By removing velocities for $\tau < 0$, one obtains:

$$\begin{aligned}
\dot{u}(\tau) &= \dot{u}_{III}(t)U(\tau) \\
&= -\omega_0 e^{-\xi\omega_0(t_{III}+t_v)} A_{III} e^{-\xi\omega_0\tau} U(\tau + t_{III} + t_v) U(\tau) \sin(\omega_d \tau) \\
&= -\omega_0 e^{-\xi\omega_0(t_{III}+t_v)} A_{III} e^{-\xi\omega_0\tau} U(\tau) \sin(\omega_d \tau) \\
&= \bar{A} e^{-\xi\omega_0\tau} U(\tau) \sin(\omega_d \tau)
\end{aligned} \tag{6.36}$$

$$\text{where:} \quad \bar{A} = -\omega_0 e^{-\xi\omega_0(t_{III}+t_v)} A_{III} \tag{6.37}$$

The velocity signal Equation (6.36) is mapped onto the DFS Equation (6.7) so that the damping ratio can be evaluated using Equation (6.7).

In practice, displacement signals are not directly measured. Only velocity signals from geophones or acceleration signals from accelerometers are available, which are discussed in the following sections.

Figure 6.6 is the S-wave reference signal measured at a depth of 7 m (22 ft) depth. The signal is 5 cycles of a 30-Hz sine wave. Figure 6.7 expands the time scale of the unfiltered signal, but the start point of the DFS equation is noisy. When the signal is noisy, a filter is necessary to locate the start point of the DFS equation. Figure 6.8 is filtered by a fourth order Butterworth filter with a cutoff frequency at 50 Hz. The start point is easier to see in the expanded figure shown in Figure 6.9 and is selected at 0.211 sec. When the entire time series starting from 0.211 sec to 2.00 sec is used for the analysis as shown in Figure 6.10, the noise becomes disruptive. To overcome the problem, interval of 0.211 to 0.300 sec is used as the DFS curve and the result is shown in Figure 6.11. Both Figures 6.10 and 6.11 yield the same damping ratio of the vibrator-earth system measured in frequency domain which is 23%. The corresponding natural frequency is 21 Hz as determined in Figure 6.11.

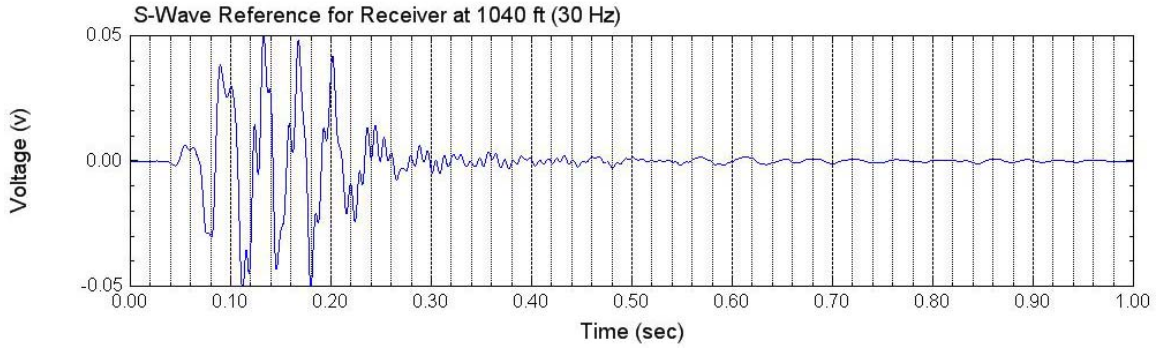


Figure 6.6 S-wave reference signal recorded with horizontal velocity transducer

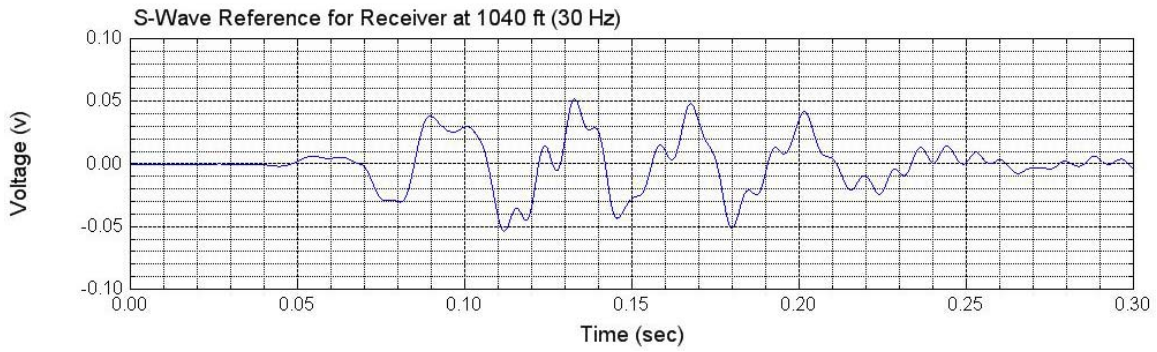


Figure 6.7 Expanded unfiltered S-wave reference signal recorded with horizontal velocity transducer

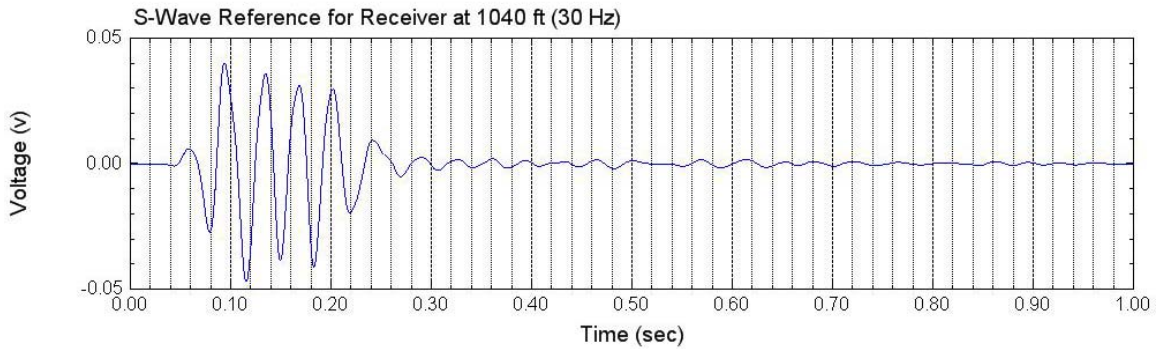


Figure 6.8 Filtered S-wave reference signal recorded with horizontal velocity transducer

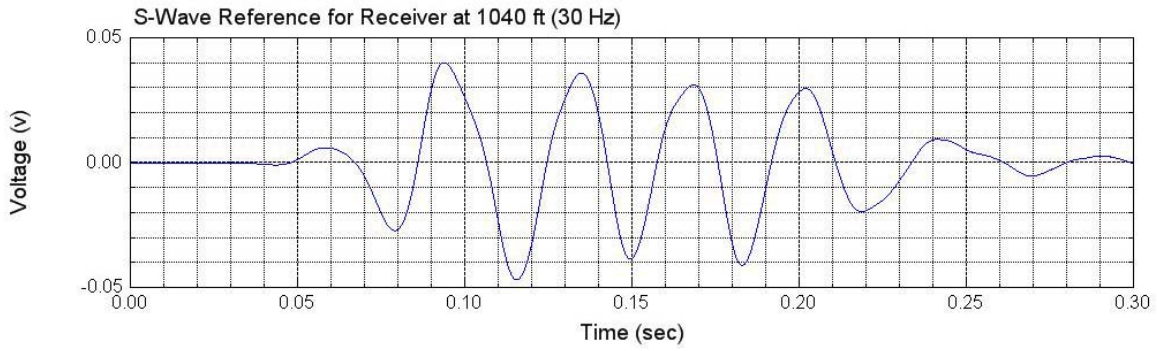


Figure 6.9 Expanded filtered S-wave reference signal recorded with horizontal velocity transducer

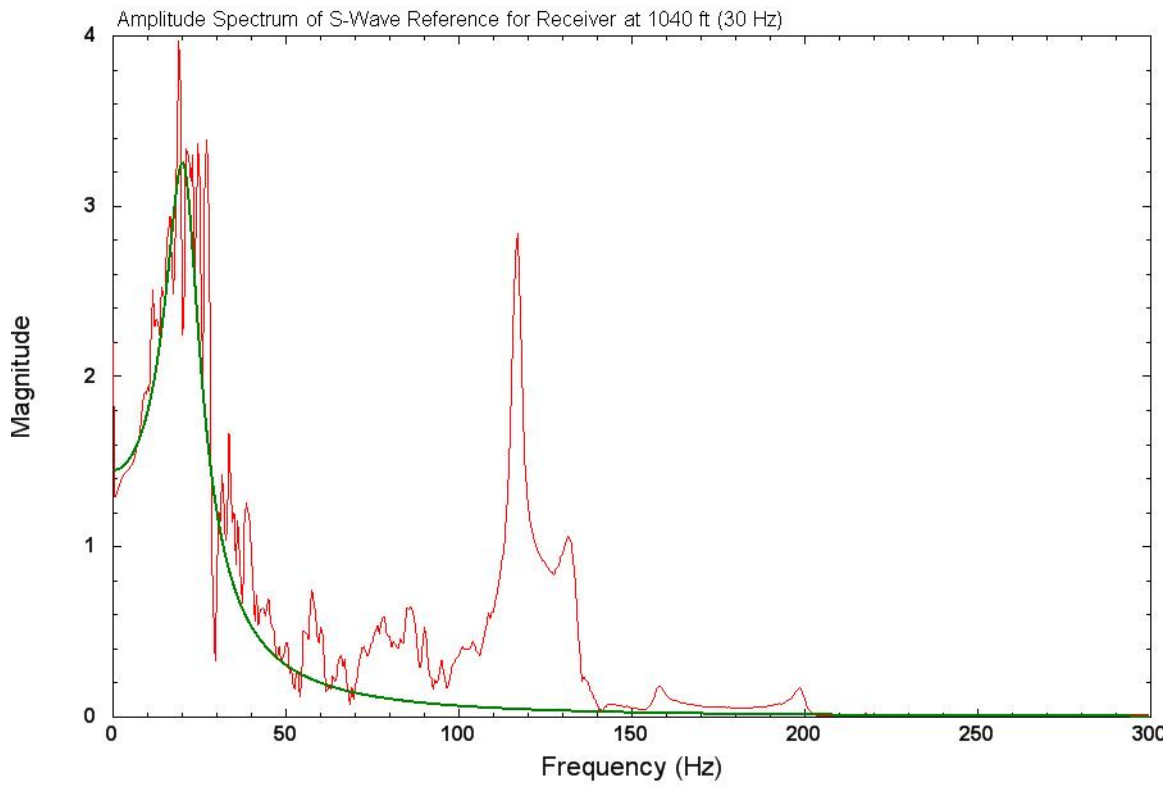


Figure 6.10 S-wave damping ratio measurement using velocity signal

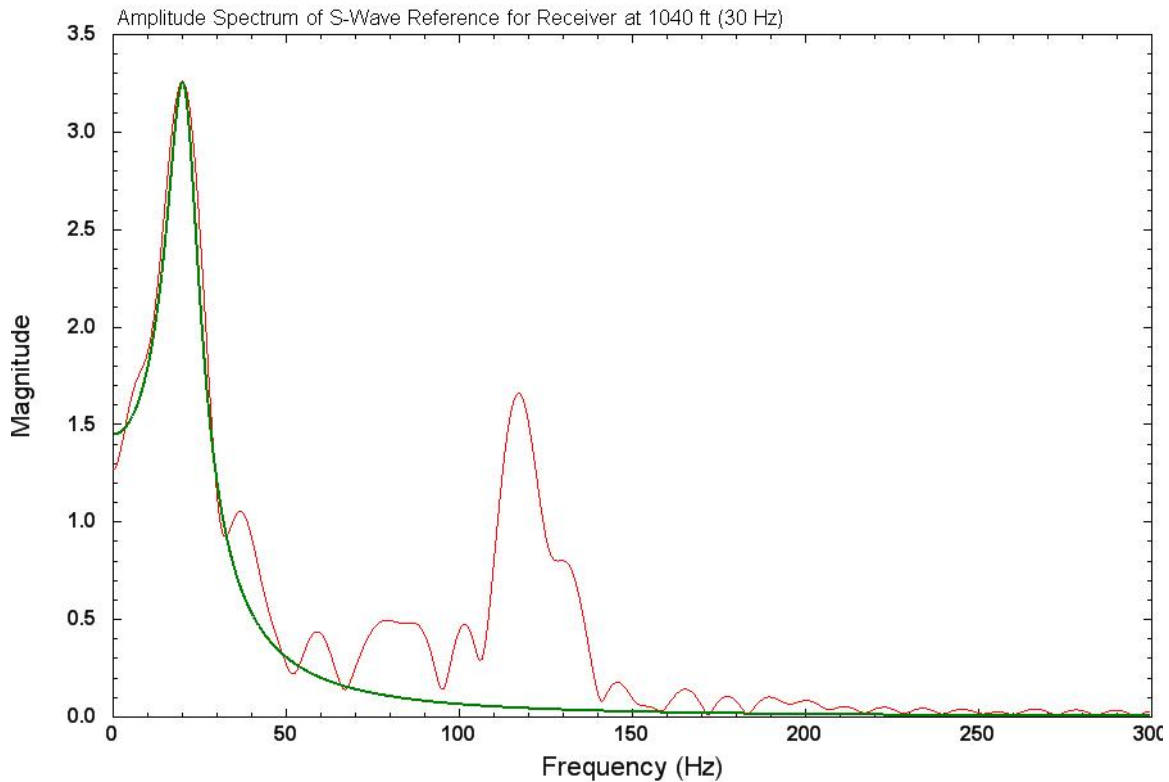


Figure 6.11 S-wave damping ratio measurement using part of the velocity signal

Figure 6.12 is a reference P-wave signal recorded by a geophone at depth 6.6 m (22 ft) below the ground surface. The signal is 5 cycles of a 50-Hz sine wave. The positive amplitudes are generally greater than the negative side because the compression and the tension caused by P-wave shaking are unequal. The mean value of the signal is biased. The DFS equation may commence at 0.1457 sec so long as the damped free vibration has started before the selected start point. As shown in Figure 6.12, the reflection comes as early as 0.2 sec. To avoid the interference of the reflection, time interval 0.1457 to 0.2 sec is used for the DFS equation.

Figure 6.13 presents a damping value of 24% and a natural frequency of 42 Hz for this measurement. The bold line is the theoretical curve calculated using the DFS

equation and the thin line is the spectrum of the measured P-wave data. The trough at about 18 Hz is due to the time truncation that corresponds to a convolution with a sinc-function in frequency domain.

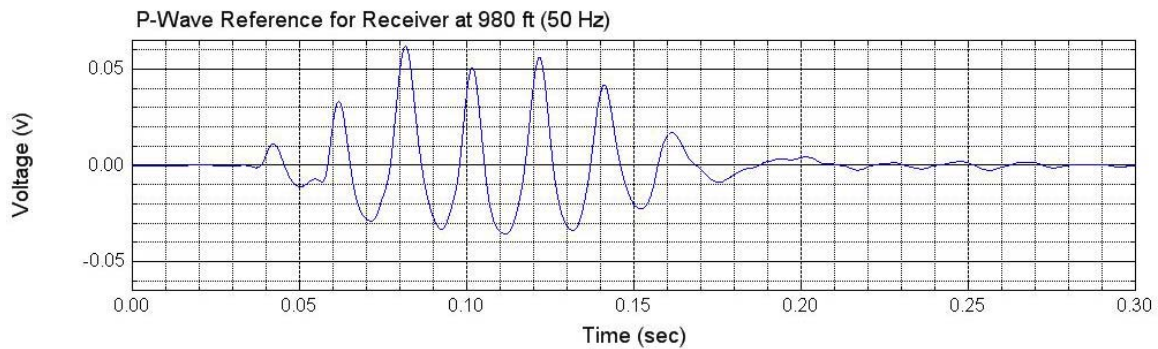


Figure 6.12 P-wave reference signal recorded with a vertical velocity transducer

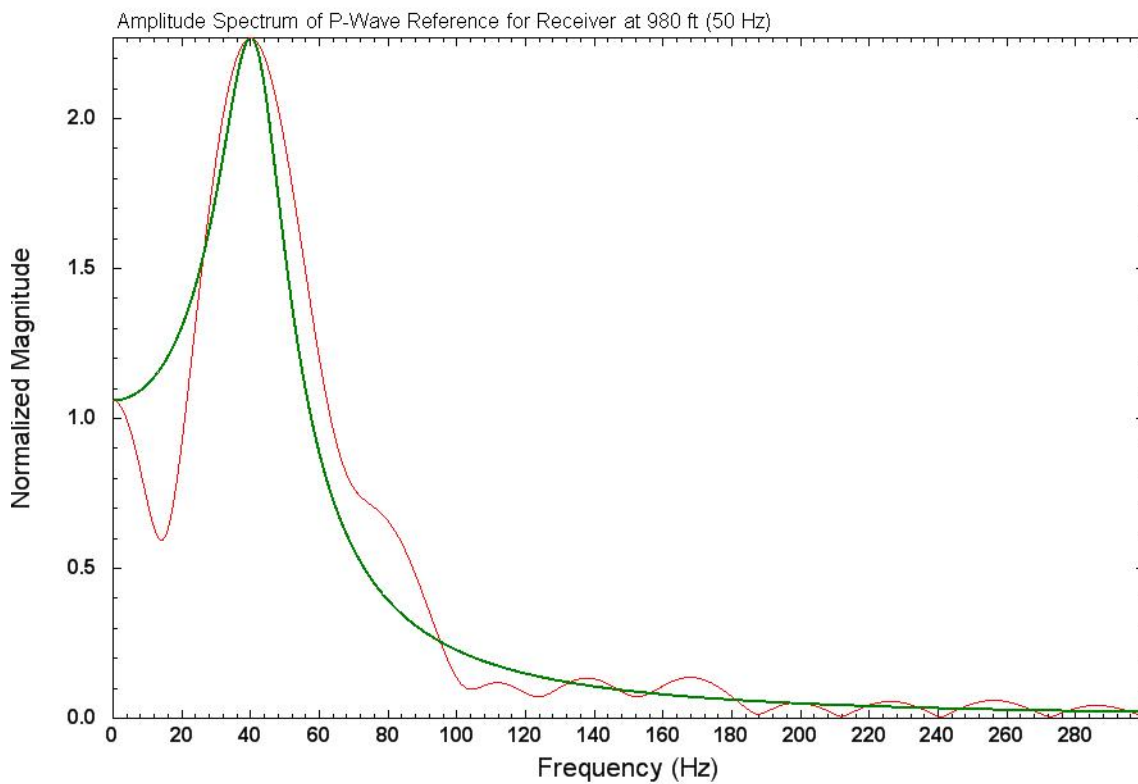


Figure 6.13 P-wave damping ratio measurement using velocity signal

6.3.3 Measurement of damping ratio using acceleration signal

The acceleration signal corresponding to Equation (6.1) is:

$$\begin{aligned}
 \ddot{u}_{III}(t) &= A_{III} e^{-\xi\omega_0 t} U(t) \{ [(\xi\omega_0)^2 - \omega_d^2] \sin[\omega_d(t - t_{III})] \\
 &\quad - 2\xi\omega_0\omega_d \cos[\omega_d(t - t_{III})] \} \\
 &= A_{III} e^{-\xi\omega_0 t} U(t) \sqrt{[(\xi\omega_0)^2 - \omega_d^2]^2 + (2\xi\omega_0\omega_d)^2} \sin[\omega_d(t - t_{III} - t_a)] \\
 &= \omega_0^2 A_{III} e^{-\xi\omega_0 t} U(t) \sin[\omega_d(t - t_{III} - t_a)]
 \end{aligned} \tag{6.39}$$

where:

$$t_a = \frac{1}{\omega_d} \arctan 2[2\xi\omega_0\omega_d, (\xi\omega_0)^2 - \omega_d^2] \tag{6.40}$$

By phase shift using $\tau = t - t_{III} - t_a$, one obtains:

$$\begin{aligned}
 \ddot{u}(\tau) &= \ddot{u}_{III}(t) U(\tau) \\
 &= \omega_0^2 A_{III} e^{-\xi\omega_0(\tau+t_{III}+t_a)} U(\tau + t_{III} + t_a) U(\tau) \sin(\omega_d \tau) \\
 &= \omega_0^2 e^{-\xi\omega_0(t_{III}+t_a)} A_{III} e^{-\xi\omega_0 \tau} U(\tau) \sin(\omega_d \tau) \\
 &= \bar{A} e^{-\xi\omega_0 \tau} U(\tau) \sin(\omega_d \tau)
 \end{aligned} \tag{6.41}$$

where: $\bar{A} = \omega_0^2 e^{-\xi\omega_0(t_{III}+t_a)} A_{III}$ (6.42)

The acceleration signal Equation (6.41) is mapped to the DSF Equation (6.7) so that the damping ratio can be evaluated using Equation (6.7).

As concluded by Baeten and Ziolkowski (1990), the base plate acceleration, the reaction mass acceleration or their weighted sum signal can not serve as the correct source signature. Evaluation of the damping ratio using these near-field accelerations is inaccurate. Acceleration signals in the far field are not available from the downhole field tests and, therefore nothing further is done with accelerations.

6.4 IDENTIFICATION OF THE SOURCE SIGNATURE

The real source signal and source signature are unknown. The accelerations of the base plate, reaction mass, or their weighted sums do not represent the far-field wavelet

(Baeten and Ziolkowski, 1990). The far-field displacement wavelet is proportional to the true ground force. Using the method discussed in Section 6.3, any signal recorded in the far field can be used to back calculate the source signature. As discussed below, the signal used for the back calculation can be any signal in the far field where nonlinear near-field effect is attenuated or filtered by the earth. The calculation is best used with the signals recorded by a reference receiver in an upper layer at some depth below the ground surface where exist the least amount of reflections of the body waves and interference of the surface waves.

The group of parameters that uniquely determines the normalized source signature are: ξ , ω_0 , ϖ , T . Parameters ξ and ω_0 are determined in Equations (6.16) and (6.19), respectively. Constants ϖ and T are the values used in the field tests and selected at the start of testing.

6.4.1 Calculation of the normalized source signature

The source signature can be a displacement, velocity, or acceleration, all of which are determined by the same group of parameters. If not specifically mentioned, the source signature refers to the displacement source signature.

The predetermined drive signal possesses exact information regarding the start and termination times of excitation. The start of the drive signal excitation, whether it is at time zero or not, is used as the time zero ($t = 0$) of the source signature. The duration T of the excitation corresponds to the time span of the sinusoidal wavelet as well as the initial transient wavelet. The damped free vibration or trailing wavelet starts at $t = T$.

Assuming the excitation force starts at zero phase ($\psi = 0$), initial phases or times t_I and t_{II} of the forced vibration Equations (5.39) and (5.59)) can be obtained from Equations (5.38) and (5.58), respectively, as:

$$t_I = \frac{1}{\varpi} \arctan 2(2\xi\beta, 1 - \beta^2) \quad (6.44)$$

$$\text{and} \quad t_{II} = \frac{1}{\omega_d} \arctan 2[-2\xi\beta, \frac{(\beta^2 + 2\xi^2 - 1)\varpi}{\omega_d}] \quad (6.45)$$

If the normalized amplitudes A_I^* and A_{II}^* are defined as:

$$A_I^* = \frac{1}{\sqrt{(1 - \beta^2)^2 + (2\xi\beta)^2}}, \quad (6.46)$$

$$\text{and} \quad A_{II}^* = \frac{\sqrt{(\frac{\varpi}{\omega_d})^2 (\beta^2 + 2\xi^2 - 1)^2 + (2\xi\beta)^2}}{(1 - \beta^2)^2 + (2\xi\beta)^2}. \quad (6.47)$$

then the amplitudes of the forced vibration obtained from Equations (5.34) and (5.57) become:

$$A_I = \frac{Q}{k} A_I^*, \quad (6.48)$$

$$\text{and} \quad A_{II} = \frac{Q}{k} A_{II}^*. \quad (6.49)$$

The boundary condition between the forced vibration and the ensuing damped free vibration is Equations (5.67) and (5.68), which are equivalent to Equations (6.50) through (6.53) shown below.

$$u_0 = A_I \sin[\varpi(T - t_I)] + A_{II} e^{-\xi\omega_0 T} \sin[\omega_d(T - t_{II})] \quad (6.50)$$

$$\begin{aligned} \dot{u}_0 = A_I \varpi \cos[\varpi(T - t_I)] + A_{II} e^{-\xi\omega_0 T} \{ \omega_d \cos[\omega_d(T - t_{II})] \\ - \xi\omega_0 \sin[\omega_d(T - t_{II})] \} \end{aligned} \quad (6.51)$$

$$u_0 = u_{III}(0) \quad (6.52)$$

$$\dot{u}_0 = \dot{u}_{III}(0) \quad (6.53)$$

The following terms for normalized initial displacement and velocity are defined as:

$$u_0^* = \frac{u_0}{\underline{Q}}, \quad \dot{u}_0^* = \frac{\dot{u}_0}{\underline{k}}, \quad (6.54)$$

By dividing both sides of Equations (6.50) and (6.51) by $\frac{Q}{k}$ and using Equations (6.48)

and (6.49), one obtains

$$u_0^* = A_I^* \sin[\varpi(T - t_I)] + A_{II}^* e^{-\xi\omega_0 T} \sin[\omega_d(T - t_{II})] \quad (6.55)$$

$$\begin{aligned} \dot{u}_0^* = & A_I^* \varpi \cos[\varpi(T - t_I)] \\ & + A_{II}^* e^{-\xi\omega_0 T} \{ \omega_d \cos[\omega_d(T - t_{II})] - \xi\omega_0 \sin[\omega_d(T - t_{II})] \} \end{aligned} \quad (6.56)$$

By dividing the numerator and the denominator of Equation (5.73) by $\frac{Q}{k}$, one obtains:

$$t_{III} = \frac{1}{\omega_d} \arctan 2\left(-u_0^*, \frac{\dot{u}_0^* + \xi\omega_0 u_0^*}{\omega_d}\right) \quad (6.57)$$

If the normalized trailing amplitude is defined as:

$$A_{III}^* = \frac{A_{III}}{\underline{Q}}, \quad (6.58)$$

Then, dividing both sides of Equation (5.72) by $\frac{Q}{k}$, one obtains:

$$A_{III}^* = \sqrt{\left(\frac{\dot{u}_0^* + \xi\omega_0 u_0^*}{\omega_d}\right)^2 + u_0^{*2}} \quad (6.59)$$

The source signature defined by Equation (5.81) becomes:

$$\begin{aligned}
u(t) &= u_I(t) + u_{II}(t) + u_{III}(t-T) \\
&= \frac{Q}{k} A_I^* [U(t) - U(t-T)] \sin[\varpi(t-t_I)] \\
&\quad + \frac{Q}{k} A_{II}^* e^{-\xi\omega_0 t} [U(t) - U(t-T)] \sin[\omega_d(t-t_{II})] \\
&\quad + \frac{Q}{k} A_{III}^* e^{-\xi\omega_0(t-T)} U(t-T) \sin[\omega_d(t-T-t_{III})]
\end{aligned} \tag{6.60}$$

If the normalized source signature is defined as the following:

$$u^*(t) = \frac{u(t)}{\frac{Q}{k}}, \tag{6.61}$$

then Equation (6.60) can be simplified as:

$$\begin{aligned}
u^*(t) &= A_I^* [U(t) - U(t-T)] \sin[\varpi(t-t_I)] \\
&\quad + A_{II}^* e^{-\xi\omega_0 t} [U(t) - U(t-T)] \sin[\omega_d(t-t_{II})] \\
&\quad + A_{III}^* e^{-\xi\omega_0(t-T)} U(t-T) \sin[\omega_d(t-T-t_{III})]
\end{aligned} \tag{6.62}$$

where: amplitudes A_I^* , A_{II}^* , and A_{III}^* are defined in Equations (6.46), (6.47), and (6.59), respectively. Initial time shifts t_I , t_{II} , and t_{III} are defined in Equations (6.44), (6.45), and (6.57), respectively.

The normalized source signature in Equation (6.62) may not be directly used for deconvolution if dispersion is present. If dispersion does exist and requires consideration, then the normalized source signature can be separated into the following source signatures defined in Equations (6.63) to (6.68), each of which is a pure wavelet that can be directly used for deconvolution. The normalized source signature indicates all the variations and applications in Equations (6.63) to (6.68).

The first term in Equation (6.62) is the normalized sinusoidal wavelet:

$$u_I^*(t) = A_I^* [U(t) - U(t-T)] \sin[\varpi(t-t_I)] \tag{6.63}$$

The second term is the normalized transient wavelet:

$$u_{II}^*(t) = A_{II}^* e^{-\xi\omega_0 t} [U(t) - U(t-T)] \sin[\omega_d(t-t_{II})] \quad (6.64)$$

The third term is the normalized trailing wavelet:

$$u_{III}^*(t) = A_{III}^* e^{-\xi\omega_0 t} U(t) \sin[\omega_d(t-t_{III})] \quad (6.65)$$

or
$$u_{III}^*(t-T) = A_{III}^* e^{-\xi\omega_0(t-T)} U(t-T) \sin[\omega_d(t-T-t_{III})] \quad (6.66)$$

The second and the third terms combined comprise the normalized twin wavelets:

$$\begin{aligned} u_T^*(t) &= A_{II}^* e^{-\xi\omega_0 t} [U(t) - U(t-T)] \sin[\omega_d(t-t_{II})] \\ &+ A_{III}^* e^{-\xi\omega_0(t-T)} U(t-T) \sin[\omega_d(t-T-t_{III})] \end{aligned} \quad (6.67)$$

When the sinusoidal and the twin wavelets feature the same carrier frequency, which means the source is being excited at the damped natural frequency of the vibrator-earth system, Equation (6.62) becomes the normalized U-wavelet:

$$\begin{aligned} u_U^*(t) &= A_I^* [U(t) - U(t-T)] \sin[\omega_d(t-t_I)] \\ &+ A_{II}^* e^{-\xi\omega_0 t} [U(t) - U(t-T)] \sin[\omega_d(t-t_{II})] \\ &+ A_{III}^* e^{-\xi\omega_0(t-T)} U(t-T) \sin[\omega_d(t-T-t_{III})] \end{aligned} \quad (6.68)$$

To demonstrate graphically and compare various source signatures and their spectra in this chapter, a model test is defined as the response to a SDOF system with natural frequency 100 Hz and damping ratio 25%. The system is excited with an excitation frequency of 50 Hz and duration of 0.1 second. All the source signatures and their wavelets are response to the same model test.

The displacement response to the model test is shown in Figure 6.14.

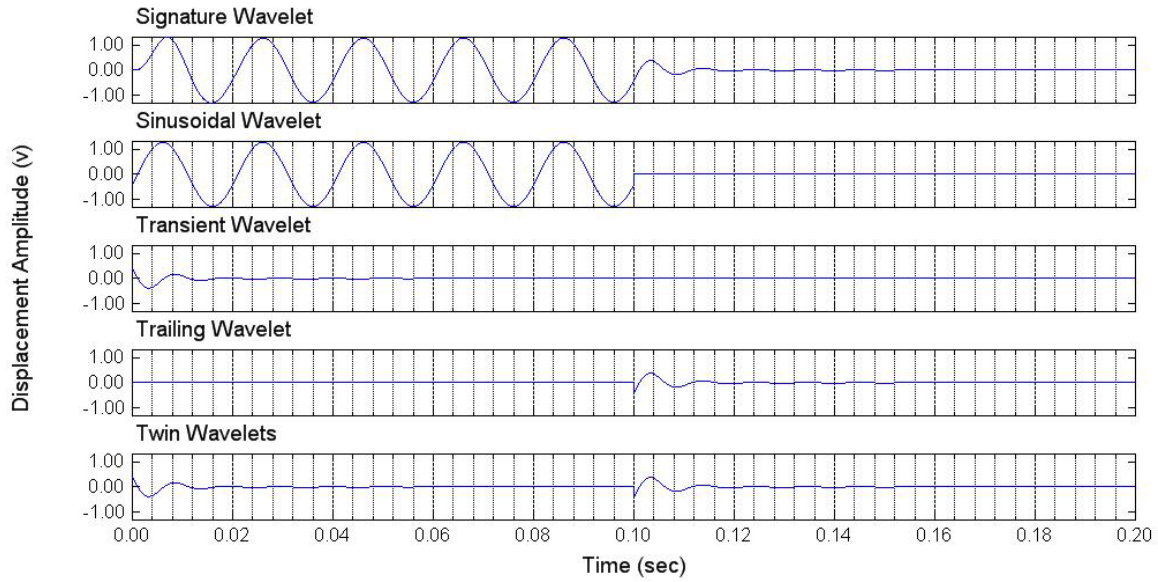


Figure 6.14 Displacement signature of the model test (excitation frequency 50 Hz, duration 0.1 sec, damped frequency 100 Hz, damping ratio 25%)

6.4.2 Calculation of the source signature

Once the initial phase or time t_{III} is known from Equations (6.57), the amplitude A_{III} of the free vibration can be calibrated from any far-field signals such as displacement, velocity, or acceleration using the amplitude of the DFS Equation (6.11) as:

$$|\bar{A}| = \frac{A_0 \omega_0}{\sqrt{1 - \zeta^2}}, \quad (6.69a)$$

or by Equation (6.14) as

$$|\bar{A}| = 2\xi\omega_0 A_m. \quad (6.69b)$$

If a displacement signal is used for the DFS equation, A_{III} is given by Equation (6.26) or (6.31) as:

$$A_{III} = \bar{A} e^{\xi\omega_0 t_{III}}, \quad (6.70a)$$

or

$$A_{III} = \bar{A} e^{\xi\omega_0 \left(\frac{\pi}{\omega_d} + t_{III}\right)}. \quad (6.70b)$$

If a velocity signal is used, A_{III} is determined by Equation (6.37) as:

$$A_{III} = -\frac{\bar{A}}{\omega_0} e^{\xi\omega_0(t_{III}+t_v)}. \quad (6.71)$$

If an acceleration signal is used, A_{III} is determined by Equation (6.42) as:

$$A_{III} = \frac{\bar{A}}{\omega_0^2} e^{\xi\omega_0(t_{III}+t_a)}. \quad (6.72)$$

The use of Equation (6.59) and any of Equations (6.70) to (6.72) allows one to obtain the normalization factor by

$$\frac{Q}{k} = \frac{A_{III}}{A_{III}^*} \quad (6.73)$$

Once $\frac{Q}{k}$ is known, the source signature and any of its variations may be obtained from the normalized source signature by using one to one mapping as shown in Equations (6.75) to (6.77) as:

$$A_I \leftrightarrow A_I^*, A_{II} \leftrightarrow A_{II}^*, A_{III} \leftrightarrow A_{III}^* \quad (6.74)$$

$$A_I = \frac{Q}{k} A_I^*, \quad (6.75)$$

$$A_{II} = \frac{Q}{k} A_{II}^*. \quad (6.76)$$

$$A_{III} = \frac{Q}{k} A_{III}^* \quad (6.77)$$

The sinusoidal, the transient, and the trailing wavelets are mapped, respectively, as follows:

$$u_I(t) = \frac{Q}{k} A_I^* [U(t) - U(t-T)] \sin[\varpi(t-t_I)] \quad (6.78)$$

$$u_{II}(t) = \frac{Q}{k} A_{II}^* e^{-\xi\omega_0 t} [U(t) - U(t-T)] \sin[\omega_d(t-t_{II})] \quad (6.79)$$

$$u_{III}(t) = \frac{Q}{k} A_{III}^* e^{-\xi\omega_0 t} U(t) \sin[\omega_d(t - t_{III})] \quad (6.80)$$

The source signature Equation (6.60) is then determined as:

$$\begin{aligned} u(t) &= u_I(t) + u_{II}(t) + u_{III}(t - T) \\ &= \frac{Q}{k} A_I^* [U(t) - U(t - T)] \sin[\varpi(t - t_I)] \\ &\quad + \frac{Q}{k} A_{II}^* e^{-\xi\omega_0 t} [U(t) - U(t - T)] \sin[\omega_d(t - t_{II})] \\ &\quad + \frac{Q}{k} A_{III}^* e^{-\xi\omega_0(t-T)} U(t - T) \sin[\omega_d(t - T - t_{III})] \end{aligned} \quad (6.81)$$

Figure 6.15 demonstrates the procedures to calculate normalized source signatures and scaled source signatures.

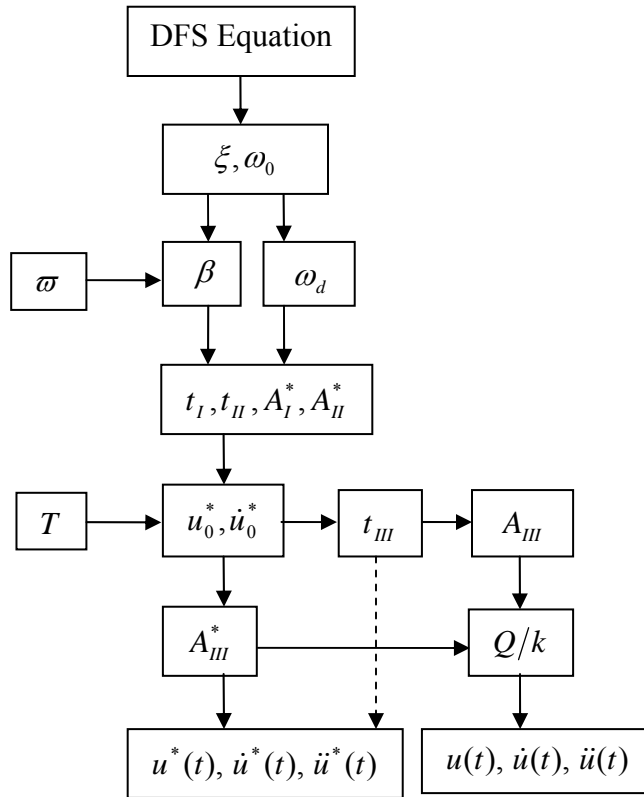


Figure 6.15 Flow chart for calculation of the source signatures

The scaled source signatures ($u(t)$, $\dot{u}(t)$, $\ddot{u}(t)$ for displacement, velocity and acceleration, respectively) can be obtained from the normalized signatures ($u^*(t)$, $\dot{u}^*(t)$ and $\ddot{u}^*(t)$ for displacement, velocity and acceleration, respectively) by the normalization factor $\frac{Q}{k}$. The same mapping Equation (6.74) applies to all other normalized signatures discussed in the next two sections. The normalized signatures are chosen because the current focus for travel time analysis is on the phase shift rather than the amplitude attenuation.

6.4.3 Calculation of the normalized velocity signature

The normalized sinusoidal velocity signature is the derivative of Equation (6.63), which is:

$$\dot{u}_I^*(t) = \varpi A_I^* [U(t) - U(t-T)] \cos[\varpi(t-t_I)] \quad (6.82)$$

If only the sine function is used, then Equation (6.82) becomes:

$$\dot{u}_I^*(t) = -\varpi A_I^* [U(t) - U(t-T)] \sin[\varpi(t-t_I - \frac{\pi}{2\varpi})] \quad (6.83)$$

The normalized transient velocity signature is the derivative of Equation (6.64) as:

$$\begin{aligned} \dot{u}_{II}^*(t) &= -A_{II}^* e^{-\xi\omega_0 t} [U(t) - U(t-T)] \\ &\quad \cdot \{\xi\omega_0 \sin[\omega_d(t-t_{II})] - \omega_d \cos[\omega_d(t-t_{II})]\} \\ &= -A_{II}^* e^{-\xi\omega_0 t} [U(t) - U(t-T)] \sqrt{(\xi\omega_0)^2 + \omega_d^2} \sin[\omega_d(t-t_{II} - t_v)] \\ &= -\omega_0 A_{II}^* e^{-\xi\omega_0 t} [U(t) - U(t-T)] \sin[\omega_d(t-t_{II} - t_v)] \end{aligned} \quad (6.84)$$

where: t_v is defined in Equation (6.34).

The normalized trailing velocity signature is the derivative of Equations (6.65), or Equation (6.66), which is:

$$\begin{aligned}
\dot{u}_{III}^*(t) &= -A_{III}^* e^{-\xi\omega_0 t} U(t) \\
&\quad \cdot \{ \xi\omega_0 \sin[\omega_d(t-t_{III})] - \omega_d \cos[\omega_d(t-t_{III})] \} \\
&= -A_{III}^* e^{-\xi\omega_0 t} U(t) \sqrt{(\xi\omega_0)^2 + \omega_d^2} \sin[\omega_d(t-t_{III}-t_v)] \\
&= -\omega_0 A_{III}^* e^{-\xi\omega_0 t} U(t) \sin[\omega_d(t-t_{III}-t_v)]
\end{aligned} \tag{6.85}$$

$$\text{or} \quad \dot{u}_{III}^*(t-T) = -\omega_0 A_{III}^* e^{-\xi\omega_0(t-T)} U(t-T) \sin[\omega_d(t-T-t_{III}-t_v)] \tag{6.86}$$

The normalized twin wavelets velocity signature is the derivative of Equation (6.67) or the superposition of Equations (6.84) and (6.86) as:

$$\begin{aligned}
\dot{u}_T^*(t) &= -\omega_0 A_{II}^* e^{-\xi\omega_0 t} [U(t) - U(t-T)] \sin[\omega_d(t-t_{II}-t_v)] \\
&\quad - \omega_0 A_{III}^* e^{-\xi\omega_0(t-T)} U(t-T) \sin[\omega_d(t-T-t_{III}-t_v)]
\end{aligned} \tag{6.87}$$

The normalized U-wavelet velocity signature is the derivative of Equation (6.68), or the superposition of Equations (6.82) and (6.87) and using $\varpi = \omega_d$ given:

$$\begin{aligned}
\dot{u}_U^*(t) &= \omega_d A_I^* [U(t) - U(t-T)] \cos[\omega_d(t-t_I)] \\
&\quad - \omega_0 A_{II}^* e^{-\xi\omega_0 t} [U(t) - U(t-T)] \sin[\omega_d(t-t_{II}-t_v)] \\
&\quad - \omega_0 A_{III}^* e^{-\xi\omega_0(t-T)} U(t-T) \sin[\omega_d(t-T-t_{III}-t_v)]
\end{aligned} \tag{6.88}$$

The normalized velocity signature is the derivative of the source signature Equation (6.62), or the superposition of Equations (6.82) and (6.87), which gives:

$$\begin{aligned}
\dot{u}(t) &= \varpi A_I^* [U(t) - U(t-T)] \cos[\varpi(t-t_I)] \\
&\quad - \omega_0 A_{II}^* e^{-\xi\omega_0 t} [U(t) - U(t-T)] \sin[\omega_d(t-t_{II}-t_v)] \\
&\quad - \omega_0 A_{III}^* e^{-\xi\omega_0(t-T)} U(t-T) \sin[\omega_d(t-T-t_{III}-t_v)]
\end{aligned} \tag{6.89}$$

The normalized velocity signature is demonstrated in Figure 6.16.

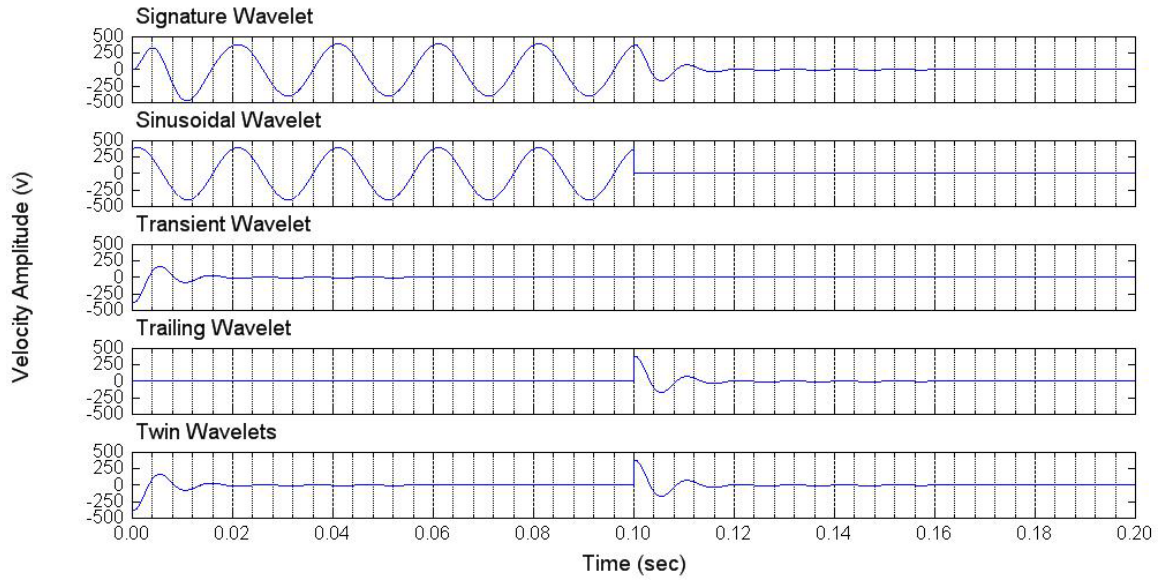


Figure 6.16 Velocity signature of the model test (excitation frequency 50 Hz, duration 0.1 sec, damped frequency 100 Hz, damping ratio 25%)

If only the sine functions are used, then Equation (6.89) becomes:

$$\begin{aligned}
 \dot{u}(t) = & -\varpi A_I^* [U(t) - U(t-T)] \sin\left[\varpi\left(t - t_I - \frac{\pi}{2\varpi}\right)\right] \\
 & - \omega_0 A_{II}^* e^{-\zeta\omega_0 t} [U(t) - U(t-T)] \sin[\omega_d(t - t_{II} - t_v)] \\
 & - \omega_0 A_{III}^* e^{-\zeta\omega_0(t-T)} U(t-T) \sin[\omega_d(t - T - t_{III} - t_v)]
 \end{aligned} \tag{6.90}$$

6.4.4 Calculation of the normalized acceleration signature

The normalized sinusoidal acceleration signature is the derivative of Equation (6.82), which is:

$$\ddot{u}_I^*(t) = -\varpi^2 A_I^* [U(t) - U(t-T)] \sin[\varpi(t - t_I)] \tag{6.91}$$

The normalized transient acceleration signature is the derivative of Equation (6.84), which is:

$$\begin{aligned}
\ddot{u}_{II}^*(t) &= A_{II}^* e^{-\xi\omega_0 t} [U(t) - U(t-T)] \\
&\quad \cdot \{[(\xi\omega_0)^2 - \omega_d^2] \sin[\omega_d(t-t_{II})] - 2\xi\omega_0\omega_d \cos[\omega_d(t-t_{II})]\} \\
&= A_{II}^* e^{-\xi\omega_0 t} [U(t) - U(t-T)] \\
&\quad \cdot \sqrt{[(\xi\omega_0)^2 - \omega_d^2]^2 + (2\xi\omega_0\omega_d)^2} \sin[\omega_d(t-t_{II}-t_a)] \\
&= \omega_0^2 A_{II}^* e^{-\xi\omega_0 t} [U(t) - U(t-T)] \sin[\omega_d(t-t_{II}-t_a)]
\end{aligned} \tag{6.92}$$

where: t_a is defined in Equation (6.40).

The normalized trailing acceleration signature is the derivative of Equation (6.85) or Equation (6.86), which is:

$$\begin{aligned}
\ddot{u}_{III}^*(t) &= A_{III}^* e^{-\xi\omega_0 t} U(t) \{[(\xi\omega_0)^2 - \omega_d^2] \sin[\omega_d(t-t_{III})] \\
&\quad - 2\xi\omega_0\omega_d \cos[\omega_d(t-t_{III})]\} \\
&= A_{III}^* e^{-\xi\omega_0 t} U(t) \sqrt{[(\xi\omega_0)^2 - \omega_d^2]^2 + (2\xi\omega_0\omega_d)^2} \sin[\omega_d(t-t_{III}-t_a)] \\
&= \omega_0^2 A_{III}^* e^{-\xi\omega_0 t} U(t) \sin[\omega_d(t-t_{III}-t_a)]
\end{aligned} \tag{6.93}$$

$$\text{or} \quad \ddot{u}_{III}^*(t-T) = \omega_0^2 A_{III}^* e^{-\xi\omega_0(t-T)} U(t-T) \sin[\omega_d(t-T-t_{III}-t_a)] \tag{6.94}$$

The normalized twin wavelets acceleration signature is the derivative of Equation (6.87) or the superposition of Equations (6.92) and (6.94) as:

$$\begin{aligned}
\ddot{u}_T^*(t) &= \omega_0^2 A_{II}^* e^{-\xi\omega_0 t} [U(t) - U(t-T)] \sin[\omega_d(t-t_{II}-t_a)] \\
&\quad + \omega_0^2 A_{III}^* e^{-\xi\omega_0(t-T)} U(t-T) \sin[\omega_d(t-T-t_{III}-t_a)]
\end{aligned} \tag{6.95}$$

The normalized U-wavelet acceleration signature is the derivative of Equation (6.88), or the superposition of Equations (6.91) and (6.95), and using $\varpi = \omega_d$ gives:

$$\begin{aligned}
\ddot{u}_U^*(t) &= -\omega_d^2 A_I^* [U(t) - U(t-T)] \sin[\omega_d(t-t_I)] \\
&\quad + \omega_0^2 A_{II}^* e^{-\xi\omega_0 t} [U(t) - U(t-T)] \sin[\omega_d(t-t_{II}-t_a)] \\
&\quad + \omega_0^2 A_{III}^* e^{-\xi\omega_0(t-T)} U(t-T) \sin[\omega_d(t-T-t_{III}-t_a)]
\end{aligned} \tag{6.96}$$

The normalized acceleration signature is the second derivative of source signature Equation (6.62), or the superposition of Equations (6.91) and (6.95), which gives:

$$\begin{aligned}
\ddot{u}^*(t) = & -\varpi^2 A_I^* [U(t) - U(t-T)] \sin[\varpi(t-t_I)] \\
& + \omega_0^2 A_{II}^* e^{-\xi\omega_0 t} [U(t) - U(t-T)] \sin[\omega_d(t-t_{II} - t_a)] \\
& + \omega_0^2 A_{III}^* e^{-\xi\omega_0(t-T)} U(t-T) \sin[\omega_d(t-T-t_{III} - t_a)]
\end{aligned} \tag{6.97}$$

The normalized acceleration signature is demonstrated in Figure 6.17.

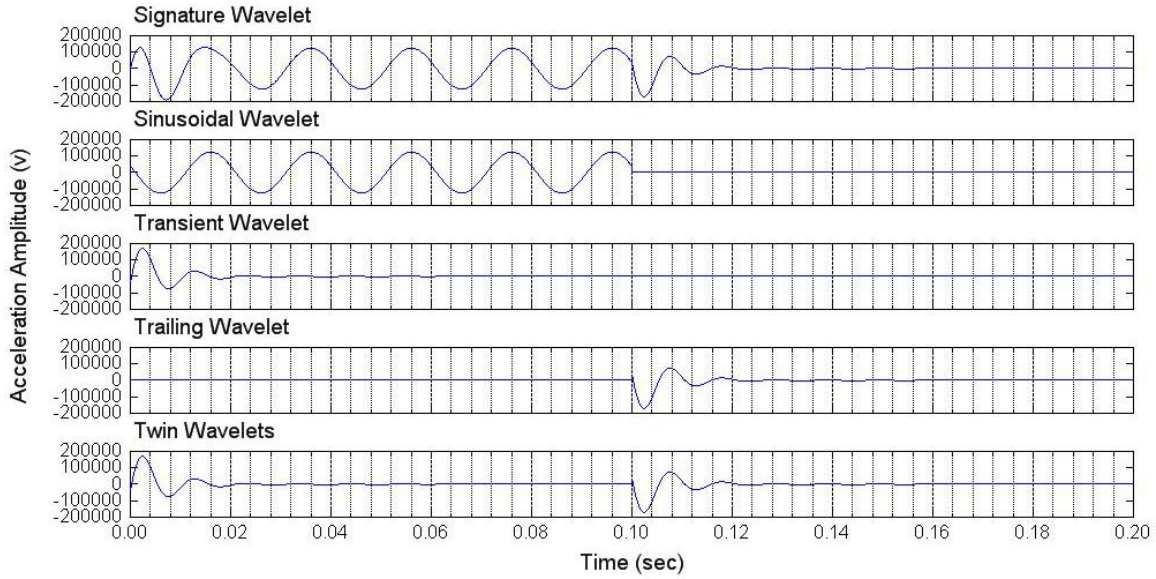


Figure 6.17 Acceleration signature of the model test (excitation frequency 50 Hz, duration 0.1 sec, damped frequency 100 Hz, damping ratio 25%)

6.5 SPECTRUM OF THE NORMALIZED SOURCE SIGNATURE

The difference between the source signature and the normalized source signature is the normalization factor $\frac{Q}{k}$, which maps the source signature amplitudes A_I , A_{II} , and A_{III} onto their normalized amplitudes A_I^* , A_{II}^* , and A_{III}^* , as shown in Equations (6.75) to (6.77) and can be expressed as:

$$A_I \rightarrow A_I^*, A_{II} \rightarrow A_{II}^*, A_{III} \rightarrow A_{III}^*. \tag{6.98}$$

Equation (6.98) applies to any mapping from the spectrum of the source signature to that of the normalized source signature.

As discussed in Chapter 5, the source signature is the superposition of the sinusoidal wavelet, the transient wavelet, and the trailing wavelet. The spectrum of the source signature is also the superposition of the spectra of the three wavelets, as shown in Equation (5.72) as:

$$F(\omega) = F_I(\omega) + F_{II}(\omega) + F_{III,T}(\omega), \quad (6.99)$$

where: $F_I(\omega)$, $F_{II}(\omega)$, and $F_{III,T}(\omega)$ are defined in Equations (6.100) to (6.102).

The spectrum of the sinusoidal wavelet is Equation (5.104), and is expressed as:

$$\begin{aligned} F_I(\omega) = & \frac{A_I}{\omega^2 - \varpi^2} [j\omega \sin(\varpi t_I) - \varpi \cos(\varpi t_I)] \\ & + \frac{jA_I}{2} [\delta(\omega + \varpi)(e^{-j\varpi t_I} + e^{j\varpi t_I}) - \delta(\omega - \varpi)(e^{-j\varpi t_I} + e^{j\varpi t_I})] \\ & - \frac{A_I}{\omega^2 - \varpi^2} [j\omega \sin(\varpi(t_I - T)) - \varpi \cos(\varpi(t_I - T))] \\ & - \frac{jA_I}{2} [\delta(\omega + \varpi)(e^{-j\varpi(t_I - T)} + e^{j\varpi(t_I - T)}) \\ & \quad - \delta(\omega - \varpi)(e^{-j\varpi(t_I - T)} + e^{j\varpi(t_I - T)})] \end{aligned} \quad (6.100)$$

The spectrum of the transient wavelet is Equation (5.114), and is expressed as:

$$\begin{aligned} F_{II}(\omega) = & \frac{jA_{II}}{2} \left[\frac{e^{j\omega_d t_{II}}}{\xi\omega_0 + j(\omega + \omega_d)} - \frac{e^{-j\omega_d t_{II}}}{\xi\omega_0 + j(\omega - \omega_d)} \right] \\ & - e^{-\xi\omega_0 T} e^{-j\omega T} \frac{jA_{II}}{2} \left[\frac{e^{j\omega_d(t_{II} - T)}}{\xi\omega_0 + j(\omega + \omega_d)} - \frac{e^{-j\omega_d(t_{II} - T)}}{\xi\omega_0 + j(\omega - \omega_d)} \right] \end{aligned} \quad (6.101)$$

The spectrum of the trailing wavelet is Equation (5.117), and is expressed as:

$$F_{III,T}(\omega) = \frac{jA_{III}}{2} e^{-j\omega T} \left[\frac{e^{j\omega_d t_{III}}}{\xi\omega_0 + j(\omega + \omega_d)} - \frac{e^{-j\omega_d t_{III}}}{\xi\omega_0 + j(\omega - \omega_d)} \right] \quad (6.102)$$

The spectrum of the twin wavelets is the superposition of Equations (6.101) and (6.102), and is given as:

$$F_{II,III}(\omega) = F_{II}(\omega) + F_{III,T}(\omega) \quad (6.103)$$

The spectrum of the U-wavelet is the superposition of Equations (6.100) and (6.103), and using $\varpi = \omega_d$ gives:

$$F_U(\omega) = F_I(\omega) + F_{II}(\omega) + F_{III,T}(\omega) \quad (6.104)$$

The mapping defined in Equation (6.98) leads to the spectrum of the normalized source signature as:

$$F^*(\omega) = F_I^*(\omega) + F_{II}^*(\omega) + F_{III,T}^*(\omega), \quad (6.105)$$

where: $F_I^*(\omega)$, $F_{II}^*(\omega)$, and $F_{III,T}^*(\omega)$ are defined in Equations (6.106) to (6.108).

The spectrum of the normalized sinusoidal wavelet is mapped from Equation (6.100) as:

$$\begin{aligned} F_I^*(\omega) = & \frac{A_I^*}{\omega^2 - \varpi^2} [j\omega \sin(\varpi t_I) - \varpi \cos(\varpi t_I)] \\ & + \frac{jA_I^*}{2} [\delta(\omega + \varpi)(e^{-j\omega t_I} + e^{j\varpi t_I}) - \delta(\omega - \varpi)(e^{-j\omega t_I} + e^{-j\varpi t_I})] \\ & - \frac{A_I^*}{\omega^2 - \varpi^2} [j\omega \sin(\varpi(t_I - T)) - \varpi \cos(\varpi(t_I - T))] \\ & - \frac{jA_I^*}{2} [\delta(\omega + \varpi)(e^{-j\omega(t_I - T)} + e^{j\varpi(t_I - T)}) \\ & \quad - \delta(\omega - \varpi)(e^{-j\omega(t_I - T)} + e^{-j\varpi(t_I - T)})] \end{aligned} \quad (6.106)$$

The spectrum of the normalized transient wavelet is mapped from Equation (6.101) as:

$$\begin{aligned} F_{II}^*(\omega) = & \frac{jA_{II}^*}{2} \left[\frac{e^{j\omega_d t_{II}}}{\xi\omega_0 + j(\omega + \omega_d)} - \frac{e^{-j\omega_d t_{II}}}{\xi\omega_0 + j(\omega - \omega_d)} \right] \\ & - e^{-\xi\omega_0 T} e^{-j\omega T} \frac{jA_{II}^*}{2} \left[\frac{e^{j\omega_d(t_{II} - T)}}{\xi\omega_0 + j(\omega + \omega_d)} - \frac{e^{-j\omega_d(t_{II} - T)}}{\xi\omega_0 + j(\omega - \omega_d)} \right] \end{aligned} \quad (6.107)$$

The spectrum of the normalized trailing wavelet is mapped from Equation (6.102) as:

$$F_{III,T}^*(\omega) = \frac{jA_{III}^*}{2} e^{-j\omega T} \left[\frac{e^{j\omega_d t_{III}}}{\xi\omega_0 + j(\omega + \omega_d)} - \frac{e^{-j\omega_d t_{III}}}{\xi\omega_0 + j(\omega - \omega_d)} \right] \quad (6.108)$$

The spectrum of the normalized twin wavelets is the superposition of Equations (6.107) and (6.108) as:

$$F_{II,III}^*(\omega) = F_{II}^*(\omega) + F_{III,T}^*(\omega) \quad (6.109)$$

The spectrum of the normalized U-wavelet is the superposition of Equations (6.106) and (6.109), and using $\varpi = \omega_d$ gives:

$$F_U^*(\omega) = F_I^*(\omega) + F_{II}^*(\omega) + F_{III,T}^*(\omega) \quad (6.110)$$

The spectra of the normalized source signature are demonstrated in Figure 6.18 through Figure 6.21.

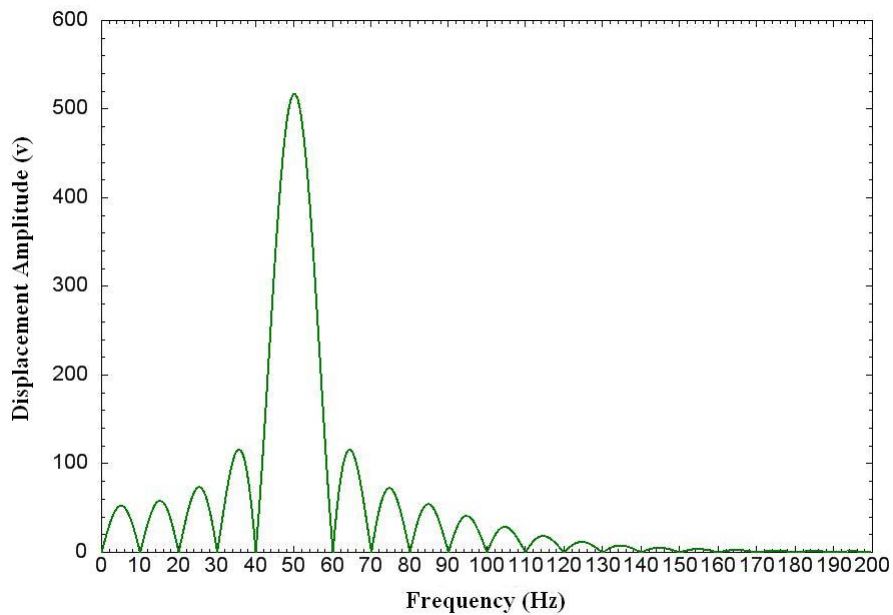


Figure 6.18 Displacement spectrum of source signature of the model test (excitation frequency 50 Hz, duration 0.1 sec, damped frequency 100 Hz, damping ratio 25%)

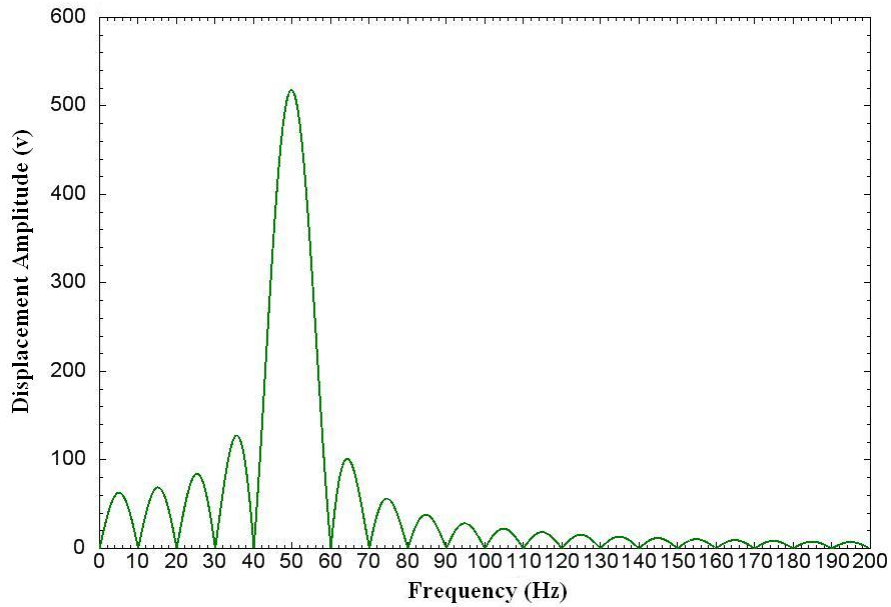


Figure 6.19 Displacement spectrum of sinusoidal wavelet of the model test (excitation frequency 50 Hz, duration 0.1 sec, damped frequency 100 Hz, damping ratio 25%)

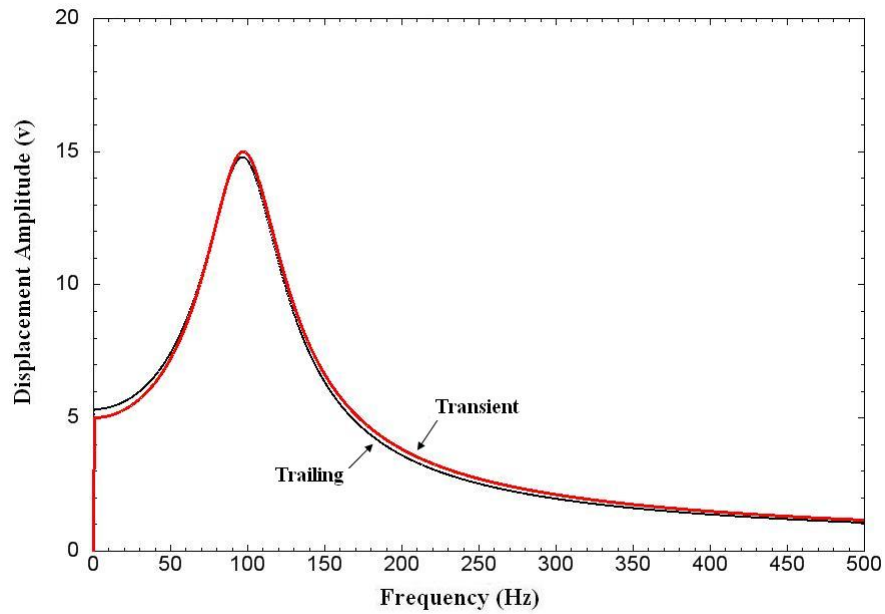


Figure 6.20 Displacement spectrum of transient and trailing wavelets of the model test (excitation frequency 50 Hz, duration 0.1 sec, damped frequency 100 Hz, damping ratio 25%)

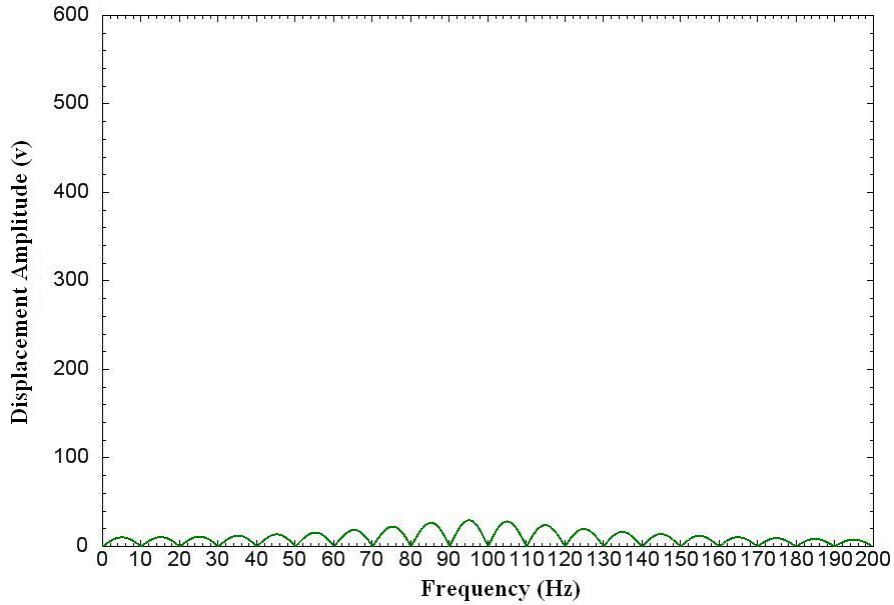


Figure 6.21 Displacement spectrum of twin wavelets of the model test (excitation frequency 50 Hz, duration 0.1 sec, damped frequency 100 Hz, damping ratio 25%)

6.6 SPECTRUM OF THE NORMALIZED VELOCITY SIGNATURE

The spectrum of the normalized velocity signature can be mapped from that of the normalized source signature. The following terms for initial time shift of velocity wavelets are defined as:

$$t_{I,v} = t_I + \frac{\pi}{2\omega}, \quad (6.111)$$

$$t_{II,v} = t_{II} + t_v, \quad (6.112)$$

$$t_{III,v} = t_{III} + t_v. \quad (6.113)$$

By comparing the amplitude and phase of the normalized source signature (Equation 6.62) with those of the normalized velocity signature (Equation 6.90) and using the definitions in Equations (6.111) to (6.113), the following mapping relationships are obtained:

$$A_I^* \rightarrow -\varpi A_I^*, t_I \rightarrow t_{I,v}, \quad (6.114)$$

$$A_{II}^* \rightarrow -\omega_0 A_{II}^*, t_{II} \rightarrow t_{II,v}, \quad (6.115)$$

$$A_{III}^* \rightarrow -\omega_0 A_{III}^*, t_{III} \rightarrow t_{III,v}. \quad (6.116)$$

Equation (6.114) maps Equation (6.106) to the velocity spectrum of the normalized sinusoidal wavelet as:

$$\begin{aligned} \dot{F}_I^*(\omega) = & -\frac{\varpi A_I^*}{\omega^2 - \varpi^2} [j\omega \sin(\varpi t_{I,v}) - \varpi \cos(\varpi t_{I,v})] \\ & - \frac{j\varpi A_I^*}{2} [\delta(\omega + \varpi)(e^{-j\omega t_{I,v}} + e^{j\varpi t_{I,v}}) - \delta(\omega - \varpi)(e^{-j\omega t_{I,v}} + e^{-j\varpi t_{I,v}})] \\ & + \frac{\varpi A_I^*}{\omega^2 - \varpi^2} [j\omega \sin(\varpi(t_{I,v} - T)) - \varpi \cos(\varpi(t_{I,v} - T))] \\ & + \frac{j\varpi A_I^*}{2} [\delta(\omega + \varpi)(e^{-j\omega(t_{I,v} - T)} + e^{j\varpi(t_{I,v} - T)}) \\ & \quad - \delta(\omega - \varpi)(e^{-j\omega(t_{I,v} - T)} + e^{-j\varpi(t_{I,v} - T)})] \end{aligned} \quad (6.117)$$

Equation (6.115) maps Equation (6.107) to the velocity spectrum of the normalized transient wavelet as:

$$\begin{aligned} \dot{F}_{II}^*(\omega) = & -\frac{j\omega_0 A_{II}^*}{2} \left[\frac{e^{j\omega_d t_{II,v}}}{\xi\omega_0 + j(\omega + \omega_d)} - \frac{e^{-j\omega_d t_{II,v}}}{\xi\omega_0 + j(\omega - \omega_d)} \right] \\ & + e^{-\xi\omega_0 T} e^{-j\omega T} \frac{j\omega_0 A_{II}^*}{2} \left[\frac{e^{j\omega_d(t_{II,v} - T)}}{\xi\omega_0 + j(\omega + \omega_d)} - \frac{e^{-j\omega_d(t_{II,v} - T)}}{\xi\omega_0 + j(\omega - \omega_d)} \right] \end{aligned} \quad (6.118)$$

Equation (6.116) maps Equation (6.108) to the velocity spectrum of the normalized trailing wavelet as:

$$\dot{F}_{III,T}^*(\omega) = -\frac{j\omega_0 A_{III}^*}{2} e^{-j\omega T} \left[\frac{e^{j\omega_d t_{III,v}}}{\xi\omega_0 + j(\omega + \omega_d)} - \frac{e^{-j\omega_d t_{III,v}}}{\xi\omega_0 + j(\omega - \omega_d)} \right] \quad (6.119)$$

The velocity spectrum of the normalized twin wavelets is the superposition of Equations (6.118) and (6.119) and is expressed as:

$$\dot{F}_T^*(\omega) = \dot{F}_U^*(\omega) + \dot{F}_{III,T}^*(\omega) \quad (6.120)$$

The velocity spectrum of the normalized U-wavelet is the superposition of Equations (6.117) and (6.119) and using $\varpi = \omega_d$ is expressed as:

$$\dot{F}_U^*(\omega) = \dot{F}_I^*(\omega) + \dot{F}_{II}^*(\omega) + \dot{F}_{III,T}^*(\omega) \quad (6.121)$$

The spectrum of the normalized velocity signature is the superposition of Equations (6.117) and (6.119) as:

$$\dot{F}^*(\omega) = \dot{F}_I^*(\omega) + \dot{F}_{II}^*(\omega) + \dot{F}_{III,T}^*(\omega) \quad (6.122)$$

The spectra of the normalized velocity signature are demonstrated in Figure 6.22 through Figure 6.24.

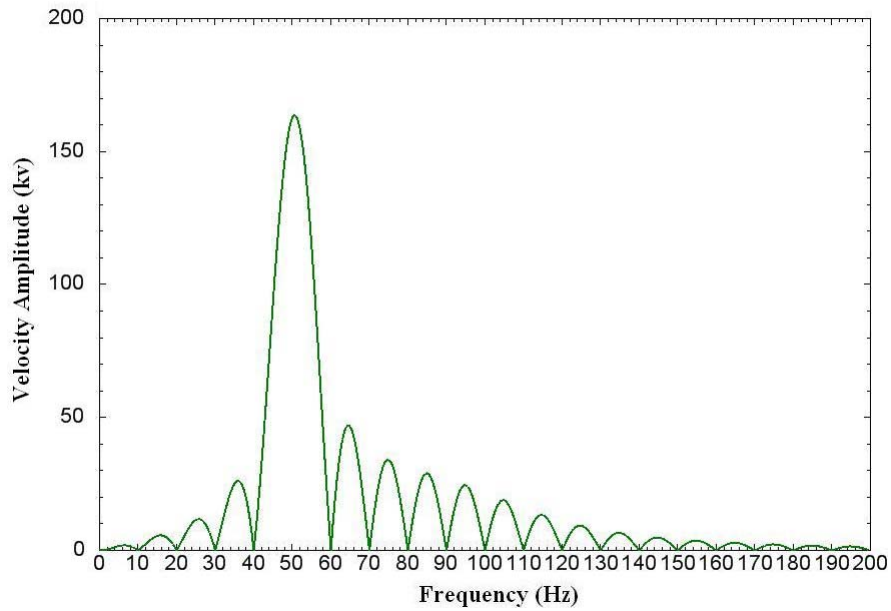


Figure 6.22 Velocity spectrum of source signature of the model test (excitation frequency 50 Hz, duration 0.1 sec, damped frequency 100 Hz, damping ratio 25%)

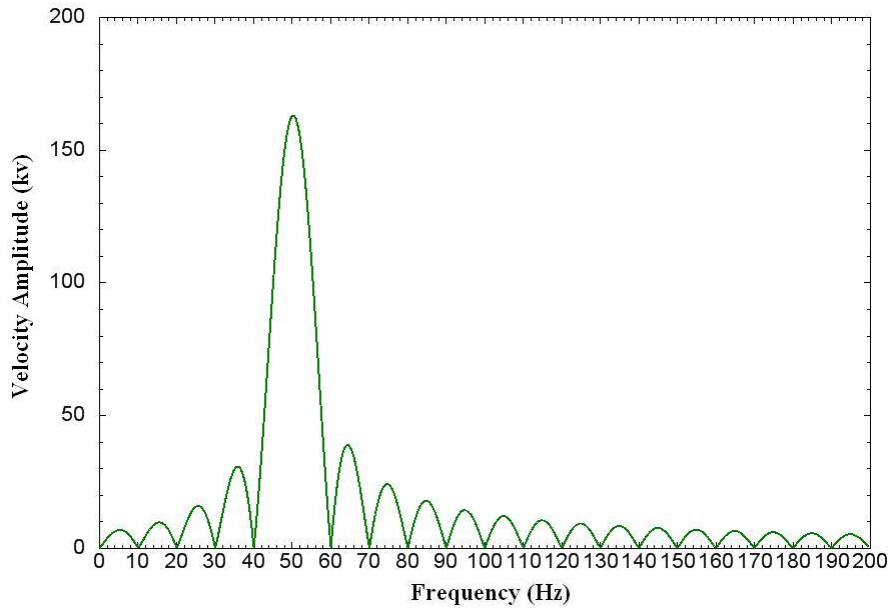


Figure 6.23 Velocity spectrum of sinusoidal wavelet of the model test (excitation frequency 50 Hz, duration 0.1 sec, damped frequency 100 Hz, damping ratio 25%)

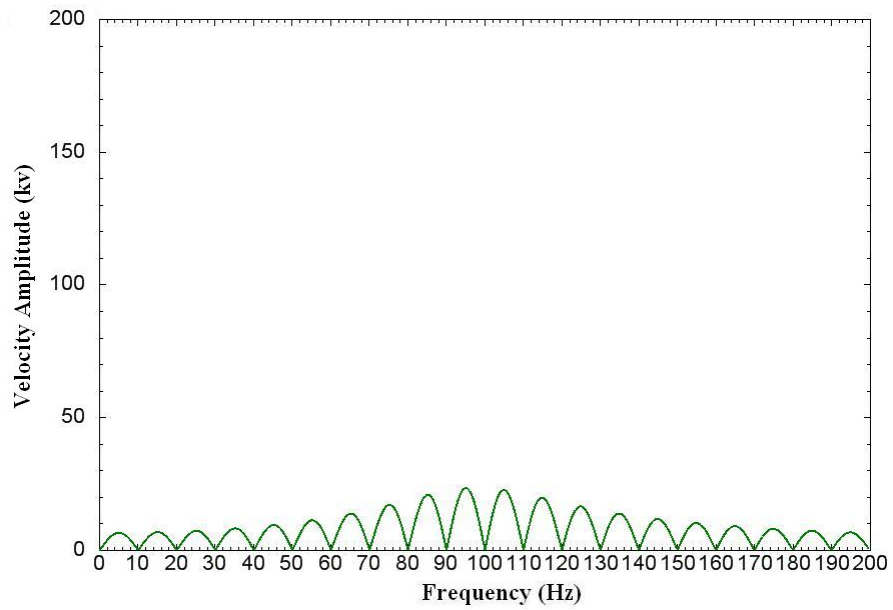


Figure 6.24 Velocity spectrum of twin wavelets of the model test (excitation frequency 50 Hz, duration 0.1 sec, damped frequency 100 Hz, damping ratio 25%)

6.7 SPECTRUM OF THE NORMALIZED ACCELERATION SIGNATURE

The spectrum of the normalized acceleration signature can be mapped from that of the normalized source signature. The terms for initial time shift of acceleration wavelets are defined as:

$$t_{II,a} = t_{II} + t_a, \quad (6.123)$$

$$t_{III,a} = t_{III} + t_a. \quad (6.124)$$

The amplitude and phase of the normalized source signature (Equation 6.62) are compared with those of the normalized acceleration signature (Equation 6.97). Using the definitions in Equations (6.123) and (6.124), the following mapping relationships are obtained:

$$A_I^* \rightarrow -\varpi^2 A_I^*, t_I \rightarrow t_I \quad (6.125)$$

$$A_{II}^* \rightarrow \omega_0^2 A_{II}^*, t_{II} \rightarrow t_{II,a} \quad (6.126)$$

$$A_{III}^* \rightarrow \omega_0^2 A_{III}^*, t_{III} \rightarrow t_{III,a} \quad (6.127)$$

Equation (6.125) maps Equation (6.106) to the acceleration spectrum of the normalized sinusoidal wavelet as:

$$\begin{aligned} \ddot{F}_I^*(\omega) = & -\frac{\varpi^2 A_I^*}{\omega^2 - \varpi^2} [j\omega \sin(\varpi t_I) - \varpi \cos(\varpi t_I)] \\ & - \frac{j\varpi^2 A_I^*}{2} [\delta(\omega + \varpi)(e^{-j\omega t_I} + e^{j\varpi t_I}) - \delta(\omega - \varpi)(e^{-j\omega t_I} + e^{-j\varpi t_I})] \\ & + \frac{\varpi^2 A_I^*}{\omega^2 - \varpi^2} [j\omega \sin(\varpi(t_I - T)) - \varpi \cos(\varpi(t_I - T))] \\ & + \frac{j\varpi^2 A_I^*}{2} [\delta(\omega + \varpi)(e^{-j\omega(t_I - T)} + e^{j\varpi(t_I - T)}) \\ & \quad - \delta(\omega - \varpi)(e^{-j\omega(t_I - T)} + e^{-j\varpi(t_I - T)})] \end{aligned} \quad (6.128)$$

Equation (6.126) maps Equation (6.107) to the acceleration spectrum of the normalized transient wavelet as:

$$\begin{aligned} \ddot{F}_{II}^*(\omega) = & \frac{j\omega_0^2 A_{II}^*}{2} \left[\frac{e^{j\omega_d t_{II,a}}}{\xi\omega_0 + j(\omega + \omega_d)} - \frac{e^{-j\omega_d t_{II,a}}}{\xi\omega_0 + j(\omega - \omega_d)} \right] \\ & - e^{-\xi\omega_0 T} e^{-j\omega T} \frac{j\omega_0^2 A_{II}^*}{2} \left[\frac{e^{j\omega_d (t_{II,a}-T)}}{\xi\omega_0 + j(\omega + \omega_d)} - \frac{e^{-j\omega_d (t_{II,a}-T)}}{\xi\omega_0 + j(\omega - \omega_d)} \right] \end{aligned} \quad (6.129)$$

Equation (6.127) maps Equation (6.108) to the acceleration spectrum of the normalized trailing wavelet as:

$$\ddot{F}_{III,T}^*(\omega) = \frac{j\omega_0^2 A_{III}^*}{2} e^{-j\omega T} \left[\frac{e^{j\omega_d t_{III,a}}}{\xi\omega_0 + j(\omega + \omega_d)} - \frac{e^{-j\omega_d t_{III,a}}}{\xi\omega_0 + j(\omega - \omega_d)} \right] \quad (6.130)$$

The acceleration spectrum of the normalized twin wavelets is the superposition of Equations (6.129) and (6.130) and is expressed as:

$$\ddot{F}_T^*(\omega) = \ddot{F}_{II}^*(\omega) + \ddot{F}_{III,T}^*(\omega) \quad (6.131)$$

The acceleration spectrum of the normalized U-wavelet is the superposition of Equations (6.128) and (6.131), and using $\varpi = \omega_d$ is expressed as:

$$\ddot{F}_U^*(\omega) = \ddot{F}_I^*(\omega) + \ddot{F}_{II}^*(\omega) + \ddot{F}_{III,T}^*(\omega) \quad (6.132)$$

The spectrum of the normalized acceleration signature is the superposition of Equations (6.128) and (6.131) as:

$$\ddot{F}^*(\omega) = \ddot{F}_I^*(\omega) + \ddot{F}_{II}^*(\omega) + \ddot{F}_{III,T}^*(\omega) \quad (6.133)$$

The spectra of the normalized acceleration signatures are demonstrated in Figure 6.25 through Figure 6.27.

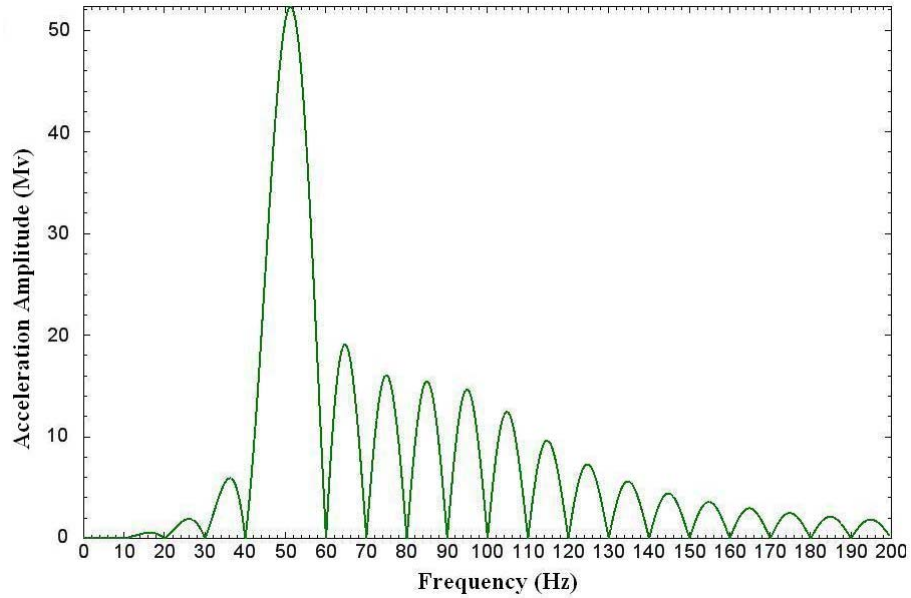


Figure 6.25 Acceleration spectrum of source signature of the model test (excitation frequency 50 Hz, duration 0.1 sec, damped frequency 100 Hz, damping ratio 25%)

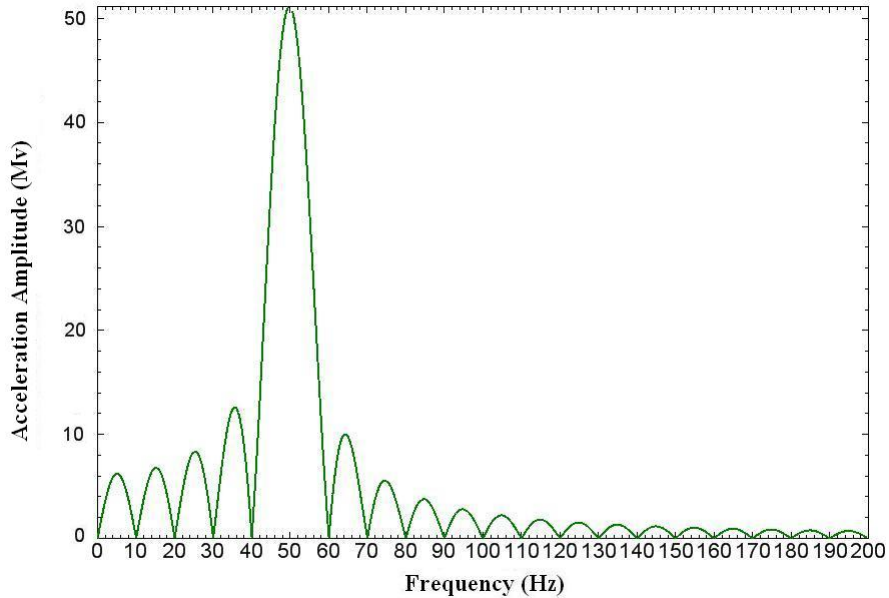


Figure 6.26 Acceleration amplitude spectrum of sinusoidal wavelet of the model test (excitation frequency 50 Hz, duration 0.1 sec, damped frequency 100 Hz, damping ratio 25%)

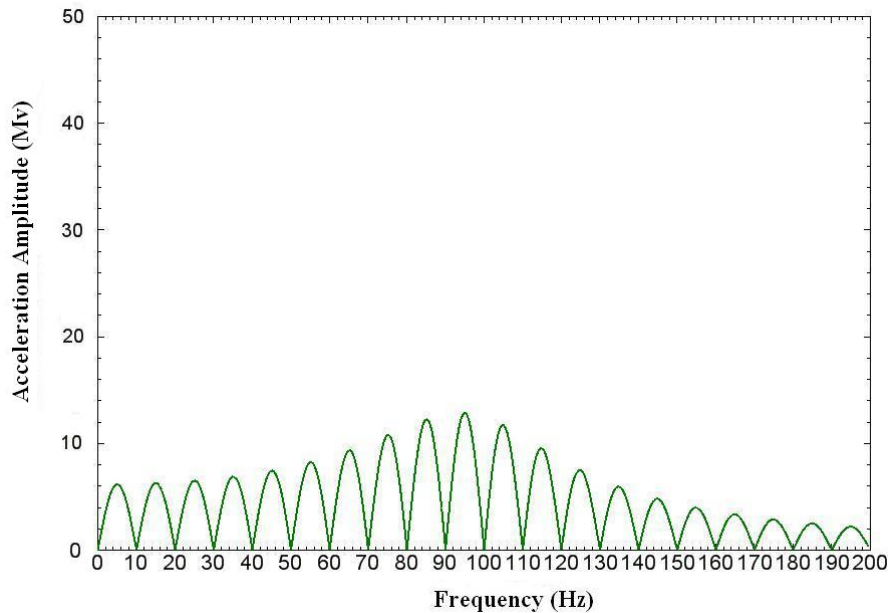


Figure 6.27 Acceleration spectrum of twin wavelets of the model test (excitation frequency 50 Hz, duration 0.1 sec, damped frequency 100 Hz, damping ratio 25%)

6.8 SUMMARY

In this chapter, a new method for measuring the damping ratio and natural frequency of the vibrator-earth system is introduced. Damped free vibration as part of the vibratory source contains the finger print of the parameters of the system. Mapping of the measured free vibration signal to the theoretical free vibration curve in the frequency domain leads to the eventual identification of the source signatures for displacement, velocity and acceleration. Normalized source signatures are preferred because the scaling constant is irrelevant to the travel time analysis.

The normalized source signature is relevant to four parameters: the excitation frequency, the duration of the excitation, the damping ratio and the natural frequency of the vibrator-earth system. The spectral analysis of the source signatures in this chapter is essential for the wavelet response analysis in the next chapter.

Chapter 7 Analysis of Wavelet Response

7.1 INTRODUCTION

In this chapter, the wavelet-response approach that is used in analyzing travel times is introduced. The wavelet-response approach was developed as part of this research. Wavelet response is generally the same as impulse response, except that the former takes into consideration the velocity dispersion for wavelets with discrete frequency contents.

This work uses deterministic deconvolution method to extract source signature from the recorded signals, and to obtain a wavelet response for travel time analysis. A wavelet response is similar to an impulse response as noted earlier. The difference between a wavelet response and an impulse response lies in how to treat the velocity dispersion of the source signature. An impulse response neglects the phase shifts caused by velocity dispersion between different frequencies in the source wavelet, and assigns one spike to represent each reflection coefficient. The wavelet response decomposes a source wavelet into separate pure wavelets, each of which has a separate spike in the wavelet response. The wavelet response method is not practical for chirp sweeps because the frequency band in a chirp sweep is continuous rather than discrete. A wavelet response degenerates to an impulse response if a durational wavelet is treated as an impulsive wavelet and the wavelet velocity dependence on frequency is ignored. As a result, the relative separation of the wavelets within the source signature during propagation is considered as the expansion of the breadth of group energy.

In this research, the source signature is divided into a few pure wavelets. The energy of the sinusoidal wavelet dominates the source signature. The advantage of the sinusoidal wavelet is that it has no time-varying wavelet envelope. Other pure wavelets

have negligible dispersion concerns within a wavelet because each pure wavelet carries only one frequency. As a result its frequency content does not vary with the propagation distance if only velocity anisotropy is considered. The frequency content of a pure wavelet remains stable during propagation. This is a unique and important feature of wavelet response analysis. The shape of each pure wavelet also remains relatively stable during propagation, especially for the sinusoidal wavelet even though it is subject to scaling when taking into account the attenuation anisotropy.

A pure wavelet does not experience a phase shift caused by frequency content variation. Thus mixed-phase issues do not exist in contrast to other deconvolution techniques assuming signals are of zero-phase or minimum-phase. Wavelet response analysis does not cause differential phase shift between traces at different depths.

The difference between a source signature and a normalized source signature is a constant amplitude scale, which does not affect the analysis of the phase shift related the travel time analysis. Hence, the normalized source signature is preferred.

The normalized source signature in Equation (6.62) is divided into two pure wavelets:

$$u^*(t) = u_I^*(t) + u_T^*(t) \quad (7.1)$$

where the sinusoidal wavelet is:

$$u_I^*(t) = A_I^*[U(t) - U(t - T)]\sin[\varpi(t - t_I)] \quad (7.2)$$

and the twin wavelets or doublet are:

$$u_T^*(t) = A_{II}^*e^{-\xi\omega_0 t}[U(t) - U(t - T)]\sin[\omega_d(t - t_{II})] \\ + A_{III}^*e^{-\xi\omega_0(t-T)}U(t - T)\sin[\omega_d(t - T - t_{III})] \quad (7.3)$$

As seen from Equations (7.2) and (7.3), the sinusoidal wavelet has a carrier frequency of ϖ , while the twin wavelets have a carrier frequency of ω_d .

Dispersion may occur if wavelets have different frequencies. Different frequencies can travel at different speeds and will attenuate at different amplitude scales. To avoid possible dispersion, the optimum excitation frequency should satisfy:

$$\varpi = \omega_d, \quad (7.4)$$

which is applicable when the measured in-situ damped frequency ω_d is within the excitation frequency range of the vibrator (Figure 3.3). Then the sinusoidal wavelet and the twin wavelets merge into one pure wavelet, specifically the U-wavelet:

$$\begin{aligned} u_U^*(t) = & A_I^*[U(t) - U(t-T)]\sin[\omega_d(t-t_I)] \\ & + A_{II}^*e^{-\xi\omega_0 t}[U(t) - U(t-T)]\sin[\omega_d(t-t_{II})] \\ & + A_{III}^*e^{-\xi\omega_0(t-T)}U(t-T)\sin[\omega_d(t-T-t_{III})] \end{aligned} \quad (7.5)$$

For convenience, $u(t)$ is used to express any pure wavelet in Equation (7.2) depending on context. Within the context of integration operation, any wavelet with a time delay t_0 is expressed as a convolution of an impulse $\delta(t-t_0)$ with the wavelet $u(t)$:

$$u(t-t_0) = \delta(t-t_0) * u(t) \quad (7.6)$$

7.2 WAVELET RESPONSE FOR U-WAVELET

Equation (7.5) implies that all reflected waves and direct waves will travel at the same speed at the same frequency ϖ or ω_d due to $\varpi = \omega_d$. The difference between the direct arrivals and the different reflections is the magnitude of the signal amplitude and its phase shift, because the time delay and amplitude attenuation vary with the lengths and traces of ray paths. Figure 7.1 demonstrates the wave propagation measured by four receivers, R1 to R4, in the same layer of geological material. Each spike (vertical line) represents the initial arrival time of a wave passing a receiver. The height of the spikes represents the wave amplitude. The solid vertical lines denote the downward wavelet

propagation; the dashed ones denote upward propagation. All the downward reflection directions have the same slope as the direct arrival because the slope represents the velocity of the layer. All the upward reflections are also parallel and have the same absolute slope as that of the downward reflections.

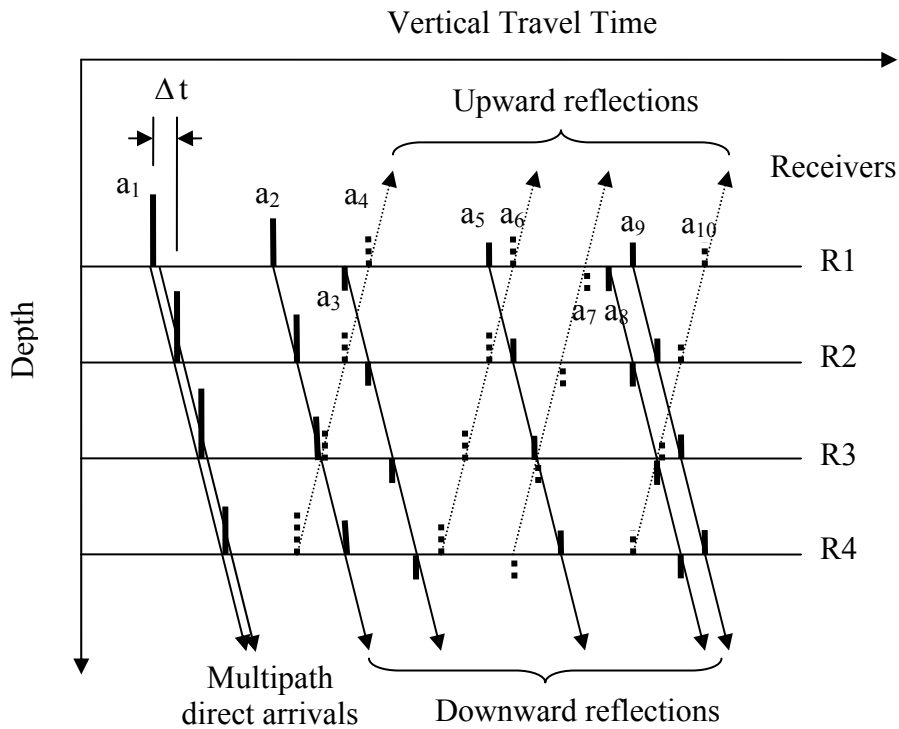


Figure 7.1 Illustration of amplitude attenuation and time delay of wave propagation

As a convention in signal processing, each of these arrivals is called a component. Any component $w_i(t)$ is a waveform similar to the source signature but is amplitude-scaled by a real constant a_i and is time-shifted by a real constant t_i as expressed by:

$$w_i(t) = a_i u(t - t_i), \quad (7.7)$$

where $u(t)$ is the U-wavelet in Equation (7.5). The receiver signal $u_R(t)$ is thus a multi-component signal of the same frequency, or:

$$u_R(t) = \sum_{i=1}^n w_i(t-t_i) \quad (7.8)$$

where: n is the total number of components. By substituting Equations (7.6) and (7.7) into the Equation (7.8), one obtains

$$\begin{aligned} u_R(t) &= \sum_{i=1}^n a_i u(t-t_i) \\ &= \sum_{i=1}^n a_i [\delta(t-t_i) * u(t)] \\ &= \left[\sum_{i=1}^n a_i \delta(t-t_i) \right] * u(t) \end{aligned} \quad (7.9)$$

The term in the square brackets in Equation (7.9) is defined as a new time series $R(t)$ as:

$$R(t) = \sum_{i=1}^n a_i \delta(t-t_i). \quad (7.10)$$

If the source wavelet $u(t)$ is an impulsive wavelet or an impulse, $R(t)$ is called the impulse response of a system, and the real coefficients a_i are called reflection coefficients when the seismic signal $u_R(t)$ is measured on the ground surface and characterized by reflections. When dispersion exists, the dominant frequency content of the impulsive wavelet may vary with depth, especially in the case of the deep downhole test. Higher frequencies attenuate faster than lower frequencies. As waves propagate significantly long distances, higher frequencies will be replaced by lower frequencies. An impulse response tracks the energy of the dominant frequencies regardless of the frequency content shift.

If the source wavelet $u(t)$ is a pure wavelet (a single frequency), the location of the spikes in Figure 7.2 depends on the frequency of $u(t)$ because of different frequency travels at a different speed. A source wavelet in a different frequency will result in a different response $R(t)$, thus $R(t)$ is termed the wavelet response for the purpose of

differentiating from the impulse response. The real coefficients a_i are actually the arrival coefficients when the measurement is in a borehole. The first spike in Figure 7.2 is the direct arrival or transmitted wave coefficient. The later spikes are multi-path direct arrivals, same path but split wave direct arrivals, or indirect arrivals consisting of one or more reflections and transmissions during the mixed up-going and down-going trips.

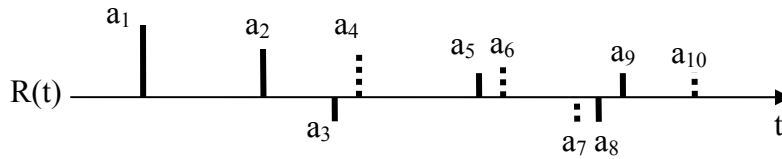


Figure 7.2 Noise-free single wavelet response

When the source signal consists of two or more pure wavelets, different wavelets travel at different speeds (Figure 7.3). All the parallel solid lines denote wavelet b while parallel dotted lines denote wavelet c. The corresponding wavelet response $R(t)$ is:

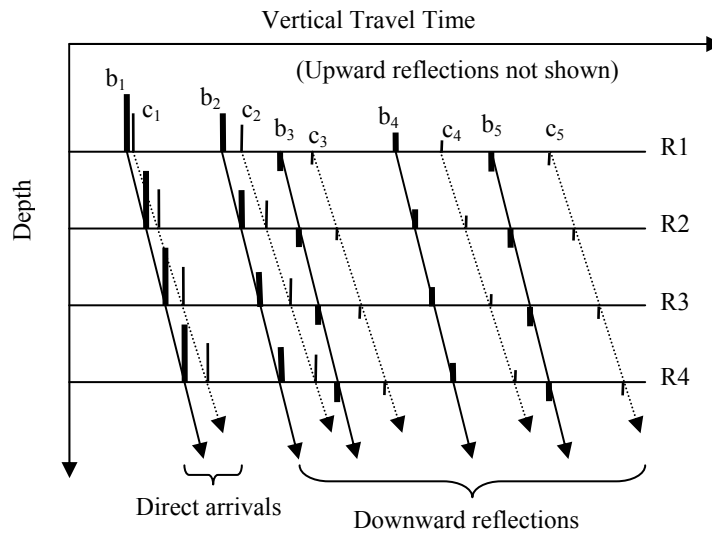


Figure 7.3 Velocity dispersion of dual wavelets with time and depth

$$R(t) = \sum_{i=1}^n b_i \delta(t - t_i) + \sum_{j=1}^m c_j \delta(t - t_j). \quad (7.11)$$

Figure 7.4 demonstrates the dispersion effect of different pure wavelets with time. The late arrival spikes in the time axis of the two wavelets (b and c) become increasingly separated because the later ones in time travel longer distances. Thus the dispersion effect accumulates with time delay.

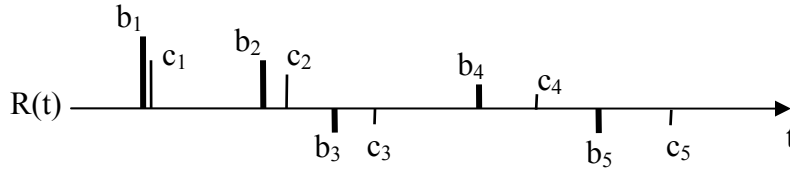


Figure 7.4 Noise-free dual wavelet response (upward reflections not shown)

When the two wavelets have the same carrier frequency, they merge into the U-wavelet which is a single wavelet. For the single wavelet case, the Fourier transform of the receiver signal in Equation (7.9) is:

$$\begin{aligned} \hat{F}\{u_R(t)\} &= \sum_{i=1}^n a_i \hat{F}\{u(t - t_i)\} \\ &= \sum_{i=1}^n a_i e^{-j\omega t_i} \hat{F}\{u(t)\} \\ &= \sum_{i=1}^n a_i e^{-j\omega t_i} F(\omega) \end{aligned} \quad (7.12)$$

where $F(\omega)$ is defined in Equation (5.123).

If the discrete coefficients a_i are considered as discrete values of a continuous function $a(t)$, this situation can be expressed by:

$$a(t) = \sum_{i=-\infty}^{+\infty} a_i \delta(t - t_i) = \begin{cases} a_i & t = t_i \\ 0 & \text{otherwise} \end{cases} \quad (7.13)$$

By comparing Equations (7.13) and (7.10), $a(t)$ is determined as the wavelet response to a single wavelet and is represented by:

$$R(t) = a(t) \quad (7.14)$$

Using the continuous wavelet response, Equations (7.9) and (7.12) become Equations (7.15) and (7.16), respectively, as:

$$u_R(t) = R(t) * u(t) \quad (7.15)$$

$$\begin{aligned} \hat{F}\{u_R(t)\} &= \int_{-\infty}^{\infty} R(t)e^{-j\omega t} dt \cdot F(\omega) \\ &= \hat{F}\{R(t)\} \cdot F(\omega) \end{aligned} \quad (7.16)$$

The wavelet response $R(t)$ is obtained using deconvolution. Rearranging Equation (7.16) yields:

$$\hat{F}\{R(t)\} = \frac{\hat{F}\{u_R(t)\}}{F(\omega)}, \quad (7.17)$$

or

$$R(t) = \hat{F}^{-1}\left\{\frac{\hat{F}\{u_R(t)\}}{F(\omega)}\right\}. \quad (7.18)$$

where: \hat{F}^{-1} denotes the inverse Fourier transform.

The receiver signal $u_R(t)$ is an ideal noise-free multi-component signal. If $\tilde{u}_R(t)$ denotes the actual measured receiver signal, $\tilde{n}_R(t)$ denotes the noise, then the following is true for a linear system as:

$$\tilde{u}_R(t) = u_R(t) + \tilde{n}_R(t). \quad (7.19)$$

By substituting Equation (7.18) into (7.17), one obtains:

$$\begin{aligned}
R(t) &= \hat{F}^{-1} \left\{ \frac{\hat{F} \{ \tilde{u}_R(t) - \tilde{n}_R(t) \}}{F(\omega)} \right\} \\
&= \hat{F}^{-1} \left\{ \frac{\hat{F} \{ \tilde{u}_R(t) \}}{F(\omega)} - \frac{\hat{F} \{ \tilde{n}_R(t) \}}{F(\omega)} \right\} \\
&\approx \hat{F}^{-1} \left\{ \frac{\hat{F} \{ \tilde{u}_R(t) \}}{F(\omega)} \right\}
\end{aligned} \tag{7.20}$$

As presented in Equation (7.20), noise $\tilde{n}_R(t)$ can be filtered significantly when the signal to noise ratio is high. In other words, the wavelet response $R(t)$ can be obtained as long as the receiver signal $\tilde{u}_R(t)$ and the source signature $u(t)$ are available.

7.3 WAVELET RESPONSE FOR DUAL WAVELETS

When the excitation frequency and the damped frequency are not equal ($\varpi \neq \omega_d$), wavelets in Equations (7.2) and (7.3) will travel at different velocities and eventually will separately attenuate (Figure 7.3). The receiver signal with n components of sinusoidal wavelet w_1 and m components of twin wavelets w_2 can be expressed as:

$$u_R(t) = \sum_{i=1}^n b_i w_1(t-t_i) + \sum_{i=1}^m c_i w_2(t-t_i). \tag{7.21}$$

The number of components m and n may not equal due to different degrees of attenuation that may filter some of the components. This situation can be expressed as:

$$\begin{aligned}
\hat{F} \{ u_R(t) \} &= \sum_{i=1}^n b_i \hat{F} \{ w_1(t-t_i) \} + \sum_{i=1}^m c_i \hat{F} \{ w_2(t-t_i) \} \\
&= \sum_{i=1}^n b_i e^{-j\omega t_i} \hat{F} \{ w_1(t) \} + \sum_{i=1}^m c_i e^{-j\omega t_i} \hat{F} \{ w_2(t) \} \\
&= \sum_{i=1}^n b_i e^{-j\omega t_i} F_I(\omega) + \sum_{i=1}^m c_i e^{-j\omega t_i} F_{II,III}(\omega)
\end{aligned} \tag{7.22}$$

where: $F_I(\omega)$ and $F_{II,III}(\omega)$ are defined in Equations (5.104) and (5.122), respectively. The terms w_1 and w_2 are defined in Equations (7.2) and (7.3), respectively.

Similar to Equation (7.13), the discrete arrival coefficients in Equation (7.22) can be regarded as the discrete values of continuous functions and are expressed as:

$$b(t) = \begin{cases} b_i & t = t_i \\ 0 & \text{otherwise} \end{cases}, \quad c(t) = \begin{cases} c_i & t = t_i \\ 0 & \text{otherwise} \end{cases} \quad (7.23)$$

where: $b(t)$ is the sinusoidal wavelet response and $c(t)$ is the twin wavelets response. Accordingly, the continuous version for Equation (7.22) becomes:

$$\begin{aligned} \hat{F}\{u_R(t)\} &= \int_{-\infty}^{\infty} b(t)e^{-j\omega t} dt \cdot F_I(\omega) + \int_{-\infty}^{\infty} c(t)e^{-j\omega t} dt \cdot F_{II,III}(\omega) \\ &= \hat{F}\{b(t)\} \cdot F_I(\omega) + \hat{F}\{c(t)\} \cdot F_{II,III}(\omega) \end{aligned} \quad (7.24)$$

When the noise item in Equation (7.19) is considered, Equation (7.24) becomes:

$$\hat{F}\{\tilde{u}_R(t)\} = \hat{F}\{\tilde{b}(t)\} \cdot F_I(\omega) + \hat{F}\{\tilde{c}(t)\} \cdot F_{II,III}(\omega) \quad (7.25)$$

where $\tilde{b}(t)$ and $\tilde{c}(t)$ are noised wavelet responses for $b(t)$ and $c(t)$, respectively. Two unknowns ($\tilde{b}(t)$ and $\tilde{c}(t)$) are presented in Equation (7.25). Direct deconvolution is not available. The wavelet response for dual wavelets is

$$R(t) = \tilde{b}(t) + \tilde{c}(t) \quad (7.26)$$

The stringent wavelet response solution for Equation (7.25) requires obtaining Equation (7.26) which is left for future work. Except cross-correlation method, two other approximations are applicable considering the twin wavelets spectrum $F_{II,III}(\omega)$ has much less energy contribution to the receiver signal $\tilde{u}_R(t)$ than the sinusoidal wavelet term. One approximation is to filter the twin wavelets and the other is to treat it as noise.

The source signature defined in Figure 7.5 is characterized by excitation frequency 50 Hz, natural frequency 40 Hz, source duration 0.1273 sec, and damping ratio 25%. Figure 7.6 is the amplitude spectrum of the source signature. The peak amplitude of the sinusoidal wavelet is 56 db, while that of the twin wavelets is 46 db, indicating a 10-db difference in peak energy. If the areas covered under the peak amplitude lobes are

considered, the energy difference is much greater or the contribution of the twin wavelets is much smaller.

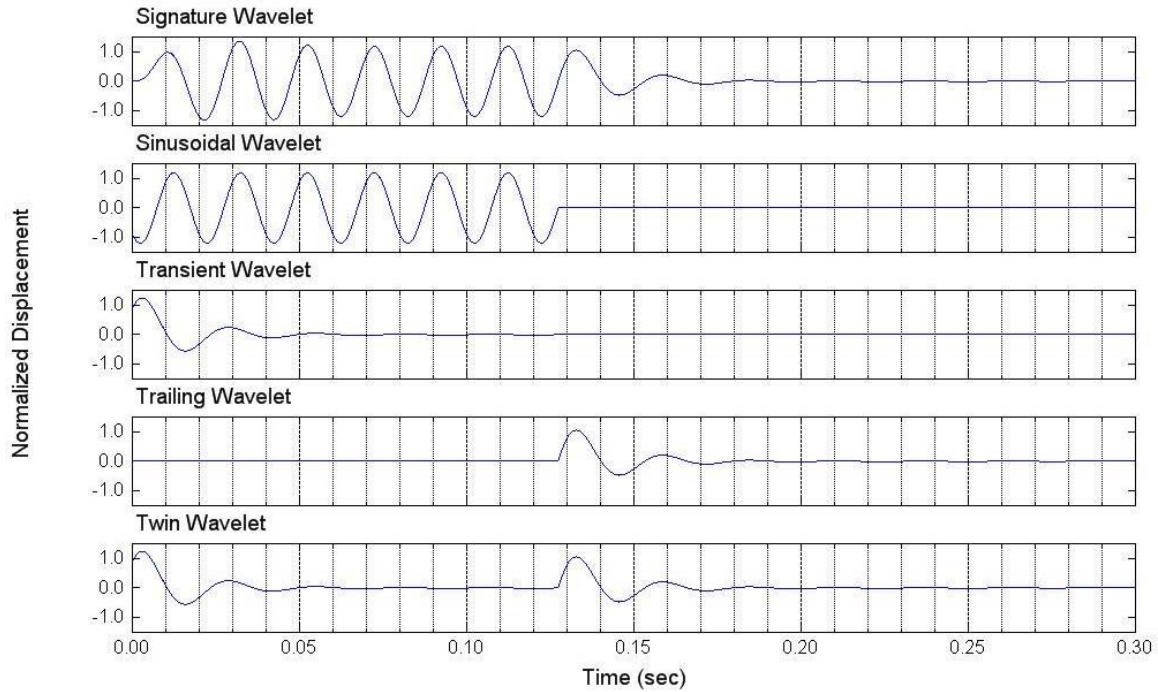


Figure 7.5 Source signature and its wavelets (excitation frequency 50 Hz, natural frequency 40 Hz, duration 0.1273 sec, damping ratio 25%)

The simplest way to approximate the wavelet response for Equation (7.25) is to filter the undesired twin-wavelet frequency, if possible, especially when the sinusoidal wavelet frequency and the twin-wavelet frequency significantly separate. A low pass filter is most appropriate when the twin wavelets have a distinctly higher frequency than does the sinusoidal wavelet. Otherwise a band-pass filter is applicable. Once the twin wavelets are eliminated, the dual wavelet propagation degenerates to the single wavelet problem as:

$$\hat{F}\{\tilde{u}_R(t)\} \approx \hat{F}\{\tilde{b}(t)\} \cdot F_l(\omega) \quad (7.27)$$

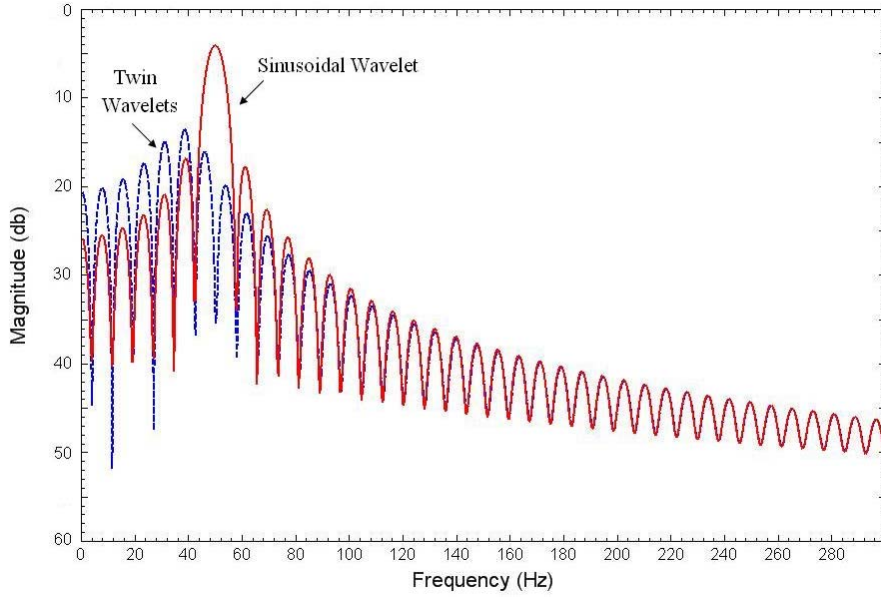


Figure 7.6 Energy contribution of the sinusoidal wavelet and the twin wavelets defined in Figure 7.5

The sinusoidal wavelet response is then obtained by:

$$\hat{F}\{\tilde{b}(t)\} \approx \frac{\hat{F}\{\tilde{u}_R(t)\}}{F_I(\omega)}, \quad (7.28)$$

or

$$\tilde{b}(t) \approx \hat{F}^{-1}\left\{\frac{\hat{F}\{\tilde{u}_R(t)\}}{F_I(\omega)}\right\}. \quad (7.29)$$

The twin wavelets can also be treated as correlated noise. Rearranging Equation (7.26) as:

$$\begin{aligned} \hat{F}\{\tilde{u}_R(t)\} &= \hat{F}\{\tilde{b}(t)\} \cdot \{F_I(\omega) + F_{II,III}(\omega)\} \\ &\quad + [\hat{F}\{\tilde{c}(t)\} - \hat{F}\{\tilde{b}(t)\}] \cdot F_{II,III}(\omega) \\ &= \hat{F}\{\tilde{b}(t)\} \cdot F(\omega) + \hat{F}\{\tilde{c}(t) - \tilde{b}(t)\} \cdot F_{II,III}(\omega) \end{aligned} \quad (7.30)$$

The first item of addition on the right hand side of Equation (7.30) is the same as the U-wavelet approach discussed in the previous section. The second item is the

multiplication of a more noisy wavelet response $[\hat{F}\{\tilde{c}(t)\} - \hat{F}\{\tilde{b}(t)\}]$ and the twin wavelets spectrum $F_{II,III}(\omega)$. The contribution of the second item must be a noise-like signal that can be neglected. Equation (7.30) becomes:

$$\begin{aligned}\hat{F}\{\tilde{u}_R(t)\} &\approx \hat{F}\{\tilde{b}(t)\} \cdot \{F_I(\omega) + F_{II,III}(\omega)\} \\ &= \hat{F}\{\tilde{b}(t)\} \cdot F(\omega)\end{aligned}\quad (7.31)$$

Therefore,

$$\tilde{b}(t) \approx \hat{F}^{-1}\left\{\frac{\hat{F}\{\tilde{u}_R(t)\}}{F(\omega)}\right\}\quad (7.32)$$

Furthermore, if the duration of the excitation increases, the energy of the twin wavelets is negligible. As a result, for the purpose of wavelet response analysis, the longer the duration, then the closer the dual wavelet response is to the single wavelet response. However, for the waveform identification methods such as first break method and arrival identification method, the increase of excitation duration does not reduce waveform distortion.

Figure 7.7 presents five cycles of a 50-Hz sinusoidal P-wave signal sampled at 0.12207 ms intervals. The source signature is defined as a 50-Hz sine wave, of excitation duration 0.1 sec, natural frequency 40 Hz, and damping ratio 25%. Using the approach given by Equation (7.29) yields the wavelet response shown in Figure 7.8, where a spike near 0.12 sec denotes the arrival of the P-wave signal. Figure 7.9 shows the filtered wavelet response in Figure 7.8 by a 90-Hz low pass filter.

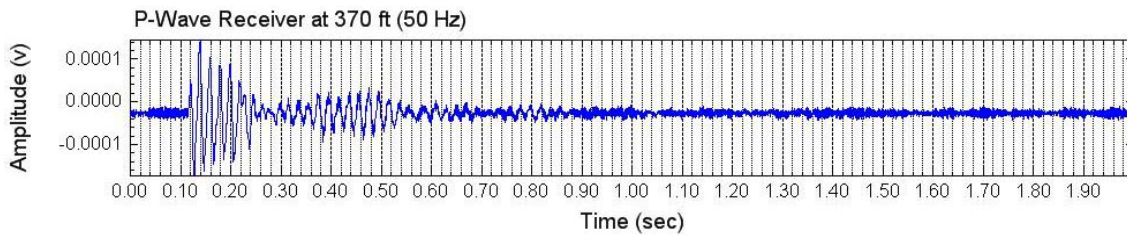


Figure 7.7 P-wave signal of five cycles of a 50-Hz sine wave

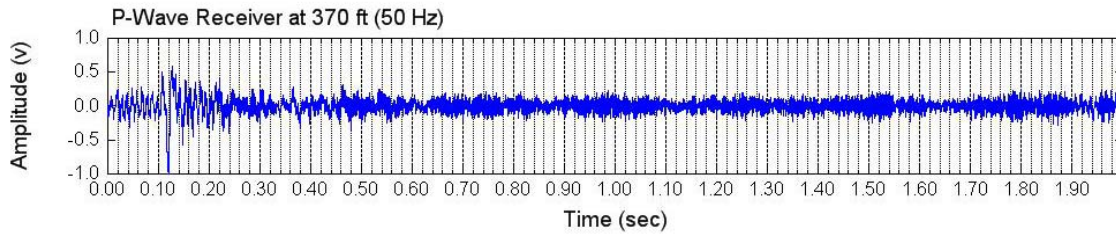


Figure 7.8 The wavelet response of the P-wave signal in Figure 7.7

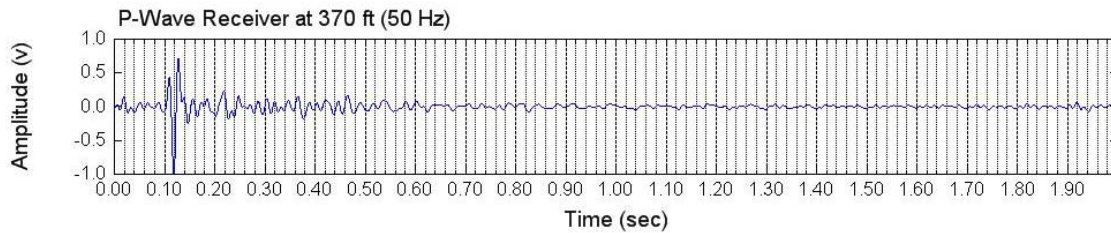


Figure 7.9 The low-pass filtered wavelet response of the P-wave signal in Figure 7.7

The amplitude spectra of two P-wave signals and their corresponding source signatures are presented in Figures 7.10 and 7.11. The spectra of the signals and the signatures both match well at frequencies below 90 Hz, even though the noise increases significantly from 90 Hz. The fact that the spectra of a signal and its source signature match very well within the significant frequency band justifies the source signature model in Chapter 5.

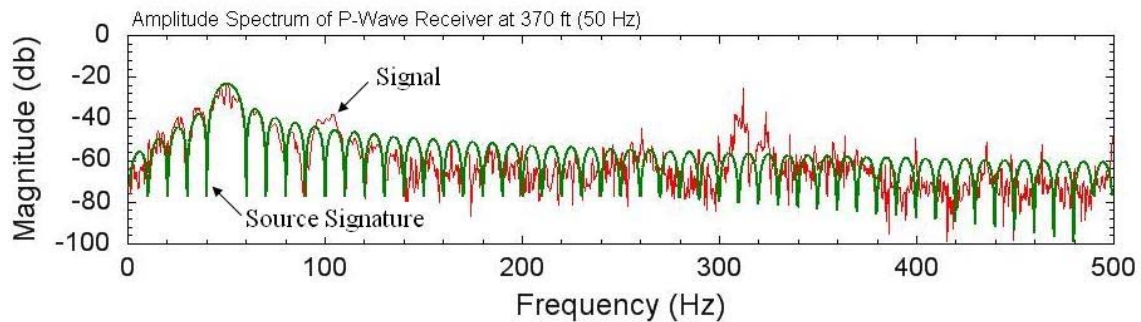


Figure 7.10 Amplitude spectra of a P-wave signal recorded at a depth of 111 m (370 ft) and its SDOF source signature

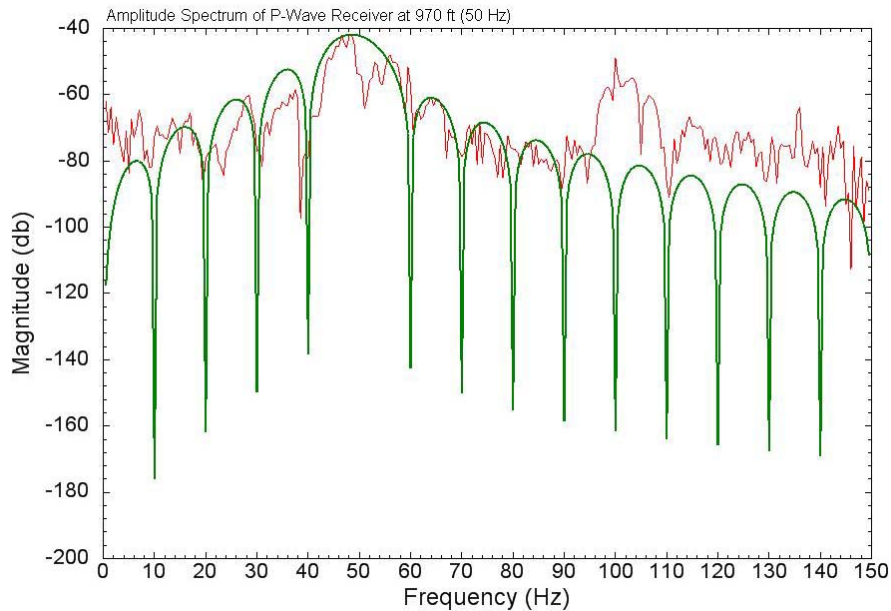


Figure 7.11 Amplitude spectra of a P-wave signal recorded at a depth of 291 m (970 ft) and its SDOF source signature

7.4 WAVELET RESPONSE FOR S-WAVE WITH NEGLIGIBLE ANISOTROPY

S-wave signals are recorded by two horizontal and orthogonal components S_1 and S_2 in a given 3-D receiver. Disorientation occurs when there is no compass to provide tool orientation as happened in this research. Hence, the field receiver tool is arbitrarily oriented. For a vertical borehole, the orientation correction is only necessary on the horizontal plane because the vertical geophone is correctly oriented.

Figure 7.12 is a hodograph that illustrates the particle trace of an S-wave motion on a horizontal plane. When the vibration is steady-state, the particle motion is along the outside ellipse. Point A and B denote the maximal amplitudes of the motion. When anisotropy is negligible, the particle motion can be simplified as along the straight line between points A and B, and angle θ denotes the correct polarization orientation of the particle motion. If one of the S-wave receiver components (S_1 or S_2) is aligned with the

polarization direction (denoted by P in Figure 7.12), the receiver tool box is correctly orientated. If two horizontal S-wave sensors S_1 and S_2 are aligned with the axes X and Y, respectively, the tool box is disorientated.

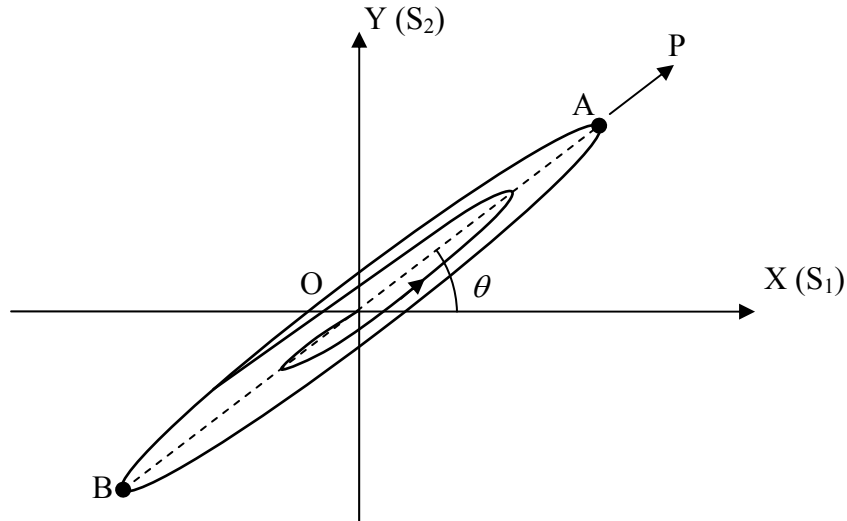


Figure 7.12 Hodograph and polarization of S-wave recorded on a horizontal plane

The particle motion $u_R(t)$ is defined by the convolution of source signature $u(t)$ and wavelet response $R(t)$ in Equation (7.15), or:

$$u_R(t) = R(t) * u(t) \quad (7.33)$$

When anisotropy is negligible, the particle motion is assumed to travel along a straight line AB (Figure 7.13). The measured components $X(t)$ and $Y(t)$ are the projections of $u_R(t)$ in terms of orientation θ and can be expressed as:

$$X(t) = u_R(t) \cos \theta \quad (7.34)$$

and
$$Y(t) = u_R(t) \sin \theta \quad (7.35)$$

The conventional methods must use $X(t)$ and $Y(t)$ in order to obtain the orientation θ . The wavelet response technique greatly simplifies the process.

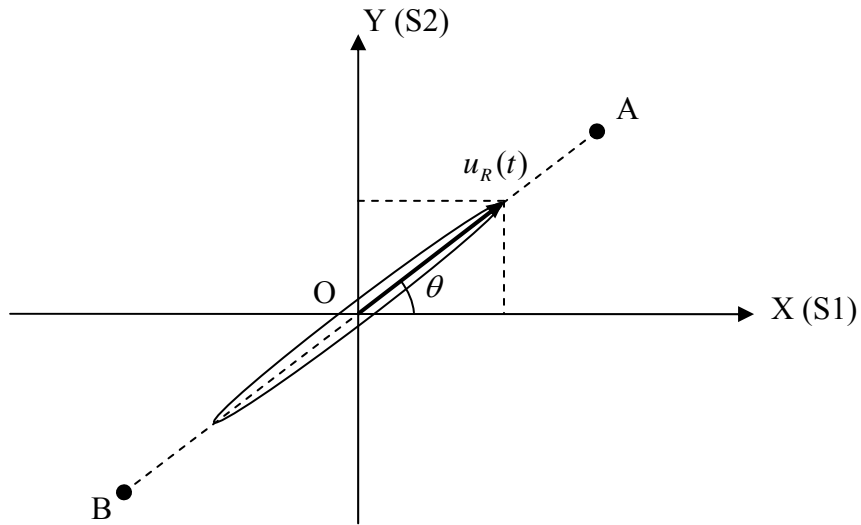


Figure 7.13 Polarization of S-wave when anisotropy is weak

By substituting Equation (7.33) into Equations (7.34) and (7.35), one obtains

$$X(t) = u(t) * R(t) \cos \theta \quad (7.36)$$

and

$$Y(t) = u(t) * R(t) \sin \theta \quad (7.37)$$

As can be seen from Equations (7.36) and (7.37), both $X(t)$ and $Y(t)$ contain the same source signature $u(t)$ that can be extracted to obtain the corresponding wavelet responses. If one defines the wavelet responses of $X(t)$ and $Y(t)$ as:

$$R_x(t) = \frac{\hat{F}\{X(t)\}}{\hat{F}\{u(t)\}}, \quad (7.38)$$

and

$$R_y(t) = \frac{\hat{F}\{Y(t)\}}{\hat{F}\{u(t)\}}, \quad (7.39)$$

then by Fourier transforming both sides of Equations (7.36) and (7.37) and using definitions in Equations (7.38) and (7.39), one obtains:

$$R_x(t) = R(t) \cos \theta \quad (7.40)$$

and
$$R_Y(t) = R(t) \sin \theta \tag{7.41}$$

Equations (7.40) and (7.41) demonstrate that the wavelet responses of both disoriented components $X(t)$ and $Y(t)$ are mapped to the correctly oriented wavelet response $R(t)$. The scaling constant $\cos \theta$ or $\sin \theta$ simply changes the amplitude and sign of the wavelet response while the arrival time remains unchanged. In other words, either $R_X(t)$ or $R_Y(t)$ can exactly reflect the arrival time defined by $R(t)$. The arrival coefficients of $R_X(t)$ and $R_Y(t)$ appear in pairs and synchronized in the time domain (Figure 7.14) as:

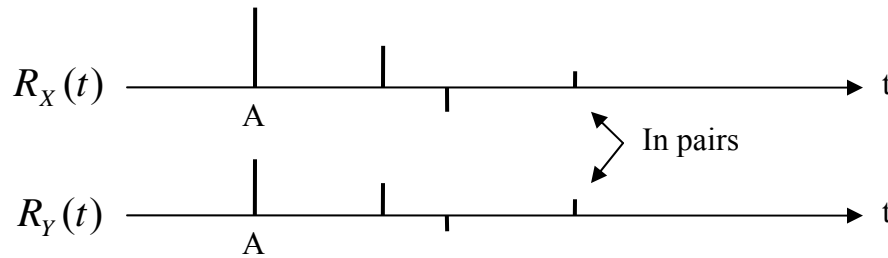


Figure 7.14 Wavelet response pairs of S-wave components

For example, Figure 7.15 shows the two out-of-phase components of an S-wave receiver signal recorded at a depth of 114 m (380 ft) in Borehole C4993. Figure 7.16 shows their corresponding spectra. Figure 7.17 presents the wavelet responses indicating the spikes are in pairs at the same arrival time but are of different signs.

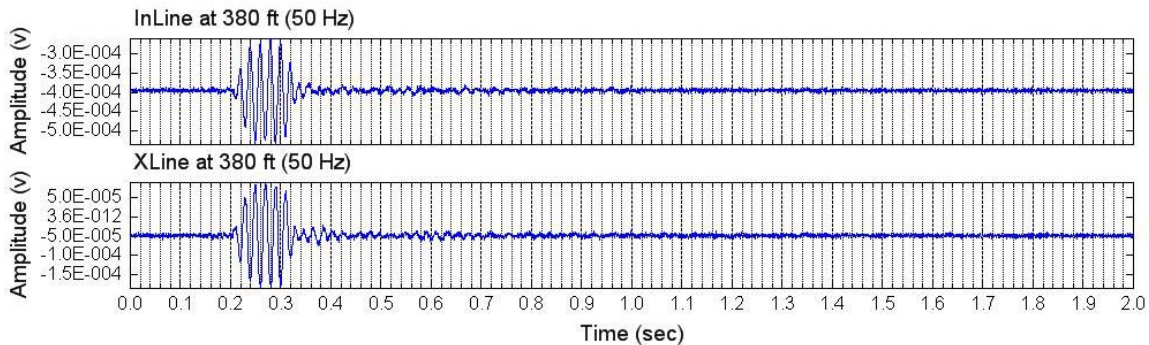


Figure 7.15 Two components of S-wave records at a depth of 114 m (380 ft)

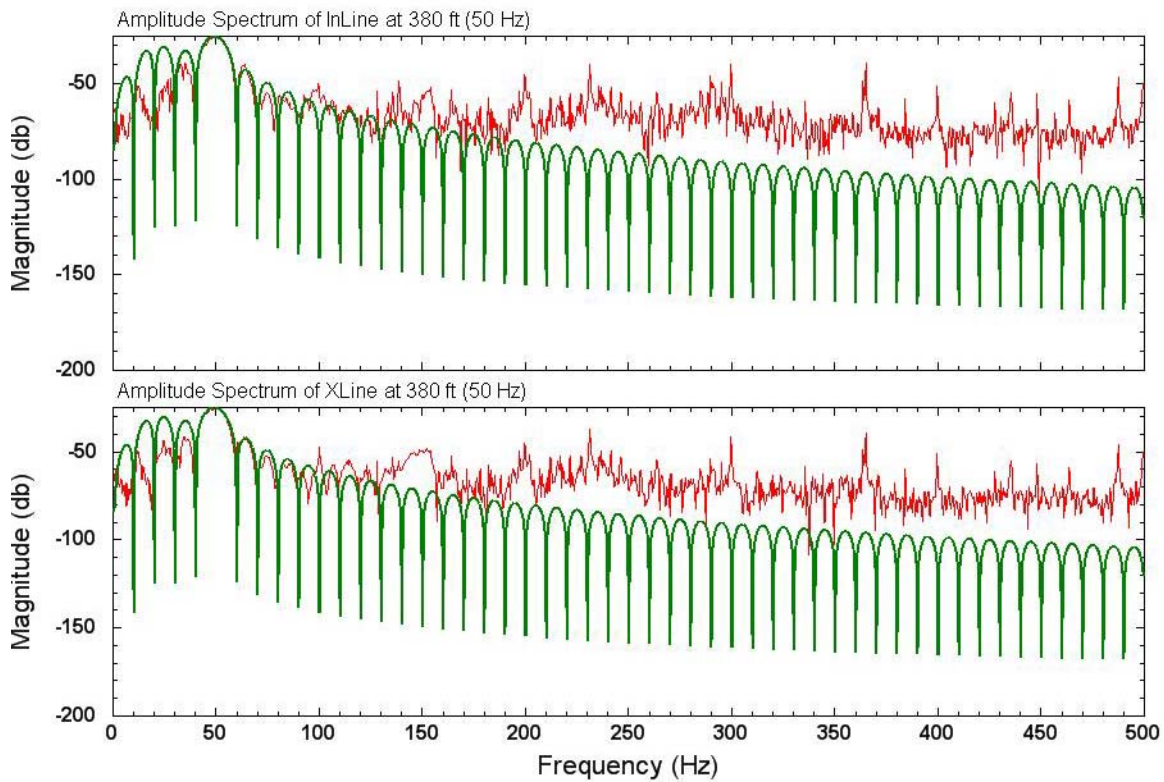


Figure 7.16 Spectra of two components of the S-wave signal and the source signature

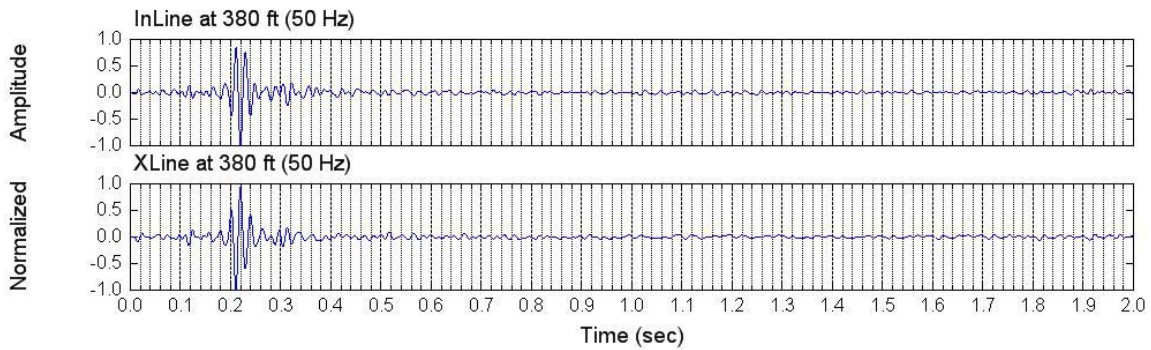


Figure 7.17 The wavelet response of the two components of the S-wave signal recorded at a depth of 114 m (380 ft)

An advantage of the wavelet response method is that the correction for the disorientation of the receiver tool is not required. The spikes of the wavelet responses are

in pairs and have the same arrival times. Whenever single spikes appear as singletons, the receiver tool is then correctly oriented (Figure 7.18). The wavelet response of one S-wave component should have dominant coefficient amplitudes or spike heights, while the other should have indistinct spikes or noise.

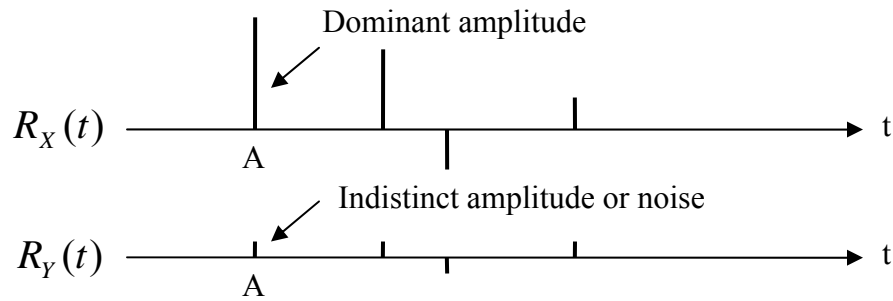


Figure 7.18 Spike singleton indicates correct orientation

The possibility of multi-polarization exists for S-wave motion due to the interference of preceding P-wave components as well as multi-path arrivals and S-wave splitting. Figure 7.19 demonstrates two separate polarizations P_1 and P_2 corresponding to θ_1 and θ_2 , respectively. If P_1 denotes the correct orientation, then conventional methods using the dominant motions or wave energy may obtain an incorrect orientation because other motions such as P-wave or SV-wave (as represented by P_2) may control the motion if the polarizations can not be separated or decoupled effectively.

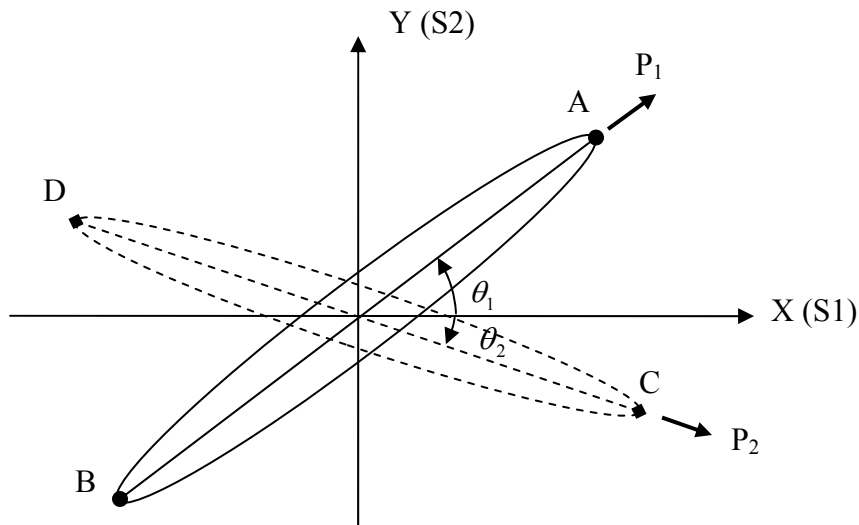


Figure 7.19 Multi-polarization hodograph of S-wave signal

The wavelet-response method avoids direct evaluation on distorted waveforms. As shown in Figure 7.20, the wavelet responses of both S-wave components always appear in pairs. Different polarizations will correspond to different pairs of spikes as shown by P_1 and P_2 in Figure 7.20. P_1 and P_2 are identical to the polarization in Figure 7.19. The correct orientation for first arrival corresponds to one pair of the spike pairs, not necessarily the first pair because P and SV waves can propagate faster than the SH wave. The correct spike pair can be distinguished from other spikes using the waterfall plot. When a singleton exists, the corresponding polarization is aligned with the receiver component. The receiver tool is correctly oriented. For example, P_3 is aligned with the X component so that the spike at Y component disappears or appears similar to noise.

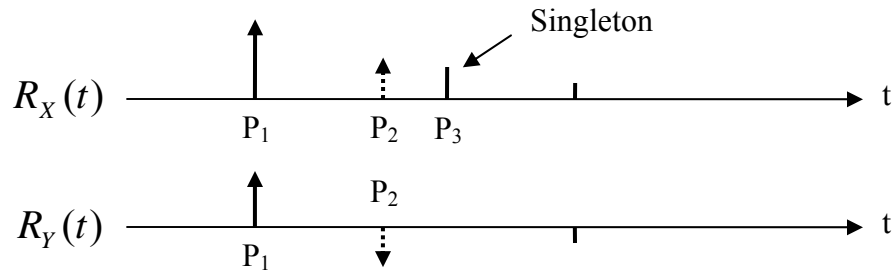


Figure 7.20 Wavelet response pair for multi-polarization S-wave signal

7.5 WAVELET RESPONSE FOR S-WAVE WITH ANISOTROPY

When anisotropy is obvious, the spike pairs in Figure 7.20 in the wavelet responses for the two S-wave components may appear shifted within the pair (Figure 7.21).

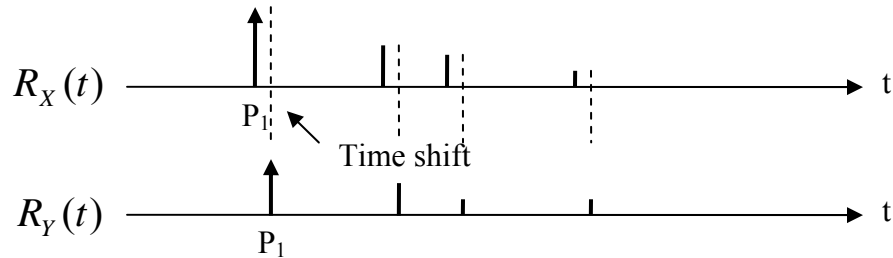


Figure 7.21 Shifted wavelet responses of the two components of the S-wave signal

The time shift caused by anisotropy is illustrated in Figure 7.22, where the motion of one cycle of the vibration is simulated as an ellipse. Point D marks the peak amplitude point of the time series $X(t)$ recorded by component S_1 . Point C denotes the peak amplitude point of the time series $Y(t)$ recorded by component S_2 . Both points C and D are tangent points to the motion trajectory. The actual peak point of the orientation corrected time series $P(t)$ should be at point A. Anisotropy causes very small shifts for the peaks (from A to C or from A to D). The desired actual peak A is between the two peaks

C and D. The peaks C and D correspond to a spike pair (x_2 at t_D and y_1 at t_C in Figure 7.23) in wavelet responses of $X(t)$ and $Y(t)$ if $X(t)$ and $Y(t)$ are centered with zero mean values as shown in Figure 7.22. The heights of the spikes for the wavelet responses are not necessarily equal to x_2 or y_1 in that they can be scaled by any constant factor as long as each time the same scale is applied to both of them.

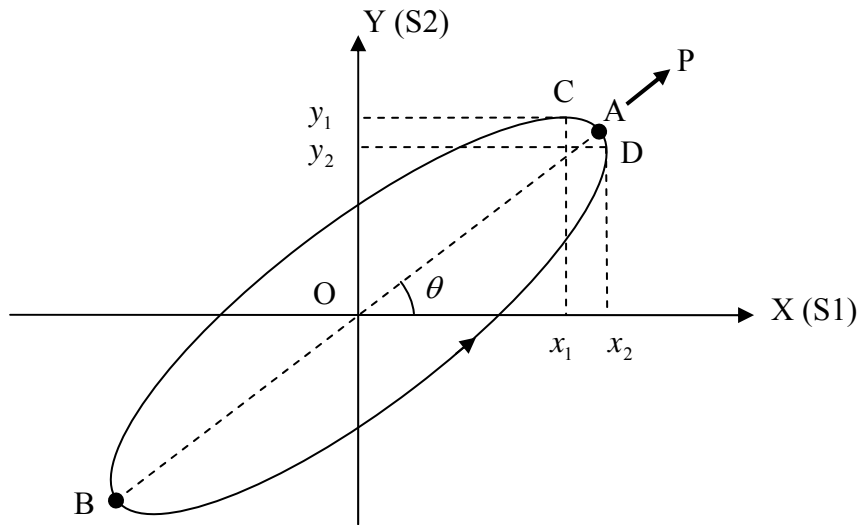


Figure 7.22 Hodograph of S-wave signal with strong anisotropy

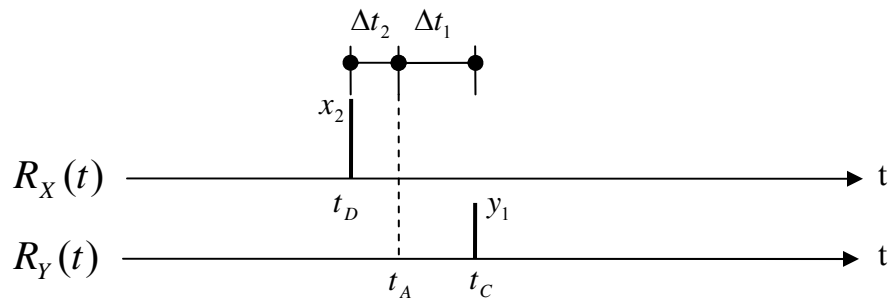


Figure 7.23 Shifted wavelet responses of S-wave components

The estimation of curve D to A to C as part of an ellipse does not require the whole trajectory to be an ellipse, nor does it imply the anisotropy is elliptical. However,

the assumption that the local curve from point D to A to C is part of an ellipse as shown in Figure 7.22 can greatly simplify the estimation of the time shifts Δt_1 and Δt_2 in Figure 7.23. t_D represents the time at point D and t_C corresponds to the time at point C. t_C and t_D can be measured from the wavelet responses of both S-wave components in Figure 7.24. t_A denotes the desired but unknown arrival time.

$$\Delta t_1 = t_C - t_A, \quad \Delta t_2 = t_A - t_D$$

thus Δt_1 and Δt_2 are unknown, but the difference of the arrival times $\Delta t = \Delta t_1 + \Delta t_2 = t_C - t_D$ of the two spikes is known from the wavelet responses. The heights of the spikes x_2 and y_1 can also be measured from the wavelet responses. Using prior knowledge of x_2 , y_1 and Δt , the arrival time at point A can be derived as follows:

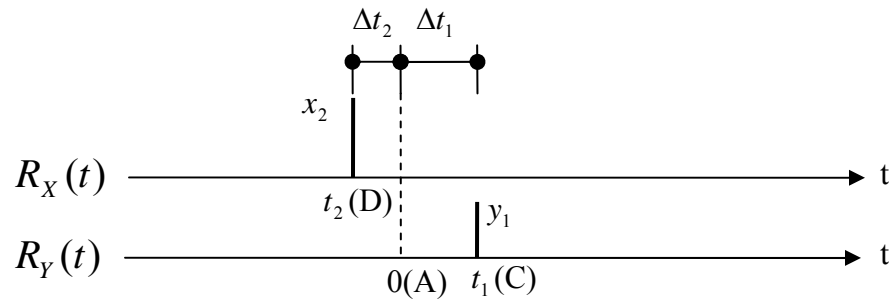


Figure 7.24 Relative time shift of wavelet responses of S-wave components

For simplification, assume the time origin is at point A ($t = 0$) and the time at points C and D are t_1 and t_2 , respectively. Therefore, Δt can be written as:

$$t_1 - t_2 = \Delta t. \quad (7.42)$$

Assuming the half length of the long axis of the ellipse is a and that of the shorter one is b , then in the local coordinate system POQ (Figure 7.25) can be expressed as:

$$p = a \cos \varpi t \quad (7.43)$$

and
$$q = b \sin \varpi t \quad (7.44)$$

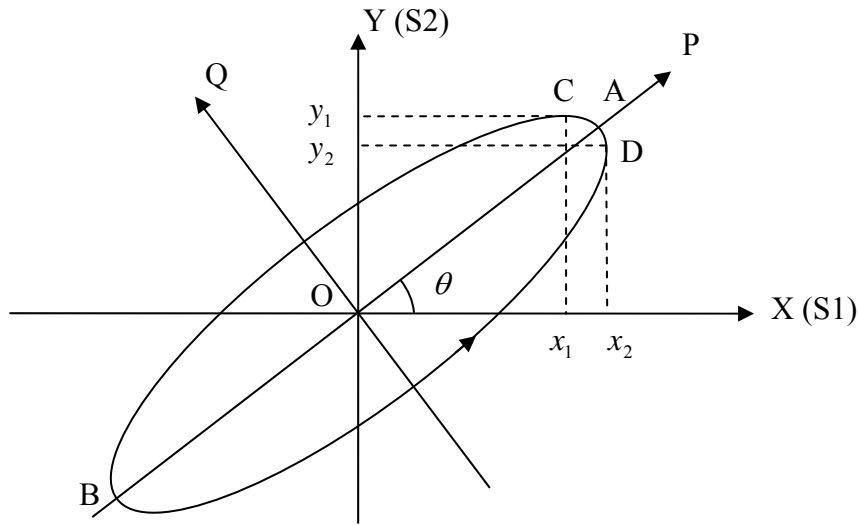


Figure 7.25 Relationship of local and general coordinate systems

The elliptical equation in local coordinate system POQ is:

$$\frac{p^2}{a^2} + \frac{q^2}{b^2} = 1 \quad (7.45)$$

The relationship between the coordinate systems XOY and POQ is defined as:

$$\begin{pmatrix} x \\ y \end{pmatrix} = \begin{bmatrix} \cos \theta & -\sin \theta \\ \sin \theta & \cos \theta \end{bmatrix} \begin{pmatrix} p \\ q \end{pmatrix} \quad (7.46)$$

or

$$\begin{pmatrix} p \\ q \end{pmatrix} = \begin{bmatrix} \cos \theta & \sin \theta \\ -\sin \theta & \cos \theta \end{bmatrix} \begin{pmatrix} x \\ y \end{pmatrix} \quad (7.47)$$

Equation (7.47) is identical to:

$$p = x \cos \theta + y \sin \theta \quad (7.48)$$

and

$$q = -x \sin \theta + y \cos \theta \quad (7.49)$$

By substituting Equations (7.48) and (7.49) into (7.45), one obtains:

$$\left(\frac{x \cos \theta + y \sin \theta}{a} \right)^2 + \left(\frac{-x \sin \theta + y \cos \theta}{b} \right)^2 = 1 \quad (7.50)$$

The following three steps bridge the three unknown elliptical parameters (a, b and θ) and three measured wavelet response parameters (x_2, y_1 and Δt).

Step 1: Relationship between y_1 and the ellipse

Derivative of x for both sides of Equation (7.50) and let $\frac{dy}{dx} = 0$ yields the tangent line at point C (x_1, y_1):

$$x = k_1 y \quad (7.51)$$

where
$$k_1 = \frac{(a^2 - b^2) \tan \theta}{(a \tan \theta)^2 + b^2} \quad (7.52)$$

By substituting Equation (7.52) into (7.50) and canceling x , one obtains:

$$y_1 = \frac{1}{\pm \sqrt{\left(\frac{k_1 \cos \theta + \sin \theta}{a}\right)^2 + \left(\frac{\cos \theta - k_1 \sin \theta}{b}\right)^2}} \quad (7.53)$$

The value y_1 is measured from $R_Y(t)$, the wavelet response of $Y(t)$ component in Figure (7.23).

Step 2: Relationship between x_2 and the ellipse

Derivative of y for both sides of Equation (7.50) and let $\frac{dx}{dy} = 0$ yields the tangent line passing point D (x_2, y_2):

$$y = k_2 x \quad (7.54)$$

$$k_2 = \frac{(a^2 - b^2) \tan \theta}{a^2 + (b \tan \theta)^2} \quad (7.55)$$

By combining Equation (7.54) and (7.50) and canceling y , one obtains:

$$x_2 = \frac{1}{\pm \sqrt{\left(\frac{\cos \theta + k_2 \sin \theta}{a}\right)^2 + \left(\frac{k_2 \cos \theta - \sin \theta}{b}\right)^2}} \quad (7.56)$$

The value x_2 can be measured from $R_x(t)$, the wavelet response of $X(t)$ component in Figure (7.23).

Step 3: Relationship between the time interval ($t_1 - t_2$) and the ellipse

Dividing (7.44) by (7.43) leads to:

$$\tan \varpi t = \frac{qa}{pb} \quad (7.57)$$

Equation (7.57) becomes:

$$\tan \varpi t_1 = \frac{q_1 a}{p_1 b} \quad (7.58)$$

and

$$\tan \varpi t_2 = \frac{q_2 a}{p_2 b} \quad (7.59)$$

Equation (7.48) becomes:

$$p_1 = x_1 \cos \theta + y_1 \sin \theta = y_1 (k_1 \cos \theta + \sin \theta) \quad (7.60)$$

and

$$p_2 = x_2 \cos \theta + y_2 \sin \theta = x_2 (\cos \theta + k_2 \sin \theta) \quad (7.61)$$

Equation (7.49) yields:

$$q_1 = -x_1 \sin \theta + y_1 \cos \theta = y_1 (-k_1 \sin \theta + \cos \theta) \quad (7.62)$$

and

$$q_2 = -x_2 \sin \theta + y_2 \cos \theta = x_2 (-\sin \theta + k_2 \cos \theta) \quad (7.63)$$

By substituting Equations (7.60) and (7.62) into Equation (7.58) and using Equation (7.52) one obtains:

$$\tan \varpi t_1 = \frac{b}{a \tan \theta} \quad (7.64)$$

By substituting Equations (7.61) and (7.63) into Equation (7.59) and using Equation (7.55), one obtains:

$$\tan \varpi t_2 = -\frac{b \tan \theta}{a} \quad (7.65)$$

Equations (7.64) and (7.65) yield:

$$\begin{aligned}
 \tan \varpi \Delta t &= \tan \varpi (t_1 - t_2) \\
 &= \frac{\tan \varpi t_1 - \tan \varpi t_2}{1 + \tan \varpi t_1 \tan \varpi t_2} \\
 &= \frac{ab}{a^2 - b^2} \left(\frac{1}{\tan \theta} + \tan \theta \right)
 \end{aligned} \tag{7.66}$$

The time interval Δt can be measured from the time difference between the two spikes of the wavelet responses in Figure 7.23, and the frequency ϖ is given in the field test. Therefore, the left hand side of Equation (7.66) is known.

The three steps above yield Equations (7.53), (7.56) and (7.66), the combination of which can solve the three ellipse parameters a , b and θ . Once a , b and θ are known, then Equations (7.64) and (7.65) become:

$$t_1 = \frac{1}{\varpi} \arctan\left(\frac{b}{a \tan \theta}\right) \tag{7.67}$$

and
$$t_2 = -\frac{1}{\varpi} \arctan\left(\frac{b \tan \theta}{a}\right) \tag{7.68}$$

The arrival time at point A is:

$$t_A = t_C - t_1 \tag{7.69}$$

or
$$t_A = t_D + t_2 \tag{7.70}$$

When the anisotropy is weak, $\frac{b}{a} \ll 1$, and $\left(\frac{b}{a}\right)^2$ can be neglected, or

$$\left(\frac{b}{a}\right)^2 \approx 0 \tag{7.71}$$

By substituting Equation (7.71) into Equations (7.53) and (7.56), one obtains:

$$y_1 \approx a \sin \theta \tag{7.72}$$

and
$$x_2 \approx a \cos \theta \tag{7.73}$$

The division of Equation (7.72) by (7.73) obtains:

$$\tan \theta \approx \frac{y_1}{x_2}. \quad (7.74)$$

By substituting Equation (7.74) into (7.66), one obtains:

$$\frac{b}{a} \approx \frac{x_2 y_1 \tan \varpi \Delta t}{x_2^2 + y_1^2}. \quad (7.75)$$

By substituting Equations (7.74) and (7.75) into Equations (7.67) and (7.68), one obtains:

$$t_1 \approx \frac{1}{\varpi} \arctan\left(\frac{x_2^2 \tan \varpi \Delta t}{x_2^2 + y_1^2}\right) \quad (7.76)$$

and

$$t_2 \approx -\frac{1}{\varpi} \arctan\left(\frac{y_1^2 \tan \varpi \Delta t}{x_2^2 + y_1^2}\right). \quad (7.77)$$

When relative time intervals are used, Equations (7.76) and (7.77) become

$$\Delta t_1 \approx \frac{1}{\varpi} \arctan\left(\frac{x_2^2 \tan \varpi \Delta t}{x_2^2 + y_1^2}\right) \quad (7.78)$$

and

$$\Delta t_2 \approx \frac{1}{\varpi} \arctan\left(\frac{y_1^2 \tan \varpi \Delta t}{x_2^2 + y_1^2}\right). \quad (7.79)$$

For convenience, the wavelet responses of the two S-wave components are illustrated in Figure 7.26 without any assumptions for coordinate systems or time origin.

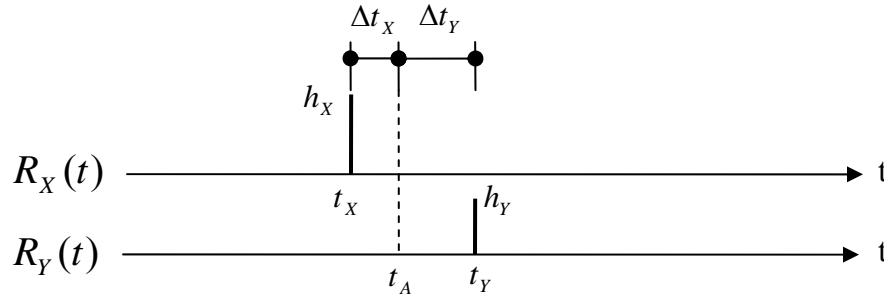


Figure 7.26 Estimation of S-wave arrival time using two S-wave components

Equations (7.78) and (7.79) become:

$$\Delta t_x \approx \frac{1}{\varpi} \arctan\left(\frac{h_y^2 \tan \varpi \Delta t}{h_x^2 + h_y^2}\right) \quad (7.80)$$

and

$$\Delta t_y \approx \frac{1}{\varpi} \arctan\left(\frac{h_x^2 \tan \varpi \Delta t}{h_x^2 + h_y^2}\right) \quad (7.81)$$

Equations (7.80) and (7.81) can be extended to estimate general trajectory without assuming that the local curve near point A is a part of an ellipsis. This extension is based on the fact that the ratio of the length of any local curve to the length of a whole cycle should be mapped to the ratio of their time spans because the pure wavelet vibrates at a single frequency.

Equations (7.69) and (7.70) become:

$$t_A = t_x + \Delta t_x \quad (7.82)$$

or

$$t_A = t_y - \Delta t_y \quad (7.83)$$

Anisotropy is weak in most rocks of geophysical interests (Thompsen, 1986). Equations (7.80) and (7.81) display adequate accuracy in the estimation of the S-wave arrival time at point A without the correction of the disorientation of the receiver tool, which proves to be an advantage of the wavelet response method.

7.6 NUMERICAL DECONVOLUTION AND WAVELET RESPONSE

7.6.1 Zeros of source signature

The spectrum of the source signature in Equation (5.123) is the addition of the spectra of the sinusoidal wavelet $F_I(\omega)$ and the twin wavelets $F_{II,III}(\omega)$. As shown in section 6.5 through 6.7, both spectra of $F_I(\omega)$ and $F_{II,III}(\omega)$ have periodic zeros. These zeros are the result of the finite excitation interval T that constitutes a truncation of a time series. As shown in Equations (5.102) and (5.103), the truncation of a time series in the

time domain is equivalent to a convolution of a sinc-function in the frequency domain. The periodic zeros of the sinc-function lead to zeros in the spectra of the source signatures. For example, the spectrum of the sinusoidal wavelet $F_l(\omega)$ is associated with the truncated time series by a square pulse in $F_l(\omega)$ as defined in Equation (5.104) as:

$$F_l(\omega) = \frac{jA_l}{2} e^{-j\omega T/2} \left\{ e^{-j\varpi(T/2-t_1)} \frac{\sin[(\omega + \varpi)T/2]}{\omega + \varpi} - e^{j\varpi(T/2-t_1)} \frac{\sin[(\omega - \varpi)T/2]}{\omega - \varpi} \right\}. \quad (7.84)$$

The locations of the zeros of $F_l(\omega)$ can be obtained by substituting:

$$\sin\left[\frac{(\omega + \varpi)T}{2}\right] = 0 \quad (7.85)$$

and
$$\sin\left[\frac{(\omega - \varpi)T}{2}\right] = 0 \quad (7.86)$$

into Equation (7.84). The solution to Equations (7.85) and (7.86) is:

$$\omega = \frac{2k\pi}{T} \pm \varpi, \quad k = 0, \pm 1, \pm 2, \pm 3 \dots \quad (7.87)$$

By substituting $f = \frac{\omega}{2\pi}$ and $\bar{f} = \frac{\varpi}{2\pi}$ into Equation (7.87), one obtains:

$$f = \frac{k}{T} \pm \bar{f}, \quad k = 0, \pm 1, \pm 2, \pm 3 \dots \quad (7.88)$$

The discrete frequencies determined by Equation (7.87) or Equation (7.88) are called comb frequencies herein. Given excitation frequency $\bar{f} = 50$ Hz and excitation duration $T = 0.1$ sec, Equation (7.88) gives the zeros at comb frequencies $f = 10k \pm 50$ Hz, as shown in Figure 6.18 through Figure 6.27.

7.6.2 Deconvolution of synthetic signal

The deconvolution in Equation (7.18) can be expressed as:

$$R(t) = \hat{F}^{-1} \left\{ \frac{1}{F(\omega)} \right\} * u_R(t). \quad (7.89)$$

where: the asterisk “*” denotes a convolution. The term $\hat{F}^{-1}\left\{\frac{1}{F(\omega)}\right\}$ actually represents an inverse filter with complex gain. The zeroes of the amplitude spectrum of $F(\omega)$ will give the filter an infinite gain at the comb frequencies defined by Equations (7.87) or (7.88). The infinite gains at these comb frequencies look like a comb in the frequency domain. A conventional way to deal with this problem to make the inverse filter practical is called “adding white noise” (Mari, 1997), which is:

$$\frac{1}{F(\omega)} = \frac{1}{|F(\omega)| e^{i\varphi(\omega)}} \approx \frac{1}{\{|F(\omega)| + \alpha \max[|F(\omega)|]\} e^{i\varphi(\omega)}} \quad (7.90)$$

where: φ is the phase angle of $F(\omega)$, and α is a real value constant presenting a ratio analogous to signal-to-noise ratio. Mari (1997) investigated the range of α values using a synthetic input trace. A very low constant $\alpha = 0.001$ is suitable for signals without noise, $\alpha \geq 0.1$ is appropriate for the synthetic trace data. When $F(\omega) \rightarrow 0$, the right-hand side of Equation (7.90) approaches a complex constant as:

$$\frac{1}{\{|F(\omega)| + \alpha \max[|F(\omega)|]\} e^{i\varphi(\omega)}} \rightarrow \frac{1}{\alpha \max[|F(\omega)|] e^{i\varphi(\omega)}} \quad (7.91)$$

As an alternative to Equation (7.90), other strategies can be employed to deal with the infinite gain of an exact inverse filter. For example, a noise spectrum N^2 can be assumed, either constant in frequency, or variable, depending on the bandwidth of the desired output.

$$\frac{1}{F(\omega)} = \frac{F^*(\omega)}{|F(\omega)|^2} \approx \frac{F^*(\omega)}{|F(\omega)|^2 + N^2} \quad (7.92)$$

where: $F^*(\omega)$ is the conjugate of $F(\omega)$, and N is any appropriate real value constant that can also be expressed as:

$$N = \alpha \max[|F(\omega)|] \quad (7.93)$$

If the noise term N is not white, it can act as a comb filter and low pass filter for the source signatures defined by Equation (5.123) or Equation (5.104), in that the right-hand side of Equation (7.92) approaches zero at the discrete comb frequencies and high frequencies where $F(\omega) \rightarrow 0$ and $F^*(\omega) \rightarrow 0$, which can be expressed as:

$$\frac{F^*(\omega)}{|F(\omega)|^2 + N^2} \rightarrow \frac{F^*(\omega)}{N^2} \rightarrow 0 \quad (7.94)$$

To investigate the range of α values, a synthetic fixed-sine source signature $u(t)$ shown in Figure 7.27 is used. The synthetic signature has an excitation frequency of 50 Hz, natural frequency of 20 Hz, source duration 0.1 sec, and damping ratio 25%, which is expressed as:

$$u(t) = u(t | \bar{f} = 50\text{Hz}, f_n = 20\text{Hz}, T = 0.1\text{sec}, \xi = 0.25) \quad (7.95)$$

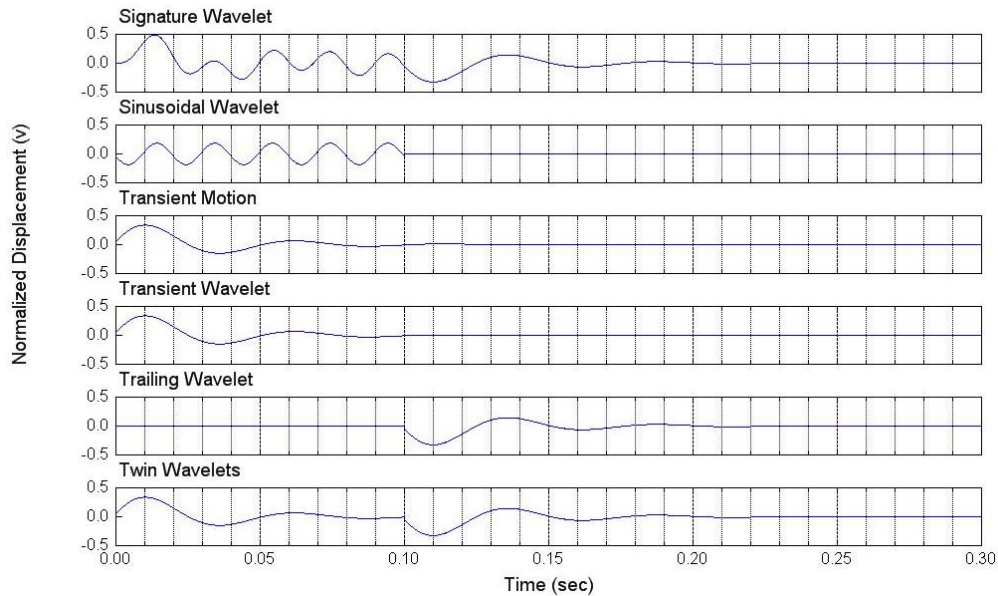


Figure 7.27 Synthetic source signature (excitation frequency 50 Hz, natural frequency 20 Hz, duration 0.1 sec, damping ratio 25%)

A synthetic signal $s(t)$ is defined as the superposition of multiple shifts of the source signature $u(t)$, which is:

$$s(t) = u(t - 0.05) + u(t - 0.30) - u(t - 0.33) + u(t - 0.36). \quad (7.96)$$

Equation (7.96) is used to simulate a noise-free receiver signal that has a first arrival at 0.05 sec, and multiple reflections at 0.30, 0.33 and 0.36 sec (see Figure 7.28).

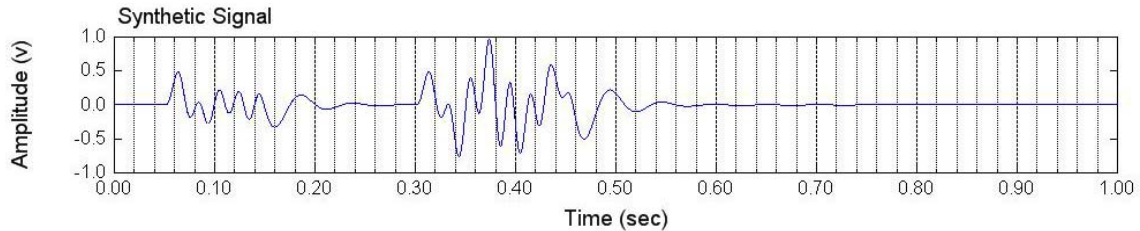


Figure 7.28 Synthetic signal $s(t)$

The amplitude spectrum of the synthetic signal is shown in Figure 7.29. The twin wavelets at 20 Hz coincide with a comb frequency (where the amplitude is zero). The twin wavelets near 20 Hz have greater energy than the sinusoidal wavelet near 50 Hz.

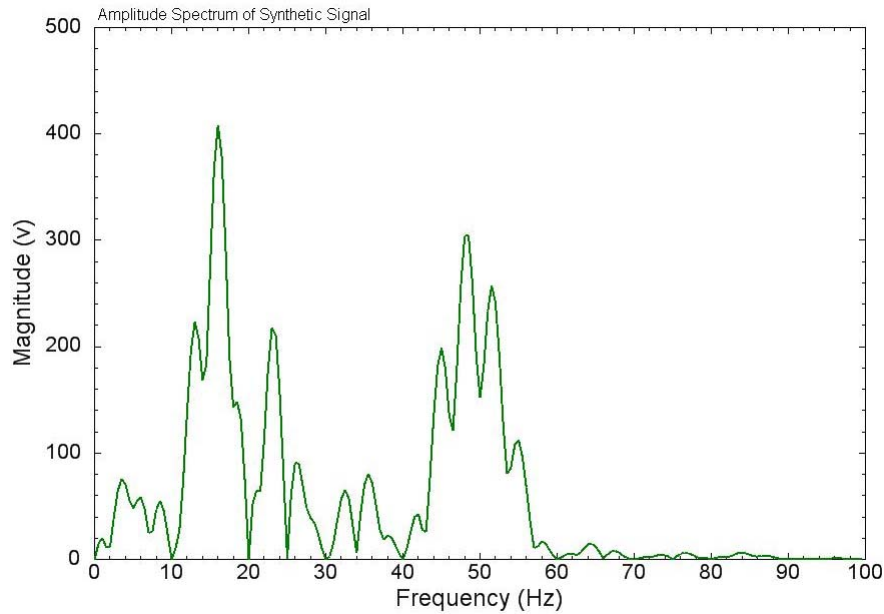


Figure 7.29 Amplitude spectrum of the synthetic signal $s(t)$ in Figure 7.28

Figure 7.30 demonstrates that the spectrum of the synthetic signal matches well with that of the source signature. The synthetic signal is noise-free, but the comparison of the two spectra implies that a point to point perfect match is not necessarily. For example, there is a significant difference between the two amplitude spectra in the first lobe between 0 and 10 Hz, and the fourth lobe between 30 and 40 Hz.

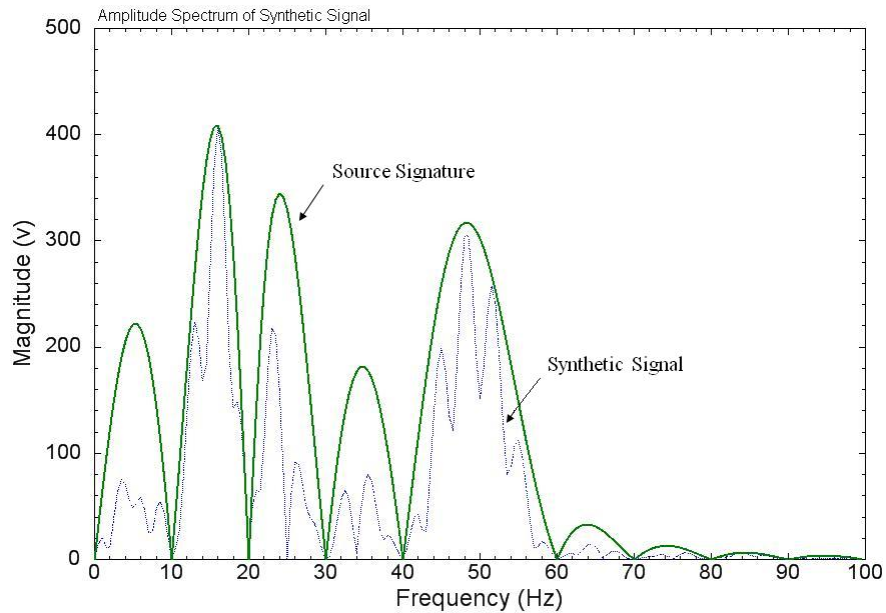


Figure 7.30 Comparison of the amplitude spectra of the synthetic signal $s(t)$ and the synthetic signature $u(t)$

The seemingly zeroes in linear scale (see Figure 7.30) at frequencies higher than 100 Hz are represented digitally by the computer as different magnitude of decimals. In Figure 7.31, the zeroes can be essentially the same for 50 db and 100 db, but they can cause significant digital fluctuations or noise for deconvolution. Figure 7.32 is the deconvolution of the synthetic signal by the synthetic signature. Those tall spikes are digital noise cause by digital representation and numeric computations. Figure 7.33 shows the same noise in decibel scale, and indicates the source of the digital noise is the zeros of the source signature. At low frequencies, the noise is typically lower, as shown

in Figure 7.34, because the “zeros” at lower frequencies have higher values in computer format than those at high frequencies.

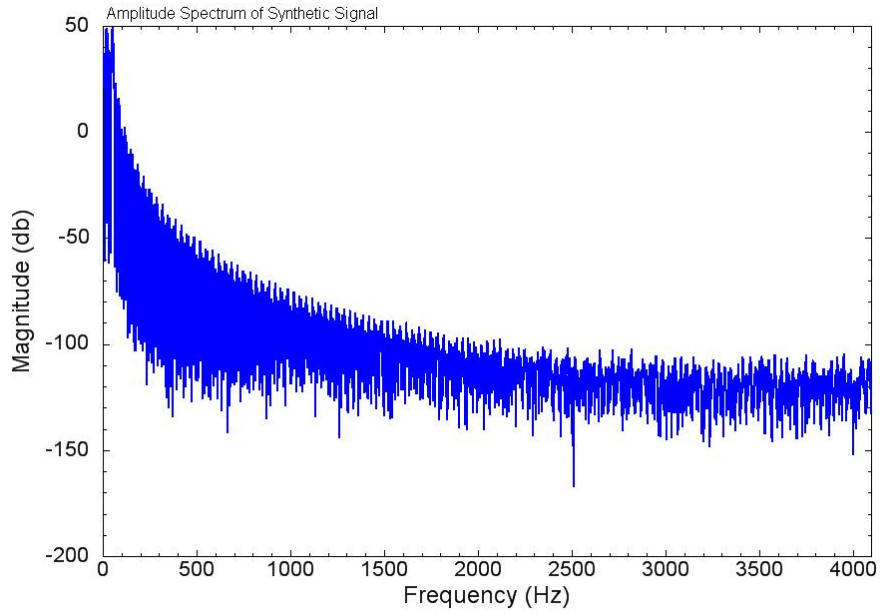


Figure 7.31 Amplitude spectrum of the synthetic signal $s(t)$ below Nyquist Frequency

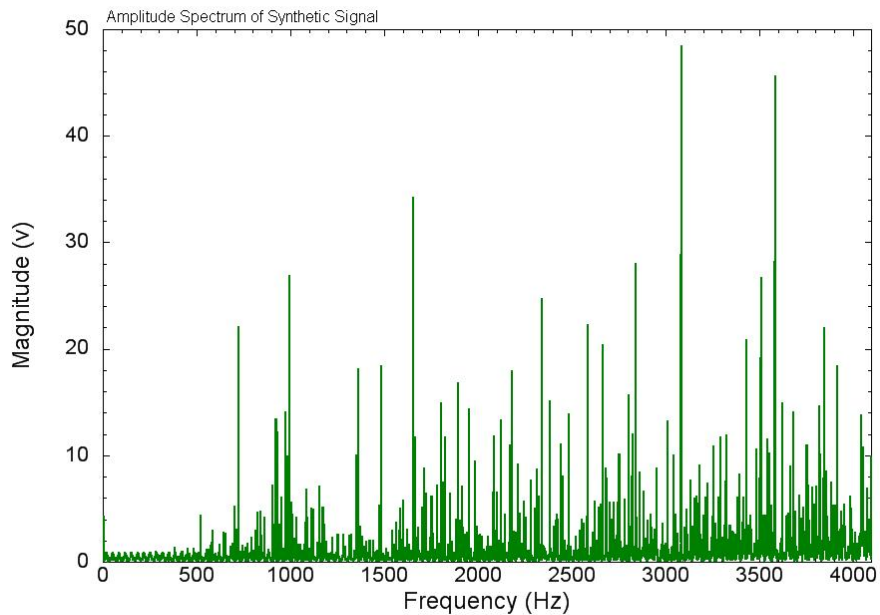


Figure 7.32 Amplitude spectrum of the wavelet response in linear scale

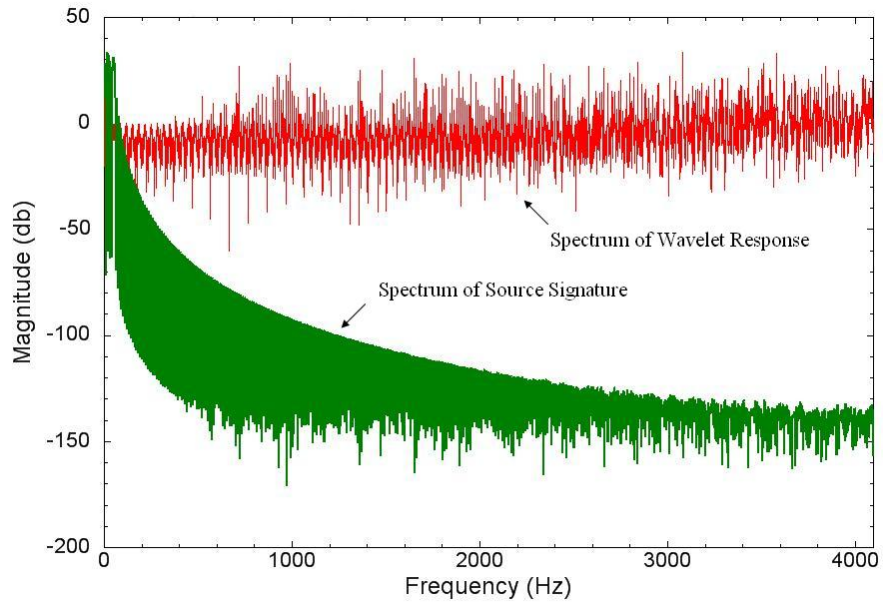


Figure 7.33 Amplitude spectrum of the wavelet response in decibel scale

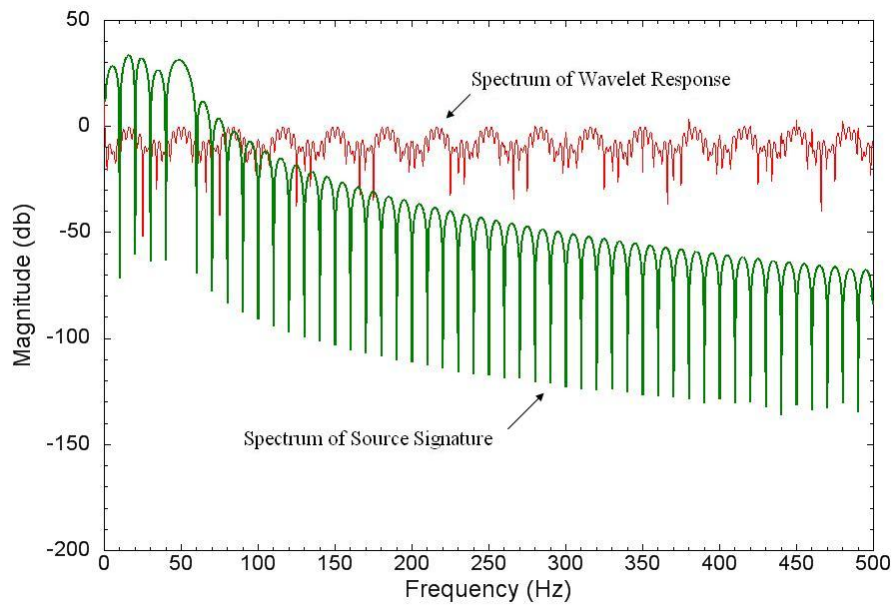


Figure 7.34 Expanded view of amplitude spectrum in Figure 7.33

The wavelet response corresponding to Figure 7.32 is shown in Figure 7.35. The first arrival at 0.05 sec and three reflections at $t = 0.30$, 0.33 and 0.36 seconds are clearly shown. The digital noise can be filtered significantly by adding white noise. For the noise-free synthetic signal, $\alpha = 0.001$ can attain a clear arrival coefficients (see Figure 7.36). The increase of α does not help with the noise-free signal. Figure 7.37 is almost the same as Figure 7.36, though α value varies dramatically.

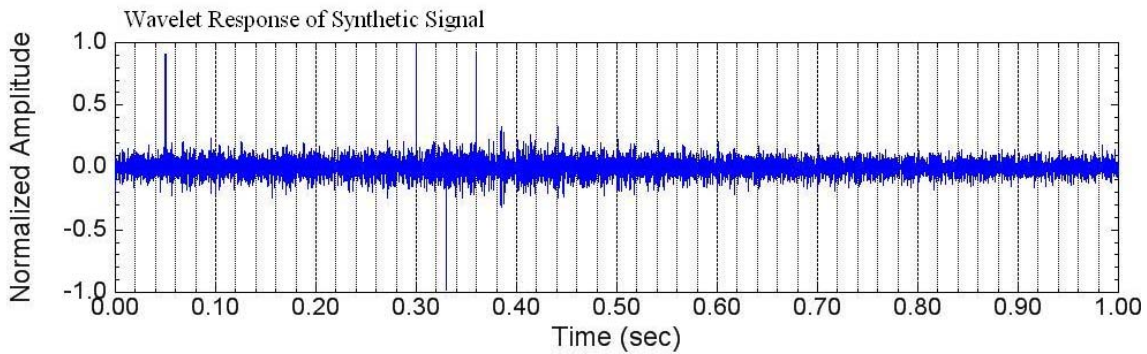


Figure 7.35 Wavelet response when $\alpha = 0$

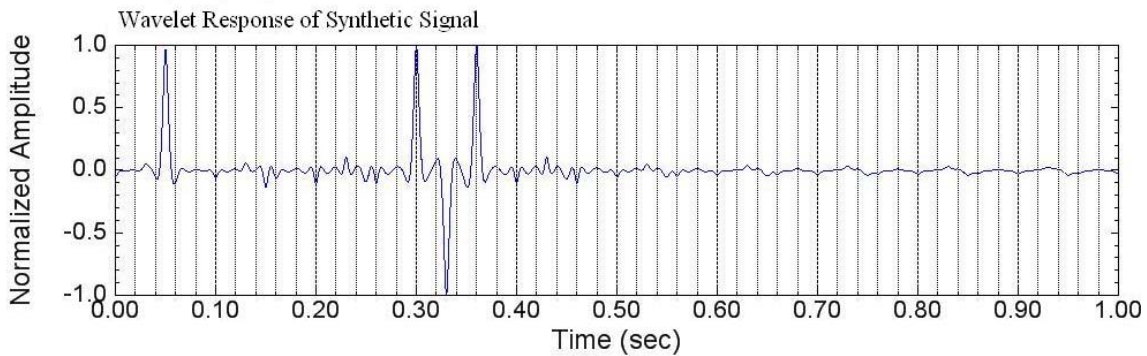


Figure 7.36 Wavelet response when $\alpha = 0.001$

Figures 7.38 and 7.39 demonstrate that the wavelet response can also be achieved by using the sinusoidal wavelet as the source signature, though a constant and consistent phase shift is observed, which does not affect the relative travel times. The twin wavelets

can work as a source signature only when their energy is relative greater than undesired signals or noise, as shown in Figure 7.40 through 7.42.

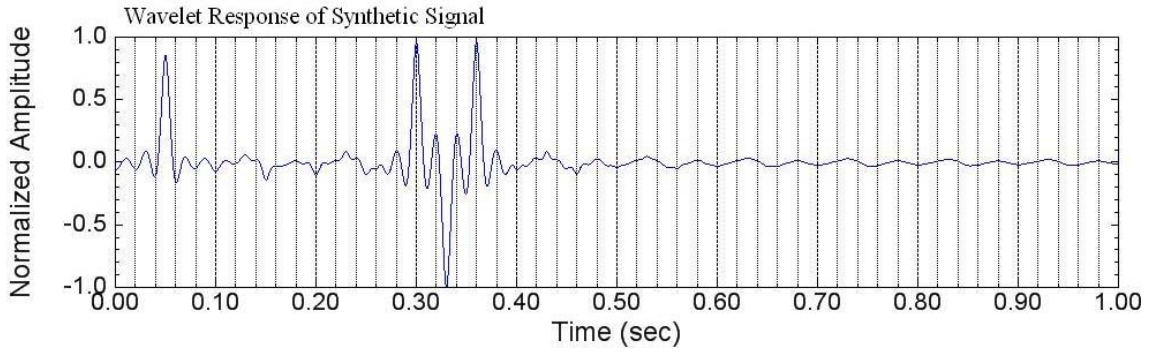


Figure 7.37 Wavelet response when $\alpha = 0.1$

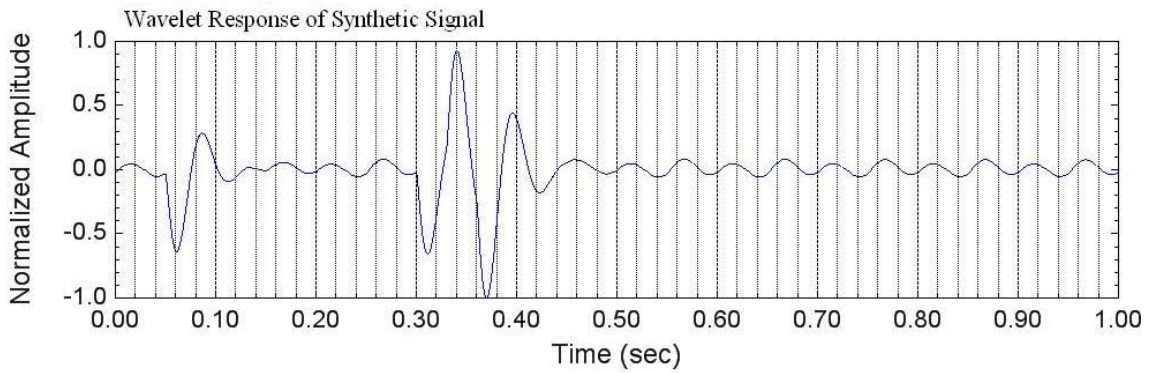


Figure 7.38 Wavelet response using sinusoidal wavelet when $\alpha = 0.001$

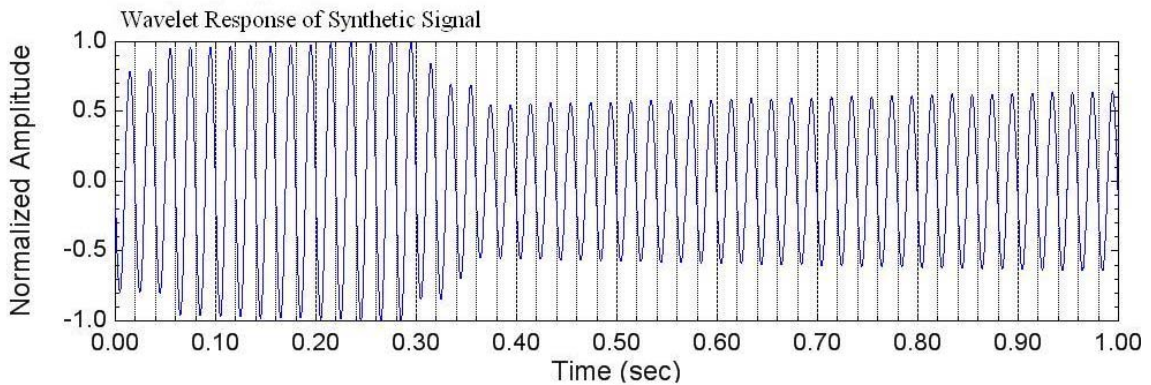


Figure 7.39 Wavelet response using twin wavelets when $\alpha = 0.001$

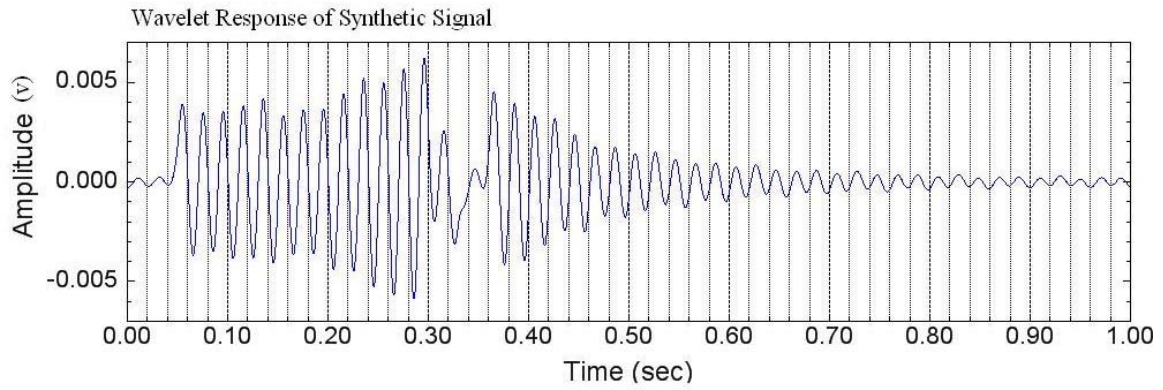


Figure 7.40 Wavelet response using twin wavelets when $\alpha = 0.1$

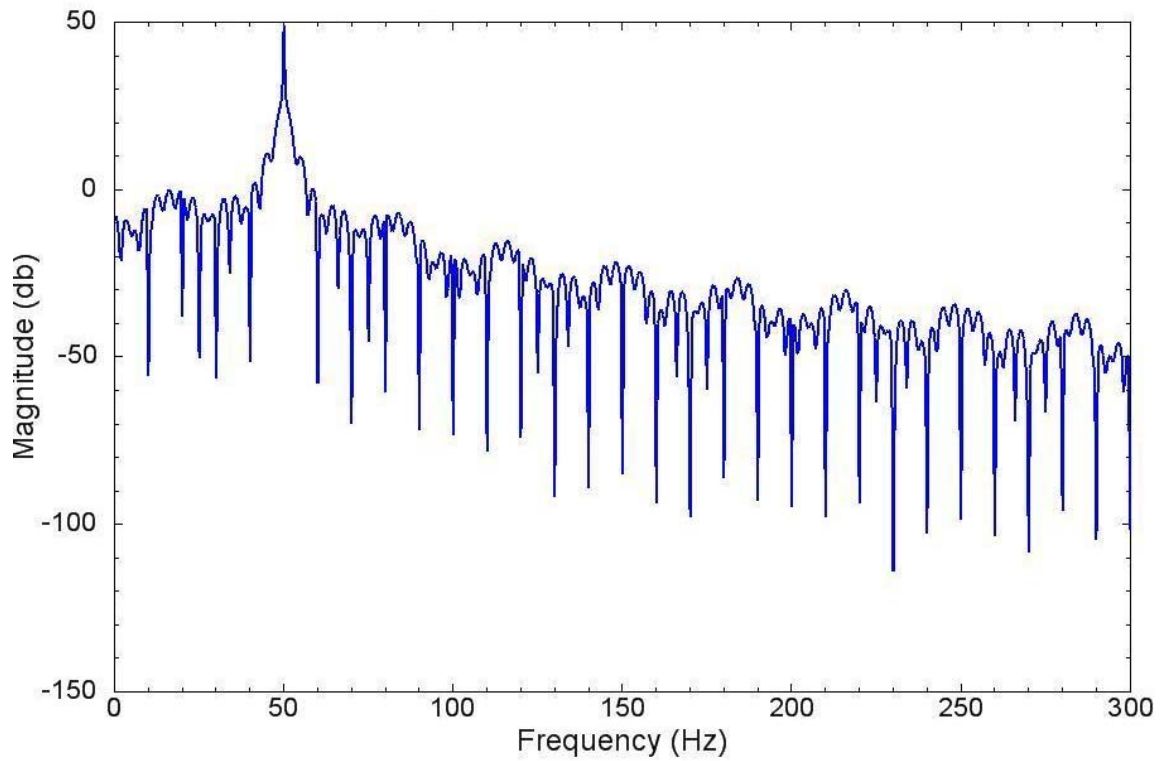


Figure 7.41 Spectrum of wavelet response using twin wavelets when $\alpha = 0.001$

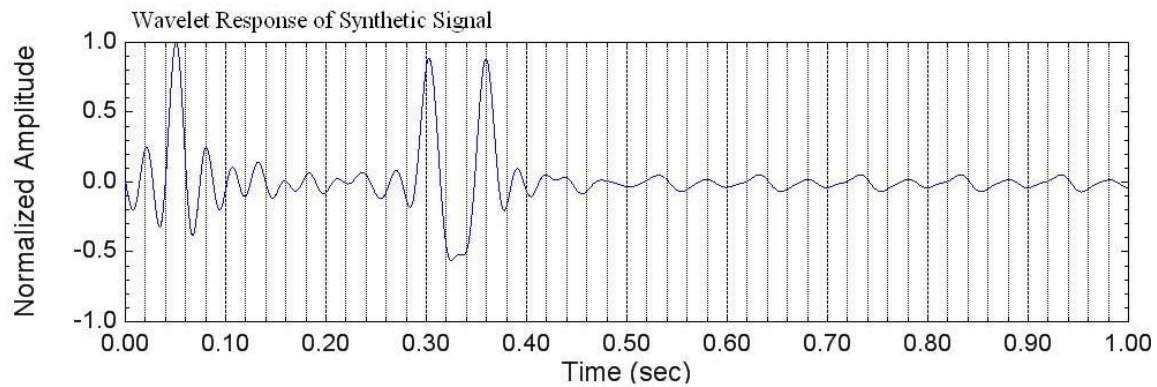


Figure 7.42 Wavelet response using twin wavelets when $\alpha = 0.001$ and filtered by low pass 40 Hz

Low pass filter works very well if none of the high spikes (digital noise) is in the low pass frequency range, otherwise, the survived spikes will smear the signal arrivals in the wavelet response (see Figure 7.43 to 7.45). Figure 7.45 and 7.46 demonstrate that error occurs if the low pass cutoff frequency is lower than 20 Hz.

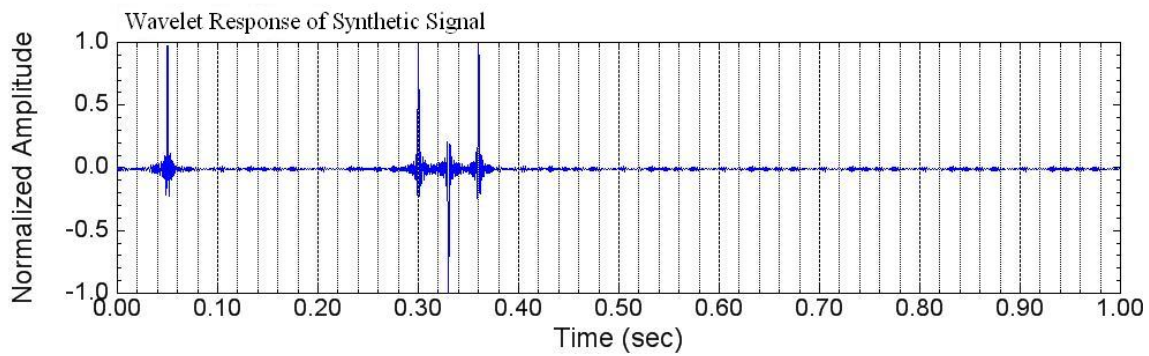


Figure 7.43 Wavelet response filtered by low pass 500 Hz

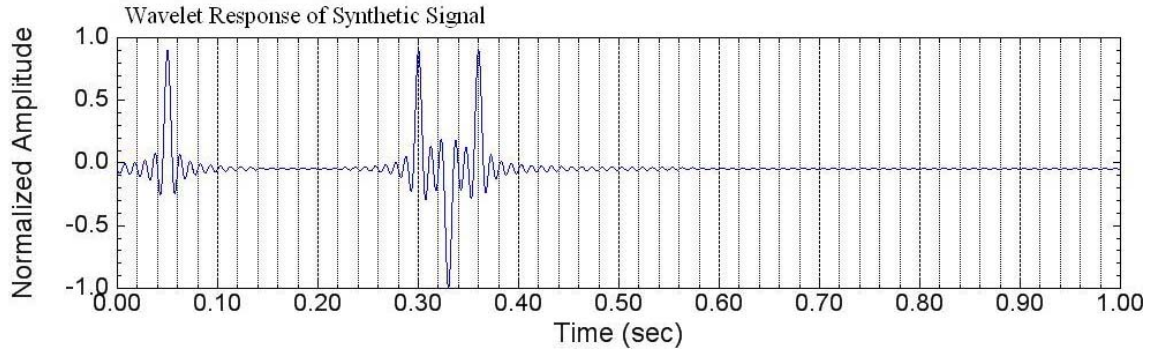


Figure 7.44 Wavelet response filtered by low pass 100 Hz

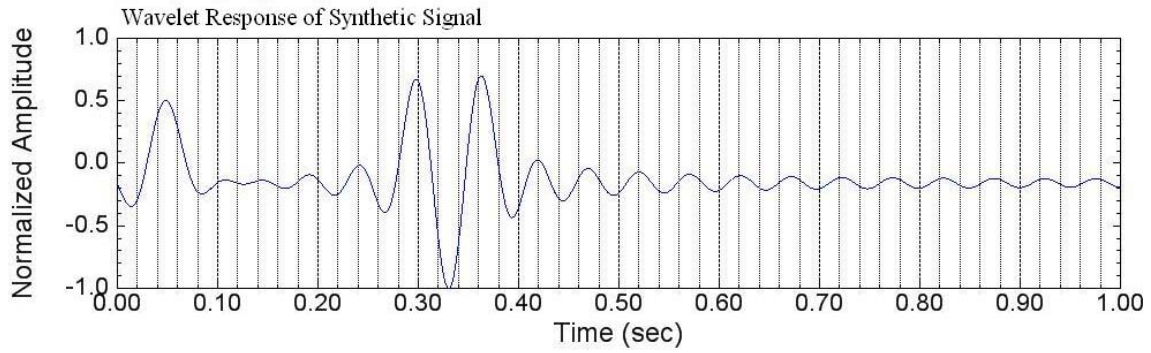


Figure 7.45 Wavelet response filtered by low pass 20 Hz

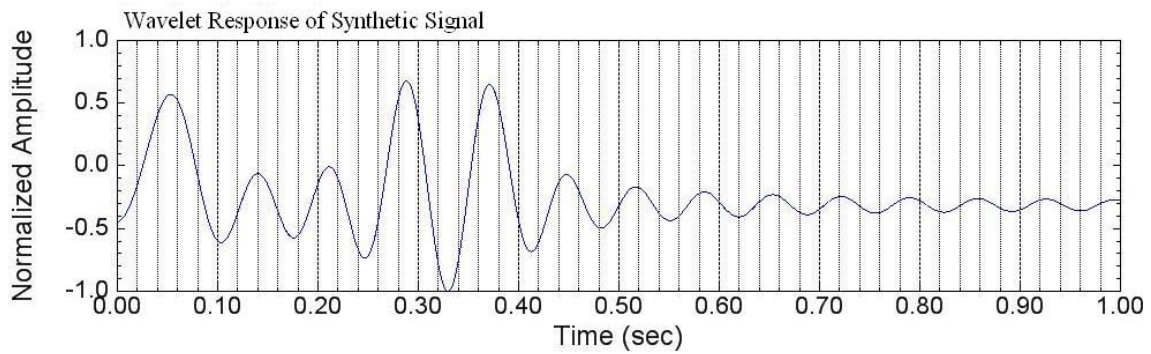


Figure 7.46 Wavelet response filtered by low pass 15 Hz

7.6.3 Deconvolution of trace data

A P-wave signal recorded at a depth of 291 m (970 ft) is shown in Figure 7.47.

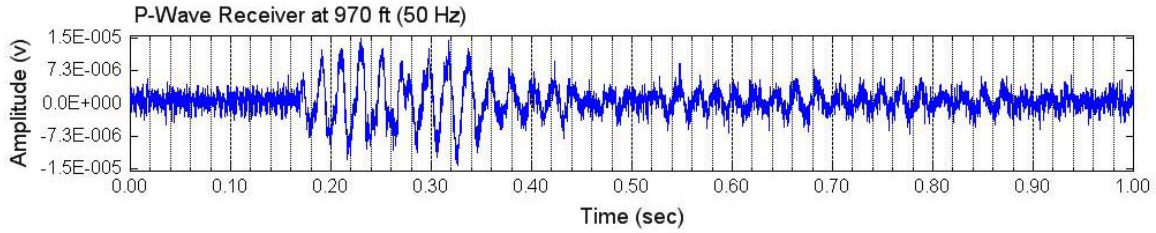


Figure 7.47 P-wave receiver signal (5 cycles of 50-Hz sine wave) at a depth of 291 m (970 ft)

The source signature for the P-wave signal is measured as:

$$u(t) = u(t | \bar{f} = 50Hz, f_n = 40Hz, T = 0.1sec, \xi = 0.25) \quad (7.97)$$

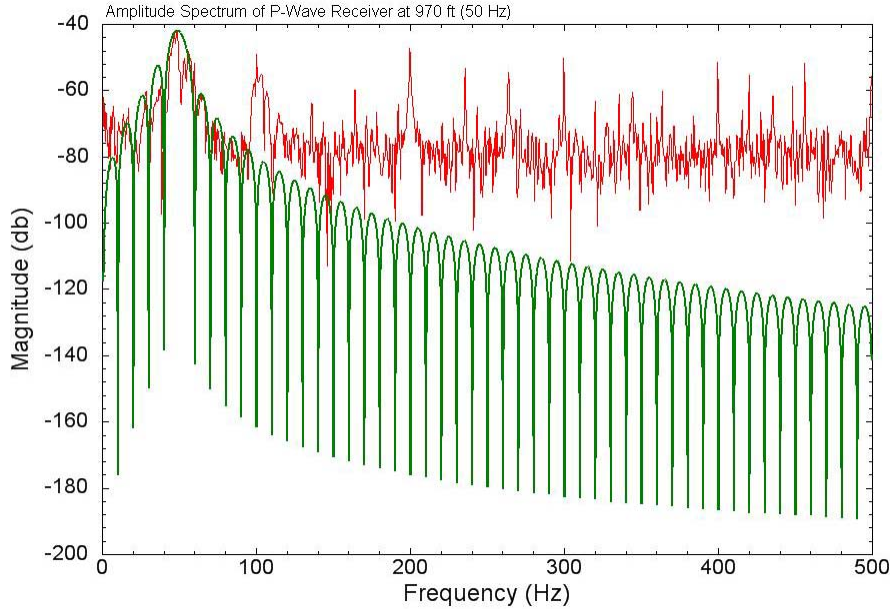


Figure 7.48 Spectra of P-wave receiver signal (5 cycles of 50-Hz sine wave) at a depth of 291 m (970 ft) and its source signature

The spectra of the P-wave signal and its signature are shown in Figure 7.48. Using $\alpha = 0.1$ leads to a spectrum of the wavelet response of the P-wave signal shown in Figure 7.49, a low pass 90 Hz will yield a wavelet response shown in Figure 7.50.

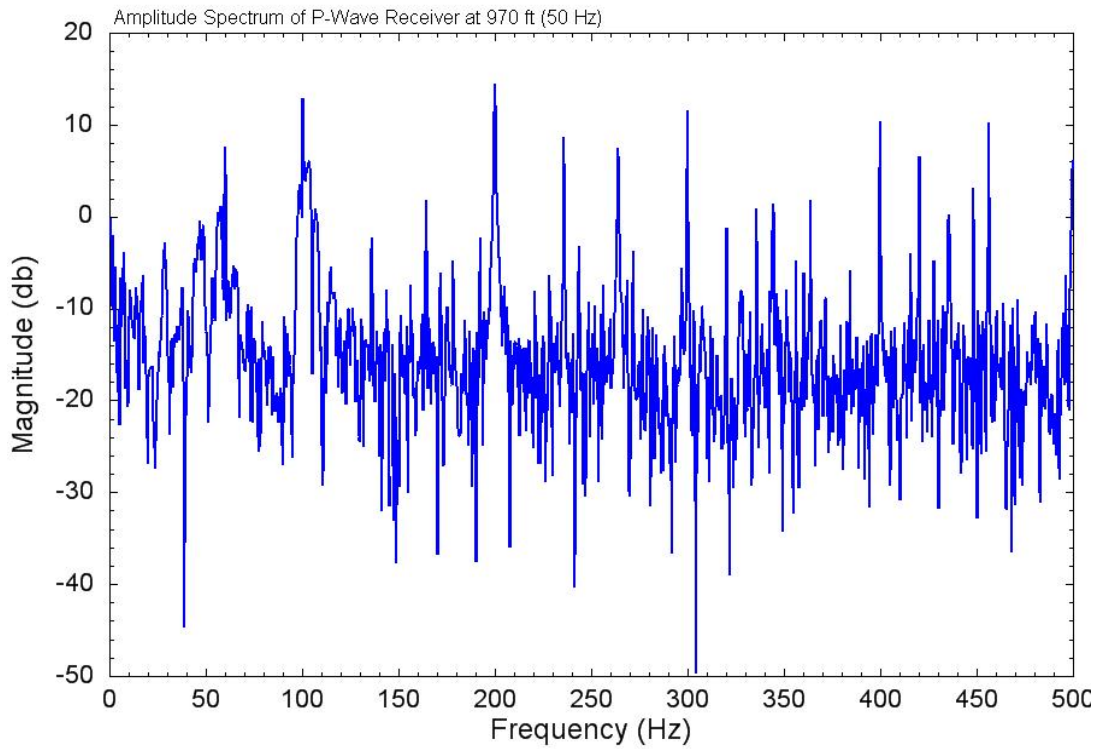


Figure 7.49 Spectrum of wavelet response ($\alpha = 0.1$) of P-wave receiver signal (5 cycles of 50 Hz sine wave) at a depth of 291 m (970 ft)

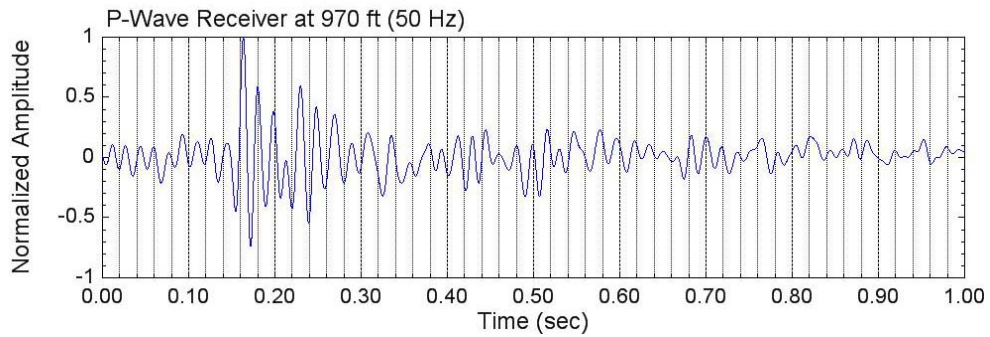


Figure 7.50 Wavelet response of P-wave receiver signal (5 cycles of 50 Hz sine wave) at a depth of 291 m (970 ft) using source signature wavelet

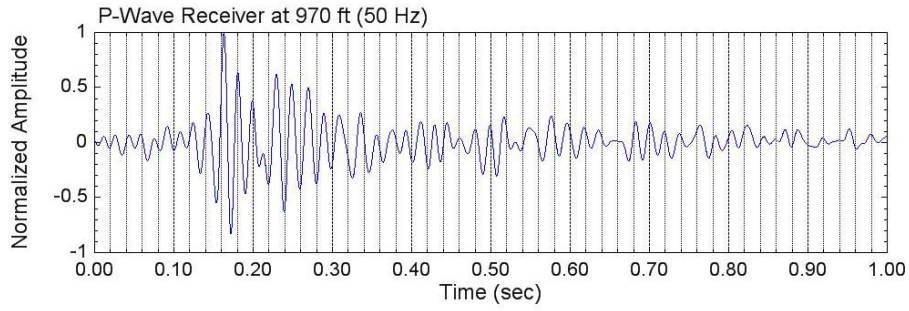


Figure 7.51 Wavelet response of P-wave receiver signal (5 cycles of 50 Hz sine wave) at a depth of 291 m (970 ft) using sinusoidal wavelet

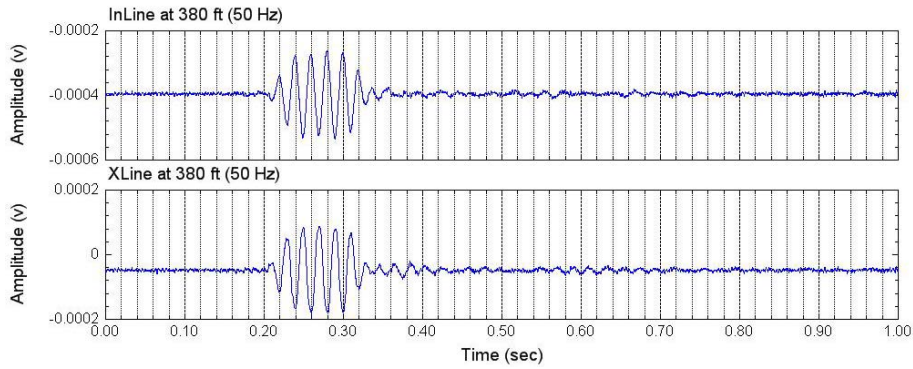


Figure 7.52 S-wave receiver signals (5 cycles of 50 Hz sine wave) at a depth of 114 m (380 ft)

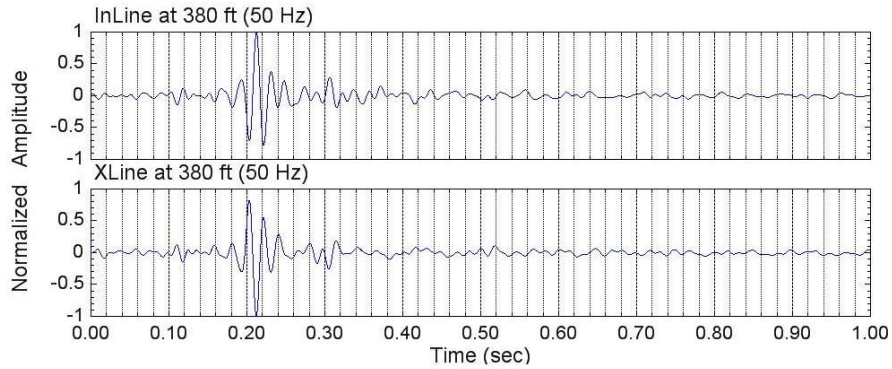


Figure 7.53 Wavelet response of S-wave receiver signals (5 cycles of 50 Hz sine wave) at a depth of 114 m (380 ft) using source signature wavelet

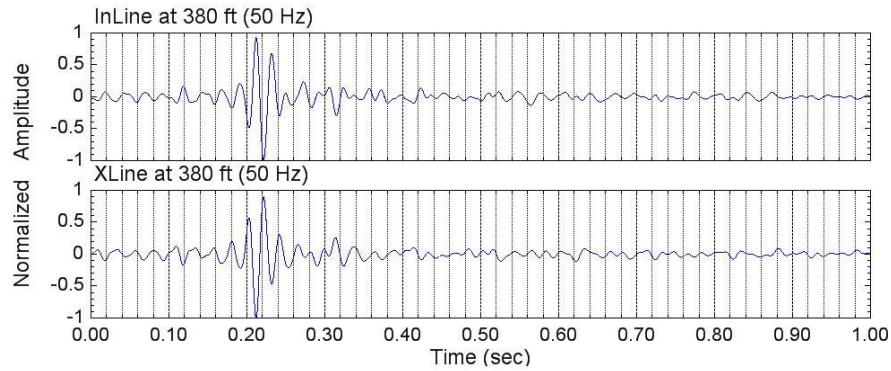


Figure 7.54 Wavelet response of S-wave receiver signals (5 cycles of 50 Hz sine wave) at a depth of 114 m (380 ft) using sinusoidal wavelet

7.7 P-WAVE WAVELET RESPONSE IN BOREHOLE C4993

The source signature of the P-wave receiver signals is defined in Equation (7.97). The sinusoidal wavelet was used as the source signature to perform the deconvolution. A white noise ratio $\alpha = 0.1$ is used. After the deconvolution, a 90-Hz low pass filter was applied to the 50-Hz signals, and a 50-Hz low pass was applied to the 30-Hz signals.

The waterfall plots determined from the wavelet responses are shown in Figures 7.55 through 7.60. These waterfall plots show a clear first peak for the P-wave measurement at each depth. The first peak has the dominant amplitude and clearly exhibits an independent waveform.

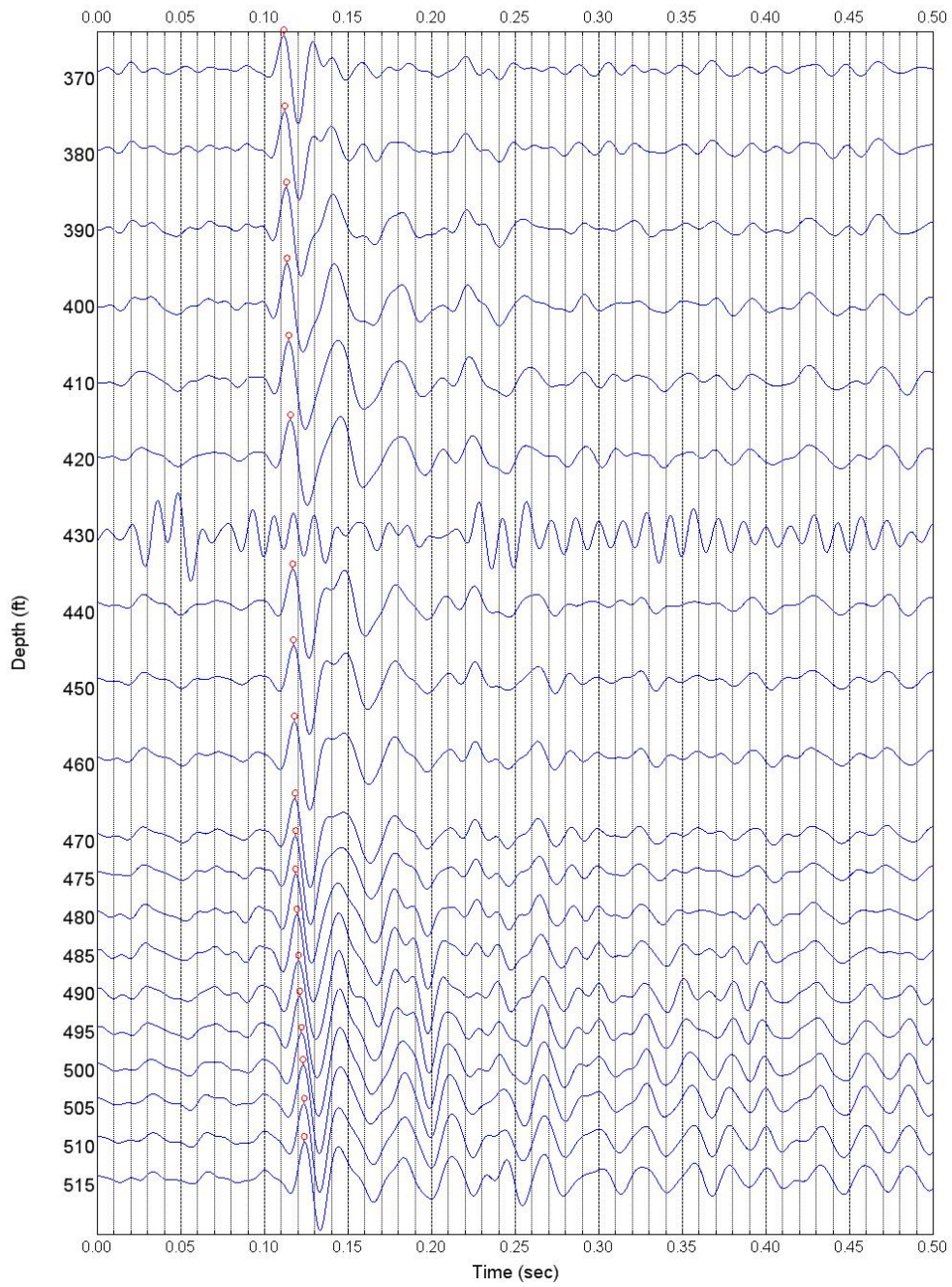


Figure 7.55 Wavelet response of 50-Hz P-wave receiver signals (370-515 ft)

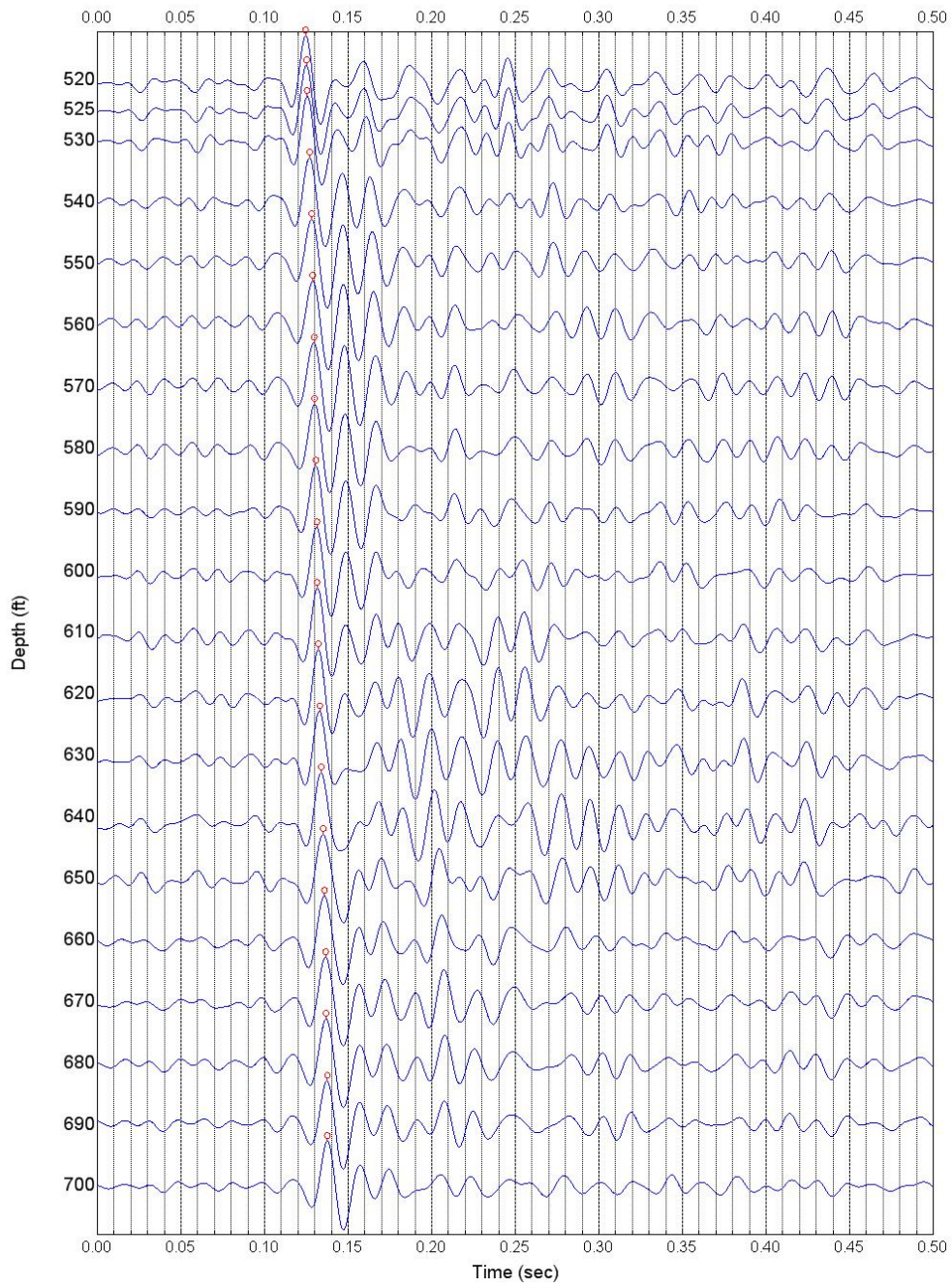


Figure 7.56 Wavelet response of 50-Hz P-wave receiver signals (520-700 ft)

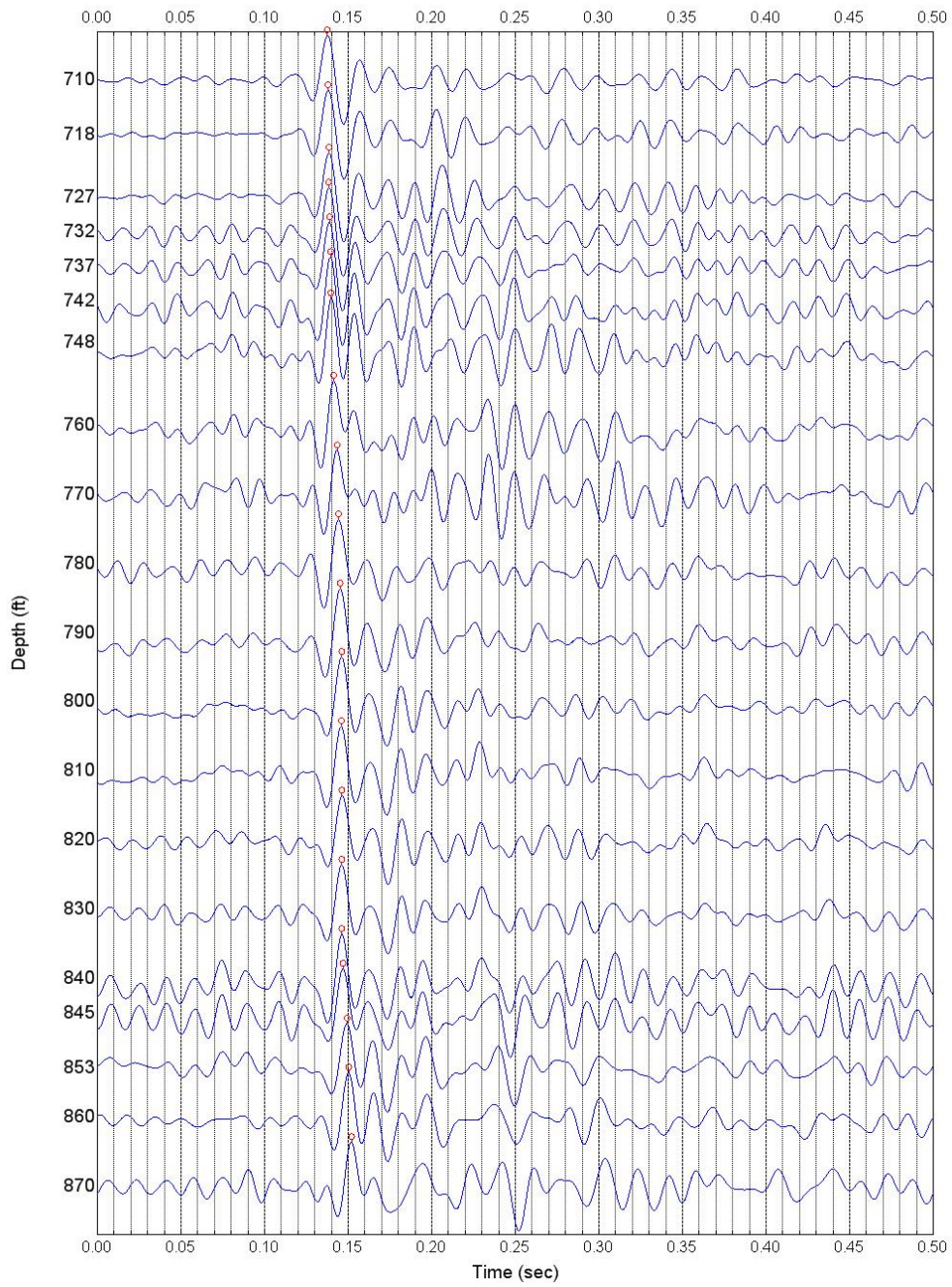


Figure 7.57 Wavelet response of 50-Hz P-wave receiver signals (700-870 ft)

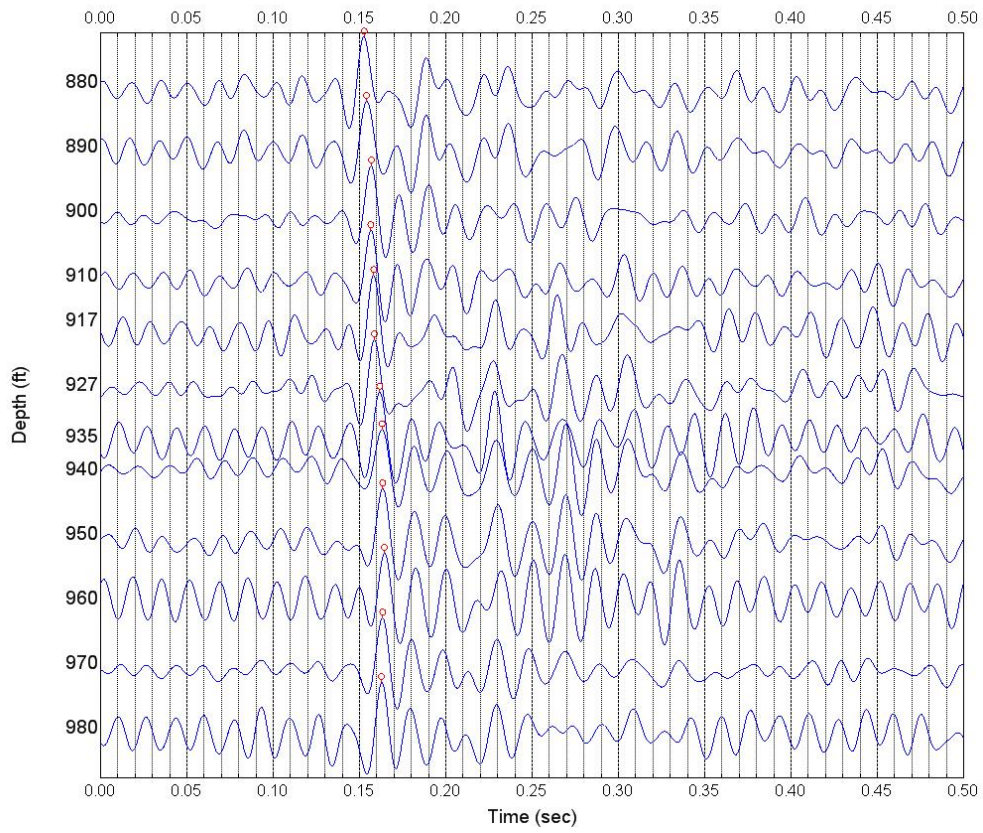


Figure 7.58 Wavelet response of 50-Hz P-wave receiver signals (880-980 ft)

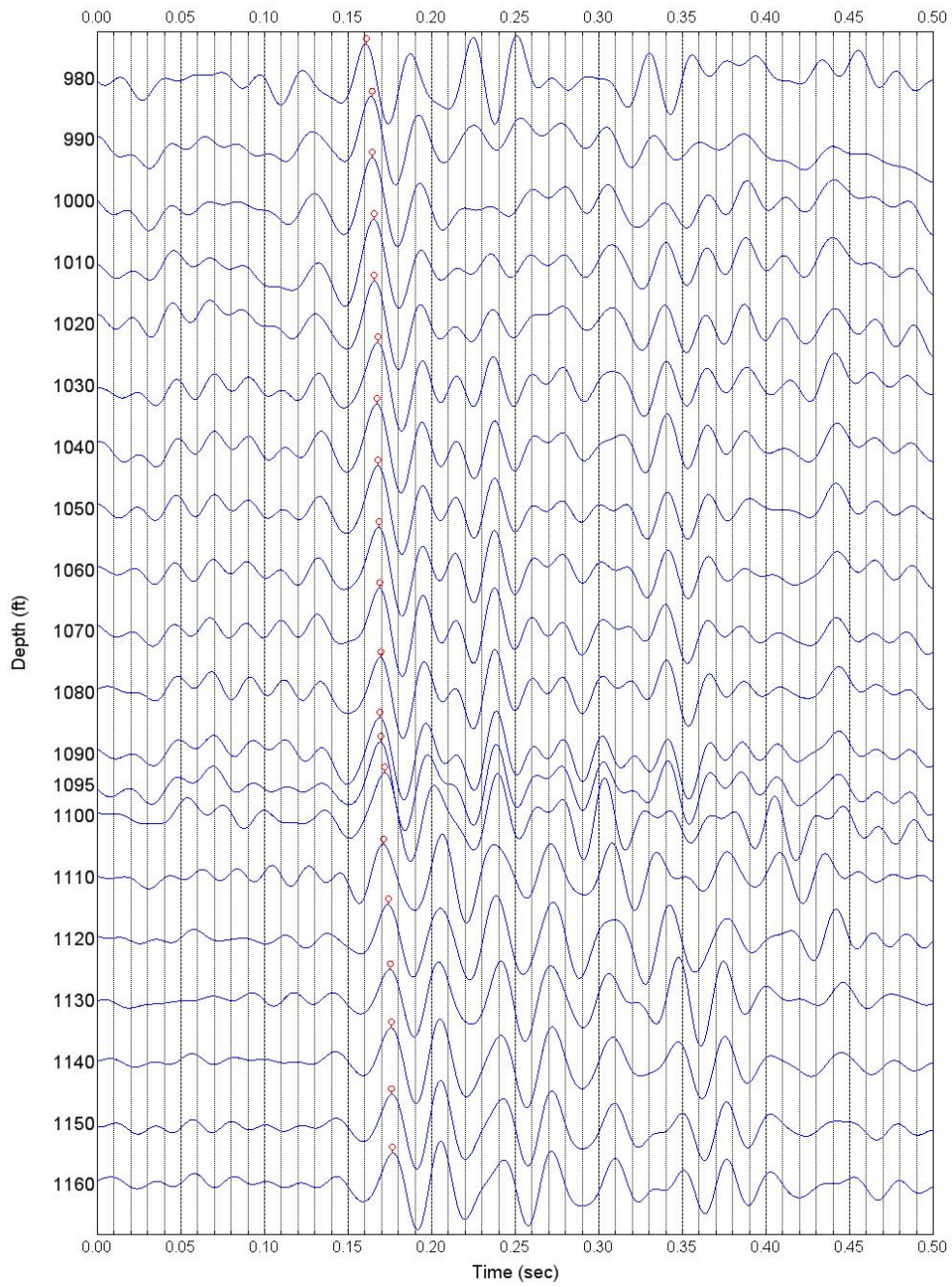


Figure 7.59 Wavelet response of 30-Hz P-wave receiver signals (980-1160 ft)

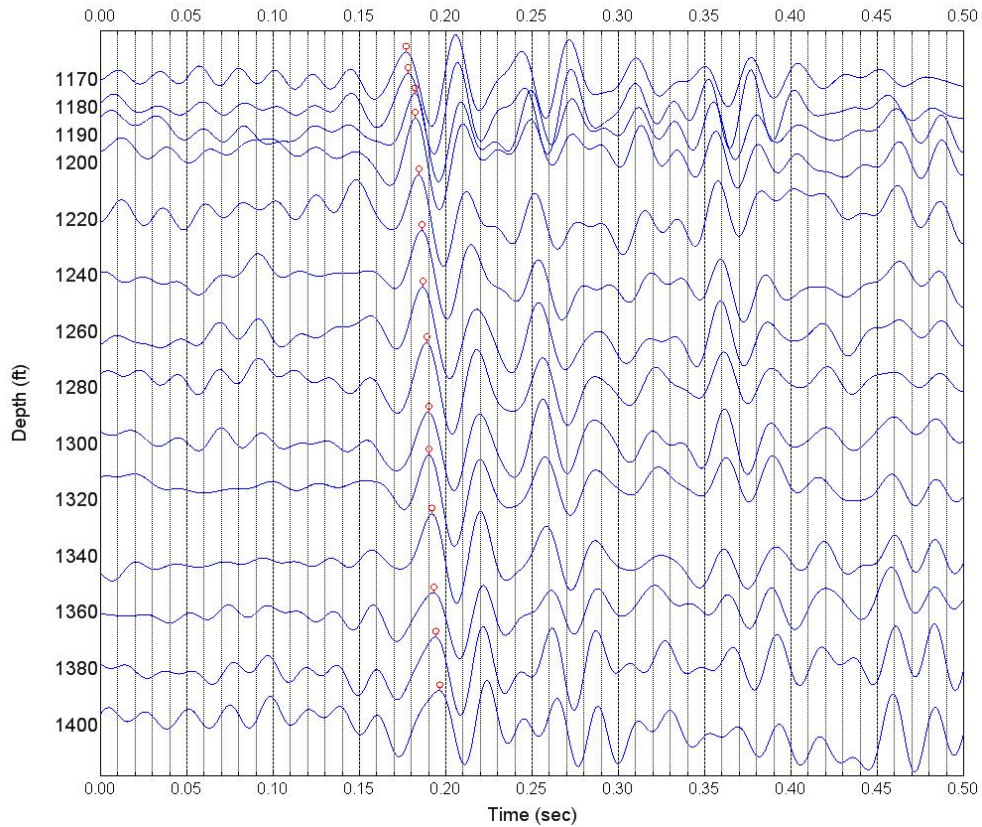


Figure 7.60 Wavelet response of 30-Hz P-wave receiver signals (1170-1400 ft)

The comparison of the travel times between the arrival-identification method and the wavelet-response method is presented in Figure 7.61. The travel times interpreted by arrival-identification method are also presented in Chapter 4. The two methods match very well. All layers have less than 5% difference in P-wave velocities except the Elephant Mountain Member where the difference is 12%. Near the boundaries, the wavelet-response method has less deviation than the arrival-identification method in that the former has less waveform distortion. However, both methods can not avoid the velocity variation caused by the effect of the effective medium theory. The measured velocity is the velocity of the effective medium that covers all the layers within a thickness equal to a wavelength discussed in Chapter 4. The actual layers covered by the

effective medium within a wavelength vary with measurement depth. For example, when the measurement moves downward, if a new thin layer with a much lower average velocity joins the effective medium from the bottom, the measured velocity may decrease. If a thin layer on top of the effective medium moves beyond a wavelength of the thickness above the measurement depth, the thin layer is no longer a part of the effective medium, and the measured velocity may increase. The variation of the content of the effective medium causes the velocity variation within a geological layer. On the other hand, if a basalt layer with much higher velocity joins the effective medium, the measured velocity may increase. When the basalt layer is no longer in the top of the effective medium, and/or a new thin layer joins from the bottom, the measured velocity may decrease.

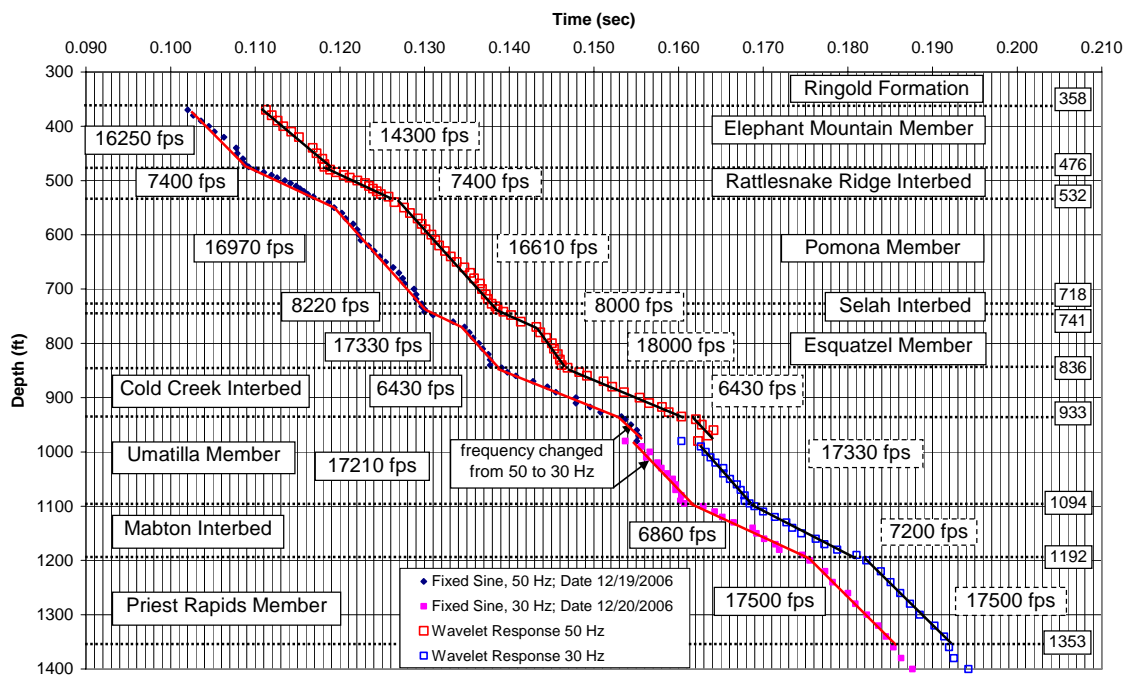


Figure 7.61 Comparison of relative travel times and interpreted V_p profiles in Borehole C4993 between arrival-identification method and wavelet-response method

7.8 S-WAVE WAVELET RESPONSE IN BOREHOLE C4993

The source signature of the 30-Hz S-wave receiver signals is defined as:

$$u(t) = u(t | \bar{f} = 30\text{Hz}, f_n = 20\text{Hz}, T = 0.133\text{sec}, \xi = 0.25) \quad (7.98)$$

The sinusoidal wavelet was used as the source signature to perform the deconvolution. A white noise ratio $\alpha = 0.1$ is used. After the deconvolution, a 50-Hz low-pass filter was applied to the wavelet responses of 30-Hz signals.

The waterfall plots determined from the wavelet responses of the forward S-wave receiver signals are shown in Figures 7.62 through 7.64. These waterfall plots show the wavelet responses of the forward S-wave receiver signals below a depth of 270 m (900 ft) where signals with multiple polarizations pose a challenge to the arrival-identification method. The wavelet responses of the reverse S-wave signals are not shown. Two wavelet responses at each depth correspond to two orthogonal components (S_1 and S_2) of the disoriented S-wave receiver. The arrival times are picked on the wavelet responses prior to correction for disorientation and denoted by a small circle for one component (S_1) and a small triangle (S_2) for the other. The disorientation is corrected using the method presented in Sections 7.4 and 7.5.

The wavelet-response method has higher resolution than the arrival-identification method for travel time analysis. The comparison of the travel times between the arrival-identification method and the wavelet-response method is presented in Figure 7.65. The travel times interpreted by arrival-identification method are also presented in Chapter 4. The two methods match very well for measurements with 50-Hz S-wave signals above a depth of 297 m (990 ft) where all layers have less than 5% difference in S-wave velocities. The difference for measurements with 30-Hz S-wave signals below a depth of 297 m (990 ft) is within 15%. The wavelet-response method has much less scatter than the arrival-identification method in that the former has less waveform distortion.

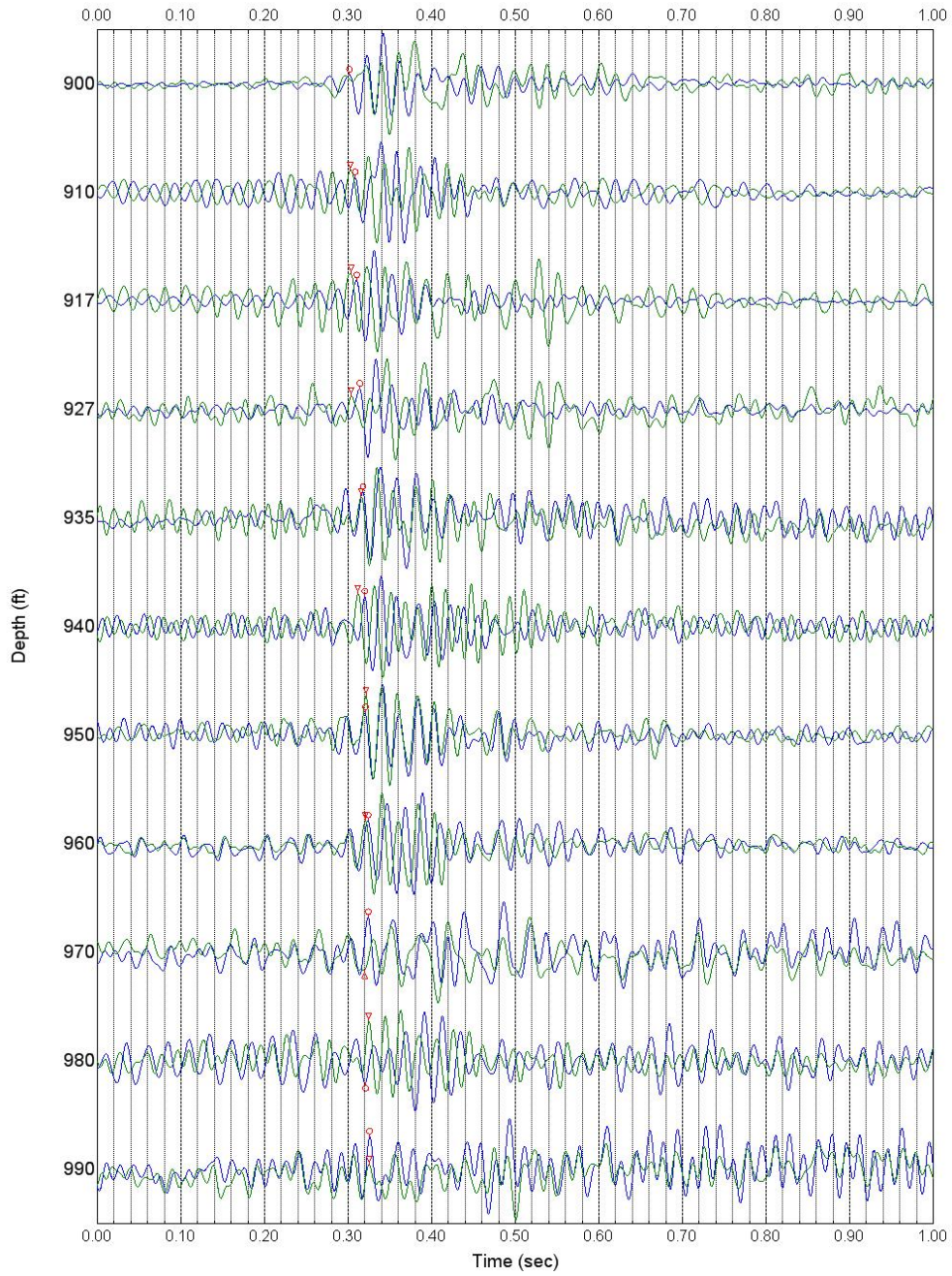


Figure 7.62 Wavelet response of 50-Hz forward S-wave signals of disoriented receiver (900–990 ft)

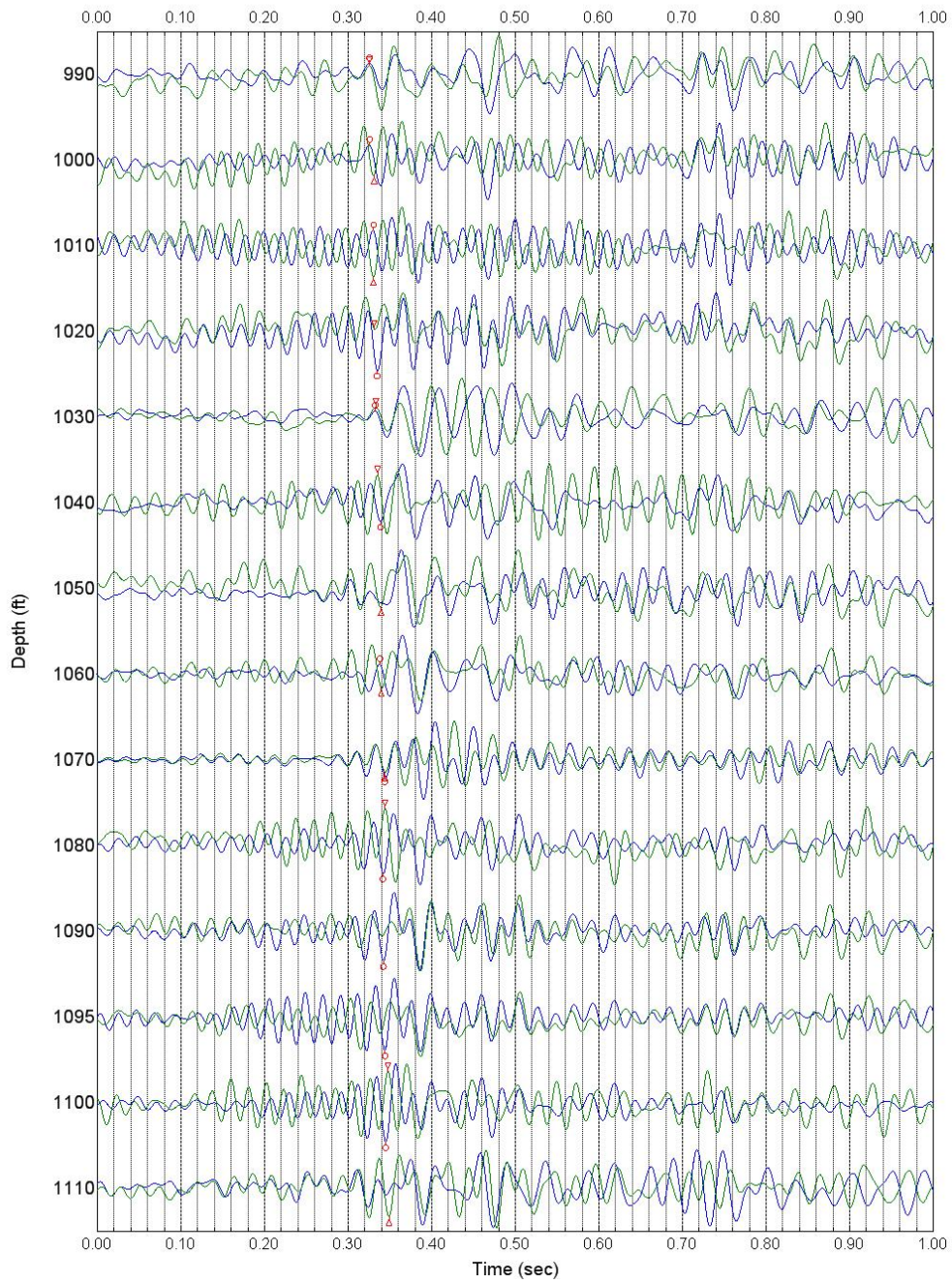


Figure 7.63 Wavelet response of 30-Hz forward S-wave signals of disoriented receiver (990–1110 ft)

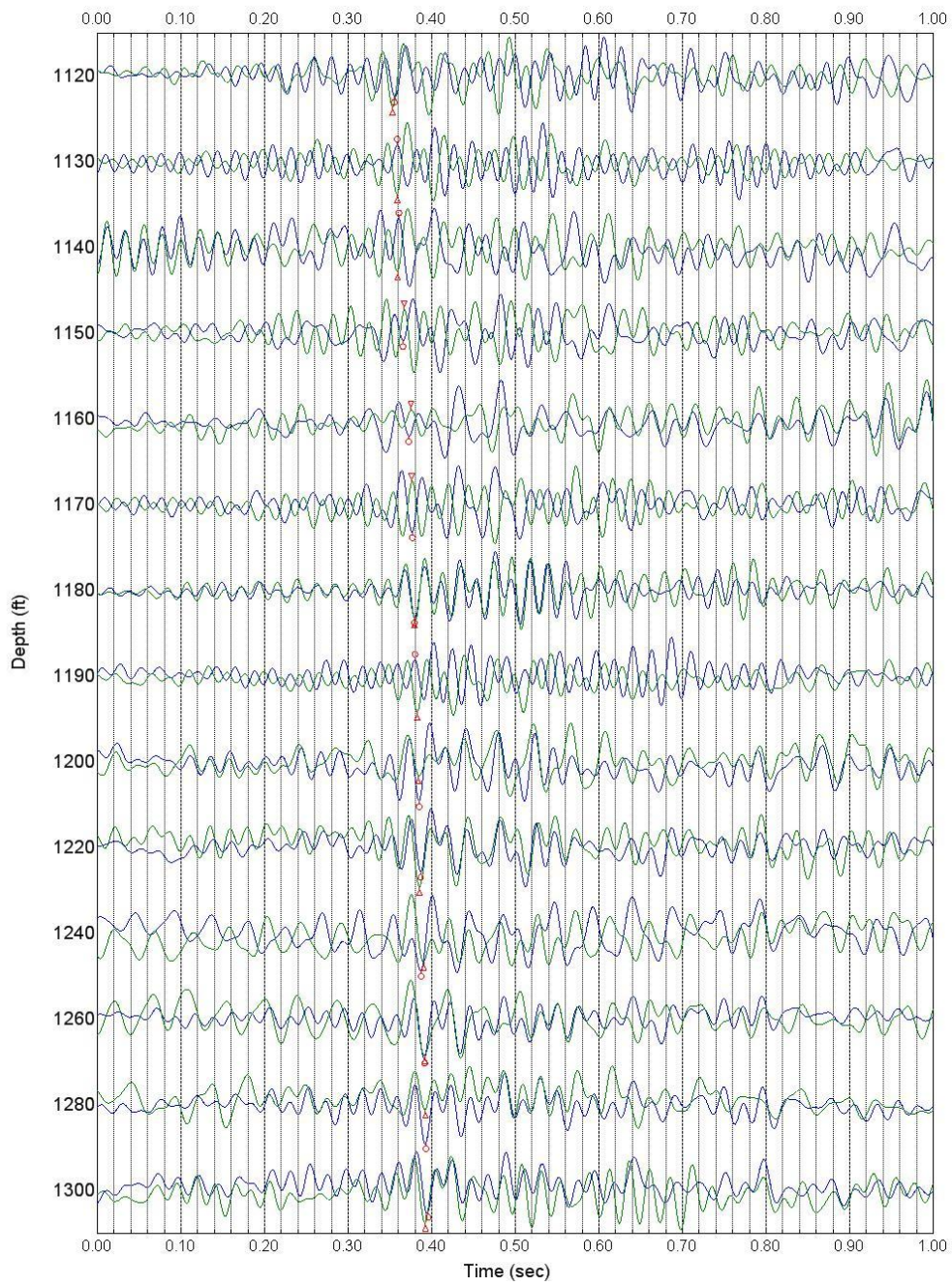


Figure 7.64 Wavelet response of 30-Hz forward S-wave signals of disoriented receiver (1120–1300 ft)

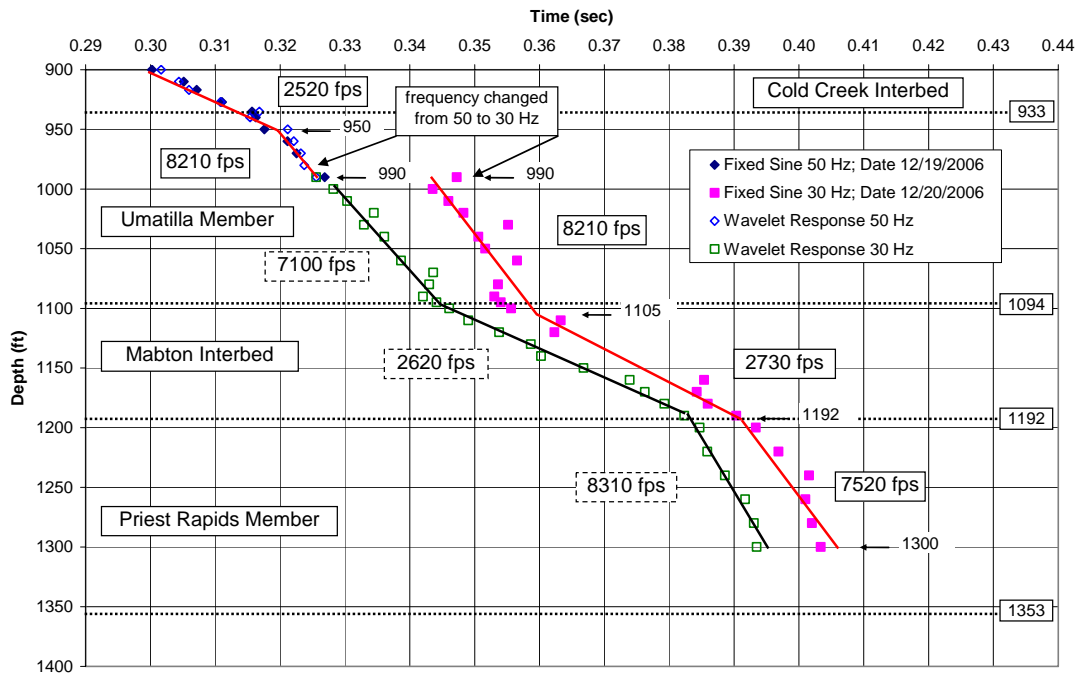


Figure 7.65 Comparison of relative travel times and interpreted Vs profiles in Borehole C4993 between arrival-identification method and wavelet-response method

7.9 SUMMARY

Wavelet response is a unique feature of the fixed-sine source wavelet that is used in this research. In this chapter, the difference between impulse response and wavelet response is explained and its application in travel-time analysis as done in deep downhole testing is presented. Dual wavelets are more complicated. The differential velocity between the dual wavelets can affect the wave identification method and other methods that are sensitive to waveform distortions. This simplification of dual wavelets into single wavelet does not affect the travel time analysis using wavelet response method.

The wavelet response method greatly simplifies the S-wave travel time analysis. The correction for disorientation of the receiver tool is sensitive to mode conversions, wave scattering and coupling, and especially multiple polarization skewing. Without

obtaining a correctly oriented S-wave signal, the arrival time corresponding to the true orientation at each depth can be calculated analytically by using the wavelet responses of the two orthogonal components of the S-wave records. The wavelet-response method demonstrates higher resolution than the arrival-identification method for travel time analysis.

Chapter 8 Summary, Conclusions and Recommendations

8.1 SUMMARY

In this research, the framework of a new method for deep downhole seismic profiling for earthquake engineering investigations was developed. Deep profiling is defined as depths exceeding 225 m (750 ft). The main purpose of seismic profiling in these investigations is the measurement of detailed V_p and V_s profiles, typically with spacings of 3 m (10 ft) or less between measurement points. Conventional VSP and downhole tests with chirp sweeps are not used for this purpose. Typically, measurement spacings are much larger and this approach involves measurement of group velocities which show velocity dispersion as the measurements go significantly deeper in the geologic strata.

The framework of the new method for deep downhole testing involves five components. First, a fixed-sine forcing function that is readily available with a tri-axial vibratory named T-Rex. Second, the identification of the source signature created with a fixed-sine source signal. Third, the technique to measure the SDOF model parameters that are customized to the local vibrator-earth system. The local vibrator-earth system varies with site conditions and testing time when the system is subjected to prolonged repetitive vibrations. Fourth, the development of a wavelet-response technique that improves the resolution of the travel time analysis for engineering purposes. Fifth, a new method to correct the disorientation of the receiver tool for multi-component and multi-polarization S-wave signals.

A computer program named DeepSeis 2.1 was developed to visualize and process signals quickly on the test site for simplified travel time analysis using the wave identification method. Least-squares fitting was used for correction of disorientation of S-

wave signals. DeepSeis 2.1 provides paneled plots and waterfall plots for various comparisons of signals such as forward and reverse, in-line and cross-line, P and S, and filtered and unfiltered. It was used at a site in Hanford, WA, and the velocity profiles were compared with results from suspension logging tests and laboratory tests. These comparisons show that DeepSeis 2.1 and the testing method work quite well. However, the wave identification method can not effectively separate multi-component signals such as multi-path arrivals, multi-reflections and multi-polarizations. Therefore DeepSeis 2.1 was improved by integrating the wavelet-response technique that deals with all of these complications of multi-component signals as well as anisotropy. The improved software called DeepSeis 3.1 has a state-of-the-art preprocessing technique that enables quick in-situ signal processing to aid decision-making to determine the best excitation frequency and source duration based on site conditions. The software also implements the newly developed method of correcting for disorientation of the S-wave signals. DeepSeis 3.1 confirms that the wavelet-response technique is superior in handling multi-component signals for better resolution in velocity profiling. The wavelet-response technique was applied to the same site in Hanford, WA, and comparisons with the wave-identification method demonstrate the improvement in VSP resolution.

Velocity dispersion is a factor that distinguishes wavelet response from the impulse response. The velocity varies with signal frequency and incident angle. When the incident angle is near vertical, the velocity dispersion is at its minimum. When the actual stratigraphy is not horizontally layered, velocity dispersion increases.

The current test procedures can be improved for a higher signal quality by customizing the excitation frequency of the vibrator to the local damped natural frequency of the earth-vibrator system. This work proposes a method to measure the site

localized damping ratio and natural frequency. Properly increasing the duration of the source signal would also contribute to improving the quality of the receiver signal.

The arrival-identification method as used in DeepSeis 2.1 is vulnerable to the waveform distortions caused by multi-path signals, strong reflectivity, velocity dispersion and anisotropy. This work suggests a frequency criterion to reduce the waveform distortion caused by velocity dispersion.

Conventional travel time analyses for a vibratory source almost universally focus on impulsive sources or chirp sweeps. After a few tests with impulsive sources and chirp sweeps were compared with the durational sinusoidal source, the sinusoidal source was then chosen. No data processing technique was found in the literature regarding trace data generated by a durational sinusoidal source wavelet. The work developed herein represents a new approach to identify the source signature of the sinusoidal source.

The normalized source signature is relevant only to four parameters: (1) the excitation frequency, (2) the source duration, (3) the damping ratio, and (4) the natural frequency of the vibrator-earth system. Two of the parameters are designated input to the vibrator and the other two parameters can be measured in the field test using the proposed method in this work.

Anisotropy is weak (approximately 10-20%) in most cases of interest to geophysicists (Thomsen, 1986). For P-wave velocity measurements, most seismic anisotropy is negligible for deep downhole testing or near-offset vertical profiling. S-waves are more susceptible to anisotropy factors such as cracks, fissures, faults, and inclined layering. Further work is needed to investigate the effect of S-wave anisotropy in these measurements.

To reduce effects such as mode conversion, scattering, coupling, and S-wave splitting, the vibrator is located as close to the borehole as possible to ensure a vertical

wave propagation. In addition, the vibrator is capable of separately generating three modes of vibration, which are P, in-line S and cross-line S, each along its projected wave polarization. During P-wave production, the vibrator moves vertically so that the three velocity surfaces do not have the same energy contribution at depth. The energy of the P mode dominates in this case and the energy for S modes is negligible. During in-line or cross-line S wave production, the energy for P modes is negligible.

Effective medium theory may be of concern when thin layers exist in these tests. The relative relationship between the wavelength of the vibratory source signal and the thickness of the layers may contribute to velocity anisotropy. The wavelengths are in the same range as the thickness of major layers and greater than the thicknesses of most thin layers. Further consideration of the effect of the effective medium theory is necessary in the future.

8.2 CONCLUSIONS

1) The fixed-sine source signal is applicable and superior in dealing with high-resolution deep downhole velocity profiling for earthquake engineering investigations with close receiver spacings.

2) The wave identification method combined with fixed-sine source signals allowed the investigation to reach about 420 m (1400 ft) with the help of DeepSeis 2.1 at a site in Hanford, WA, with complex site conditions due to the alternating high contrasts in velocity of multi-layered geological materials.

3) Improvement in resolution of the V_p and V_s profiles was made through the development of a method to identify the source signature of the fixed-sine source signals and by development of a new wavelet-response technique. A new method to correct for disorientation of the receiver tool is employed to significantly reduce the effect of

waveform distortion. These improvements increased the resolution in velocity profiling under conditions of multi-arrivals, multi-reflections, and multi-polarizations.

4) A practical approach is explored to measure in-situ site conditions. Guidelines for excitation frequency and source duration for the test procedures are recommended. Excitation frequency and duration should be customized to site conditions. P waves and S waves should use different excitation frequencies if the measured site localized damping ratio is different for P and S modes.

8.3 RECOMMENDATIONS

Wavelet response for dual wavelets should be further explored, especially when the two wavelets have a similar energy contribution to the source signature.

Effective medium theory should be studied to investigate the wavelength effect on thin layers.

Attenuation anisotropy should be studied as complementary to the velocity anisotropy.

References

- Aki, K. and Richards, P.G. (1980) "Quantitative Seismology: Theory and Methods", Volume 1, pp. 74, W.H. Freeman and Company, San Francisco.
- Alford, R.M. (1986) "Shear Data in the Presence of Azimuthal Anisotropy", SEG Expanded Abstracts, pp. 476-479
- Archuleta, R.J., Seale, S.H., Sangas, P.V., Baker, L.M. and Swain, S.T., (1992) "Garner Valley downhole array of accelerometers: Instrumentation and preliminary data analysis", Bulletin of the Seismological Society of America, Volume 82, No. 4, pp. 1592-1621
- Auld, B.A. (1973) "Acoustic Fields and Waves in Solids", Volume 1: John Wiley and Sons
- Backus, G.E. (1962) "Long-wave elastic anisotropy produced by horizontal layering", J. Geophysical Research. Volume 67, pp. 4427-4440
- Baeten, G. and Ziolkowski, A. (1990) "The Vibroseis Source", ISBN 0-444-88879-9, New York: Elsevier Science Publishing Company Inc.
- Bagaini, C. (2006) "Enhancing the Low-Frequency Content of Vibroseis Data", SEG/New Orleans 2006 Annual Meeting
- Bakulin, A. and Grechka, V. (2003) "Short Note: Effective Anisotropy of Layered Media", Geophysics, Volume 68, pp. 1817-1821
- Barnett, D.B., K.R. Fecht, S.P. Reidel, B.N. Bjornstad, D.C. Lanigan and C.F. Rust (2007) "Geology of the Waste Treatment Plant Seismic Boreholes", PNNL-16407, Rev. 1. Pacific Northwest National Laboratory, Richland, Washington
- Ben-Menahem, A. and Sena, A.G. (1990) "Seismic Source Theory in Stratified Anisotropic Media", Journal of Geophysical Research, Volume 95, pp. 15395-15427.
- Berkhout, A.J. (1984) "Seismic Resolution", Elsevier Science Publishing Co.
- Berryman, J.G. (1979) "Long-Wave Elastic Anisotropy in Transversely Isotropic Media", Geophysics, Volume 44, No.5, pp. 896-917
- Berryman, J.G., Grechka, V.Y. and Berge, P.A. (1999) "Analysis of Thomsen parameters for finely layered VTI media", Geophysical Prospecting, Volume 47 (6), pp. 959-978

- Bickel, S.H. (1982) "The Effects of Noise on Minimum-Phase Vibroseis Deconvolution", *Geophysics*, Volume 47, pp. 1174-1184
- Bland, D.R. (1969) "Nonlinear Dynamic Elasticity", Blaisdell, Waltham, MA, pp. 49
- Bogges, A. and Narcowich, F.J. (2001) "A First Course in Wavelets with Fourier Analysis", New Jersey: Prentice Hall
- Borcherdt, R.D. (1977) "Reflection and Refraction of Type-II S Waves in Elastic and Inelastic Media", *Bulletin of the Seismological Society of America*, Volume 67, pp. 43-67
- Braga, A.M.B. (1990) "Wave Propagation in Anisotropic Layered Composites", PhD Dissertation: Stanford University, Stanford, California
- Brand, L. (1947) "Vector and Tensor Analysis", New York: Wiley
- Brittle, K.F., Lines, L.R. and Dey, A.K. (2001) "Vibroseis Deconvolution: A Comparison of Cross-Correlation and Frequency Domain Sweep Deconvolution", *Geophysical Prospecting*, Volume 49, pp. 675-686
- Brotz, R., Marschall, R. and Knecht, M. (1987) "Signal Adjustment of Vibroseis and Impulsive Source Data", *Geophysical Prospecting*, Volume 35, pp. 739-766
- Cambois, G. (2000) "Zero-Phasing the zero-phase source", *The Leading Edge*, Volume 19, pp. 72-75
- Cerveny, V. (2001) "Seismic Ray Theory", ISBN: 0-521-36671-2, Cambridge University Press
- Chapman, M. (2003) "Frequency Dependent anisotropy due to Meso-Scale Fractures in the Presence of Equant Porosity", *Geophysical Prospecting*, Volume 51, pp. 369-379
- Chen, S.T., Eriksen, E.A., Miller, M.A., Murray and T.J. Jr. (1990) "Multishot Downhole Explosive Device as a Seismic Source", Patent Number: 4895218
- Ching, P.C., So, H.C. and Wu, S.Q. (1999) "On Wavelet Denoising and Its Applications to Time Delay Estimation", *IEEE Transactions on Signal Processing*, Volume 47, pp. 2879-2882
- Chopra, A.K. (1995) "Dynamics of Structures: Theory and Applications to Earthquake Engineering", ISBN 0-13-855214-2, New Jersey: Prentice Hall, Inc.
- Cohen, L. (1992) "What is a Multi-Component Signal?" *IEEE Proceedings ICASSP*, San Francisco, CA, Volume 5, pp. 113-116.

- Crampin, S. (1981) "A Review of Wave Motion in Anisotropic and Cracked Elastic Media", *Wave Motion*, Volume 3, pp. 343-391
- Crampin, S. and Yedlin, M. (1981) "Shear-wave Singularities of Wave Propagation in Anisotropic Media", *Journal of Physics*, Volume 49, pp. 43-46
- Daley, T.M., McEvelly, T.V., and Majer, E.L. (1988) "Analysis of P and S Wave Vertical Seismic Profile Data From the Salton Sea Scientific Drilling Project", *Journal of Geophysical Research*, Volume 93, No. B11, pp. 13025-13036
- Dietrich, M., Menard, G. and Cornou, C. (2005) "Combined P and SH Vibroseis Profiling in the Isere Valley near Grenoble, France", *Geophysical Research Abstracts*, Volume 7, pp. 10387
- Digranes, P., Kristoffersen, K. and Karajev, N. (1996) "An analysis of shear waves observed in VSP data from the superdeep well at Kola, Russia", *Geophysical Journal International*, Volume 126 (2), pp. 545-554.
- Dimitriu, P.P. (1990) "Preliminary Results of Vibrator-Aided Experiments in Nonlinear Seismology Conducted at Uetze, F.R.G.", *Physics of the Earth and Planetary Interiors*, Volume 63, pp. 172-180
- Di Siena, J.P., Gaiser, J.E. and Corrigan, D. (1984) "Horizontal Components and Shear Wave Analysis of Three-Component VSP Data", *Vertical Seismic Profiling*, Geophysical Press, pp. 177-189
- Djurovic, I., Urlaub, M., Stankovic, L.J. and Beohme, J.F. (2004) "Estimation of Multicomponent Signals by Using Time-Frequency Representations with Application to Knock Signal Analysis", *Proc. Of EUSIPCO 2004*, Vienna, Austria, pp. 1785-1788
- Djurovic, I. (2007) "Estimation of the Sinusoidal Signal Frequency Based on the Marginal Median DFT", *IEEE Trans. Sig. Proc.* Volume 87, No.6, pp. 1537-1544
- Droujinine, A. (2006) "Multi-scale Geophysical Data Analysis Using the Eigenimage Discrete Wavelet Transform", *Journal of Geophysics and Engineers*, Volume 3, pp. 59-81
- Esmersoy, C. (1984) "Polarization Analysis, Rotation and Velocity Estimation in Three-Component VSP", *Vertical Seismic Profiling, Handbook of Geophysical Exploration*, 14B, pp. 236-255
- Fine, A.D. and Shield, R.T. (1966) "Second-Order Effects in the Propagation of Elastic Waves through Homogeneous Isotropic Media", *International Journal of Solids and Structures*, Volume 2, pp. 605-620

- Fokkema, J.T. and Ziolkowski, A. (1987) "The Critical Reflection Theorem", *Geophysics*, Volume 52, pp. 965-972
- Folstad, P.G. and Schoenberg, M. (1992) "Low Frequency Propagation through Fine Layering", *SEG Expanded Abstracts*, pp. 1278-1281
- Fox, P.A. (1955) "Perturbation Theory of Wave Propagation Based on the Method of Characteristics", *Journal of Mathematical Physics*, Volume 34, pp. 133-151
- Francos, A., Porat, M. (1999) "Analysis and Synthesis of Multi-component Signals Using Positive Time-Frequency Distributions", *IEEE Transactions on Signal Processing*, Volume 47, Number 2.
- Fryer, G.J. and Frazer, L.N. (1984) "Seismic Waves in Stratified Anisotropic Media", *Geophysical Journal of the Royal Astronomical Society*, Volume 78, pp.691-710
- Fryer, G.J. and Frazer, L.N. (1987) "Seismic Waves in Stratified Anisotropic Media-II", *Geophysical Journal of the Royal Astronomical Society*, Volume 91, pp.73-101
- Futterman, W.I. (1962) "Dispersive Body Waves", *J. Geophysical Research*, Volume 67, pp. 5279-5291
- Gaiser, J.E., Ward, R.W. and Disiena, J.P. (1984) "Three-Component Vertical Seismic Profiles: Velocity Anisotropy Estimates from P Wave Particle Motion in Vertical Seismic Profiling", London: Geophysics Press, pp. 189-204
- Gaiser, J.E. (1990) "Transversely Isotropic Phase Velocity Analysis from Slowness Estimates", *Journal of Geophysical Research*, Volume 95, No. B7, pp. 11,241–11,254
- Goldberg, Z.A. (1961) "On Interactions between Plane Longitudinal and Transverse Elastic Waves", *Soviet Physics-Acoustics*, Volume 6, pp. 306-310
- Gardner, M.G. and Price, R.K. (2007) "Summary Report of Geophysical Logging for the Seismic Boreholes Project at the Hanford Site Waste Treatment Plant", DTS-RPT-090 / PNNL-16395. Energy Solutions and Pacific Northwest Geophysics, Richland, Washington
- Grech, M.G.K., Lawton, D.C. and Gray, S.H. (2002) "A Multi-offset Vertical Seismic Profiling Experiment for Anisotropy Analysis and Depth Imaging", *Geophysics*, Volume 67, Issue 2, pp. 348-354
- Gupta, I.N. (1966) "Dispersion of Body Waves in Layered Media", *Geophysics*, Volume 31, Issue 4, pp. 821-823.

- Gupta, I.N. (1972) "A Comparison of Short-Wave and Long-Wave Velocities in Layered Media", *Pure and Applied Geophysics*, Volume 98, No.1, pp. 40-48.
- Hardage, B.A. (1983) "Vertical Seismic Profiling", Part A: Principles, London: Geophysical Press, 2nd Edition. pp. 509
- Hardage, R. (2000) "Vertical Seismic Profiling: Principles", ISBN: 0-08-043518-1
- Haskell, N. A. (1953) "Dispersion of surface waves on multilayered media," *Bulletin of the Seismological Society of America*, Volume 43, pp. 17-34
- Hauksson, E., Teng, T. L. and Henyey, T. (1987) "Results from a 1500 m Deep Three-Level Downhole Seismometer Array: Site Response, Low Q Values and Fmax", *Bulletin of the Seismological Society of America*, Volume 77, pp. 1883-1904
- Helbig, K. (1994) "Foundations of Anisotropy for Exploration Seismics", ISBN 0-08-037224-4
- Hero, A.O. and Schwartz, S.C. (1985) "A New Generalized Cross Correlator", *IEEE Transactions on Acoustics, Speech and Signal Processing*, Volume 33, pp. 38-45
- Ikelle, L.T. and Roberts, R. (1999) "Source Signature Determination and Multiple Reflection Reduction", Patent Number 5995905, Issue Date: Nov 30, 1999
- Jeffrey, A. and Taniuti, T. (1964) "Non-Linear Wave Propagation", Academic Press, New York
- Jeffrey, B. and Martin, J. (2003) "Method and Apparatus for Increasing Low Frequency Content During Vibroseismic Acquisition", United Kingdom Patent 04155180
- Jeffrey, B.P. (1996) "Far-field Sinusoidal Measurement for Seismic Vibrators", 66th Annual International Meeting, SEG, Expanded Abstracts, pp. 60-63
- Jiang, Z.J., Qiu, X.J., Lin, J. and Chen, Z. (2006) "Extracting Reflection with Wavelet Transform in Vibroseis Signal Processing", *Journal of Geophysics and Engineering*, Volume 3, pp. 236-242
- Jones, G.L. and Kobett, D.R. (1963) "Interaction of Elastic Waves in an Isotropic Solid", *The Journal of the Acoustical Society of America*, Volume 35, Issue 1, pp. 5-10
- Keith, C.M. and Crampin, S. (1977) "Seismic Waves in Anisotropic Media: Reflection and Refraction at a Plane Interface", *Geophysical Journal of the Royal Astronomical Society*, Volume 49, pp. 181-208
- Kennett, B.L.N. (1979) "Theoretical Reflection Seismograms for Elastic Media", *Geophysical Prospecting*, Volume 27, pp. 301-321

- Kennett, B. L. N. (1991) "The removal of free surface interactions from 3-component seismograms", *Geophysics Journal International*, Volume 104, pp. 153–163
- Kluwisch, A. and Nayfeh, A.H. (1979) "Nonlinear Waves in Homogeneous and Heterogeneous Elastic Solids", *J. Physique, Colloque*, Volume C8, pp. 207-211
- Kommedal, J.H. and Tjostheim, B.A. (1989) "A Study of Different Methods of Wavefield Separation for Application to VSP Data", *Geophysical Prospecting*, Volume 37, Issue 2 pp. 117
- Konovalov, G.E. and Kuzavko, I.A (1991) "Elastic Wave Harmonic Generation by a Nonlinear Boundary in a Two-layer Structure at Normal Incidence", *Akusticheskii Zhurnal* (ISSN 0320-7919), Volume 37, Sept.-Oct., pp. 950-955 (In Russian)
- Kramer, S.L. (1996) "Geotechnical Earthquake Engineering", ISBN 0-13-374943-6, New Jersey: Prentice Hall, Inc.
- Krey, T, and Helbig, K. (1956) "A Theorem Concerning Anisotropy of Stratified Media and Its Significance for Reflection Seismics", *Geophysical Prospecting*, Volume 4, pp. 294-302
- Lardner, R.W. (1986) "Nonlinear Surface Acoustic Waves on an Elastic Solid of General Anisotropy", *Journal of Elastic Volume* 16, pp. 63-73
- Lebedev, A.V. and Beresnev, I.A. (2004) "Nonlinear Distortion of Signals Radiated by Vibroseis Sources", *Geophysics*, Volume 69, No.4, pp. 968-977
- Lee, J.M. (1990) "In Situ Seismic Anisotropy and Its Relationship to Crack and Rock Fabrics", Ph.D Thesis, Pennsylvania State University
- Lee, M.W. (1987) "Particle Displacements on the Wall of a Borehole from Incident Plane Waves", *Geophysics*, Volume 52, pp. 1290-1296
- Lefeuvre, F., Nicoletis, L. Ansel, V. and Cllet, C. (1992) "Detection and Measure of the Shear Wave Birefringence from Vertical Seismic Data", *Geophysics*, Volume 57, pp. 1463-1481
- Lerwill, W.E. (1981) "The Amplitude and Phase Response of a Seismic Vibrator", *Geophysical Prospecting*, Volume 29, pp. 503-528
- Lin, C.C. (1954) "On a Perturbation Theory Based on the Method of Characteristics", *Journal of Mathematical Physics*, Volume 33, pp. 117-134
- Lindsey, J.P. (1991) "Seismic Sources I Have Known", *Geophysics: The Leading Edge of Exploration*, October

- Liu, E., Chapman, M., Li, X., Queen, J.H. and Lynn, H. (2006) "Kinematical and Dynamic Anisotropy: Implication for Seismic Fracture Characterization", SEG Technical Program Expanded Abstracts, pp. 135-139
- Loewenthal, D., Lee, S.S. and Gardner, G.H.F. (1985) "Deterministic estimation of a wavelet using impedance type technique", Geophysical Prospecting, Volume 33, pp. 956-969
- Loveridge, M.M., Parkes, G.E., Hatton, L. and Worthington, M.H. (1984) "Effects of marine source array directivity on seismic data and source signature deconvolution", First Break, July
- Macbeth, C. (2002) "Multi-Component VSP Analysis for Applied Seismic Anisotropy", ISBN: 0-08-042439-2, Elsevier Science Ltd.
- Majer, E.L., McEvelly, T.V., Eastwood, F.S., and Myer, L.R. (1988) "Fracture Detection Using P-Wave and S-wave Vertical Seismic Profiling at the Geysers", Geophysics, Volume 53, No.1, pp. 76-84
- Mari, J.L., Glangeaud, F. and Coppens, F. (1999) "Signal Processing for Geologists and Geophysicists", ISBN: 2-7108-0752-1, Paris: Editions Technip
- Marion, D., Mukerji, T., and Mavko, G. (1994) "Scale Effect on Velocity Dispersion: from Ray to Effective Medium Theories in Stratified Media", Geophysics, Volume 59, pp. 1613-1619
- Martin, J.E. and Jack, I.G. (1990) "The Behavior of a Seismic Vibrator using Different Phase Control Methods and Drive Level", First Break, Volume 8, pp. 404-414
- Martinez, D.R. (1987) "Method of Suppressing Vibration Seismic Signal Correlation Noise", Patent No. 4707812
- Mewhort, L., Bezdan, S. and Jones, M. (2002) "Does it Matter What Kind of Vibroseis Deconvolution is Used", CSEG Geophysics 2002
- Miller, D.E. and Spencer, C. (1994) "An Exact Inversion for Anisotropy Moduli from Phase Slowness Data", J. Geophysical Research, Volume 99, pp. 21651-21657
- Miller, G.F. and Pursey, H. (1954) "The field and radiation pattern of mechanical radiators on the free surface of a semi-infinite isotropic solid", Proceedings of the Royal Society, A223, pp. 521-541
- Musgrave, M.J.P. (1970) "Crystal Acoustics", Holden-Day

- Nair, S. and Nemat-Nasser, S. (1971) "On Finite Amplitude Waves in Heterogeneous Elastic Solids", International Journal of Engineering Science, Volume 9, pp. 1087-1105
- Naville, C. (1986) "Detection of Anisotropy Using Shear-Wave Splitting in VSP surveys", SEG Expanded Abstracts, pp. 391-394
- Nayfeh, A.H. (1973) "Perturbation Methods", New York: Wiley-Interscience
- Nayfeh, A. H. (1981) "Introduction to Perturbation Techniques", New York: Wiley-Interscience
- Nayfeh, A. H. (1986) "Problems in Perturbation", Applied Optics, Volume 25, Issue 18, pp. 3145
- Nayfeh, A.H. and Balachandran B. (1994) "Applied Nonlinear Dynamics: Analytical, Computational, and Experimental Methods", ISBN: 9780471593485
- Nayfeh, A.H. (1995) "Wave Propagation in Layered Anisotropic Media: with Application to Composites", ISBN: 0-444-89018-1, Elsevier Science
- Nayfeh, A.H. (2000) "Nonlinear Interactions: Analytical, Computational, and Experimental Methods", ISBN: 9780471175919
- Nicoletis, L, Cllet, C. and Lefeuvre, F. (1988) "Shear-Wave Splitting Measurements from MultiShot VSP Data", SEG Expanded Abstracts, pp. 527-530
- Okaya, D.A. Karageorgi, E., McEvelly, T.V. and Malin, P.E. (1992) "Removing Vibrator-Induced Correlation Artifacts by Filtering in Frequency-Uncorrelated Time", Geophysics, Volume 57, pp. 916-926
- Oppenheim, A.V. and Schafer, R.W. (1975) "Digital Signal Processing", Prentice Hall, Inc. Englewood Cliffs
- Oye, V. and Ellsworth, W.L. (2005) "Orientation of Three-Component Geophones in the San Andreas Fault Observatory at Depth Pilot Hole, Parkfield, California", Bulletin of the Seismological Society of America, Volume 95, No.2, pp. 751-758
- Papoulis, A. (1962) "The Fourier Integral and Its Applications", New York: McGraw-Hill Book Company, Inc.
- Poletto, F. and Dordolo, G. (2002) "A New Approach to Offshore Drill-bit Reverse Vertical Seismic profiling", Geophysics, Volume 67, No. 4, pp. 1071-1075

- Pujol, J., Burridge, R. and Smithson, S.B. (1985) "Velocity Determination from Offset Vertical Seismic Profiling Data", *Journal of Geophysical Research*, Volume 90, pp. 1871-1880
- Puzirev, N.N. et al. (1985) "Seismic Prospecting by Method of Shear and Converted Waves", Nedra, Moscow
- Qian, Z.W. (1989) "Equations of the Second-Order Potentials of Finite-Amplitude Waves in Elastic Solids", *Journal of the Acoustical Society of America*, Volume 86, Issue 5, pp. 1965-1967
- Rabbel, W., et al. (2004) "Superdeep Vertical Seismic Profiling at the KTB Deep Drill Hole (Germany): Seismic Close-up View of a Major Thrust Zone Down to 8.5 km Depth", *J. Geophys. Res.*, Volume 109
- Redpath, B.B. (2007) "Downhole Measurements of Shear- and Compression- Wave Velocities in Boreholes C4993, C4997, C4997 and C4998 at the Waste Treatment Plant DOE Hanford Site", PNNL-16559, Redpath Geophysics, Murphys, California
- Rice, R.B. (1962) "Inverse Convolution Filters", *Geophysics*, Volume 27, pp. 4-18
- Richard, F. E. Jr., Woods, R.D. and Hall, J.R. (1970) "Vibrations of Soils and Foundations", Prentice-Hall
- Ricker, N. (1940) "The Form and Nature of Seismic Waves and the Structure of Seismograms", *Geophysics*, Volume 5, pp. 348-366
- Robinson, E.A. (1957) "Predictive Decomposition of Seismic Traces", *Geophysics*, Volume 22, pp. 767-778
- Robinson, E.A. and Saggaf, M. (2001) "Klauder Wavelet Removal before Vibroseis Deconvolution", *Geophysical Prospecting*, Volume 49, pp. 335-340
- Rohay, A.C. and Brouns, T.M. (2007) "Site-Specific Velocity and Density Model for the Waste Treatment Plant, Hanford, Washington". PNNL-16652, Pacific Northwest National Laboratory, Richland, Washington
- Ryan-Grigor, S. (1997) "Empirical relationships between transverse isotropy parameters and V_p/V_s : Implications for AVO", *Geophysics*, Volume 62, pp 1359-1364
- Sallas, J.J. and Weber, R.M. (1982) "Comments on 'The amplitude and phase response of a seismic vibrator' by W.E. Lerwill", *Geophysical Prospecting*, Volume 30, pp. 935-938

- Sallas, J.J. (1984) "Seismic Vibrator Control and the Downgoing P-Wave", *Geophysics*, Volume 49, pp. 732-740
- Sato, H. and Fehler, M.C. (1998) *Seismic Wave Propagation and Scattering in the Heterogeneous Earth*.
- Sharma, M. D. (2002) "Group Velocity Along General Direction in a General Anisotropic Medium", *International Journal of Solids and Structures*, Volume 39, pp. 3277-3288
- Shu, K. T. (1990) *Multidimensional Reflection and Refraction of Finite Amplitude Stress Waves in Elastic Solids*, PhD Dissertation: Georgia Institute of Technology, Atlanta, Georgia
- Sonneland, L. and Berg, L.E. (1985) "A New Method for Separating Wave Fields into Up- and Down-going Components", 47th EAEG Meeting, Budapest
- Sonneland, L. et al (1986) "2-D Deghosting Using Vertical Receiver Arrays", *SEG Technical Program Expanded Abstracts*, Volume 5, pp. 516-519
- Stewart, R.R. (1983) "Vertical Seismic Profiling: the One-Dimensional Forward and Inverse problems", Ph.D. Thesis, Massachusetts Institute of Technology, Cambridge, MA
- Stewart, R.R. (1984) "VSP Interval Velocities from Travel Time Inversion", *Geophysical Prospecting*, Volume 32, pp. 608-628
- Stokoe, K.H., II, Rosenblad, B.L., Wong, I.G., Bay, J.A., Thomas, P.A., and Silva, W.J., (2004A) "Deep Vs profiling along the Top of Yucca Mountain using a Vibroseis Source and Surface Waves", Paper No.538, 13th World Conference on Earthquake Engineering, Vancouver, Canada, August 1st-6th.
- Stokoe, K.H., II, Rathje, E.M., Wilson, C. and Rosenblad, B. (2004B) "Development of Large-Scale Mobile Shakers and Associated Instrumentation for In Situ Evaluation of Nonlinear Characteristics and Liquefaction Resistance of Soils," 13th World Conference on Earthquake Engineering, Vancouver, B.C. Canada, August 1-6
- Svenningsen, L. and Jacobsen, B. H. (2007) "Absolute S-velocity estimation from Receiver Functions", *Geophysical Journal International*, Volume 170 (3), pp. 1089–1094
- Thomsen, L. (1986) "Weak Elastic Anisotropy", *Geophysics*, Volume 51, No.10. pp. 1954-1966

- Thomson, W. T. (1950) "Transmission of Elastic Waves through a Stratified Solid Medium," *Journal of Applied Physics*, Volume 21, pp. 89-93, 1950
- Thompson R.B. and Tiersten, H.F. (1977) "Harmonic Generation of Longitudinal Elastic Waves", *The Journal of the Acoustical Society of America*, Volume 62, Issue 1, July, pp.33-37
- Trantham, E.C. (1995) "Seismic Vibrator Signature Deconvolution", Patent No.5400299
- Treitel, S., Gutowski, P.R. and Wagner, D.W. (1982) "Plane-wave Decomposition of Seismograms", *Geophysics*, Volume 47, pp. 1375-1401
- Tsvankin, I. (2001) "Seismic Signatures and Analysis of Reflection Data in Anisotropic Media," ISBN: 0-08-043649-8, 1st Edition: Elsevier Science
- Tsvankin, I. (2005) "Seismic Signatures and Analysis of Reflection Data in Anisotropic Media," 2nd Edition: Elsevier Science
- Tygel, M. and Hubral P. (1987) "Transient Waves in Layered Media", *Methods of Geophysics and Geochemistry*, Volume 26, New York: Elsevier Science Publication Co. Inc.
- Tygel, M., Huck, H. and Hubral P. (1991) "Mixed-delay Wavelet Deconvolution of the Point-Source Seismogram", *Geophysics*, Volume 56, No.9, pp. 1405-1411
- Ursin,B. and Stovas, A. (2006) "Traveltime Approximations for a Layered Transversely Isotropic Medium", *Geophysics*, Volume 71, No.2, pp. D23-D33
- Voigt, W. (1928) "Lehrbuch der Kirstallphysik", Teubner, Leipzig
- Walker, D., (1995) "Harmonic resonance structure and chaotic dynamics in the earth-vibrator system", *Geophysical Prospecting*, Volume 43, pp. 487-507
- Wason, C.B. and Potts, M.J. (1984) "Some Salient Issues in Vibrator Data Processing", *SEG Technical Program Expanded Abstracts*, Volume 3, pp, 767
- Weglein, A. and Secret, B.G. (1990) "Wavelet Estimation for a Multidimensional Acoustic or Elastic Earth", *Geophysics*, Volume 55, pp. 902-913
- Wei, Y. and Bi, G. (2005) "Efficient Analysis of Time-Varying Multicomponent Signals with Modified LPTFT", *EURASIP Journal on Applied Signal Processing*, Volume 8, pp. 1261-1268
- White, J.E. (1982) "Computed Waveforms in Transversely Isotropic Media", *Geophysics*, Volume 47, pp. 771-783

- Winterstein, D.F. (1990) "Velocity Anisotropy Terminology for Geophysicists", *Geophysics*, Volume 55, No.8, pp. 1070-1088
- Winterstein, D.F. and Meadows, M.A. (1991A) "Changes in Shear Wave Polarization Azimuth with Depth in Cymric and Railroad Gap Oil Fields", *Geophysics*, Volume 56, pp. 1349-1364
- Winterstein, D.F. and Meadows, M.A. (1991B) "Shear Wave Polarizations and Subsurface Stress Directions at Lost Hills Field", *Geophysics*, Volume 56, pp. 1331-1348
- Winterstein, D.F. and Paulsson, B.N.P. (1990) "Velocity Anisotropy in Shale Determined from Cross-hole Seismic and VSP Data", *Geophysics*, volume 55, pp. 470-479
- Yamshchikov, V.S. (1965) "Attenuation Elastic Waves in Rocks in the Region of Low-Intensity Oscillations", *Zhurnal Prikladnoi Mekhaniki i Tekhnicheskoi Fiziki*, No. 3, pp. 134-136
- Yu, J.H. and Schuster, G. (2006) "Crosscorrelogram Migration of Inverse Vertical Seismic Profile Data", *Geophysics*, Volume 71, Issue 1, pp. s1-s11
- Zeng, X.W and Macbeth, C. (1993) "Algebraic Processing Techniques for Estimating Shear-Wave Splitting in Near-Offset VSP Data: Theory", *Geophysical Prospecting*, Volume 41 (8), pp. 1033-1066
- Zhu, Y., Tsvankin, I., Dewangan, P., and Wijk, K.V. (2007) "Physical Modeling and Analysis of P-wave Attenuation anisotropy in Transversely Isotropic Media", *Geophysics*, Volume 72, No. 1, pp. D1-D7
- Zilmer, M. D., Gajewski, D. and Kashtan, B. M. (1998) "Anisotropic Reflection Coefficients for a Weak Contrast Interface", *Geophysical Journal International*, Volume 129, pp. 389-398
- Ziolkowski, A.M. and Lerwill, W.E. (1979) "A Simple Approach to High Resolution Seismic Profiling for Coal", *Geophysical Prospecting*, Volume 27, pp.360-393
- Ziolkowski, A.M., Lerwill, W.E., March, D.W. and Peardon, L.G. (1980) "Wavelet Deconvolution Using a Source Scaling Law", *Geophysics Prospecting*, Volume 28, pp. 872-901
- Ziolkowski, A., Ras, P.A.W. and Fokkema, J.T. (1987) "Extraction of the Dynamite Wavelet on Real Data Using the Critical Reflection Theorem", *Intermediate Report of Project No. 2011-01610, Delft University*

Vita

Songcheng Li was born in Hunan, China, on March 27, 1968, the son of Wanquan Li and Xiangqun Liao. He graduated from Tsinghua University, Beijing, China, and received Bachelor of Science degree in Civil Engineering in June 1991. He worked in Mid-South Design and Research Institute, China, before his graduate study in Tsinghua University. He received his Master of Science degree in Civil Engineering in June 1996. He worked in Shanghai Foundation Engineering Company, China, and in CapitaLand China until he enrolled at the University of Texas at Austin in spring 2003.

Permanent address: 302/11/70 Songbin Road, Shanghai, China, 200940

This dissertation was typed by the author